Technical Report: Deliverable 9

Title: Crack Width Limit for UHPC Structural Members in Coastal and Marine Environment

FDOT Contract Number: BED30 977-05

Submitted to

The Florida Department of Transportation Research Center
605 Suwannee Street, MS 30 Tallahassee, FL 32399

FDOT Project Manager: Steve Nolan
State Structures Design Office

Submitted by:

Dr. Qian Zhang (qzhang@eng.famu.fsu.edu) (Principal Investigator)
Dr. Kyle Riding (kyle.riding@essie.ufl.edu) (Co-Investigator)
Peizhi Wang (pwang9@fsu.edu) (Graduate Assistant)
Randa Zeidan (zeidan.randa@ufl.edu) (Graduate Assistant)

Civil & Environmental Engineering
FAMU-FSU College of Engineering
Florida State University
2525 Pottsdamer Street, Suite B316
Tallahassee FL 32310

Engineering School of Sustainable Infrastructure and Environment
University of Florida
365 Weil Hall PO Box 116580
Gainesville, Florida 32611

June 2026

Department of Civil & Environmental Engineering
FAMU-FSU College of Engineering
Florida State University

Department of Civil Engineering
Engineering School of Sustainable Infrastructure and Environment
College of Engineering
University of Florida

DISCLAIMER

The Florida Department of Transportation does not concur with the findings and conclusions of this research.

The opinions, findings, and conclusions expressed in this publication are those of the authors and not necessarily those of the Florida Department of Transportation

The contents of this report reflect the views of the authors, who are responsible for the facts and the accuracy of the information presented herein. This document is disseminated under the sponsorship of the Department of Transportation's University Transportation Centers Program, in the interest of information exchange. The U.S. Government assumes no liability of the contents or use thereof.

SI (MODERN METRIC) CONVERSION FACTORS (FROM FHWA)

Symbol	When You Know	Multiply By	To Find	Symbol
Length				
in	inches	25.4	millimeters	mm
ft	feet	0.305	meters	m
yd	yards	0.914	meters	m
mi	miles	1.61	kilometers	km
Area				
in^2	square inches	645.2	square millimeters	mm^2
ft^2	square feet	0.093	square meters	m^2
yd^2	square yard	0.836	square meters	m^2
mi^2	square miles	2.59	square kilometers	km^2
Volume				
fl oz	fluid ounces	29.57	milliliters	mL
gal	gallons	3.785	liters	L
ft^3	cubic feet	0.028	cubic meters	m^3
yd^3	cubic yards	0.765	cubic meters	m^3
NOTE: volumes greater than 1000 L shall be shown in m^3				
Mass				
oz	ounces	28.35	grams	g
lb.	pounds	0.454	kilograms	kg
Temperature (exact degrees)				
°F	Fahrenheit	5 (F-32)/9 or (F-32)/1.8	Celsius	°C
Illumination				
fc	foot-candles	10.76	lux	lx
fl	foot-Lamberts	3.426	candela/m^2	cd/m^2
Force and Pressure or Stress				
lbf	pound-force	4.45	newtons	N
lbf/in^2	pound-force per square inch	6.89	kilopascals	kPa

TECHNICAL REPORT DOCUMENTATION

1. Report No.	2. Government Accession No.	3. Recipient's Catalog No.
4. Title and Subtitle Crack Width Limit for UHPC Structural Members in Coastal and Marine Environment		5. Report Date June 2026 6. Performing Organization Code
7. Author(s) Qian Zhang, Kyle Riding, Peizhi Wang, Randa Zeidan		8. Performing Organization Report No.
9. Performing Organization Name and Address Florida State University 874 Traditions Way, Tallahassee, FL 32306 University of Florida 365 Weil Hall PO Box 116580, Gainesville, FL 32611		10. Work Unit No. 11. Contract or Grant No. BED30 977-05
12. Sponsoring Agency Name and Address Florida Department of Transportation 605 Suwannee Street, MS 30 Tallahassee, FL 32399		13. Type of Report and Period Covered Written technical report Deliverable 9 May 2021 – Jun. 2026 14. Sponsoring Agency Code
15. Supplementary Notes – N/A		

16. Abstract

Ultra-high-performance concrete (UHPC) is increasingly used in transportation infrastructure because of its high strength, dense microstructure, low permeability, fiber-bridged crack control, and self-healing potential. These properties make UHPC suitable for structural members exposed to coastal and marine environments, where chloride-induced corrosion of embedded reinforcement is a major durability concern. However, the durability performance of cracked UHPC remains less clearly defined, particularly with respect to chloride ingress, crack geometry, self-healing, and reinforcement corrosion under realistic marine exposure conditions. This report evaluates crack-width limits for UHPC structural members exposed to chloride-rich environments. The study included a literature review, mixture characterization of four UHPC mixtures, chloride migration testing, long-term bulk diffusion testing, laboratory wetting–drying corrosion exposure, and tidal-zone marine exposure at Seahorse Key Island. The results showed that uncracked UHPC provided very high resistance to chloride ingress and maintained passive reinforcement conditions. In cracked UHPC, chloride transport was governed by crack width, crack depth, crack density, crack interaction, and self-healing behavior. Although cracked regions showed higher chloride transport than uncracked UHPC, corrosion activity generally remained low when cracks were tight and adequate cover was provided. Based on the experimental results, crack-width action levels are recommended for UHPC members with cover thickness greater than 25.4 mm (1.0 in.), including routine acceptance for cracks not exceeding 0.20 mm (0.008 in.), monitoring or preventive sealing for cracks from 0.20 to 0.40 mm (0.008 to 0.016 in.), engineering review for cracks from 0.40 to 0.80 mm (0.016 to 0.031 in.), and immediate repair review for cracks greater than 0.80 mm (0.031 in.).

17. Key Word	18. Distribution Statement
UHPC, transport properties, corrosion rate, influence of cracks	No restrictions.

19. Security Classif. (of this report)	20. Security Classif. (of this page)	21. No. of Pages	22. Price
Unclassified.	Unclassified.	209	

ACKNOWLEDGEMENTS

The authors gratefully acknowledge the financial support provided by the Florida Department of Transportation Research Center under Contract No. BED30 977-05, prepared in cooperation with the U.S. Department of Transportation. The authors also extend their sincere appreciation to Steven Nolan of the FDOT State Structures Design Office for serving as the FDOT Project Manager and for his guidance, coordination, and support throughout the project.

The authors would like to thank the FDOT Structures Research Center staff for their assistance during the experimental program. Special appreciation is extended to Christina Freeman for coordinating casting activities and providing support during testing, and to Olga Iatsko for assistance with specimen casting, testing, and technical recommendations. The authors also acknowledge Miguel Ramirez, Chris Schild, Michael Waters, Paul Tighe, Ben Allen, Yukai Yang, Clark Conyers, and Wade Johnson for their assistance with specimen casting, sample preparation, and construction of the testing platform.

The authors also gratefully acknowledge the support provided by the FDOT State Materials Office. Appreciation is extended to Ronald Simmons for assisting with specimen exposure and corrosion testing. The authors also thank Charlotte Kasper and Elizabeth Miller for their assistance with titration testing.

PREFACE

This report was prepared as part of Florida Department of Transportation Contract No. BED30 977-05, titled *Crack Width Limit for UHPC Structural Members in Coastal and Marine Environment*. The work was sponsored by the Florida Department of Transportation Research Center in cooperation with the U.S. Department of Transportation. The FDOT project manager for this study was Steve Nolan of the State Structures Design Office.

The purpose of this study was to evaluate the durability performance of cracked ultra-high-performance concrete structural members exposed to coastal and marine environments and to develop recommended crack-width action levels for UHPC members subjected to direct chloride exposure. The investigation focused on chloride ingress, self-healing behavior, corrosion activity of embedded steel reinforcement, and the influence of crack width and reinforcement cover thickness.

The research was performed by the Department of Civil and Environmental Engineering at the FAMU-FSU College of Engineering, Florida State University, and the Engineering School of Sustainable Infrastructure and Environment at the University of Florida. The project team included Dr. Qian Zhang as Principal Investigator, Dr. Kyle Riding as Co-Investigator, Peizhi Wang as Graduate Assistant, and Randa Zeidan as Graduate Assistant.

EXECUTIVE SUMMARY

Ultra-high-performance concrete (UHPC) has been increasingly considered for transportation infrastructure exposed to coastal and marine environments because of its dense microstructure, high mechanical strength, low permeability, fiber-bridged cracking behavior, and potential for autogenous self-healing. These properties allow UHPC to provide improved protection for embedded steel reinforcement compared with conventional concrete. However, the durability of cracked UHPC members remains an important concern because cracks can create preferential pathways for chloride ions, moisture, and oxygen to reach the reinforcement. This issue is particularly relevant for structural members exposed to seawater, tidal action, salt spray, or other chloride-rich environments. Although uncracked UHPC has been shown to provide strong corrosion protection, the effects of crack width, crack depth, crack density, crack interaction, self-healing, and reinforcement cover thickness on chloride penetration and corrosion activity have not been fully established.

The primary objective of this study was to develop recommended crack-width action levels for reinforced UHPC structural members exposed to coastal and marine environments. To support this objective, the report reviewed the corrosion mechanisms of steel reinforcement in concrete, the transport properties and corrosion resistance of uncracked UHPC, and the influence of cracking on chloride ingress and corrosion behavior. The experimental program evaluated four UHPC mixtures, including three commercial mixtures and one non-proprietary mixture. Testing included mechanical characterization, modified electrochemical chloride migration testing, long-term bulk diffusion testing, laboratory chloride wetting–drying exposure, and realistic tidal-zone marine exposure at Seahorse Key Island.

The results confirmed that uncracked UHPC provides very high resistance to chloride ingress and reinforcement corrosion. Apparent chloride diffusion coefficients for uncracked UHPC were on the order of 10^{-14} m²/s (10^{-13} ft²/s) (10^{-13} ft²/s), and chloride penetration depths measured by silver nitrate colorimetric testing were limited to approximately 1 to 4 mm (0.04 to 0.16 in.). The corrosion current density of embedded steel reinforcement in uncracked UHPC remained within the passive range throughout the exposure period. These results indicate that the dense UHPC matrix can substantially restrict the transport of chlorides, moisture, and oxygen to embedded reinforcement when cracking is not present.

For cracked UHPC, chloride transport was controlled primarily by crack geometry and crack network characteristics rather than by surface crack width alone. Single cracks acted as localized chloride transport pathways, while multiple cracks created interacting and overlapping chloride penetration zones. In cracked regions, the apparent chloride diffusion coefficient increased by approximately two to three orders of magnitude compared with uncracked UHPC, reaching values on the order of 10^{-12} to 10^{-11} m²/s (10^{-11} to 10^{-10} ft²/s). The results showed that crack width, crack depth, crack number, crack spacing, tortuosity, and interaction between adjacent cracks all influenced chloride ingress. Surface self-healing reduced chloride penetration, especially for narrow cracks, but did not fully restore the impermeability of the uncracked UHPC matrix.

The laboratory wetting–drying exposure tests showed that cracking increased corrosion activity at the beginning of chloride exposure, but corrosion current density generally decreased and stabilized with time. This reduction was attributed to continued hydration, precipitation of healing products inside cracks, increased electrical resistivity, and reduced transport of oxygen, moisture, and chloride ions to the steel surface. Crack width was the primary factor controlling corrosion performance, while reinforcement cover thickness provided additional protection. Increasing the cover thickness from 12.7 mm (0.5 in.) to 25.4 mm (1.0 in.) generally reduced corrosion activity in cracked specimens, although the effect of cover thickness was secondary to the effect of crack width. The results also showed that corrosion potential alone may not be used to evaluate corrosion activity in UHPC because several specimens indicated high corrosion risk by potential measurements while maintaining low corrosion current densities.

The tidal-zone marine exposure at Seahorse Key Island provided additional evidence of the durability performance of cracked UHPC under realistic marine conditions. After 270 days of exposure, the specimen with a primary crack width of approximately 309 μm (0.0122 in.) achieved complete crack-mouth closure, while specimens with larger cracks ranging from approximately 447 to 771 μm (0.0176 to 0.0304 in.) showed only partial closure. Corrosion current densities remained low or decreased during exposure for specimens with crack widths below approximately 603 μm (0.0237 in.), while wider cracks produced higher corrosion activity. Compared with the laboratory wetting–drying exposure, the marine-exposed specimens generally showed lower corrosion current densities, indicating that the laboratory exposure condition was more aggressive.

Based on the combined chloride transport, self-healing, and corrosion results, recommended crack-width action levels were developed for UHPC members with reinforcement cover greater than 25.4 mm (1.0 in.). Cracks not exceeding 0.20 mm (0.0079 in.) are recommended as the preferred design target and routine field acceptance range when the crack system is stable, non-leaking, not through-depth, and not connected to reinforcement. Cracks from 0.20 to 0.40 mm (0.0079 to 0.0157 in.) should be documented and monitored, with preventive sealing considered in severe exposure zones or locations where cracks are likely to remain wet. Cracks from 0.40 to 0.80 mm (0.0157 to 0.0315 in.) should not be treated as routine acceptable cracking and should require engineering review, with sealing or repair unless a project-specific durability assessment supports continued service. Cracks greater than 0.80 mm (0.0315 in.) should require immediate engineering review and repair, particularly when associated with leakage, rust staining, delamination, spalling, exposed reinforcement, abnormal deflection, or rapid crack growth.

Overall, the study indicates that UHPC can provide strong resistance to chloride-induced corrosion in coastal and marine environments, even when cracking occurs, provided that crack widths are controlled and adequate reinforcement cover is used. However, allowable crack-width criteria for UHPC should not be based on surface crack width alone. Crack morphology, crack connectivity, crack density, cover thickness, exposure severity, self-healing behavior, chloride penetration, and measured corrosion current density should be considered together when evaluating durability risk and selecting monitoring or repair actions. The proposed crack-width action levels provide a practical framework for inspection, maintenance, and durability-based decision-making for UHPC structural members exposed to chloride environments.

TABLE OF CONTENTS

LIST OF FIGURES

LIST OF TABLES

1 Introduction

1.1 Research problem and background

Steel corrosion is one of the most significant deterioration mechanisms affecting reinforced concrete infrastructure in coastal and marine environments. In sound concrete, the highly alkaline pore solution forms a passive film on the surface of embedded reinforcing steel, which protects the steel from active corrosion. This passive condition can be disrupted when chloride ions penetrate through the concrete cover and accumulate at the steel surface. Once the chloride concentration reaches a critical level, localized depassivation and corrosion can occur. The propagation of corrosion depends on the availability of oxygen, moisture, ionic conductivity, and the transport properties of the surrounding concrete.

Ultra-high performance concrete (UHPC) is expected to improve corrosion resistance because its dense matrix and disconnected pore structure greatly reduce the transport of aggressive substances. Previous studies have shown that uncracked UHPC exhibits very low porosity, sorptivity, water permeability, gas permeability, chloride migration, and chloride diffusion compared with conventional concrete. These properties allow UHPC to provide strong protection for steel reinforcement under uncracked conditions. In addition, steel fibers in UHPC can bridge cracks, restrict crack opening, and promote tight crack patterns, which may further improve durability.

However, the durability performance of UHPC under cracked conditions is not fully understood. Cracks can locally bypass the dense UHPC matrix and provide direct pathways for chloride ions, water, and oxygen. Although some studies have shown that transport properties of cracked UHPC increase with crack width, the roles of crack depth, crack density, crack interaction, realistic V-shaped flexural cracks, and self-healing are still not well established. The literature also contains limited data on corrosion of steel reinforcement embedded in cracked UHPC, especially under realistic marine exposure. This creates uncertainty when selecting allowable crack-width limits for UHPC members used in coastal bridge and marine infrastructure applications.

The development of crack-width limits for UHPC members exposed to chloride environments requires consideration of both chloride ingress and reinforcement corrosion response. Although cracks may provide preferential pathways for chloride penetration, chloride ingress alone does not necessarily indicate sustained corrosion propagation in UHPC. The dense matrix, high electrical resistivity, restricted oxygen transport, fiber-bridged crack morphology, and potential autogenous self-healing of UHPC can limit corrosion activity even when localized chloride penetration occurs along cracks. Therefore, crack-width criteria for UHPC should be established based on a combined evaluation of chloride penetration, corrosion current density, crack morphology, reinforcement cover thickness, and exposure severity.

1.2 Research objectives

The primary objective of this study was to develop guidance for crack-width action levels for UHPC structural members exposed to coastal and marine environments. The action levels were intended to support durability assessment, inspection, maintenance, and repair decisions for reinforced UHPC members subjected to chloride exposure.

The specific objectives of this research were to:

1. Review the corrosion mechanisms of steel reinforcement in concrete and identify the key factors controlling corrosion initiation and propagation in chloride-rich environments. In addition, summarize the transport properties and corrosion resistance of uncracked UHPC, including porosity, sorptivity, water permeability, gas permeability, chloride migration, chloride diffusion, and the corrosion behavior of steel fibers and embedded steel reinforcement.

2. Evaluate the influence of cracking on chloride transport in UHPC, with emphasis on crack patterns.
3. Quantify chloride penetration in cracked UHPC specimens and assess how different crack patterns affect chloride ingress.
4. Evaluate the corrosion behavior of steel reinforcement embedded in cracked UHPC under laboratory wetting–drying cycles and realistic tidal-zone marine exposure conditions.
5. Develop recommendations for UHPC structural members exposed directly to chloride environments.

The outcomes of this study provided a technical basis for evaluating acceptable cracking in UHPC members exposed to coastal and marine environments. The recommended crack-width action levels were intended to improve durability-based decision-making for UHPC structures in chloride-rich environment.

2 Literature review

2.1 Corrosion of steel in concrete

Corrosion is a natural phenomenon, which refers to an electrochemical reaction between the reinforcing steel and the environment causing deterioration of steel members and their properties (Covino, Bernard and Stephen, 2012). Steel reacts with water and oxygen resulting in production of rust ($Fe(OH)_2$, $Fe(OH)_3$, and $Fe_2O_3 \cdot H_2O$) (Goyal *et al.*, 2018). Steel corrosion also occurs in reinforced concrete elements. Water (liquid or moisture) and oxygen could penetrate the concrete cover, reach the surface of steel reinforcements, and react with reinforcing steel resulting in corrosion. Corrosion of steel reinforcement reduces the cross-sectional area of steel reinforcement, which lowers the load carrying capacity of reinforced concrete members. Additionally, rust is a highly porous mixture with volume six to ten times larger than steel (Bertolini *et al.*, 2014). The expansion of steel due to corrosion also cause cracks, spalling and delamination of the concrete cover, further reducing the capacity of reinforcement concrete members (Goyal *et al.*, 2018). Corrosion damage of steel reinforcement is the most common reason for reinforced concrete structural failures (Berrocal, Lundgren and Löfgren, 2016).

Reinforcing steel corrosion typically involves two stages: corrosion initiation and propagation. During hydration of cement, a highly alkaline pore solution is created, containing primarily NaOH and KOH. The pH value of the pore solution is between 13 and 14 (Bertolini *et al.*, 2014). A thin protective oxide film, also named passive film, is produced spontaneously on the reinforcing steel surface within such highly alkaline environment. This passive film mainly consists of γ-Fe_2O_3 and Fe_3O_4 tightly adhering to the steel reinforcement with thickness in the range of 10^{-3} to 10^{-1} μm (3.94×10^{-8} in. to 3.94×10^{-6} in.)(Goyal *et al.*, 2018). It prevents the steel reinforcement from contacting the oxygen and water, blocking the movement of ions between the steel and adjacent concrete, therefore preventing corrosion from occurring. However, this passive film is only stable in a highly alkaline environment (pH value in the range of 12 to 14) (Bertolini *et al.*, 2014) . The passive film would be damaged if the pH value of pore solution decreases, for example, due to carbonation. Also, when chloride ion concentration on the steel reinforcement reaches a threshold level, the passive film will break down (Bertolini *et al.*, 2014). In these cases, the reinforcing steel is depassivated and corrosion of steel reinforcement initiates. The depassivation of reinforcing steel due to carbonation of concrete or presence of chloride is considered the corrosion initiation stage, and the subsequent propagation stage is characterized by the corrosion reaction of steel reinforcement, and cracking and spalling of concrete covers. This process is illustrated in Figure 2-1.

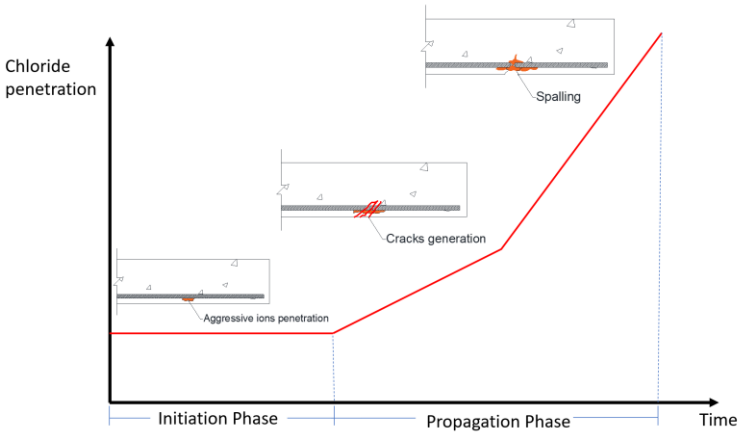

Figure 2-1 The initiation and propagation periods for corrosion in a reinforced concrete structure

2.1.1 Corrosion initiation

During the initiation phase, there are two major sources which lead to the breakdown of the passive film:

1) Chloride ions. Sometimes, the mixture of concrete contains chloride ions inside, when water containing salts, sea-degraded sand and gravel, or chloride-containing admixtures are used to produce the concrete. External chloride ions could also penetrate the concrete cover and be present at the surface of steel reinforcement. When the chloride ion concentration next to the passive film reaches a critical value, the passive film is locally broken down (Parangusan, Bhadra and Al-Thani, 2021), and so-called pitting corrosion occurs. The threshold value for the initiation of pitting corrosion mainly depends on several interrelated factors, such as temperature and humidity of the environment, moisture content inside concrete, pH of pore solution, electrochemical potential of the steel, and presence of interconnected channels (pore system) between steel and concrete. To avoid the initiation of pitting corrosion, some factors are adopted to represent the threshold value of chloride content. It has been reported that if the chloride content by weight of cement exceeds 0.1 to 0.5 wt.%, the initiation of pitting corrosion would begin (Ann and Song, 2007). The ratio of Cl^- and OH^- can also be used as a criterion to control the threshold value for initiation of pitting corrosion. It has been reported that if the ratio exceeds the range of 0.3 to 40, the initiation of pitting corrosion has been observed (Ann and Song, 2007). Besides the observation from research, the threshold values of chloride content for normal concrete are also recommended by standards. The maximum total chloride content is recommended as 0.08 wt.% by weight of cementitious mixture by the AASHTO LRFD Bridge Construction Specification (2010). ACI 318-19 Building Code Requirements for Structural Concrete (2019) limits the free or water-soluble chloride content for concrete exposed to seawater to 0.15 % and 0.06 % by weight of cementitious mixture for non-prestressed concrete and prestressed concrete, respectively. The maximum total chloride limit (acid soluble chlorides) for conventional concrete under FDOT Specification 346-3.4.2 is 0.40 lbs/CY (FDOT, 2022). The proposed limit for UHPC under the recently completed FDOT research project BDV31 977-105 is 0.50 lbs/CY (Riding *et al.*, 2022). During the initiation of pitting corrosion, the Fe^{2+} of the passive film will react with Cl^- and produce $FeCl_2$ as Equation 1. The $FeCl_2$ further reacts with water to produce $Fe(OH)_2$, H^+, and Cl^- as shown in Equation 2. During this process, the chloride ions are only consumed at the intermediate stage, and continue to aggress the environment, reducing the local pH of pore solution and further undermining the passive film.

$$Fe^{2+} + 2Cl^- \rightarrow FeCl_2 \quad \text{(Equation 1)}$$

$$FeCl_2 + 2H_2O \rightarrow Fe(OH)_2 + 2H^+ + 2Cl^- \quad \text{(Equation 2)}$$

2) Concrete carbonation: carbon dioxide from atmosphere penetrates concrete and neutralizes alkaline pore solution, which leads to a significant reduction of pH value of pore solution from the range of 13 - 14 to the range of 8 - 9 (Bertolini *et al.*, 2014). The process is shown as Equation 3 and Equation 4. The CO_2 reacts with water and produces H_2CO_3 shown in Equation 3. The H_2CO_3 subsequently reacts with $Ca(OH)_2$ in pore water, which neutralizes the alkaline pore solution as Equation 4. The passive film is unstable and dissolves within pore solution for pH values lower than 12 (Banaś et al., 2007; Bertolini et al., 2014). Then the reinforcing steel begins to corrode as it is exposed to oxygen and water. Carbonation-induced corrosion is often referred to as general corrosion, which usually happens to the whole surface of steel reinforcement.

$$CO_2 + H_2O \rightarrow H_2CO_3 \quad \text{(Equation 3)}$$

$$H_2CO_3 + Ca(OH)_2 \rightarrow CaCO_3 + 2H_2O \quad \text{(Equation 4)}$$

2.1.2 Corrosion propagation

During the propagation phase, steel reinforcement corrosion is the result of a series of electrochemical reactions. When depassivation occurs at adjacent parts of the same reinforcing steel induced by carbon dioxide or chloride ions ingress, the so-called microcell corrosion occurs, as shown in Figure 2-2 (Popov, 2015). The electrochemical cell is such that the anodic regions (located at the depassivated reinforcing steel) and cathodic regions (located at the passive reinforcing steel) are on the steel reinforcement, while the pore solution inside the concrete acts as an electrolyte conductor. Depending on whether the corrosion is induced by chloride ions or carbonation, either pitting corrosion or general corrosion could happen.

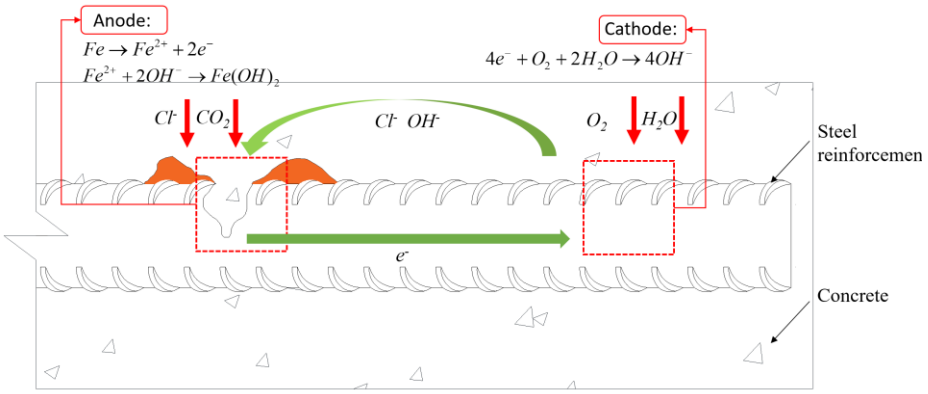

Figure 2-2 Schematic illustration of microcell corrosion

1) Pitting corrosion. When the passive film is locally broken down at the presence of chloride ions, the steel is exposed to the environment containing water and oxygen. The electrochemical reactions can be described by Equation 1, 2, 5, 6, and 7 (Neville, 1995). At the anode, *Fe* loses electrons and becomes Fe^{2+}, and Fe^{2+} reacts with chloride ions and further reacts with water as Equation 1 and 2 to produce $Fe(OH)_2$. Then, $Fe(OH)_2$ reacts with water and oxygen to produce $Fe(OH)_3$ as Equation 5. The $Fe(OH)_3$ dehydrates to become $Fe_2O_3 \cdot H_2O$ as Equation 6. At the cathode, water and oxygen are consumed to produce OH^-, as shown in Equation 7. The chloride ions are not consumed during reactions and thus continue to participate in the next round of corrosion. In addition, due to chloride ions being negatively charged, chloride ions can be migrated to the anode from both inside the concrete and the environment until reaching stable propagation. Stable propagation is when chloride ions carried by currents are equal to the chloride ions moved away by diffusion. The final local pH value of the anode could be lower than 3 (Bertolini *et al.*, 2014). As more chloride ions enter the concrete, the corrosion behavior is aggravated.

Anodic Reaction:

$$4Fe(OH)_2 + 2H_2O + O_2 \rightarrow 4Fe(OH)_3 \quad \text{(Equation 5)}$$

$$2Fe(OH)_3 \rightarrow Fe_2O_3 \bullet H_2O + 2H_2O \quad \text{(Equation 6)}$$

Cathodic Reaction:

$$4e^- + O_2 + 2H_2O \rightarrow 4OH^- \quad \text{(Equation 7)}$$

2) General corrosion. At the anode, without the participation of chloride ions, reactions occur as Equation 8 and 9 instead of equation 1 and 2. Also, corrosion continues as equation 5 to 6 to produce rust. At the cathode, reaction occurs as equation 7. For this type of corrosion, the coupling electrodes are defined as infinitely close (François, Laurens and Deby, 2018). During carbonation, the chloride ions bound in the form of calcium chloroaluminate hydrates or C-S-H gel may be released, causing chloride ion corrosion

(Geng *et al.*, 2016). In addition, when the CH is depleted, the carbon dioxide reacts with C-S-H gel, which causes shrinkage, leading to further microcracks (Bertolini *et al.*, 2014). In this scenario, more carbon dioxide, oxygen, water (liquid or moisture), and chloride ions can penetrate the concrete and present at the surface of steel reinforcements. The corrosion induced by carbonation occurs on the whole surface of reinforcing steel contacting with carbonated concrete, also named general corrosion or uniform corrosion.

$$Fe \rightarrow Fe^{2+} + 2e^{-} \quad \text{(Equation 8)}$$

$$Fe^{2+} + 2OH^{-} \rightarrow Fe(OH)_2 \quad \text{(Equation 9)}$$

In addition to microcell corrosion, macrocell corrosion could also occur such that the anodic and cathodic reactions occur between the surfaces of corroding rebars (anode region) and another passive rebars (cathode region) when they are bonded together as shown in Figure 2-3. Macrocell corrosion is usually observed in large reinforced structural members. Only when the microcell corrosion has already begun, can macrocell corrosion occur because the electrochemical reaction happens between the already corroded region and the passive region, and the concrete is the electrolyte, and macrocell corrosion further increases the corrosion rate. Macrocell corrosion is governed by the ratio of the surface area of passive to active region. With a higher ratio of surface area of the passive region to the active region, the corrosion rate caused by macrocell corrosion is larger. It has been reported that when the ratio exceeds 50, the macrocell corrosion will be the dominant form of corrosion. The maximum macrocell corrosion effect can increase the corrosion rate 2 to 5 times more than that of microcell corrosion alone(Andrade *et al.*, 1992; Hansson, Poursaee and Laurent, 2006).

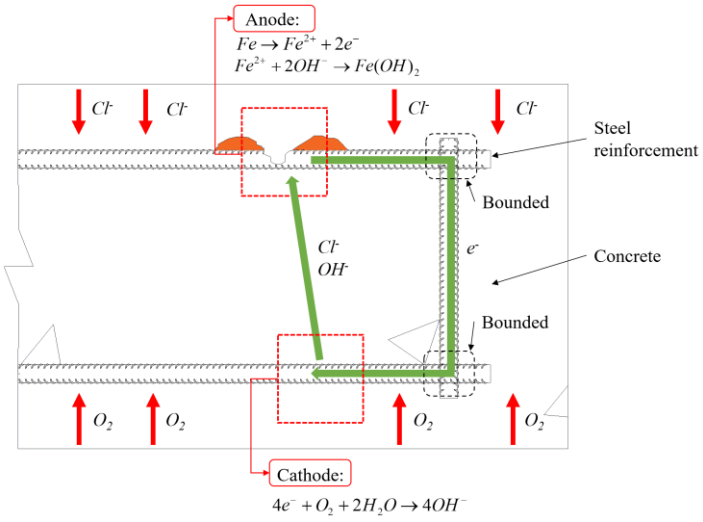

Figure 2-3 Schematic illustration of macrocell corrosion

2.1.3 Influencing factors of corrosion of steel rebar

Propagation of corrosion begins only after the steel reinforcement is depassivated at the anode, the oxygen presents at the surface at cathode of steel reinforcement, and the current is transported within the concrete. The concrete plays an important role in the corrosion process as electrolyte and pathway for ingress of external substances.

The current is mostly transported by the ions inside the pore solution. If the pores are limited and disconnected within the concrete, the electrical conductivity of the concrete will be low, and the corrosion of steel reinforcement could be very slow (Goyal *et al.*, 2018). Because the electricity conducts primarily

through the pore solution, the electrical resistivity of concrete is influenced by the moisture content of concrete, ionic composition of pore solution, continuity of the pore system, and temperature (Neville, 1995).

Concrete transport properties will influence when corrosion begins and the corrosion rate. Corrosion will initiate either because sufficient chlorides have penetrated to the steel or because the concrete has carbonated down to the steel from carbon dioxide ingress. Because water and oxygen are required to sustain the corrosion reaction, their transport rates into the concrete can limit the corrosion rate. Concrete transport properties describe the ability to transport external substances into the interior. The porosity, referring to the pore volume inside the concrete, the pore size distribution, and the pore network connectivity determines the resistance of concrete to the intrusion of external substances. The pore system is influenced by the water-to-cementitious mixtures ratio (w/cm), supplement cementitious mixture, and the addition of steel fibers. Several physical factors such as sorptivity, water permeability, gas permeability, chloride penetration can be measured to evaluate the concrete transport properties and consequently durability. Concrete pore system and transport properties are discussed more in Section 2.

Cracks on the concrete surface can act as flow channels for penetration of external substances, including water, gas, and aggressive ions (Bertolini *et al.*, 2014; Gu, Ye and Sun, 2015; Berrocal, Lundgren and Löfgren, 2016). The crack width, depth, and crack density all affect the corrosion process. It has been reported that apparent chloride diffusion coefficient increases with increasing crack width; chloride penetration depth within concrete increases with increasing crack depth (Gu, Ye and Sun, 2015); and steel reinforcement depassivation time decreases with increasing crack width (Gu, Ye and Sun, 2015). Thus, cracking should be carefully controlled to prevent corrosion. More detailed information regarding the influence of cracks is provided in section 3.

2.1.4 Methods for preventing reinforcement concrete structures from corrosion

In general, based on the previous discussion, the following main approaches can be adopted in practice preventing or delaying corrosion (Bertolini *et al.*, 2014; Goyal *et al.*, 2018):

(1) Suitable cover thickness must be provided to increase the time required for chlorides to penetrate the concrete to the steel;
(2) Concrete with low transport properties should be used; and
(3) Cracks need to be controlled because cracks could increase the transport properties of concrete.

Other methods can also be adopted, like using 1) corrosion-resistant reinforcing mixtures, 2) use of corrosion inhibitors including anodic inhibitors to suppress the anodic corrosion reaction or cathodic inhibitors to suppress the cathodic corrosion reaction; and 3) use of migratory inhibitors to form a self-replenishing monomolecular protective layer on steel reinforcements. These methods are difficult to implement in practice, are costly, and may not be as reliable as the main corrosion prevention methods.

To implement the three main corrosion prevention methods, UHPC can be adopted into practice. Due to its low transport properties, disconnected pore system, and better performance under cracking, UHPC is an ideal mixture to control corrosion of embedded steel reinforcement, which is discussed in detail in section 2.2 and section 2.3. However, research regarding corrosion of steel reinforcement under crack UHPC, the influence of crack patterns on corrosion behavior, and the suitable cover thickness for reinforcement in UHPC members has not been comprehensively studied and the information in this area is limited, which is further discussed in section 2.3.

2.1.5 Measurement of corrosion condition of steel reinforcement

Measurement of corrosion is primarily based on the electrical features of the corrosion process. During corrosion, electrons are released from the anode, and move towards the cathode through the steel. To

finish the circuit, the current is transported by the ions within the interconnected pore system. Also, in order to finish the corrosion process, the anodic regions need to be depassivated; the oxygen needs to be transported at the surface of cathodic region; and the interconnected pore system needs to be established within the concrete. Once these three conditions are satisfied simultaneously, corrosion could occur. Based on the three requirements, the corrosion rate of steel reinforcement can be measured.

Corrosion rate is usually used to estimate the remaining life and predict of service life of structural components. Corrosion rate can be expressed as a current density within the circuit, a rate of weight loss of steel reinforcement, or the rate of section loss of steel reinforcement. Two methods can be adopted to measure the reinforcing steel corrosion rate. The first one is physically measuring the weight loss or section loss of steel reinforcement. Although this test is the most intuitive, the destruction of structural component cannot be avoided. Consequently, non-destructive electrochemical assessment methods based on measuring the corrosion electrical circuit is often preferred. The relationship between anodic current I_a and mass loss of steel reinforcement obeys Faraday's first law of electrochemical stoichiometry, as shown in Equation 10 (Bertolini *et al.*, 2014).

$$\Delta m = e_{ech} q = e_{ech} \bullet I_a \bullet t \qquad \text{(Equation 10)}$$

Δm: the loss of mass at the corrosion region (anode);
e_{ech}: the electrochemical equivalent of corrosion metal, as shown in Equation 11;
q: charge passed;
I_a: the corrosion current (anodic current);
t: time *t.*

$$e_{ech} = M/(z \bullet F) \qquad \text{(Equation 11)}$$

M: the molar mass of the metal (55.8 g/mol for iron);
F: 96490 C/mol (Faraday's constant);
z: the valence of ion at anodic reaction ($z = 2$ for steel reinforcement corrosion $Fe \rightarrow Fe^{2+} + 2e$).

Corrosion current density is typically used to represent the corrosion rate of steel reinforcement. It has been reported that 1 mA/m^2 corrosion current density approximates to 10 g/m^2 weight loss of steel reinforcement (Glass, 2003). Common methods used to determine the probability of corrosion or corrosion rate are detailed in the following sections.

In general, three experimental tests are recommended and commonly adopted for measuring corrosion behavior of steel members embedded in UHPC matrix (Ghafari et al., 2015; Fan et al., 2019; Fan et al., 2020; Fan et al., 2021; Wang et al., 2022; Zheng et al., 2022): 1) open circuit potential test for measuring corrosion potential; 2) linear polarization test and Tafel extrapolation test for measuring polarization resistance and corrosion rate; and 3) electrochemical impedance spectroscopy test for measuring corrosion resistance of UHPC matrix, passive film, and steel rebar. By combining these three methods, the corrosion behavior of steel rebar in initiation phase and propagation phase and corresponding corrosion resistance of UHPC matrix and corrosion potential can be obtained, and the corrosion rate of steel reinforcement can be monitored. In addition, destructive testing could also be performed to confirm the corrosion condition and rate of the reinforcements.

2.1.5.1 Half-cell potential mapping (open circuit potential test)

Half-cell potential measures the open circuit potential (OCP) (E_{corr}), also called corrosion potential. A larger corrosion potential means higher probability of steel reinforcement active corrosion, which can be adopted for indirectly evaluating the corrosion condition of steel reinforcement. The setup is shown in Figure 2-4, and this method is recommended by ASTM C 876 Standard Test Method for Corrosion Potentials of Uncoated Reinforcing Steel in concrete (2015). The steel reinforcement is connected to the

setup, and a reference electrode is placed on the saturated sponge connected to the concrete cover. A high impedance voltmeter is used to obtain the open circuit potential. Several standard reference electrodes such as copper/copper sulphate electrode (CSE), silver/silver chloride electrode (SSCE), standard hydrogen electrode (SHE), and saturated calomel electrode (SCE) can be used as reference electrode during the test. The type of reference electrode used will influence the measured results and should always be reported to assess the probability of corrosion, as shown in Table 2-1. While this quick method can measure the corrosion potential, it cannot quantify the corrosion rate.

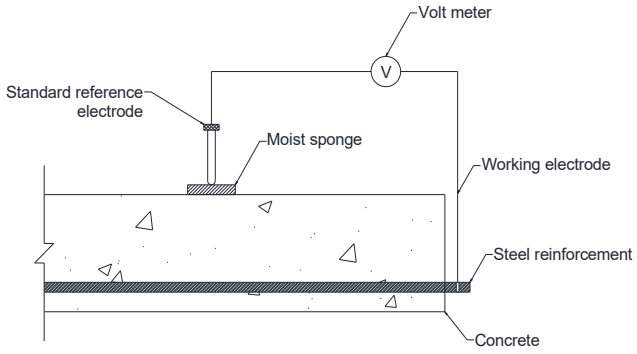

Figure 2-4 Setup for half-cell potential mapping test

Table 2-1 Corrosion risk related to open circuit potential value (Song and Saraswathy, 2007; Daniyal and Akhtar, 2020)

mV vs. CSE (mV)	mV vs. SSCE (mV)	mV vs. SHE (mV)	mV vs. SCE (mV)	Corrosion risk
<-500	<-406	<-184	<-426	Severe
<-350	<-256	<-34	<-276	High
-350 to -200	-256 to -106	-34 to +106	-276 to -126	Intermediate
>-200	>-106	>+106	> - 126	Low

2.1.5.2 Linear polarization resistance test and Tafel polarization test

Linear polarization resistance (LPR) measurement and the Tafel polarization test are the most common methods used to obtain the polarization resistance R_P and corrosion rate expressed as corrosion current density (i_{corr}), respectively. Polarization resistance R_P refers to the resistance of steel rebar against oxidation (Rodrigues *et al.*, 2021), and this test method is recommended by ASTM G59: Standard Test Method for Conducting Potentiodynamic Polarization Resistance Measurements (2020). Linear polarization resistance is inversely related to corrosion current density. Higher linear polarization resistance means higher risk of steel rebar being corroded; and higher corrosion rate means more serious corrosion condition of steel reinforcement.

The setup for LPR is shown in Figure 2-5. During the test, a potentiostat is connected to steel reinforcement, a given reference electrode, and a counter electrode with a wet sample surface. During LPR measurements, a
small scanning potential in the range of ± 10 to ± 25 mV is applied around the OCP E_{corr} with a certain scanning rate, eg: 0.1mV/s. The corresponding current increase ΔI from the applied potential is recorded. The polarization resistance R_P can be calculated using Equation 12, which equals the sum of concrete resistance R_c and charge transfer resistance R_{ct} (or the real polarization resistance) (Rodrigues *et al.*, 2021). Due to the high resistance between the rebar and concrete, a potential drop also called the Ohmic drop must be compensated by an additional test or automatically compensated by the LPR device

(Ahmad, 2003; Rodrigues *et al.*, 2021). The corrosion rate expressed as corrosion current can be obtained using the Stern–Geary formula as Equation 13. The Tafel constant B is usually set as 26 mV for active corroding steel reinforcement, and 52 mV for passive steel reinforcement (Bertolini *et al.*, 2014; Daniyal and Akhtar, 2020). When the accurate Tafel constant B is needed, the Tafel polarization test is needed to quantify the actual Tafel constant B. The Tafel polarization test process uses the same test setup as LPR, with the only difference being that the steel reinforcement is polarized to within ± 250 mV during the Tafel test. The Tafel constant B can be obtained by Equation 14. In Equation 14, β_a and β_c can be obtained by Tafel polarization curve, as shown in Figure 2-6. However, in order to get the accurate corrosion current, high potential may be required to be applied to reinforcement in the Tafel polarization test, it may cause irreversible change to steel reinforcement. Table 2-2 shows the relationship between corrosion condition of steel reinforcement and polarization resistance or corrosion rate, respectively.

$$R_p = \frac{\Delta E}{\Delta I} = R_c + R_{ct} \quad \text{(Equation 12)}$$

R_p: the polarization resistance (kΩ);
R_c: the concrete resistance (kΩ);
R_{ct} the current transfer resistance (kΩ);
ΔE: the increment of voltage mV;
ΔI: the increment of current (μA).

$$I_{corr} = \frac{B}{AR_p} \quad \text{(Equation 13)}$$

I_{corr}: the corrosion current rate (corrosion rate μA/cm^2);
B: the constant containing anodic Tafel slopes and cathodic Tafel slopes, as the slopes of polarization curves (mV);
A: the surface contacts to samples (cm^2);
R_p: the polarization resistance (kΩ cm^2).

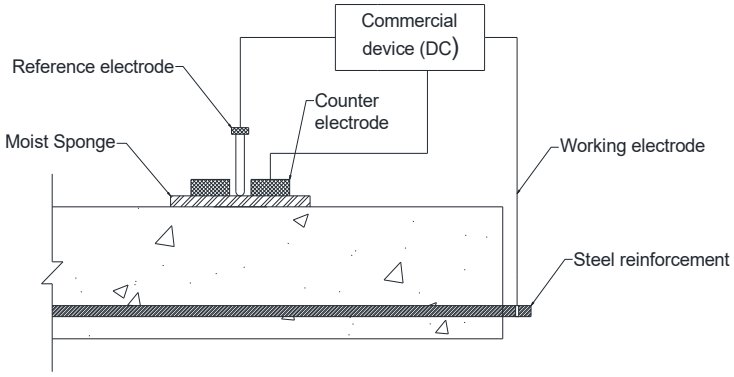

Figure 2-5 LPR and Tafel polarization test setup

$$B = \frac{\beta_a \times \beta_c}{2.3(\beta_a + \beta_c)} \quad \text{(Equation 14)}$$

β_a : Tafel coefficient (or Tafel slope) at anode;
β_c: Tafel coefficient (or Tafel slope) at cathode.

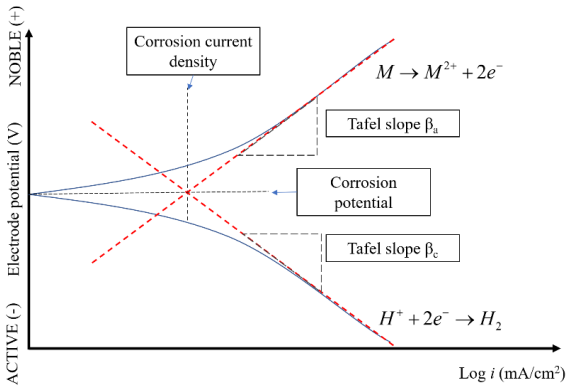

Figure 2-6 Typical Tafel polarization curve for samples

Table 2-2 Corrosion condition related to polarization resistance, current density, and corrosion penetration (Daniyal and Akhtar, 2020)

Corrosion condition	Polarization resistance (kΩ cm^2) (kΩ in^2)	Current density μA/cm^2 (μA/ in^2)	Corrosion penetration rate (μm/year) (in./year)
Very high	2.5-0.25 (0.39 - 0.039)	10-100 (64.52 – 645.16)	100-1000 (3.94×10^{-3} - 3.94×10^{-2})
High	25-2.5 (3.88 - 0.39)	1-10 (6.45 – 64.52)	10-100 (3.94×10^{-4} - 3.94×10^{-3})
Low/moderate	250-25 (38.75 - 3.88)	0.1-1 (0.65 – 6.45)	1-10 (3.94×10^{-5} - 3.94×10^{-4})
Passive	>250 (>38.75)	<0.1 (<0.65)	<1 (<3.94×10^{-5})

2.1.5.3 Electrical resistivity test

Concrete electrical resistivity is an important parameter for evaluating the ability of concrete to keep aggressive ions and gases from penetrating into the concrete and the ability of concrete to limit the rate of corrosion once it begins. There are inverse relationships between concrete resistivity and chloride penetration/corrosion risk of steel reinforcement, which are shown in Table 2-3 and Table 2-4, respectively. The lower the electrical resistivity of concrete, the easier chloride ions penetrate the concrete sample. The test setup is shown in Figure 2-7 and was standardized as an AASHTO T358 test method in 2015 (AASHTO T358, 2021). This test is used for example by the Florida Department of Transportation (FDOT, 2004), Louisiana Transportation Research Center (Rupnow and Icenogle, 2012), and Kansas Department of Transportation (Jenkins, 2015). During the test, a small current is applied to the outer electrodes at the surface of concrete, while the potential between the inner electrodes is recorded. The surface resistivity is calculated using Equation 15 (Daniyal and Akhtar, 2020).

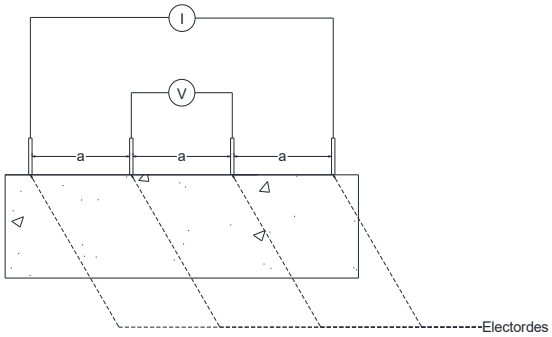

Figure 2-7 Test setup for concrete resistivity

$$\varrho = Ka\frac{V}{I} \quad \text{(Equation 15)}$$

ρ: surface concrete resistivity kΩ-cm;
K: geometry factor (2π for semi-finite body, eg: concrete slabs);
a: the distance between electrodes;
V: the measured potential between inner electrodes;
I: the given current between outer electrodes.

Table 2-3 Chloride ion permeability measured by concrete electrical resistivity (Azarsa and Gupta, 2017)

Chloride ion permeability	Surface resistivity test kΩ-cm (kΩ-in.)		
	100 mm diameter x 200 mm height (4.0 in. diameter x 8.0 in. height) cylinder (FDOT & LTRC)	150 mm diameter x 300 mm height (6.0 in. diameter x 12.0 in. height) cylinder (LTRC)	100 mm diameter x 200 mm height (4.0 in. diameter x 8.0 height) cylinder (KDOT)
High	<12 (< 4.72)	<9.5 (< 3.74)	<7.0 (<2.76)
Moderate	12-21 (4.72-8.72)	9.5-16.5 (3.74-6.50)	7.0-13.0 (2.76-5.12)
Low	21-37 (8.72 -14.57)	16.5-29 (6.50-11.42)	13.0-24.3 (5.12-9.57)
Very low	37-254 (14.57-100)	29-199 (11.42-78.35)	24.3-191 (9.57-75.20)
Negligible	>254 (>100)	>199 (>78.35)	>191 (>75.20)

Table 2-4 Electrical resistivity of concrete tested by surface resistivity method against corrosion risk of steel reinforcement (Azarsa and Gupta, 2017)

Corrosion risk of steel reinforcements	Corrosion resistivity (kΩ-cm (kΩ-in))	
	(Polder, 2001)	(Song and Saraswathy, 2007)
High	<10 (< 3.94)	<5 (<1.97)
Moderate	10–50 (3.94-19.69)	5–10 (1.97-3.94)
Low	50–100 (19.69-39.37)	10–20 (3.94-7.87)
Negligible	>100 (>39.37)	>20 (>7.87)

2.1.5.4 Electrochemical impedance spectroscopy

Electrochemical impedance spectroscopy (EIS), also called alternating current (AC) impedance spectroscopy, is a powerful tool for determining the corrosion conditions of steel rebar and researching the mechanism of corrosion process. The setup of EIS is similar to LPR test, as shown in Figure 2-8. EIS can measure concrete matrix resistance, passive film resistance, and charge transfer resistance. Lower concrete resistance leads to higher chloride penetration and further leads to higher risks of steel reinforcement being corroded. Lower resistance of passive film leads to lower initiation time of corrosion, and lower charge transfer resistance leads to higher corrosion rate of steel reinforcement. During the test, a commercial device is connected to a working electrode (steel reinforcement), a reference electrode, and a counter electrode. By applying an alternating excitation potential about 5 to 20mV to the steel

reinforcement with varying frequency usually in the range of 10 mHz to 100kHz, the response as a complex impedance Z consisting of real (resistive) component Z' and imaginary (capacitive or inductive) component Z'' can be obtained (Daniyal and Akhtar, 2020). The impedance Z is the ratio of AC voltage to AC current. The complex impedance Z can be calculated according to Equation 16 and Equation 17. EIS techniques provide more information about the corrosion process of reinforced concrete than LPR test and OPC test. Due to the low excitation potential, the influence of applied potential on steel reinforcement is limited with EIS.

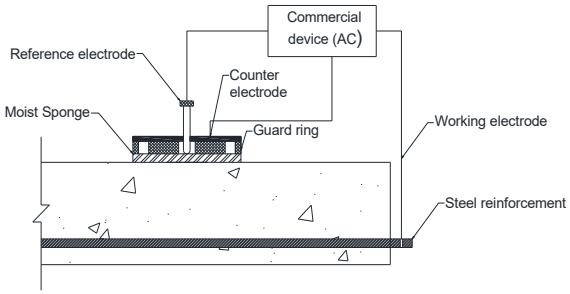

Figure 2-8 Test setup for EIS test

$$Z = \frac{E(t)}{I(t)} = \frac{E_0 cos(\omega t)}{I_0 cos(\omega t - \Phi)} = Z_0 \frac{cos(\omega t)}{cos(\omega t - \Phi)} \quad \text{(Equation 16)}$$

Z: the complex impedance;
$E(t)$: the potential at time t;
$I(t)$: the current at time t;
E_0: the amplitude of potential;
ω: radial frequency;
I_0: the amplitude of current;
Z_0: the magnitude of complex impedance;
Φ: phase difference between the potential and current;
t: time t.

$$Z = Z_0[e^{j \bullet \Phi}] = Z_0[cos(\Phi) + j \bullet sin(\Phi)] = Z' + jZ'' \quad \text{(Equation 17)}$$

j^2: -1.

EIS data can be processed using either a Nyquist plot or Bode plot (Rodrigues *et al.*, 2021), as recommended by ASTM G3 Standard Applicable to Electrochemical Measurements in Corrosion Testing (2019). Each plot can be used to obtain the concrete matrix resistance, passive film resistance, and charge resistance can be obtained. For the Nyquist plot, the x axis is Z', and the y axis is Z''. One simple example is shown in Figure 2-9, and the corresponding electrical equivalent circuit (EEC) for steel reinforcement is shown in Figure 2-9. In Figure 2-9, R_c is the resistance of concrete, and R_{ct} is the polarization resistance of steel reinforcement. In Figure 2-10, C_{dl} is the double layer capacitor, which is developed at the surface between the steel reinforcement and the electrolyte. The interlayer is developed by the negatively charged free electrons, and the outer layer is developed by the positively charged molecules in the pore solution, as shown in Figure 2-11 (Daniyal and Akhtar, 2020). The concrete resistance and the polarization resistance can be determined based on the frequency as shown in Figure 2-9.

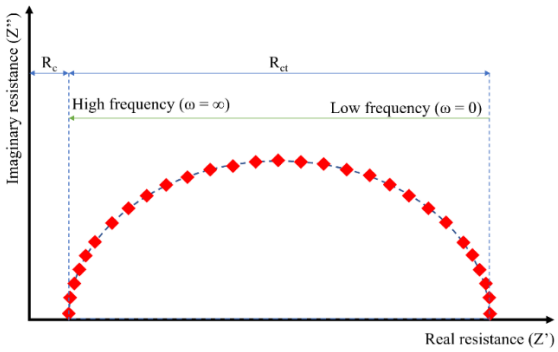

Figure 2-9 Typical Nyquist plot for steel reinforcement

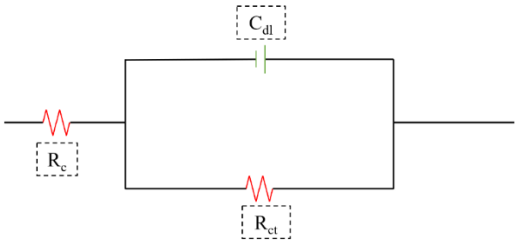

Figure 2-10 The simplest EEC for steel reinforcement

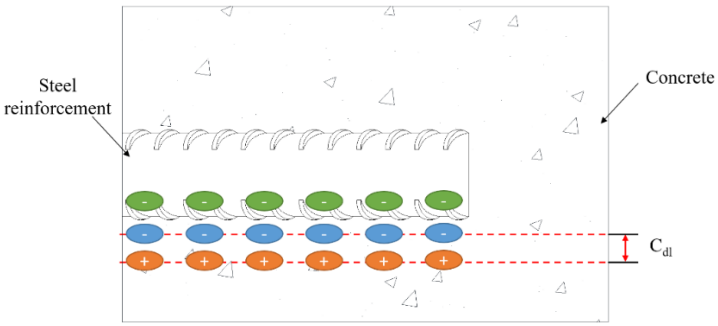

Figure 2-11 The impedance components in steel interface

Bode plots are plotted on log-log scales, with the x-axis as the frequency, and the y-axis as the complex impedance. One example is shown in Figure 2-12 (Fan *et al.*, 2020), and the corresponding EEC is shown in Figure 2-13 (Fan *et al.*, 2020). In Figure 2-13, R_s is the resistance of the immersed solution, CPE_c and R_c are the capacitance and resistance of concrete, CPE_f and R_f are the capacitance and resistance of the passive film, and CPE_{dl} and R_{ct} are the double layer capacitance and charge transfer resistance (polarization resistance) at the steel-electrolyte interface.

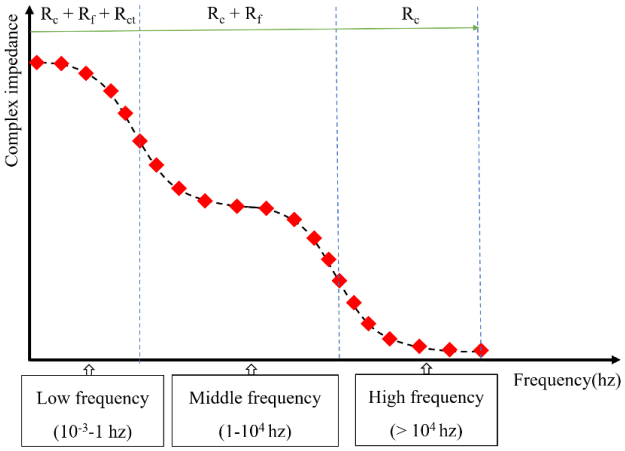

Figure 2-12 Typical Bode plot for steel reinforcement

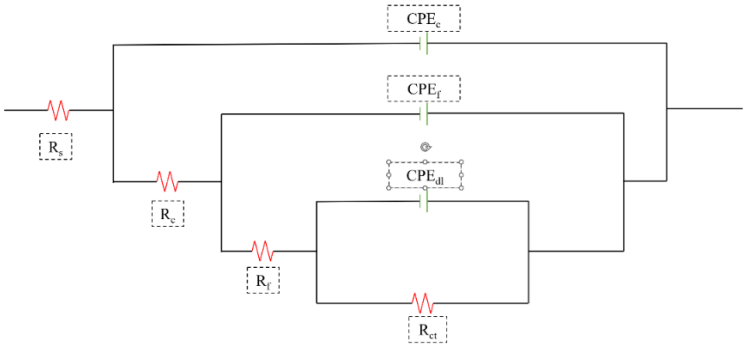

Figure 2-13 The EEC for Figure 2-12

2.1.6 Summary

In this section, the corrosion mechanism of concrete structural member, influencing factors for corrosion of embedded steel rebar, and the measurement for detecting corrosion condition of steel reinforcement were reviewed. The intrusion of chloride ions can effectively and efficiently initiate the corrosion and aggravate the corrosion propagation of steel reinforcement. Thus, high corrosion protection can be provided by concrete with low transport properties, such as UHPC. In general, UHPC with very low transport properties is expected to provide better corrosion protection to steel reinforcement. However, when crack occurs, the transport properties of UHPC may be increased, which is not fully studied. Generally, corrosion of embedded steel member within concrete components is an electrochemical reaction. Based on the electrical circuits, non-destructive methods can be used to evaluate the corrosion rate of steel reinforcement and corrosion risk of steel reinforcement. Three methods are recommended to fully examine the corrosion behavior of reinforcement including open circuit potential test, linear polarization test and Tafel polarization test, and electrochemical impedance spectroscopy. In addition, water and oxygen are basic elements required by corrosion. In the following sections, the transport properties of uncracked UHPC, the corrosion condition of steel fiber/steel reinforcement embedded in uncracked UHPC, the influence of cracks on transport properties of cracked UHPC and normal concrete, and the influence of cracks on corrosion condition of steel fiber/steel reinforcement embedded in cracked UHPC are reviewed.

2.2 Corrosion resistance of UHPC

As mentioned in section 1, UHPC could offer great corrosion protection to steel reinforcement. UHPC is a cementitious mixture with high mechanical property with discontinuous pore system that provides extraordinary durability, usually designed with water-to-cementitious mixture ratio or water-to-binder ratio (w/b) less than 0.25. UHPC typically does not contain coarse aggregate (diameter larger than 5 mm (0.2 in.)) (Xue *et al.*, 2020). A discontinuous pore network is generated during hydration because of the low w/b, particle packing effect, and pozzolanic reaction of SCMs. High resistance of UHPC to liquid, gas, and aggressive ion transport can lead to high protection of steel reinforcement from corrosion. Up to now, more than 340 bridges have been constructed in the United States and Canada that use UHPC in at least part of the structure, with most of them in either coastal environments or locations that use deicer salts, as shown in Figure 2-14 (FHWA, 2022).

Figure 2-14 UHPC bridge distribution up to 2022 (FHWA, 2022)

2.2.1 Transport properties of uncracked UHPC

Water, solution containing chloride ions or carbonate ions, and oxygen needs to penetrate concrete to reach the surface of steel members through the connected pores (or cracks) to initiate corrosion. Harmful matter can penetrate into the concrete using four mechanisms (Betrolini et al., 2014):

1) Capillary suction which is driven by capillary force in pores. When a concrete (or UHPC) member contact water, solution containing chloride ions will penetrate concrete by capillary suction. This process mainly depends on the capillary pore structure of the concrete (dimension, tortuosity, and continuity of capillary pore system).

2) Permeation, which refers to the movement of permeants into the concrete due to pressure difference. When concrete (or UHPC) member contact with liquid (water, chloride ions or carbonate ions solution) or gases (moisture, oxygen or carbon dioxide) under pressure, the liquid and gases will penetrate concrete.

3) Diffusion, which refers to the movement of permeants from high concentration region to low concentration region.

4) Migration, which refers to the movement of ions induced by electric field. For example, the negatively charged ions like chloride ions move to the anode area located at a depassivated region of steel during corrosion process by migration.

Therefore, the pore structures and transport properties dramatically influence the durability, including the corrosion resistance of UHPC. In this section, the relevant properties of UHPC including porosity, sorptivity, water permeability, gas permeability, and chloride ions penetration are reviewed. In general, the results show that UHPC generally shows much lower transport properties than conventional concrete.

2.2.1.1 Porosity of UHPC

Porosity is the rate of total volume of pores-to-volume of concrete members. Generally, three types of pores are formed during hydration including gel pores, capillary pores, and air voids (Figure 2-15). Gel pores are intrinsic parts of C-S-H gel, which is the main hydration product of concrete. For gel pores, the dimension is smaller than 10 nm (3.94×10^{-7} in.) (Gao *et al.*, 2015). Capillary pores are considered to be remnants of the initially water-filled space during mixing of concrete. The size of capillary pores is in the range of 10 nm to 1000 nm (3.94×10^{-7} in. to 3.94×10^{-5} in.) (Gao *et al.*, 2015). The air voids are caused by air mixed into the concrete during mixing operation that can be stabilized by chemical admixtures, which may be added purposely to entrain very small air voids inside the cement paste. For air voids, the dimension is in the range of 50 to 200 μm (0.002 in. to 0.008 in.). Larger air voids can also be present in the concrete because of imperfect compaction.

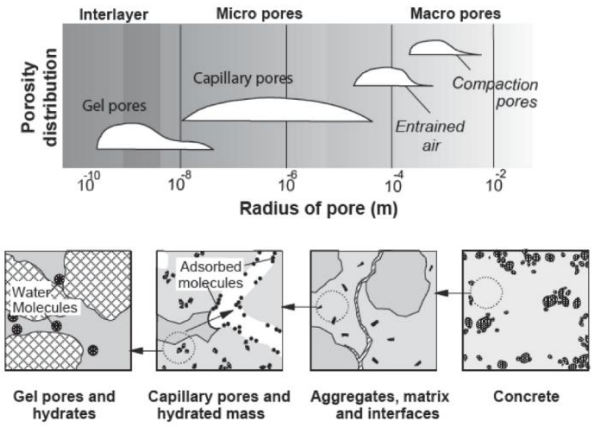

Figure 2-15 Dimensional range of pore system in concrete (Chen *et al.*, 2012)

Porosity is closely related to the transport properties and highly influences the durability of concrete (or UHPC) (Mather and Ozyildirim, 2002), although the transport properties not only depend on the porosity of concrete but also the dimension, distribution, tortuosity and continuity of pore system. Gel pores and part of air voids which are connected are also involved in the permeation process with limited contribution. Ions penetrate concrete by migration and diffusion primarily within interconnected capillary pores. The interfacial transition zone (ITZ) has been reported as the weakest and highest penetrability region in the concrete(Scrivener and Gartner, 1987). By strengthen the ITZ through use of SCMs, the transport properties of cementitious mixture can be reduced (Leemann *et al.*, 2006; Leemann, Loser and Münch, 2010; Liu *et al.*, 2019).

Three test methods are generally used to determine the porosity of concrete and UHPC in the literature:

1) Saturation test in accordance with ASTM C 642 (Standard Test Method for Density, Absorption, and Voids in Hardened Concrete) (2021). During the test, the concrete samples with volume larger than 350 cm^3 (21.35 $in.^3$), are first oven-dried (100-110℃ (212 - 230 °F)), then cooled down (20-25℃ (68 - 77°F)) and weighed (oven-dried mass denoted as A). the samples are subsequently immersed in 21℃ (70 °F) water for more than 48 hours, boiled in tap water for 5 hours, and cooled down to 20 ℃ to 25 ℃ (68 to 77 °F). Then, the surface is dried by toweling, and measure the mass as C. Also, mass D is recorded when the sample is suspending in water. The porosity can be calculated by Equation 18. This test can measure capillary pores in the range of 10 nm to 1000 nm (3.94×10^{-7} in. to 3.94×10^{-5} in.). However, due to discontinuous pore and narrow entrance impeding the water to fully fill all capillary pores, it could lead to underestimation of the capillary porosity. On the other hand, the specimens are pre-dried at high

temperature, causing microcracks, and cracks may further act as channels for water intrusion. Thus, due to the pre-conditioning of samples, the results may also be overestimated.

$$Porosity(\%) = \frac{C - A}{C - D} \times 100 \quad \text{(Equation 18)}$$

2) Vacuum saturation test (RILEM TC: CPC 11.3, 1994; Bu, Spragg and Weiss, 2014). During vacuum saturation test, the pre-dried samples (dried at 100-110℃ (212 -230 ℉) by oven heating (mass recorded as m_{OD}) are placed in a vacuum environment for 4 hours with controlled vacuum levels (7, 20, 50, 100, 150, and 380 Torr), and then the samples are subsequently immersed by water for 20 hours. After the samples are removed out of water and the surfaces are dried by toweling, the mass is recorded as m_{SS}. Subsequently, the mass of sample is recorded as m_{SSB} when they are suspended in water. The porosity of concrete can be calculated as Equation 19. In this test, gel pores and more capillary pores are filled by water than by conventional saturation test (Chaudhry, 2018). It has been reported that the porosity measured by vacuum saturation test with highest level of vacuum (7 Torr) is close to the theoretical total porosity (paste matrix pore volume + entrained air volume + aggregate pore volume), while the porosity measured using a lower vacuum pressure (380 Torr) is close to the porosity measured by conventional saturation test (Bu, Spragg and Weiss, 2014). Vacuum saturation is generally considered more promising compared to saturation test and able to capture more volume of pores inside the concrete. This test method can evaluate the gel pore, capillary pores, and part of the air voids. However, this method has the same drawback as the saturation test in that microcracks could be induced during drying by oven heating, leading to an overestimate of the porosity of samples.

$$Porosity(\%) = \frac{m_{SS} - m_{OD}}{m_{SS} - m_{SSB}} \times 100 \quad \text{(Equation 19)}$$

3) Mercury intrusion porosimetry (MIP)-ASTM D 4404 - Standard Test Method for Determination of Pore Volume and Distribution of Soil and Rock by Mercury Intrusion Porosimetry (2018). MIP can provide the porosity of gel pores, capillary pores, and air voids in the range of 2.5 nm to 100 μm (9.8×10^{-8} to 0.004 in.) (ASTM D 4404, 2018). During the test, the dried and outgassed (outgassed in vacuum of at least 1.3 Pa (13 bar) and at temperature of 150 ℃ (302 ℉) for at least 24 hours) concrete samples are put in the penetrometer (Figure 2-16). The penetrometer containing the test sample is firstly evacuated at least 1.3 Pa (13 bar), then is placed in the pressure vessel of porosimeter, and the penetrometer is filled by mercury. Then, a risen mercury pressure is applied to samples for intrusion, recording both the absolute pressure and the volume of intruded mercury with 10-15 pressure intervals. In each interval, the volume of intruded mercury equals the volume of pores that are filled under this pressure level, and through Equation 20, the corresponding pore diameter can be obtained. By taking the measurement over all intervals, the volume of pores corresponding to different sizes and the pore size distribution can be obtained. At the end of the test, porosity of samples can be obtained that the total volume of pores is the volume of total intrusion mercury. However, the method, by its principle, only measures the dimension of the entrance of pores. The real pore size could be larger than the dimension of entrance of pores, leading to underestimation of the pore size by MIP, which is called “ink bottle” effect.

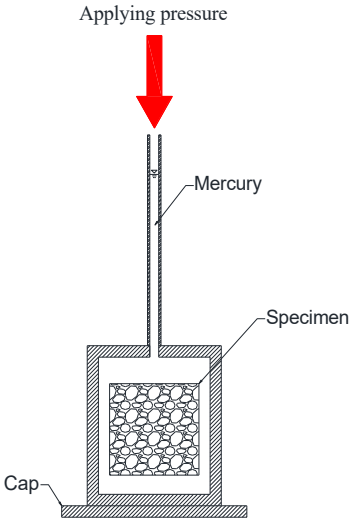

Figure 2-16 MIP setup

$$d = -4\gamma(cos\theta)/P \quad \text{(Equation 20)}$$

d = apparent pore diameter being intruded;
γ = surface tension of the mercury;
θ = contact angle between the mercury and the pore wall;
P = absolute pressure causing the intrusion.

In addition to these quantitative methods, scanning electron microscope (SEM) is often used to observe the dimension of pores and their distribution. By this method, the pore size of capillary pores, gel pores and air voids and corresponding distribution can be measured when pore size is above 10 nm (3.94×10^{-8} in.) (Asmatulu and Khan, 2019). However, this method cannot provide the total pore volume of concrete or porosity. Therefore, this method is usually used in combination with the above three methods.

Pore system of UHPC mainly depends on the w/cm, type and dosage of SCMs, curing regime, and addition of fibers. With low w/cm, the space between cementitious particles is low, leading to efficient space filling during hydration (Aïtcin, 2016). The pozzolanic reaction contributes more C-S-H gel during hydration, filling additional space between cementitious particles (Bertolini *et al.*, 2014). Some SCMs have very small particles that can physically fill the pores, further reducing porosity and disconnecting the pore network. Heat curing regimes are commonly used with accelerate the pozzolanic reaction (Yazıcı, 2007). Fiber reinforcement provides tensile strength and reduces microcrack propagation (Abbas, Soliman and Nehdi, 2015).

Generally, UHPC has much lower porosity and finer pore system compared to concrete, because the micro-structure is denser than that of normal concrete, and the interfacial transition zone (ITZ) between cementitious matrix and aggregates are also improved, which typically has much higher porosity than the bulk paste (Leemann, Loser and Münch, 2010; Abbas, Soliman and Nehdi, 2015). For reference, the measured porosity of UHPC reported in the literature is in the range of 0.59% to 7.52%, compared to the porosity in the range of 9% to 10% of normal-strength concrete (de la Cruz, Colorado and del Campo, 2015). Table 2-5 shows a set of criteria for evaluation the porosity of concrete, according to which, the porosity of UHPC is considered very low. More review of UHPC porosity is provided below.

Table 2-5 Criteria for evaluation of porosity of concrete (Wang *et al.*, 2014)

Porosity evaluation method	Very Low	Average	High	Very High
Saturation method	6 to 9 %	9 to 12 %	12 to 14 %	14 to 16 %
Porosity measure by MIP	3 to 6 %	6 to 9 %	9 to 13 %	13 to 16 %

SCMs play an important role in reduction of UHPC porosity. Pozzolanic reaction from SCMs provides additional C-S-H gel during hydration of UHPC, which leads to fill the pore and disconnect the pore network. The unhydrated pozzolanic mixture physically fill the pores, which further contributes to the low porosity of UHPC. Ghafari et al. (2014) experimentally investigated the porosity of UHPC with different dosages of nanosilica by MIP. The measured total porosities (capillary porosities) are 6.35% (2.65%), 4.74% (2.56%), 4.66% (2.44%), 4.3% (1.72%), and 4.8% (2.33%) corresponding to the samples with nanosilica in dosage of 0, 1, 2, 3, 4 wt.% by weight of cement, respectively, as shown in Figure 2-17. It shows that with increasing the dosage of nanosilica, the porosity of UHPC decreases. However, excessive nanosilica causes chemical shrinkage and volume shrinkage at the early age of cementitious mixture, which may lead to microcrack generation and further increase the tested porosity (Wang *et al.*, 2020). Tafraoui, Escadeillas and Vidal (2016) experimentally compared the porosity of UHPC with silica fume and metakaolin by the vacuum saturation method. The measured porosity of UHPC was 6.1% and 7.1 % for UHPC with silica fume and metakaolin with a dosage of 25 wt.% by cement, respectively. The reason could be that addition of metakaolin increases the viscosity, which leads to air bubbles trapped in the fresh UHPC and causing an increase of porosity (Song *et al.*, 2019). Alharbi et al., (2021) also reported silica fume reduces capillary porosity more than metakaolin for reactive powder concrete. Shanmugasundaram and Jayakumar (2022) investigated the porosity of UHPC with ultra-fine fly ash or ultra-fine slag as a partial replacement of silica fume of 25% to 100%, respectively. The test result shows that after partially or fully replacing silica fume, the porosity of UHPC increases. Compared to the porosity in the range of 3.44 to 7.52% for samples with 100% silica fume cured by different conditions (water curing, steaming curing, and oven heating curing), when the silica fume was replaced by ultra-fine fly ash or ultra-fine slag from 25% to 100%, the porosity of samples increased from the range of 4.26 ~ 7.96% to 4.74 - 9.87% and from the range of 4.54 - 8.15 % to 5.13 - 9.16 %, respectively. The author indicated that silica fume has better filling behavior since the size of silica fume particle is 50 times smaller than ultra-fine fly ash and ultra-fine slag. More detailed test results can be found in Table 2-6. Generally, SCMs highly influence the porosity of UHPC, and lower porosity can be found with higher dosage of SCMs.

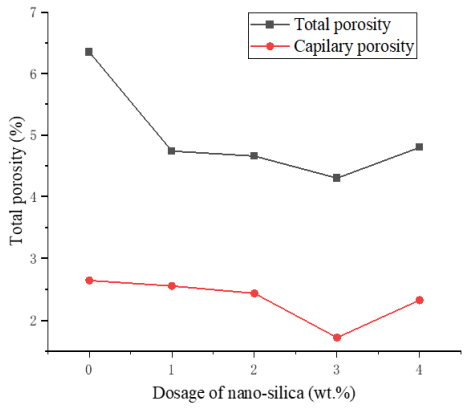

Figure 2-17 The relationship between porosity and dosage of nano-silica

Table 2-6 Representative porosity of UHPC reported in the literature

References	Test method	w/b ratio	Compressive strength (MPa/ksi, 28 days)	Additional notes		Curing regimes	Curing period (days)	Total porosity (%)
Charron, Denarié and Brühwiler (2008)	Vacuum saturation method	0.14	168 (24.37 ksi)	6 vol.% steel fibers and 10 wt.% of silica fume by concrete		20 ℃ (68 ℉)	28	4.2
Ghafari et al. (2014)	MIP	0.20	137 (19.87 ksi)	1 wt. % cement replaced by nanosilica	12.5 wt. % silica fume by concrete	Water immersion at 20 ℃ (68 ℉)	28	4.74
			138 (20.01 ksi)	2 wt. % cement replaced by nanosilica				4.66
			142 (20.60 ksi)	3 wt. % cement replaced by nanosilica				4.3
			140 (20.31 ksi)	4 wt. % cement replaced by nanosilica				4.8
Abbas, Soliman and Nehdi (2015)	Saturation test	0.15	156 (22.63 ksi)	8 mm (0.31 in.) steel fiber length	1 vol.% dosage of fiber	21 ℃ (70 ℉) RH ≥ 95%	28	3.28
			164 (23.79 ksi)		3 vol.% dosage of fiber			3.11
			171 (24.80 ksi)		6 vol.% dosage of fiber			2.25

References	Test method	w/b ratio	Compressive strength (MPa/ksi, 28 days)	Additional notes		Curing regimes	Curing period (days)	Total porosity (%)
Tafraoui, Escadeillas and Vidal (2016)	Vacuum saturation method	0.22	158 (22.92 ksi)	12 mm (0.47 in.) steel fiber length	1 vol.% dosage of fiber	Water immersion at 20 ℃ (68 ℉)	28	3.30
			166 (24.08 ksi)		3 vol.% dosage of fiber			3.10
			173 (25.09 ksi)		6 vol.% dosage of fiber			2.27
			159 (23.06 ksi)	16 mm (0.63 in.) steel fiber length	1 vol.% dosage of fiber			3.31
			165 (23.93 ksi)		3 vol.% dosage of fiber			3.13
			170 (24.66 ksi)		6 vol.% dosage of fiber			2.29
			155 (22.48 ksi)	6.0 wt. % steel fibers	25 wt.% silica fume by cement			6.1
			146 (21.18 ksi)		25 wt.% metakaolin by cement			7.1
Shanmugasundaram and Jayakumar (2022)	MIP	0.18	129.5-107.9 (18.78-15.65 ksi)	25 wt.% to 100 wt. % silica fume replaced by ultra-fine fly ash		Water immersion at 27 ℃ (81 ℉)	28	7.79-9.87
			125.5-102.6 (18.20-14.88)	25 wt.% to 100 wt. % silica fume replaced by ultra-fine slag				8.15-9.16

References	Test method	w/b ratio	Compressive strength (MPa/ksi, 28 days)	Additional notes	Curing regimes	Curing period (days)	Total porosity (%)
			135.1 (19.59 ksi)	Non-replacement of silica fume	Moisture at 90 ℃ (194 ℉) + Water immersion at 27 ℃ (81 ℉)	1+27	7.52
			150.0-142.9 (21.76-20.72 ksi)	25 wt.% to 100 wt. % silica fume replaced by ultra-fine fly ash			4.59-6.54
			156.2-145.3 (22.65-21.07 ksi)	25 wt.% to 100 wt. % silica fume replaced by ultra-fine slag			5.15-5.87
			158.4 (22.97 ksi)	Non-replacement of silica fume	Heat air at 160 ℃ (320 ℉)+ Water immersion at 27 ℃ (81 ℉)	1+27	4.61
			155.0 – 163.6 (22.48-23.73 ksi)	25 wt.% to 100 wt. % silica fume replaced by ultra-fine fly ash			4.26-4.74
			157.5 – 148.4 (22.84-21.57 ksi)	25 wt.% to 100 wt. % silica fume replaced by ultra-fine slag			4.54-5.13
			168.4 (24.42 ksi)	Non-replacement of silica fume			3.44
				0 vol.% steel fiber	Fog curing: 21 to 25℃ (69.8 to 77.0 ℉) with RH ≥ 95%		7.5
				1.5 vol.% steel fiber			6.39
				2 vol.% steel fiber			6.39
Riding et al. (2022)	MIP	0.163	124~145 (18-21 ksi)	0 vol.% steel fiber	Steam curing: water bath with sealed contained in oven at 90 ℃ (194 ℉) for 2 days + moist room curing for 26 days	28	4.28
				1.5 vol.% steel fiber			2.11
				2 vol.% steel fiber			2.11

References	Test method	w/b ratio	Compressive strength (MPa/ksi, 28 days)	Additional notes	Curing regimes	Curing period (days)	Total porosity (%)
		0.156	≥145 (≥21 ksi)	0 vol.% steel fiber	Precast curing: Cured with molds in room temperature for 4 hours + oven curing with lid at 70℃ (158 ℉) for 18 hours + cooling for 2 hours + 27 days moist room curing		5.97
				1.5 vol.% steel fiber			3.86
				2 vol.% steel fiber			2.83
				0 vol.% steel fiber	Fog curing: 21 to 25℃ (69.8 to 77.0 ℉) with RH ≥ 95%		4.68
				1.5 vol.% steel fiber			2.15
				2 vol.% steel fiber			2.56
				0 vol.% steel fiber	Steam curing: water bath with sealed contained in oven at 90 ℃ (194 ℉) for 2 days + moist room curing for 26 days		1.76
				1.5 vol.% steel fiber			1.23
				2 vol.% steel fiber			0.59
				0 vol.% steel fiber	Precast curing: Cured with molds in room temperature for 4 hours + oven curing with lid at 70℃ (158 ℉) for 18 hours + cooling for 2 hours + 27 days moist room curing		2.82
				1.5 vol.% steel fiber			2.08
				2 vol.% steel fiber			2.08

Steel fiber is usually employed to reinforce the internal mixture. Past research shows that with addition of steel fiber, the porosity of UHPC decreases due to effectively blocking the channel for intrusion and limiting microcracks at the early age of UHPC. The fiber content are found to influence the porosity of UHPC. Abbas, Soliman and Nehdi (2015) experimentally investigated the effect of steel fiber content on porosity of UHPC by saturation method. The result shows that with increasing steel fiber dosage from 1 vol. % ~ 6 vol. % for samples with fiber in length of 16 mm (0.62 in.), the porosity of UHPC decreases 3.31% to 2.29%. The author reported that lower capillary porosity has been found with increasing dosage of steel fibers, and the fibers also partially disconnect the capillary pore system. In addition, Charron, Denarié and Brühwiler (2008) experimentally investigated the porosity of UHPC with high dosage of steel fiber by vacuum saturation method. The porosity of UHPC is only 4.2%, which also agrees to the test results of Abbas, Soliman and Nehdi (2015). More detailed test results can be found in Table 2-6. In addition, scholars reported that the length of steel fiber has limited influence on porosity of UHPC. Abbas, Soliman and Nehdi (2015) experimentally investigated the effect of steel fiber length on the porosity of UHPC using the saturation method. With fiber length increasing from 8 mm to 16 mm (0.31 in. to 0.62 in.), the porosity of UHPC with fiber content of 6 vol.% slight increases from 2.25 to 2.29%. the difference may be caused by the error of experiment.

Adoption of proper curing methods can reduce the porosity of UHPC. Shanmugasundaram and Jayakumar (2022) investigated the porosity of UHPC under different curing regimes by MIP. Water curing (immersed in water at a temperature 27 ℃ (81 ℉), steam curing (exposed to moisture for 24 hours at 90 ℃ (194 ℉), then immersed in water), and oven heat curing (exposed to hot air oven at 160 ℃ (320 ℉) for 24 hours, then immersed in water) were considered in the experiments. The lowest porosity was found in oven-cured samples. For samples with 27.7 wt.% (by weight of cement) silica fume, compared to the porosity of samples cured by water of 7.52% and cured by steam of 4.61%, samples cured by oven heat had the lowest porosity of 3.44%. Yazıcı (2007) reported thermal curing regimes provide perfect hydration media to accelerate the hydration process for concrete added with SCMs. Alharbi et al. (2021) reported pozzolanic reaction can be increased due to thermal curing regime, which leads to more hydrated products. More detailed test results can be found in Table 2-6.

Riding et al. (2022) comprehensively investigated the influence of steel fiber content and curing regime on porosity of non-proprietary UHPC with different mixture designs for different compressive strength. In this test, two different UHPC mixtures were designed: the first group of mixture with compressive strength in the range of 124~145 MPa (18-21 ksi); the other group of UHPC with compressive strength above 145 MPa (21 ksi). Three steel fiber contents of 0, 1.5, and 2.0 vol.% were designed for two different UHPC mixtures. Three curing regimes were designed for two different UHPC mixtures: 1) fog curing regime - specimens cured in standard moist room at 21 to 25℃ (69.8 to 77.0 ℉) with RH ≥ 95% ; 2) steam curing regime - specimens firstly partially immersed in water within a container under oven heating at 90 ℃ (194 ℉) for 2 days then placed in moist room curing for next 26 days; and 3) precast curing (simulation of realistic curing regime of precast structural members) – after four hours of curing within molds, specimens were covered by a lid (without water addition) and oven heated at 70 ℃ (158 ℉) for 22 hours with subsequently cooling in the air for 2 hours, specimens were cured in moist room until curing age of 28 days. In terms of the effect of steel fiber contents, the test results show that with steel fiber contents increasing from 0 to 2 vol.%, porosity for UHPC mixture with compressive strength in the range of 124~145 MPa (18-21 ksi) decreased from the range of 4.28 - 7.5% to the range of 2.11 - 6.39%. The same trend was also observed for UHPC mixture with compressive strength above 145 MPa (21 ksi) that with steel fiber increasing from 0 to 2 vol.%, porosity decreased from the range of 1.76 –

4.67% to the range of 0.59 – 2.56%. In terms of the effect of curing regime, steam curing regime is much better than fog curing regime and precast curing regime. For fog curing regime, the porosity is in the range of 6.39 to 7.5% for UHPC mixture with compressive strength in the range of 124~145 MPa (18-21 ksi) and in the range of 2.56 to 4.68% for UHPC mixture with compressive strength above 145 MPa (21 ksi); for steam curing regime, the porosity is in the range of 2.11 to 4.25% for UHPC mixture with compressive strength in the range of 124~145 MPa (18-21 ksi) and in the range of 0.59 to 1.76% for UHPC mixture with compressive strength above 145 MPa (21 ksi); and for precast curing regime, the porosity is in the range of 2.83 to 5.95% for UHPC mixture with compressive strength in the range of 124~145 MPa (18-21 ksi) and in the range of 2.08 to 2.82% for UHPC mixture with compressive strength above 145 MPa (21 ksi). In addition, the test results show that the porosity for UHPC with higher compressive strength tends to have lower porosity

2.2.1.2 Sorptivity of UHPC

Sorptivity evaluates the ability of concrete to absorb water into capillary pores. Water absorption is driven by capillary suction, and water absorption coefficient is used to evaluate the sorptivity of concrete by experimental test. The water absorption coefficient (or sorptivity coefficient) is defined as the mass of water absorbed by sample per unit of surface (i) in time t, as developed in Equation 21. Sorptivity depends on the capillary porosity, pore size distribution, and continuity of the pore system. Thus, it can be adopted to evaluate the capillary pore system (San Nicolas, Walkley and van Deventer, 2017). A close relationship has been commonly agreed between porosity and sorptivity. A high porosity tends to be higher sorptivity of cementitious mixture (Bertolini *et al.*, 2014; San Nicolas, Walkley and van Deventer, 2017). For samples with high water absorption coefficients, it implies that a highly continuous pore structure or low tortuosity exists (San Nicolas, Walkley and van Deventer, 2017). Small pores have a strong capillary suction force, however, the smaller pore size also reduces the water absorption speed due to increasing friction (Bertolini *et al.*, 2014). Overall, a higher water absorption coefficient was observed for samples with higher concentration of large pore size (Pia, Casnedi and Sanna, 2016; Ye *et al.*, 2017). In general, sorptivity highly influences the durability of concrete because concrete is often partially saturated, making capillary suction a significant water and aggressive ion penetration mechanism.

$$i = S \times \sqrt{t} \qquad \text{(Equation 21)}$$

i: the mass of absorbed water per unit cross-section (exposure surface);
S: water absorption coefficient;
t: exposed time.

Sorptivity is usually measured according to ASTM 1585- Standard Test Method for Measurement of Rate of Absorption of Water by Hydraulic Cement Concretes (2020). Other sorptivity measurements (Kumaran, 1999) include a French recommendation from AFPC-AFREM (French Competitiveness Clusters Alliance - French Association for the Research and Testing of Mixtures and Structures) called Durabilité des Bétons: Méthodes recommandées pour la mesure des grandeurs associées à la durabilité (Durability of Concretes: Recommended methods for measuring the quantities associated with durability) (1997), and RILEM TC 116-PCD: Permeability of Concrete as a Criterion of its Durability (1999). The test procedure is similar for all standards. During the test, the saturated samples in size of 100 mm diameter × 50 mm disc (3.94 in. diameter × 1.97 in. length) are placed in a sealable environmental container to equilibration of the moisture distribution. Then, the mass of samples is recorded, and

subsequently moved into a water tank with 1 to 3 mm (0.04 in. to 0.12 in.) water above the bottom surface of samples for saturation, as shown in Figure 2-18. The mass of samples is recorded after one minute of saturation and periodically up to 7 days. Finally, the absorption can be calculated by Equation 22. An example result of sorptivity of concrete test is shown in Figure 2-19. It has been reported that the initial absorption is related the small dimension capillary pores and the secondary absorption is related to the relatively larger capillary pores and microcracks inside the samples (Yang, Weiss and Olek, 2006; Bao and Wang, 2017).

$$I = \frac{m_t}{a*d} \qquad \text{(Equation 22)}$$

I: the absorption;
m_t: the change in specimen mass in grams, at the time t;
a: the exposed area of the specimen, in mm^2;
d: the density of the water in g/mm^3.

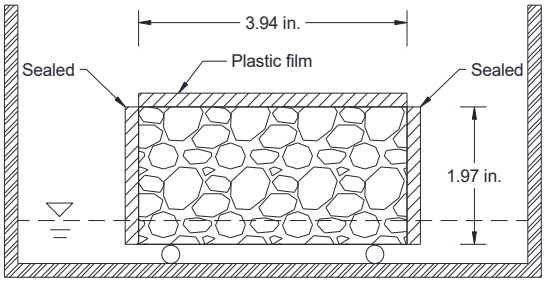

Figure 2-18 Schematic of the procedure

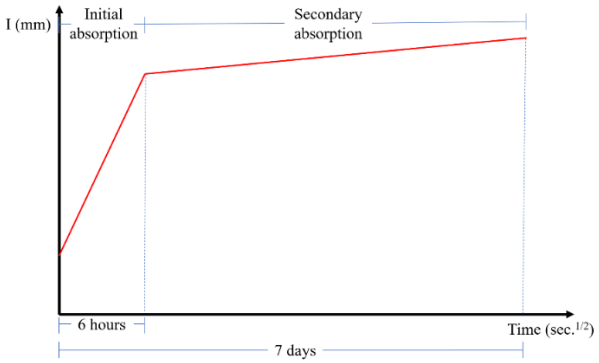

Figure 2-19 Example results of sorptivity of concrete test

Generally, sorptivity of UHPC is very low due to its dense microstructure and low capillary porosity. The influencing factors such as SCMs and steel fibers for porosity discussed in section 2.2.1.1 also affect the sorptivity. In the literature, the sorptivity of UHPC has been investigated and reported by several researchers and a brief review is provided below. In general, the measured sorptivity of UHPC is in the range of 0.0178 to 0.156 $kg/m^2\ h^{0.5}$ (0.0036 to 0.032 $lb./ft^2\ h^{0.5}$), which is extremely low compared to the typical range of 0.3 to 0.78 $kg/m^2\ h^{0.5}$ (0.06 to 0.16 $lb./ft^2\ h^{0.5}$) for normal concrete (Bertolini *et al.*, 2014; Dobias, Pernicova and Mandlik, 2016).

The addition of SCMs refines the pore system and reduces porosity of UHPC as described in section 2.2.1.1, which further leads to the low sorptivity of UHPC. Ghafari et al. (2014) experimentally investigated the sorptivity of UHPC with different dosages of nano-silica. With 0,1, 2. 3, 4 wt. % nano-silica by weight of cement, the corresponding secondary rate of water absorption of UHPC decreased from 0.0209 kg/ m^2 $h^{0.5}$ (0.043 lb./ft^2 $h^{0.5}$) to 0.0196 kg/ m^2 $h^{0.5}$ (0.040 lb./ft^2 $h^{0.5}$), 0.0189 kg/ m^2 $h^{0.5}$ (0.039 lb./ft^2 $h^{0.5}$), 0.0178 Figure 2-20. Tafraoui, Escadeillas and Vidal (2016) experimentally investigated the sorptivity of UHPC with silica fume or metakaolin, respectively. Both the initial and secondary rate of water absorption of UHPC with metakaolin was measured to be 0.055 kg/ m^2 $h^{0.5}$ (0.011 lb./ft^2 $h^{0.5}$), while both the initial and secondary rate of water absorption of UHPC with silica fume was measured to be 0.038 kg/ m^2 $h^{0.5}$ (0.078 lb./ft^2 $h^{0.5}$). Also, Dobias, Pernicova and Mandlik (2016) compared the sorptivity of UHPC and normal strength concrete. The result shows that both initial and secondary rate of water absorption of UHPC and normal concrete is 0.156 kg/m^2 $h^{0.5}$ (0.032 lb./ft^2 $h^{0.5}$) and 0.786 kg/m^2 $h^{0.5}$ (0.16 lb./ft^2 $h^{0.5}$), respectively. More detailed test results can be found in Table 2-7.

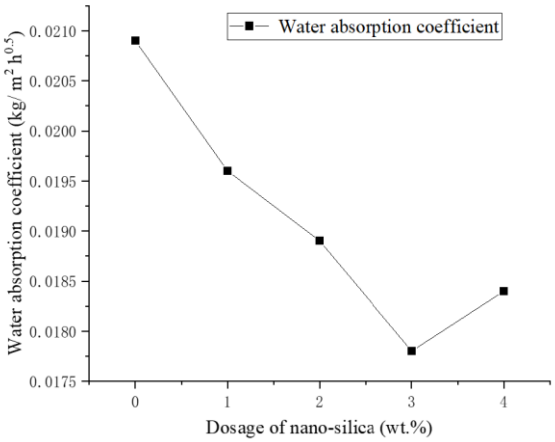

Figure 2-20 The relationship between dosage of nano-silica and sorptivity of UHPC

By addition of steel fibers, the porosity of UHPC decreases as mentioned in section 2.2.1.1, which further leads to the low sorptivity of UHPC. The steel fiber content was reported to affect the sorptivity of UHPC. Abbas, Soliman and Nehdi (2015) experimentally investigated the effect of fiber content on sorptivity of UHPC. The results show that with increasing dosage of steel fibers from 1 vol.% to 6 vol.%, water absorption coefficient of UHPC decreases the initial rate of water absorption and secondary rate of water absorption from 0.0582 kg/ m^2 $h^{0.5}$ (0.012 lb./ft^2 $h^{0.5}$) to 0.0470 kg/ m^2 $h^{0.5}$ (0.0096 lb./ft^2 $h^{0.5}$) (19% reduction) and from 0.0382 kg/ m^2 $h^{0.5}$ (0.011 lb./ft^2 $h^{0.5}$) to 0.0271 kg/ m^2 $h^{0.5}$ (0.0056 lb./ft^2 $h^{0.5}$) (29% reduction), respectively. The same trend was also observed by Wang et al. (2018) that with fiber content increasing from 0 vol.% to 3 vol.%, the water absorption coefficient decreases from 0.097 to 0.081 kg/ m^2 $h^{0.5}$ (0.020 to 0.017 lb./ft^2 $h^{0.5}$). Also, Charron, Denarié and Brühwiler (2008) experimentally investigated the sorptivity of UHPC with high dosage of steel fibers. The test results show that with 6 vol.% steel fiber content, the water absorption coefficient was measured to be 0.02118 kg/m^2 $h^{0.5}$ (0.0043 lb./ft^2 $h^{0.5}$). More detailed test results can be found in Table 2-7. Moreover, length of steel fiber has limited influence of sorptivity of UHPC. Abbas, Soliman and Nehdi (2015) experimentally investigated the effect of steel fiber length on sorptivity of UHPC. With increasing length of steel fibers, sorptivity of UHPC slightly increases. For samples with 1 vol.% fiber content and length increasing from 8 mm (0.63 in.) to 16 mm (1.26 in.), the initial rate of water absorption and the secondary rate of water absorption slightly increases from 0.0582 kg/ m^2 $h^{0.5}$ (0.012 lb./ft^2 $h^{0.5}$) to 0.0591 kg/ m^2 $h^{0.5}$ (0.012 lb./ft^2 $h^{0.5}$) and from 0.0382 kg/ m^2 $h^{0.5}$ (0.0078 lb./ft^2 $h^{0.5}$) to 0.0390 kg/ m^2 $h^{0.5}$ (0.0080 lb./ft^2 $h^{0.5}$) , respectively. More detailed test results can be found in Table 2-7.

Table 2-7 Representative sorptivity results for UHPC

References	w/b ratio	Compressive strength (MPa-28 days)	Special Note		Curing regimes	Curing period (days)	Initial rate of water absorption ($kg/m^2 h^{0.5}$) ($lb./ft^2 h^{0.5}$)	Secondary rate of water absorption ($kg/m^2 h^{0.5}$) ($lb./ft^2 h^{0.5}$)
Charron, Denarié and Brühwiler (2008)	0.14	168 (24.37 ksi)	6 vol.% steel fibers and 10 wt.% of silica fume by concrete		20 ℃	28	0.02118 (0.0043)	
Ghafari et al. (2014)	0.16	133 (19.29 ksi)	0 wt. % cement replaced by nanosilica	12.5 wt. % silica fume by concrete	Water immersion at 20 ℃	28	-	0.0209 (0.0043)
		137 (19.87 ksi)	1 wt. % cement replaced by nanosilica					0.0196 (0.0040)
		138 (20.01 ksi)	2 wt. % cement replaced by nanosilica					0.0189 (0.0039)
		144 (20.89 ksi)	3 wt. % cement replaced by nanosilica					0.0178 (0.0036)
		140 (20.31 ksi)	4 wt. % cement replaced by nanosilica					0.0184 (0.0038)
Abbas, Soliman and Nehdi (2015)	0.15	156 (22.63 ksi)	8 mm (0.31 in.) steel fiber length	1 vol.% dosage of fiber	21 ℃ RH ≥ 95%	28	0.0582 (0.012)	0.0382 (0.0078)
		164 (23.79 ksi)		3 vol.% dosage of fiber			0.0534 (0.011)	0.0310 (0.0063)
		171 (24.80 ksi)		6 vol.% dosage of fiber			0.0470 (0.0096)	0.0271 (0.0056)
		158 (22.92 ksi)	12 mm (0.41 in.) steel fiber length	1 vol.% dosage of fiber			0.0589 (0.012)	0.0387 (0.0079)
		166 (24.08 ksi)		3 vol.% dosage of fiber			0.0540 (0.011)	0.0314 (0.0064)

References	w/b ratio	Compressive strength (MPa-28 days)	Special Note		Curing regimes	Curing period (days)	Initial rate of water absorption ($kg/m^2\ h^{0.5}$) ($lb./ft^2\ h^{0.5}$)	Secondary rate of water absorption ($kg/m^2\ h^{0.5}$) ($lb./ft^2\ h^{0.5}$)
Tafraoui, Escadeillas and Vidal (2016)	0.22	173 (25.09 ksi)	16 mm (0.63 in.) steel fiber length	6 vol.% dosage of fiber	Water immersion at 20 ℃	28	0.0477 (0.0098)	0.0275 (0.0056)
		159 (23.06 ksi)		1 vol.% dosage of fiber			0.0591 (0.012)	0.0390 (0.0080)
		165 (23.93 ksi)		3 vol.% dosage of fiber			0.0544 (0.011)	0.0316 (0.0065)
		170 (24.66 ksi)		6 vol.% dosage of fiber			0.0479 (0.0098)	0.0277 (0.0057)
		155 (22.48 ksi)	6.0 wt. % steel fibers in size of 160 µm diameter ×13 mm length (0.006 in. diameter ×0.51 in. length)	25 wt.% silica fume by cement			0.038 (0.0078)	
		146 (21.18 ksi)		25 wt.% metakaolin by cement			0.055 (0.011)	
Dobias, Pernicova and Mandlik (2016)	0.23	149.7 (21.71 ksi)	5 wt. % coated steel fiber		23 ℃ RH ≥ 50%	28	0.156 (0.032)	
Wang et al. (2018)	0.22	-	0 vol. % dosage of steel fiber		Steam curing at 90℃ for 72 hours + 22 ℃ with RH of 90%	28	0.097 (0.020)	
			3 vol. % dosage of steel fiber				0.081 (0.017)	

2.2.1.3 Permeability of UHPC

Permeability (or permeation) of concrete (or UHPC) is governed by the pore system. Liquids or gases can penetrate concrete (or UHPC) through pores. For water permeability (liquid permeation), air voids, capillary pores and gel pores can be penetrated by permeation (Chaudhry, 2018); and for gas permeability (gas permeation), only air voids and capillary pores can be penetrated. In addition, if the continuity of pore network is high, the permeation of samples increases. Thus, if the permeation of samples is high, the porosity and continuity of samples tends to be high (Sandoval *et al.*, 2017; Zhang *et al.*, 2020). In general, the permeability of concrete (or UHPC) mainly depends on the capillary porosity (Bertolini *et al.*, 2014; Sandoval *et al.*, 2017; Zhang *et al.*, 2020). In this section, water permeability and gas permeability of UHPC are reviewed.

2.2.1.3.1 Water permeability of UHPC

Water is assumed as incompressible and entirely viscous during the concrete water permeability test. For flow in a saturated concrete, it can be defined by Darcy's law, as shown in Equation 23 (Bertolini *et al.*, 2014).

$$\frac{dq}{dt} = \frac{K \times \Delta P \times A}{L \times \mu} \quad \text{(Equation 23)}$$

dq/dt: the flow rate (m^3/s);
K: the intrinsic permeability of concrete (m^2);
ΔP: the pressure head applied (Pa);
A: the surface of the cross section (m^2);
L: the thickness (m) of the specimen;
μ: the viscosity of the fluid ($N\ s/m^2$).

Water permeability of pervious concrete is usually tested by constant head test or falling head test. It has been reported that falling head test is more suitable for the mixture with low permeability (water permeability coefficient smaller than 10^{-6} m/s (3.28×10^{-6} ft./s)), and constant head test usually be adopted for more permeable mixture (water permeability coefficient larger than 10^{-6} m/s (3.28×10^{-6} ft./s)) (Hossain *et al.*, 2022). Constant head test is recommended by ASTM D5084 Standard Test Methods for Measurement of Hydraulic Conductivity of Saturated Porous Mixtures Using a Flexible Wall Permeameter (2016) and falling head test is recommended by ASTM D5084 (2016), ACI Committee 522 (2010) (2010), and FDOT (FDOT FM (5-565), 2015). During the water permeability test, the water level is kept in a constant height for constant head test, and the water level changes with time for falling head test, which is shown in Figure 2-21. After the outflow of water is steady, the quantity (ΔQ) of outflow of water in a certain time Δt are recorded for constant head test; and the original height of water head level h_1 (upper water level at inlet) and the height of water head level h_2 (upper water level at inlet) after a certain time Δt for outflow of water are denoted for falling head test. Then, the water permeability tested by constant head test and falling head test can be obtained by Equation 24 and Equation 25, which are based on Equation 23, respectively.

$$k = \frac{\Delta Q \times L}{A \times h \times \Delta t} \quad \text{(Equation 24)}$$

ΔQ: quantity of overflow of water for a given time Δt (m^3);
k: water permeability coefficient (m/s);
L: thickness of specimen (m);
A: area of cross section of sample (m^2);
h: the distance of water head above specimen (m);
Δt: interval of time (s).

$$k = \frac{a \times L}{A \times \Delta t} ln(\frac{h_1}{h_2}) \quad \text{(Equation 25)}$$

k : water permeability coefficient (m/s);
a: inside cross-sectional area of the reservoir containing water (m^2);
L: thickness of specimen (m);
A: area of cross section of sample (m^2);
Δt: interval of time (s);
h_1: first record of water head height (m);
h_2: second record of water head height (m).

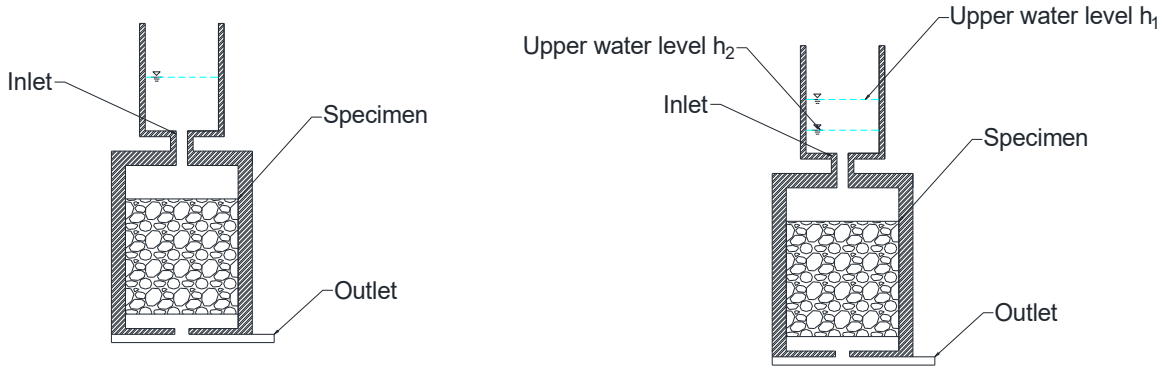

(a) Constant head test (b) Falling head test

Figure 2-21 Test setup for measuring water permeability of pervious concrete

For concrete with extremely low porosity, such as UHPC, water cannot fully penetrate the entire thickness of samples. In this scenario, the water permeability test is conducted by the setup as shown in Figure 2-22, which is recommended by EN 12390 – Testing Hardened Concrete Depth of Penetration of Water under Pressure (2019) and German standard DIN 1048 Test Methods of Concrete Impermeability to water: Part 2 (1978). During the test, a water pressure of 0.5 MPa (5 bar) is applied at the top surface of the pre-saturated samples for 72 hours, then samples are split for measuring the water permeation depth, which is recommended by EN 12390 - Testing Hardened Concrete Depth of Penetration of Water under Pressure (2019). Same procedure is also recommended by German standard DIN 1048 Test Methods of Concrete Impermeability to water: Part 2 (1978)but using water pressure of 0.1 MPa (1 bar), 0.3 MPa (3 bar), and 0.7 MPa (7 bar) consecutively applying for samples for 48 hours, 24 hours, and 24 hours, respectively. The water permeability coefficient can be calculated by Equation 26. Water permeability can be measure by the average water permeation depth and volume of intrusion water. Moreover, water permeation depth can also be adopted to represent the water permeation of concrete with

extremely low porosity. For water permeation depth lower than 30 mm (1.18 in.) under water pressure up to 0.7 MPa (7 bar) and test period up to 96 hours, the cement-based mixture is generally considered to be impermeable (Bertolini *et al.*, 2014).

$$k_v = \frac{x_p^2 \times v_t}{2 \times H \times t} \quad \text{(Equation 26)}$$

k_v: permeability coefficient (m/s);
x_p: average depth of the wet front (m);
v_t: volume of spaces filled during the test (m^3/m^3);
H: the pressure head of water (m);
t: water penetration time (s);

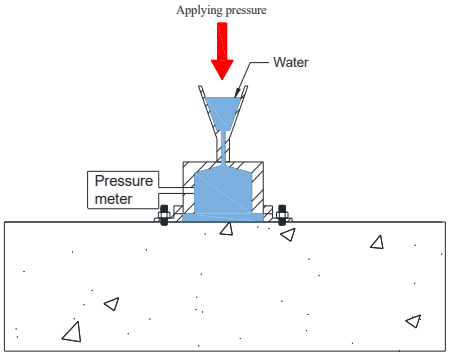

Figure 2-22 Water permeability test for concrete with low porosity

Generally, the water permeability coefficient (or water permeation) of UHPC is extremely low due to its dense microstructure and low porosity. Influencing factors such as w/cm and SCMs discussed in section 2.1.1 also influence water permeation. Moreover, superplasticizer content also shows the influence on water permeation, and effect of the steel fiber content on water permeation shows a opposite trend compared to the effect of steel fiber content on porosity. In the literature, the water permeation of UHPC has been investigated by several scholars, and a brief review is provided below. In general, the measured water permeability coefficient of UHPC reported in the literature is in the range of 0.00050 to 0.006712 mm^2/s bar (7.75×10^{-7} to 1.04×10^{-5} $in.^2/s$ bar) for 28 days curing, compared to typical water permeability of normal concrete as 0.006679 to 0.007857 mm^2/s bar (1.04×10^{-5} to 1.22×10^{-5} $in.^2/s$ bar) (Tam, 2005). Also, water permeation depth of UHPC is in the range of 9 to 22.5 mm (0.354 to 0.886 in.) under 24 hours water permeation, which is lower than 30 mm (1.18 in.) and can be regarded as impermeable.

Tam, Tam and Ng (2012) experimentally investigated the influence of w/b on water permeability of UHPC. The test is conducted by GWT 4000 – German Water permeability Test (GWT, 2002), and the test result is shown in Figure 2-22. It can be observed that as the w/b decreases, the water permeability first decreases and then increases. For samples at a curing age of 28 days, as the w/b decreases from 0.40 to 0.20, the water permeability coefficient decreases from 0.017954 to 0.000507 mm^2/s bar (2.87×10^{-5} to 7.86×10^{-7} $in.^2/s$ bar). As the w/b further decreases to 0.17, the water permeability coefficient increases to 0.001722 mm^2/s bar (2.76×10^{-6} $in.^2/s$ bar). The author explained that for excessively low w/b mixtures, poor workability leads to poor compaction and increased water permeability. More detailed test results can be found in Table 2-8.

Table 2-8 Representative water permeability results

References	w/b ratio	UHPC type	Curing regimes	Curing period (days)	Water permeability (mm^2/s bar) ($in.^2/s$ bar)	Water penetration depth (mm)
Tam, Tam and Ng (2012)	0.17	2.5 % SP dosage	27 ℃ (81 ℉) water tank	1 ~ 105 days	0.001722 (28 days) (2.67×10^{-6}) 0.001019 (105 days) (1.58×10^{-6})	-
	0.20				0.000507 (28 days) (7.86×10^{-7}) 0.000552 (105 days) (8.56×10^{-7})	
	0.23				0.001808 (28 days) (2.80×10^{-6}) 0.001569 (105 days) (2.43×10^{-6})	
	0.40				0.017954 (28 days) 0.010242 (105 days) (1.59×10^{-5})	
	0.20	2 % SP dosage			0.004623 (28 days) (7.17×10^{-6}) 0.001295 (105 days) (2.01×10^{-6})	

References	w/b ratio	UHPC type		Curing regimes	Curing period (days)	Water permeability (mm^2/s bar) ($in.^2$/s bar)	Water penetration depth (mm)
Zhang et al. (2019)	0.29	2.5 % SP dosage		20 °C (68 °F) with RH greater than 95%	28 days	0.00050 (28 days) (7.57×10^{-7}) 0.000552 (105 days) (8.56×10^{-7})	
		3 % SP dosage				0.004412 (28 days) (6.84×10^{-6}) 0.00098 (105 days) (1.52×10^{-6})	
		3.5 % SP dosage				0.006712 (28 days) (1.04×10^{-5}) 0.001646 (105 days) (2.55×10^{-6})	
		Without steel fiber & 15% fly ash	1% nano-SiO_2			-	22 (0.87 in.)
			5% nano-SiO_2				9 (0.35 in.)
			9% nano-SiO_2				14 (0.55 in.)
		5% nano- SiO_2 & 15% fly ash	0.5% steel fiber				13 (5.2 in.)
			2.5% steel fiber				22.5 (0.89 in.)

Note: no information about compressive strength is provided by the references.

Tam, Tam and Ng (2012) additionally experimentally investigated the influence of superplasticizer (SP) on water permeability of UHPC. The test result is shown in Figure 2-23. With increasing SP dosage, the water permeability coefficient first decreases and then increases. At curing age of 28 days, water permeability coefficient increased from 0.004623 to 0.00507 mm^2/s bar (7.17×10^{-6} to 7.86×10^{-7} $in.^2/s$ bar) when the SP content increased from 2 wt.% to 2.5 wt.% by cement. The author explained that with sufficient SP, water content and porosity is reduced, and cementitious particles can be dispersed better. The water permeability coefficient increased to 0.006712 mm^2/s bar (1.04×10^{-5} $in.^2/s$ bar) with SP content increasing to 3.5 wt.% by cement. The author indicated that due to excessive SP addition, large slump loss and segregation occur, causing more air trapped during mixing, which leads to higher porosity and further leads to higher water permeability. More detailed test results can be found in Table 2-8.

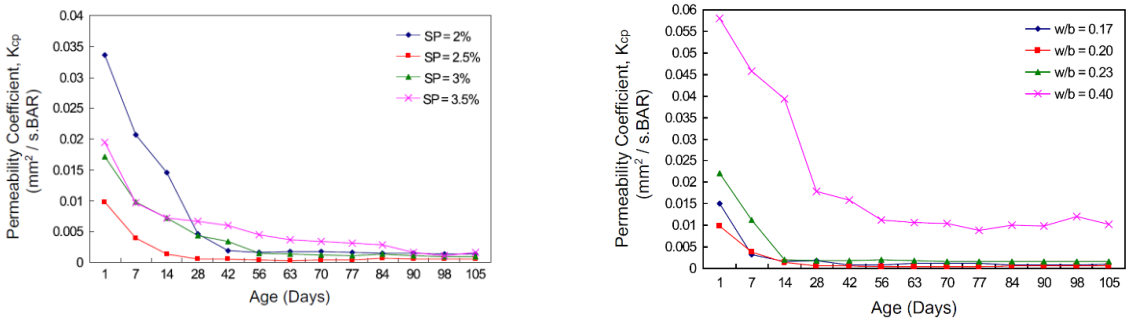

(a) Water permeability coefficient against different water-to-binder ratios

(b) Water permeability coefficient against different SP dosage

Figure 2-23 Water permeability test result (Tam, Tam and Ng, 2012)

Zhang et al. (2019) experimentally investigated the influence of dosage of nano-SiO_2 on water permeability of UHPC. The specimens were subjected to 1.2 MPa (12 bar) water pressure for 24 hours and the water permeation depth was reported. The results show that with increasing dosage of nano-SiO_2, the water permeation depth firstly decreases and then increases. With the dosage of nano-SiO_2 increased from 0 wt.% to 5 wt.%, the depth of water permeation of samples without steel fibers decreased from 22 mm to 9 mm (0.87 in. to 0.35 in.). The author explained that due to the small particle size of nano-SiO_2, the spacing between cement particles can be physically filled and block the water permeation channel. Then, with the dosage of nano-SiO_2 further increasing from 5 wt.% to 9 wt.%, the depth of water permeation increased from 9 mm to 16 mm (0.35 in. to 0.63 in.). The author explained that excessive nano-SiO_2 absorbs a larger amount of water, leading to more serious chemical shrinkage, causing microcracks, which could increase the water permeability. More detailed test results can be found in Table 2-8.

Zhang et al. (2019) also experimentally investigated the influence of steel fiber content on water permeability of UHPC. With the increasing dosage of steel fibers from 0.5 vol. % to 2.5 vol. %, the depth of water permeation increases from 13 mm to 22.5 mm (0.51 in. to 0.89 in.). The author explained that due to the presence of weak ITZ between cement paste and steel fiber, microcracks can easily occur on the interface, and it may further increase water permeability. More detailed test results can be found in Table 2-8

2.2.1.3.2 Gas permeability of UHPC

Gas permeability is the transport rate of gas under a pressure gradient. Gas permeation occurs mainly through interconnected pores, including capillary pores and air voids, although air voids are usually considered disconnected and evenly distributed in mixture. Gas permeability not only depends on

porosity but also continuity and tortuosity of the pore system. For gas permeability, gas is regarded as compressible fluid, and can be defined as Equation 27. In general, high porosity tends to result in high gas permeability.

$$\frac{dq}{dt} = \frac{k_{gas} \times A \times (P_1^2 - P_2^2)}{L \times \mu \times 2P_2} \quad \text{(Equation 27)}$$

dq/dt: the flow (m^3/s);

k_{gas}: the gas permeability coefficient (m^2);
P_1: flow-out (inlet) pressure (Pa);
P_2: gas applied (outlet) pressure (Pa);
A: the surface of the cross section (m^2);
L: the thickness of the specimen (m);
μ:the viscosity of the fluid (N s/m^2).

The steady state (constant head) method is usually adopted to test gas permeability of concrete (or UHPC). The CEMBUREAU method proposed by Kollek (1989) has been recommended by RILEM TC 116-PCD: Permeability of Concrete as a Criterion of its Durability (1999) and French standard AFPC-AFREM (French Competitiveness Clusters Alliance – French Association for the Research and Testing of Mixtures and Structures): Durabilité des Bétons: Méthodes recommandées pour la mesure des grandeurs associées à la durabilité (Durability of Concretes: Recommended methods for measuring the quantities associated with durability) (1997), which were adopted to determine the gas permeability of concrete (or UHPC). During the test, samples are pre-dried either at 50 ℃ (RILEM TC 116-PCD, 1999) or 80 ℃ (AFPC-AFREM, 1997) until the mass change of sample is less than 5 % (RILEM TC 116-PCD, 1999) or 1% (AFPC-AFREM, 1997) and then stored in a sealed chamber at 20 ℃ (68 ℉) and 64% R.H. for 28 days (sealed condition), or 7 days drying at 105 ℃ (221 ℉) (dried condition). Then, samples are removed to permeameter cell, ensuring there is no leak between the side surface and cell wall. Further, oxygen (or nitrogen) is applied to samples with pressure from 0.15 MPa (1.5 bar) to 0.30 MPa (3 bar) (RILEM TC 116-PCD, 1999) or 0.2 MPa (2 bar) (AFPC-AFREM, 1997) at gas inlet, as shown in Figure 2-24. Finally, the gas flow rate at gas outlet is recorded. Gas permeability coefficient can be calculated as Equation 28, which is based on Equation 27. The mean gas permeability coefficient is the mean of gas coefficients at different gas pressures.

$$K_i = \frac{2P_a Q_i L_t \mu}{A(P_i^2 - P_a^2)} \quad \text{(Equation 28)}$$

K_i : the gas permeability coefficient at stage i (m^2);
P_a : atmospheric pressure, absolute (Pa);
P_i: applied test pressure, absolute (Pa);
Q_i : flow rate at pressure stage i (m^3/s);
L: thickness of the specimen (m);
μ: dynamic viscosity of the fluid at test temperature (N $s\ m^{-2}$);
A: cross section of the specimen (m^2).

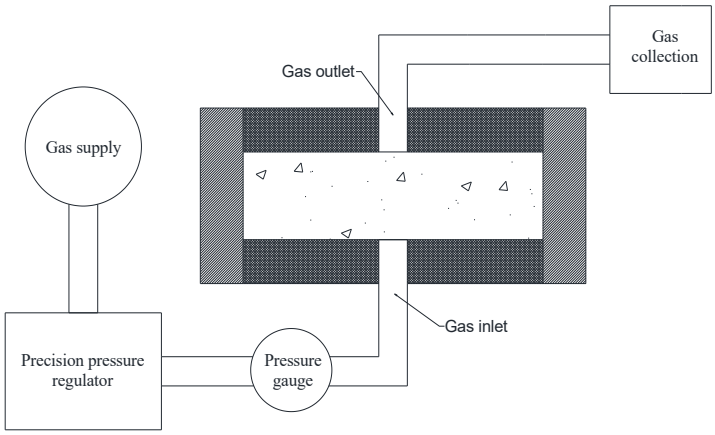

Figure 2-24 Steady-state gas permeability test

In addition, it should be noted that gas permeability coefficient also depends on the applied gas pressure for test. As the gas pressure increases, the gas permeability coefficient decreases. There are two reasons contribute for this phenomenon (Qian *et al.*, 2020): 1) with increasing gas pressure, small pores are considered part of the flow channel for gas transport, which leads to higher tortuosity of pore system and further leads to lower gas permeability; and when increasing applied pressure, the gas-medium gradually condenses to a liquid, which leads to lower gas permeability. Thus, the applied gas pressure is important, and the test results can be compared only after being normalized (eg: using the mean value of gas permeability coefficient under different pressure stages (RILEM TC 116-PCD, 1999). Moreover, for different sample preconditioning, the gas permeability will be different. For example, microcracks will be generated under oven heating at 105℃ (221℉), and these cracks act as channels for gas intrusion, leading to a higher gas permeability (Bertolini *et al.*, 2014).

Moreover, several non-standard transient flow gas permeability tests have been developed by scholars. During the test, the flow of applied gas was set with pressure changing with time, namely, applying pressure gradient to specimen. The transition change of applied pressure gradient with gas flow is recorded and adopted for measuring gas permeability. Torrent method and Oxygen Permeability Test (OPT) can be adopted for measure gas permeability. The Torrent method can be adopted to evaluate the gas permeability of concrete in-situ (Torrent, 1992). During the test, two-chamber system is placed on the surface of concrete and then is vacuumed to provide a unidirectional air flow flowing into the inner chamber, as shown in Figure 2-25 (a). Then, the gas permeability can be calculated by recording the pressure in the inner chamber, as shown in Equation 28. Also, OPT is an indoor test for measuring gas permeability (oxygen) for concrete specimens. During the test, the side surface of sample is firstly sealed by covering rubber collar, then was put into a chamber with opening inlet for oxygen intrusion (applying pressure) and outlet closed, as shown in Figure 2-25 (b). Then, oxygen starts to penetrate samples and the decreasing pressure inside the chamber is recorded for calculating gas permeability of samples, as shown in Equation 29.

$$k=4\left(\frac{V_c\left(dP_I/dt\right)}{A\left(P_a^2-P_I^2\right)}\right)^2\frac{\mu P_a}{\varepsilon}\int_0^t\left[1-\left(\frac{P_I}{P_a}\right)^2\right]dt \qquad \text{(Equation 29)}$$

k: gas permeability coefficient (m^2);

μ: dynamic viscosity of air (N s m^{-2});
V_c: capacity of the inner chamber plus elements into which the air flows of the concrete (m^3);
A: cross-sectional area of the concrete 'cylinder' where the air flow into the inner chamber takes place (m^2);
P_I: the pressure in inner chamber as a function of time (N m^{-2});
dP_I/dt: derivative with time calculated at time t (N m^{-2} S^{-1});
P_a: the atmospheric pressure.

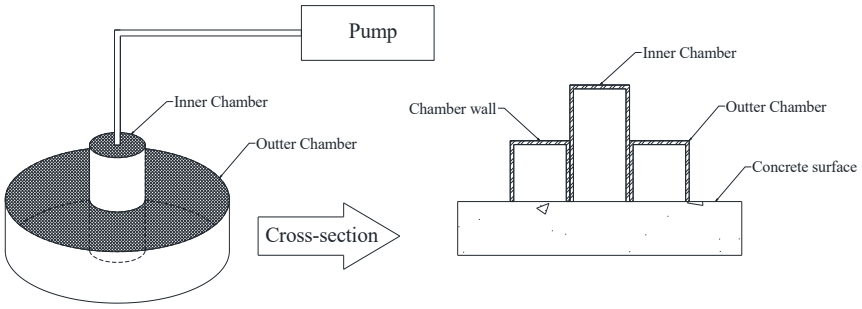

(a) Torrent method

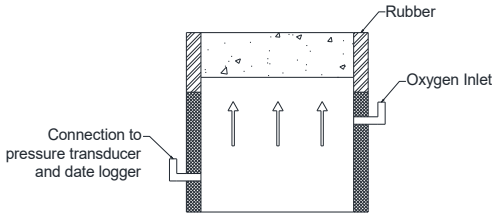

(b) Oxygen permeability test

Figure 2-25 Transition state gas permeability

Due to the dense microstructure and low porosity, UHPC gas permeability is extremely low compared to the normal concrete. Influencing factors such as SCMs and steel fiber discussed in section 2.2.1.1 also affect the gas permeability. In the literature, the gas permeability of UHPC has been investigated, and several scholars reported the gas permeability coefficient of UHPC. A brief review is provided. The measured gas permeability coefficient of UHPC is in the range of 0.3 to 2.54 × 10^{-19} m^2 (3.23 to 27.34 × 10^{-19} $ft.^2$) corresponding to an applied pressure from 0.6 Mpa (6 bar) to 0.3 Mpa (3 bar), compared to that of normal concrete with typical permeability between 5 × 10^{-16} to 10^{-18} m^2 (5.382 × 10^{-15} to 10^{-17} $ft.^2$) under low pressure (lower than 10 bar) (Bertolini *et al.*, 2014). More detailed information is provided as follow, and the corresponding test results are listed in Table 2-9.

Table 2-9 Representative gas permeability results for UHPC

References	w/b ratio	Compressive Strength (MPa)	Gas type (Pre condition)	Special note		Curing regimes	Curing period (days)	Maximum gas pressure (bar)	Gas permeability coefficient/ mean gas permeability coefficient ($\times 10^{-19} m^2$) ($\times 10^{-19}$ ft.^{2})
Ghafari et al. (2014)	0.16	133 (19.29 ksi)	Oxygen (Sealed Condition)	0 wt. % cement replaced by nanosilica	12.5 wt. % silica fume by concrete	Water immersion at 20 °C (68 °F)	28	2.5	2.54 (27.34)
		137 (19.87 ksi)		1 wt. % cement replaced by nanosilica					2.35 (25.30)
		138 (20.01 ksi)		2 wt. % cement replaced by nanosilica					2.17 (23.36)
		144 (20.89 ksi)		3 wt. % cement replaced by nanosilica					1.99 (21.42)
		140 (20.31 ksi)		4 wt. % cement replaced by nanosilica					2.14 (23.03)
Tafraoui, Escadeillas and Vidal (2016)	0.22	155 (22.48 ksi)	Oxygen (Sealed Condition)	25 wt.% silica fume by cement		20 °C (68 °F) in water	28	6	< 1.5 (< 16.15)
		146 (21.18 ksi)		25 wt.% metakaolin by cement					
Wang et al.(2018)	0.22	-	Nitrogen (Sealed Condition)	0% dosage of steel fiber		Steam curing at 90°C (194 °F) for 72 hours + 22 °C (71.6 °F) with RH of 90%	28	6	0.8 (8.61)
				3% dosage of steel fiber					0.3 (3.23)

As discussed in section 2.2.1.1, by addition of SCMs, the pore system can be highly refined, leading to low porosity, which further leads to decreasing of gas permeability. Thus, the addition of SCMs is the key factor for UHPC to decrease gas permeability. Ghafari et al. (2014) experimentally investigated the gas permeability of UHPC with nano-silica of different dosages with maximum applied gas pressure of 0.25 MPa (2.5 bars). The mean gas permeability coefficient of UHPC with 0, 1, 2, 3, 4 wt. % dosage of silica fume replaced by nanosilica was measured to be 2.54, 2.35, 2.17, 1.99, and 2.14 × 10^{-19} m^2 (2.73, 2.53, 2.34, 2.14, and 2.30 × 10^{-18} $ft.^2$), respectively, as shown in Figure 2-26. Tafraoui, Escadeillas and Vidal (2016) experimentally investigated the gas permeability of UHPC with silica fume and metakaolin, respectively, with a maximum applied gas pressure of 0.6 MPa (6 bar). The results that for both samples with silica fume and metakaolin, the gas permeability coefficient is lower than 1.5 × 10^{-19} m^2 (1.61 × 10^{-18} $ft.^2$). More detailed information can be found in Table 2-9.

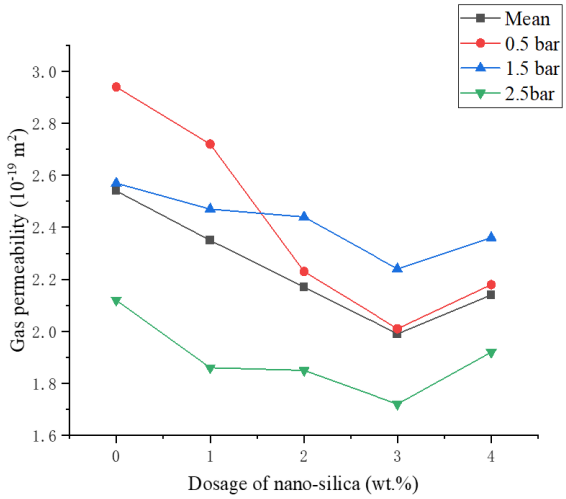

Figure 2-26 The relationship between gas permeability and dosage of nano-silica

It has been pointed out that with a higher steel fiber content, the gas permeability of UHPC decreases. Wang et al. (2018) experimentally investigated the influence of steel fiber content on gas permeability of UHPC. The dosages of steel fibers were 0, 1, 2, and 3 vol.% and the applied gas pressure was set from 0.3 MPa to 0.6 MPa (3 bar to 6 bar). The result shows that with increasing dosage of steel fibers from 0 vol.% to 3 vol.%, the mean gas permeability decreased from 0.8 × 10^{-19} m^2 to 0.3 × 10^{-19} m^2 (8.61× 10^{-19} $ft.^2$ to 3.23 × 10^{-19} $ft.^2$). More detailed information can be found in Table 2-9.

2.2.1.4 The chloride ion penetration of UHPC

External chloride ions could enter concrete or UHPC through capillary suction, permeation, diffusion, and migration. Intrusion of chloride ions could lead corrosion of steel members, and further cause capacity reduction of structural components and deterioration of whole structures. For the past studies, rapid chloride penetration test (RCPT), salt ponding test, bulk diffusion test, and rapid migration test (RCMP) were adopted to evaluate the chloride penetration of UHPC. Compared to normal concrete, UHPC shows significantly higher resistance to chloride penetration, and much lower maximum chloride content, chloride penetration depth, chloride diffusion coefficient, and migration coefficient, which is further detailed discussed in section 2.1.4.1 to 2.1.4.3.

In addition, for cementitious mixtures, two factors are generally adopted to evaluate the chloride content of concrete samples: total chloride content and free chloride content. In terms of total chloride content, it refers to both chloride ions bound by hydration products and chloride ions contained in pore solution, which can be measured by NordTest NT Build 208 – Concrete, Hardened: Chloride Content by Volhard

Titration (1996), AASHTO T 260 – Sampling and Testing for Chloride Ion in Concrete and Concrete Raw Mixtures Procedure A (1997) or ASTM C 1152 - Standard Test Method for Acid-Soluble Chloride in Mortar and Concrete (2020). In terms of free chlorides, it only refers to the chloride ions in pore solution, which can be measured according to AASHTO T 260 – Sampling and Testing for Chloride Ion in Concrete and Concrete Raw Mixtures Procedure B (1997)or ASTM C 1218 – Standard Test Method for Water-Soluble Chloride in Mortar and Concrete (2020). Concrete carbonation can release some of the chloride bound by hydration products(Brown, Thelemann and Sletten, 2020). Chloride binding by hydration products is beneficial because the bound chlorides cannot migrate further into the concrete nor interact with the reinforcing steel (Brown, Thelemann and Sletten, 2020).

2.2.1.4.1 Electrical tests for chloride migration potential

Negatively charged chloride ions can migrate into the concrete through the pore solution due to an electrical potential. Currently, two major standard methods have been developed to measure the migration behavior of chloride ions within UHPC: the rapid chloride penetration test (RCPT) and rapid chloride migration test (RCMT), and one non-standard method – steady-state chloride migration test is generally adopted for research purpose.

2.2.1.4.1.1 Rapid chloride penetration test

The rapid chloride penetration test (RCPT) is described by ASTM C 1202 – Standard Test Method for Electrical Indication of Concrete's Ability to Resist Chloride Ion Penetration (2022). During the test, a pre-saturated sample in size of 100 mm diameter x 50 mm height (3.94 in. diameter x 1.97 in. height) cylinder is placed in a chamber with one side exposed to sodium chloride solution (3 wt.%) and the other side exposed to sodium hydroxide solution (0.3 M), an external power supply of 60 V DC is applied to drive the ions through the samples for 6 hours, as shown in Figure 2-27. The total charge passing through the sample is monitored and analyzed by Equation 30. The total charge passed during the six-hour test is related to the concrete resistance to chloride penetration, which can be evaluated according to Table 2-10. However, this method has been criticized in practice: 1) the charges counted for passing through the cross section are related to all ionic movement instead of only chloride ions; 2) due to the high potential application, temperature of samples can be raised up quickly, further influencing the test results; and 3) the testing period is too short for stabilizing the flow steady-state migration, although the short testing period is favored by scholars and engineers.

$$Q = 900(I_0 + 2I_{30} + 2I_{60} + \ldots + 2I_{300} + 2I_{330} + 2I_{360}) \quad \text{(Equation 30)}$$

Q: charge passed (coulombs);
I_0: current (amperes) immediately after voltage is applied;
I_t: current (amperes) at t min after voltage is applied.

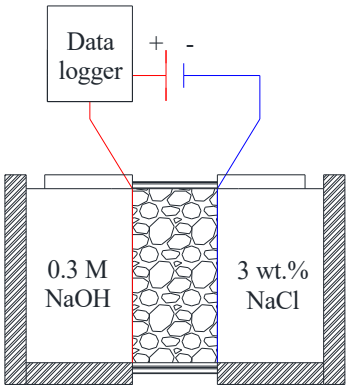

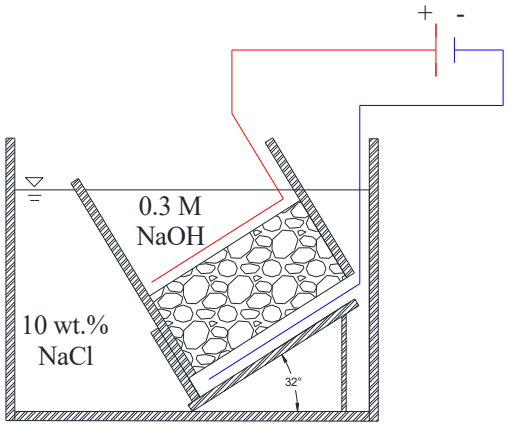

Figure 2-27 RCPT test setup Figure 2-28 Rapid chloride migration test scheme

Table 2-10 RCPT measuring criteria (ASTM C 1202, 2022)

Charge passed (Coulombs)	Chloride Ion Penetration
>4000	High
2000-4000	Moderate
1000-2000	Low
100-1000	Very low
< 100	Negligible

2.2.1.4.1.2 Non-steady-state rapid chloride migration test

Rapid chloride migration test measures the chloride migration behavior of concrete, which is recommended by Nordtest Method NT Build 492-Concrete, Mortar and Cement-based Repair Mixtures: Chloride Migration Coefficient from Non-Steady-State Migration Experiment (1999). During the test, a pre-saturated concrete sample in size of 100 mm diameter × 50 mm height (3.97 in. diameter × 1.97 in. height) is immersed in a container with the anode exposed to 0.3 M sodium hydroxide solution and the cathode exposed to 10 wt. % sodium chloride solution with an externally applied electric field, as shown in Figure 2-28. After the migration test, samples are split to measure the chloride penetration depth. The chloride migration coefficient can be obtained based on the chloride penetration depth, as shown in Equation 31. RCMT has a number of advantages over RCPT, such as 1) it measures the chloride penetration rather than measuring the number of all ions passing through the samples; 2) it reduces the bias due to lower heat generation with lower applied voltage; and 3) it measures the results with a longer test period than RCPT test. However, during the test, samples that contain conductive metals like steel fibers can cause a short-circuit for current flow leading to a larger migration coefficient. If the chloride ions cannot penetrate to the layer containing conductive mixture, there will be no issues. This drawback is expected to be solved by lower applied voltage and longer testing period (Riding *et al.*, 2022).

$$D_{nssm} = \frac{0.0239(273+T)L}{(U-2)t}\left(x_d - 0.0238\sqrt{\frac{(273+T)Lx_d}{U-2}}\right) \quad \text{(Equation 31)}$$

D_{nssm}: non-steady state migration coefficient (× 10^{-12} m^2/s);
T: average value of the initial and final temperatures in the anolyte solution (°C);

L: thickness of the specimen (mm);
U: absolute value of the applied voltage (V);
t: test duration (hour);
x_d: average value of the penetration depths (mm).

2.2.1.4.1.3 Steady-state chloride migration test

Steady-state chloride migration test measures the chloride penetration under electrical field. The chloride diffusion coefficient under electrical field can be obtained by this test. The test setup is similar to RCPT but not that intensive. Usually, a voltage at least 10-15 V is applied to samples in size of 100 mm diameter (3.94 in.) × 15 to 50 mm (0.59 to 1.97 in.) height (Stanish, Hooton and Thomas, 2001). The cathodic chamber is usually filled with chloride solution (upstream), and the anodic chamber is usually filled with chloride-free solution (downstream). The chloride concentration in cathodic solution is monitored periodically to ensure the chlorides from upstream cell reaching downstream cell for achieving steady-state condition. The change of chloride concentration in upstream via time is constant in steady-state condition, which equals to the chloride flux. Then, the change of chloride concentration in cathodic solution during steady-state condition can be adopted for chloride diffusion coefficient calculation, as shown in Equation 32. It should be noted that the chloride diffusion coefficient measured by steady-state migration test cannot be compared to that measured by bulk diffusion test due to electrical field. Compared to RCPT, the heating problem can be solved by steady-state chloride migration test due to lower applied voltage, and only chloride ions are measured for more accurate test results by periodically measuring chloride concentration in upstream cell. Compared to RCPT test, the time for conducting test is longer for steady-state chloride migration test since the steady-state condition of chloride flux is required during the test.

$$D_{ssm} = \frac{RTL}{ZFU}\frac{V}{A}\frac{1}{C}\left|\frac{\Delta C}{\Delta t}\right| \qquad \text{(Equation 32)}$$

D_{ssm}: Chloride diffusion coefficient (m^2/s);
R: the gas constant (=8.3145 J/mol K);
T: the absolute temperature (K);
L: specimen thickness (m);
Z: the ionic valence;
F: the Faraday constant (=96485 C per equivalent);
U: the applied potential (V);
V: the volume of upstream cell (m^3);
A: the area of cross section of specimen (m^2);
C: the initial chloride concentration in cathodic chloride solution;
ΔC: the change of chloride concentration in cathodic chloride solution against time;
Δt: the test time in steady-state condition.

The fine pore system and dense microstructure of UHPC gives it a high resistance to chloride penetration, low chloride migration coefficient and low maximum chloride penetration depth. Influence factors such as w/b, addition of SCMs, length of steel fiber, and curing regime discussed in section 2.1.1 also affect the chloride migration behavior. Curing conditions and steel fiber content also influence UHPC chloride migration behavior. In literature, past scholars reported that the charge passed for UHPC was 18 to 360 Coulombs. This is extremely low compared to typical values of normal-strength concrete in the range of 2290 to 5445 Coulombs (Tai *et al.*, 2020). UHPC has much a lower non-steady state migration coefficient measured using the RCMT in the range of 3×10^{-14} m^2/s to 6.63×10^{-12} m^2/s (3.2×10^{-13} $ft.^2/s$ to 7.14×10^{-11} $ft.^2/s$) compared to that of normal-strength concrete 5.2×10^{-12} m^2/s (5.60×10^{-11} $ft.^2/s$) to 19.1×10^{-12} m^2/s (2.05×10^{-10} $ft.^2/s$) (Liu et al., 2015).. More details on RCPT and RCMT results can be found in Table 2-11 and Table 2-12.

Past scholars reported higher dosages of SCMs leads to higher resistance of UHPC to chloride penetration, lower chloride migration coefficient, and lower maximum chloride penetration depth. Ghasemzadeh Mosavinejad et al. (2020) investigated the influence of the dosage of silica fume on chloride penetration resistance of UHPC by RCPT test. Test result shows that with increasing dosage of silica fume from 15 to 40 vol.% of cementitious mixture, the number of charges passed decreases from the range of 46 to 62 Coulombs to the range of 29 to 41 Coulombs. It can be seen that with addition of silica fume, chloride ion penetration can be considered "Negligible" according to Table 2-10. More detailed information can be found in Table 2-7. Literature also reported that chloride migration coefficient and maximum chloride penetration depth decrease with higher contents of SCMs of UHPC. Karim, Najimi and Shafei (2019) experimentally investigate the influence of silica fume content on chloride migration behavior by RCMT test. The dosages of silica fume are respectively designed as 0.07 and 0.25 by weight of cement. The results show that with increasing dosage of silica fume from 0.07 to 0.25 wt.% by cement, the chloride penetration depth decreases from 5.64 mm to 4.83 mm (0.22 in. to 0.19 in.), and the migration coefficient decreases from 2.32×10^{-12} m^2/s (2.50×10^{-11} $ft.^2/s$) to 1.23×10^{-12} m^2/s (1.32×10^{-11} $ft.^2/s$). In addition, scholars reported that different types of SCMs influence the chloride migration coefficient and maximum chloride penetration depth. Song et al. (2019) investigated the influence of addition of silica fume and metakaolin on chloride migration by RCMT test. Three different ratios of silica fume (SF) to metakaolin (MK) were designed for this test as 100% SF (90 kg/m^3 SF), 60%SF + 40% MK (54 kg/m^3 SF + 36 kg/m^3 MK), and 100% MK (90 kg/m^3 MK), and the corresponding migration coefficients are 4.361×10^{-12} m^2/s (4.70×10^{-11} $ft.^2/s$), 3.959×10^{-12} m^2/s (4.26×10^{-11} $ft.^2/s$), and 4.705×10^{-12} m^2/s (5.06×10^{-11} $ft.^2/s$), respectively; and the corresponding penetration depths are 7.423 mm (0.292 in.), 6.831 mm (0.269 in.), and 7.925 mm (0.312 in.), respectively. The author indicated that since hydration degree of metakaolin is higher than silica fume and chloride ion can be absorbed to form Friedel's salt because of high content of aluminum of metakaolin, chloride migration coefficient decreases with higher ratio of metakaolin addition. However, excessive dosage of metakaolin causes increasing chloride migration coefficient. The author explained that metakaolin is in structure of layer, addition of metakaolin leads to higher viscosity, which causes more macro pores in UHPC and further lead chloride to easily penetrating samples.

Table 2-11 Representative RCPT results

References	w/b ratio	Compressive strength (MPa/ksi, 28 days)	UHPC type		Curing regimes	Curing period (days)	Average Coulombs passed
Graybeal (2006)	-	193 (27.99 ksi)	UHPC with 2 vol.% steel fibers		Steam curing -steam at 90°C (194 ºF) (95% RH) for 48 h + untreated curing	28	18
		126 (18.27 ksi)			Untreated curing - standard laboratory environment	28	360
						56	76
		171 (24.80 ksi)			Tempered Steam - steam at 60°C (140 ºF) (95% RH) for 48 h + Untreated curing	28	39
						56	26
		171 (24.80 ksi)			Delayed Steam - untreated curing (15 days) + Steam curing (2 days) + untreated curing	28	18
Habel et al., (2008)	0.20	-	UHPC without steel fibers		Immersion in water at 20 °C (68 ºF)	28	88
		128 (18.56 ksi)	UHPC with steel fibers with dosage of 5.5 vol.%				72
Abbas, Soliman and Nehdi (2015)	0.16	156 (22.63 ksi)	1% steel fibers	8 mm (0.31 in.) length of steel fiber	Environmental chamber at 45 °C (113 ºF) with 95% RH for 5 hours + moist curing at 45 °C (113 ºF) with 95% RH for 5 days + 20 °C (68 ºF) ambient curing (RCPT tested by 3 to 10 wt.% sodium solution)	28	60-65
		164 (23.79 ksi)	3% steel fibers				45-50
		171 (24.80 ksi)	6% steel fibers				36-42
		159 (23.06 ksi)	1% steel fibers	12 mm (0.47 in.) length of steel fiber			60-67
		165 (23.93 ksi)	3% steel fibers				47-52
		170 (24.66 ksi)	6% steel fibers				38-40
		159 (23.06 ksi)	1% steel fibers	16 mm (0.63 in.) length of steel fiber			65-72
		165 (23.93 ksi)	3% steel fibers				52-56

References	w/b ratio	Compressive strength (MPa/ksi, 28 days)	UHPC type		Curing regimes	Curing period (days)	Average Coulombs passed
Ghasemzadeh Mosavinejad et al.(2020)	0.17	170 (24.66 ksi)	6% steel fibers		Immersed in 20 ℃ (68 ºF) lime water	28	43-48
		106 (15.37 ksi)	15% silica fume	0 vol.% PVA fiber			62
		116 (16.82 ksi)		1.2 vol.% PVA fiber			51
		116 (16.82 ksi)	40% silica fume	0 vol.% PVA fiber			40
		107 (15.52 ksi)		1.2 vol.% PVA fiber			29
		105 (15.23 ksi)	15% silica fume	0 vol.% PVA fiber			60
		110 (15.95 ksi)		1.2 vol.% PVA fiber	immersed in 70 ℃ (158 ºF) hot water for 72 hours + Immersed in 20 ℃ (68 ºF) lime water		46
		108 (15.66 ksi)	40% silica fume	0 vol.% PVA fiber			41
		105 (15.23 ksi)		1.2 vol.% PVA fiber			33

Table 2-12 Representative RCMT results

References	w/b ratio	Compressive Strength (MPa/ksi)	Additional notes	Curing regimes	Chloride ions penetration depth (mm/in.)	Chloride migration coefficient
Peng, Chen and Hu (2011)	0.28 (w/c)	-	Steel fiber in size of 0.2 mm diameter × 13 mm length dosage of 2 vol. %	Cured in water at 20 ℃ (68 ℉) for 3 days + 90 ℃ for 3 days	-	0.51×10^{-13} m^2/s (5.50×10^{-13} $ft.^2/s$)
	0.29 (w/c)					0.53×10^{-13} m^2/s (5.70×10^{-13} $ft.^2/s$)

References	w/b ratio	Compressive Strength (MPa/ksi)	Additional notes		Curing regimes	Chloride ions penetration depth (mm/in.)	Chloride migration coefficient
Chen et al. (2018)	0.30 (w/c)		Steel fiber in size of 0.2 mm diameter × 13 mm length (0.008 in. diameter × 0.51 in. length), dosage of 2 vol. %		-		0.56×10^{-13} m^2/s (6.03×10^{-13} $ft.^2/s$)
	0.18	145.1 (21.04 ksi)		0 wt.% (C-LDHs)		4.8 - 5.9 (0.19 to 0.23 in.)	1.99×10^{-12} m^2/s (2.14×10^{-11} $ft.^2/s$)
	0.19	157.5 (22.84 ksi)		1 wt.% (C-LDHs)		3.8 - 4.5 (0.15 to 0.18 in.)	1.48×10^{-12} m^2/s (15.93×10^{-11} $ft.^2/s$)
	0.20	135.2 (19.61 ksi)		2 wt.% (C-LDHs)		6.4 - 6.8 (0.25 to 0.27 in.)	2.55×10^{-12} m^2/s (2.74×10^{-11} $ft.^2/s$)
Karim, Najimi and Shafei (2019)	0.20 (w/c)	-	Steel fiber in size of 0.2 mm diameter × 13 mm length (0.008 in. diameter × 0.51 in. length), dosage of 2 vol. %	Silica fume-to-cement ratio 0.07	Curing room for 28 days	5.64 (0.22 in.)	2.32×10^{-12} m^2/s (2.50×10^{-11} $ft.^2/s$)
	0.25 (w/c)			Silica fume-to-cement ratio –0.25		4.83 (0.19 in.)	1.23×10^{-12} m^2/s (1.32×10^{-11} $ft.^2/s$)
Song et al. (2018)	0.17	134.3 (19.48 ksi)	Steel fiber in size of 0.2 mm diameter × 13 mm length (0.008 in. diameter × 0.51 in. length)	0.5 vol.%	Water tank at 23℃ (73 ℉) for 7 days	10.60 (0.41 in.)	4.74×10^{-12} m^2/s (5.10×10^{-11} $ft.^2/s$)
		152.8 (19.48 ksi)		1.0 vol.%		11.07 (0.43 in.)	4.97×10^{-12} m^2/s

References	w/b ratio	Compressive Strength (MPa/ksi)	Additional notes		Curing regimes	Chloride ions penetration depth (mm/in.)	Chloride migration coefficient
							(5.35×10^{-11} $ft.^2/s$)
		161.5 (23.42 ksi)		1.5 vol.%		11.52 (0.45 in.)	5.19×10^{-12} m^2/s (5.59×10^{-11} $ft.^2/s$)
		169.5 (24.58 ksi)		2.0 vol.%		12.11 (0.48 in.)	5.49×10^{-12} m^2/s (5.91×10^{-11} $ft.^2/s$)
		172.1 (24.96 ksi)		2.5 vol.%		13.42 (0.53 in.)	6.14×10^{-12} m^2/s (6.61×10^{-11} $ft.^2/s$)
		173.4 (25.15 ksi)		3.0 vol.%		14.41 (0.57 in.)	6.63×10^{-12} m^2/s (7.14×10^{-11} $ft.^2/s$)
Song et al. (2019)	0.17	-	Steel fiber in size of 0.2 mm diameter × 13 mm length (0.008 in. diameter × 0.51 in. length), dosage of 21 wt. %	100% SF (90 kg/m^3 SF)	20 ℃ (68 °F) for 7 days	7.423	4.361×10^{-12} m^2/s (4.69×10^{-11} $ft.^2/s$)
				60%SF + 40% MK (54 kg/m^3 SF + 36 kg/m^3 MK		6.831 (0.27 in.)	3.959×10^{-12} m^2/s (4.26×10^{-11} $ft.^2/s$)
				100% MK (90 kg/m^3 MK)		7.925 (0.31 in.)	4.705×10^{-12} m^2/s (5.06×10^{-11} $ft.^2/s$)

References	w/b ratio	Compressive Strength (MPa/ksi)	Additional notes		Curing regimes	Chloride ions penetration depth (mm/in.)	Chloride migration coefficient
Pourjahanshahi and Madani (2021)	0.17	146.4 (21.23 ksi)	Steel fiber in size of 0.7 mm diameter × 25 mm length (0.03 in. diameter × 0.98 in. length)	0 vol. % steel fiber	Lime-saturated water at 23℃ (73 ℉)	-	0.46×10^{-12} m^2/s (4.95×10^{-12} $ft.^2/s$)
		166.1 (24.09 ksi)		0.5 vol. % steel fiber			0.62×10^{-12} m^2/s (6.67×10^{-12} $ft.^2/s$)
		148.2 (21.50 ksi)		1.5 vol. %			0.82×10^{-12} m^2/s (8.83×10^{-12} $ft.^2/s$)
Riding et al. (2022)	0.163	124~145 (18-21 ksi)	0 vol.% steel fiber		Fog curing: 21 to 25℃ (69.8 to 77.0 ℉) with RH ≥ 95%	6.3 (0.25 in.)	0.28×10^{-12} m^2/s (3.01×10^{-12} $ft.^2/s$)
			1.5 vol.% steel fiber			11.5 (0.45 in.)	0.54×10^{-12} m^2/s (5.81×10^{-12} $ft.^2/s$)
			2 vol.% steel fiber			9.5 (0.37 in.)	0.43×10^{-12} m^2/s (4.62×10^{-12} $ft.^2/s$)
			0 vol.% steel fiber		Steam curing: water bath with sealed contained in oven at 90 ℃ (194 ℉) for 2 days + moist room curing for 26 days	1.1 (0.04 in.)	0.04×10^{-12} m^2/s (0.43×10^{-12} $ft.^2/s$)
			1.5 vol.% steel fiber			1.6 (0.06 in.)	0.03×10^{-12} m^2/s

References	w/b ratio	Compressive Strength (MPa/ksi)	Additional notes	Curing regimes	Chloride ions penetration depth (mm/in.)	Chloride migration coefficient
						(0.32×10^{-12} $ft.^2/s$)
			2 vol.% steel fiber		3.4 (0.13 in.)	0.14×10^{-12} m^2/s (1.51×10^{-12} $ft.^2/s$)
			0 vol.% steel fiber	Precast curing: Cured with molds in room temperature for 4 hours + oven curing with lid at 70℃ (158 ℉) for 18 hours + cooling for 2 hours + 27 days moist room curing	3.2 (0.13 in.)	0.14×10^{-12} m^2/s (1.51×10^{-12} $ft.^2/s$)
			1.5 vol.% steel fiber		4.3 (0.17 in.)	0.13×10^{-12} m^2/s (1.40×10^{-12} $ft.^2/s$)
			2 vol.% steel fiber		5.0 (0.20 in.)	0.21×10^{-12} m^2/s (2.26×10^{-12} $ft.^2/s$)
			0 vol.% steel fiber		6.2 (0.24 in.)	0.25×10^{-12} m^2/s (2.69×10^{-12} $ft.^2/s$)
	0.156	≥145 (≥21 ksi)	1.5 vol.% steel fiber	Fog curing: 21 to 25℃ (69.8 to 77.0 ℉) with RH ≥ 95%	4.3 (0.17 in.)	0.16×10^{-12} m^2/s (1.72×10^{-12} $ft.^2/s$)
			2 vol.% steel fiber		2.6 (0.10 in.)	0.07×10^{-12} m^2/s (0.75×10^{-12} $ft.^2/s$)

References	w/b ratio	Compressive Strength (MPa/ksi)	Additional notes	Curing regimes	Chloride ions penetration depth (mm/in.)	Chloride migration coefficient
			0 vol.% steel fiber	Steam curing: water bath with sealed contained in oven at 90 ℃ (194 ℉) for 2 days + moist room curing for 26 days	1.5 (0.06 in.)	0.04×10^{-12} m^2/s (0.43×10^{-12} $ft.^2/s$)
			1.5 vol.% steel fiber		1.9 (0.07 in.)	0.08×10^{-12} m^2/s (0.86×10^{-12} $ft.^2/s$)
			2 vol.% steel fiber		1.7 (0.07 in.)	0.03×10^{-12} m^2/s (0.32×10^{-12} $ft.^2/s$)
			0 vol.% steel fiber	Precast curing: Cured with molds in room temperature for 4 hours + oven curing with lid at 70℃ (158 ℉) for 18 hours + cooling for 2 hours + 27 days moist room curing	2.4 (0.09 in.)	0.07×10^{-12} m^2/s (0.75×10^{-12} $ft.^2/s$)
			1.5 vol.% steel fiber		3.5 (0.14 in.)	0.12×10^{-12} m^2/s (1.29×10^{-12} $ft.^2/s$)
			2 vol.% steel fiber		2.0 (0.08 in.)	0.06×10^{-12} m^2/s (0.65×10^{-12} $ft.^2/s$)

In addition, an environment-friendly mixture named Calcined Layered Double Hydroxide (C-LDHs) is added to UHPC to measure the influence of C-LDHs content on chloride migration coefficient of UHPC. C-LDHs is a multi-layer structure mixture in size of 30 to 300 nm (98.4 nft. to 984 nft.), which can combine with negatively charged ions, like chloride ions, and usually applied for water treatment and environmental protection. Past research reported that addition of C-LDHs can effectively reduce the chloride migration of UHPC. Chen et al. (2018) experimentally investigated the influence of addition of calcined Layered Double Hydroxide (C-LDHs) on the chloride migration coefficient of UHPC by RCMT test. The test result shows that with increasing dosage of C-LDHs from 0 wt.% to 1 wt.%, the migration coefficient decreases from 1.99×10^{-12} m^2/s to 1.48×10^{-12} m^2/s (2.14 to 1.94×10^{-11} $ft.^2/s$), and the chloride penetration depth decreases from the range of 4.8 - 5.9 mm (0.19 – 0.23 in.) to the range of 3.8 – 4.5 mm (0.15 – 0.18 in.). The author explained that during hydration, C-LDHs will fill the pores, reducing the volume of capillary pores and further leading to the low migration coefficient. However, with further increasing dosage of C-LDHs from 1 wt.% to 2 wt.%, the migration coefficient increases to 2.55×10^{-12} m^2/s (2.75×10^{-11} $ft.^2/s$), and the chloride penetration depth increases to 6.4 – 6.8 mm (0.25– 0.27 in.). The author indicated that excessive addition of C-LDHs causes higher viscosity, leading to more air entrapped in fresh concrete, further causing higher volume of capillary pores, leading to higher migration coefficient.

In terms of fiber content, it is shown that with higher fiber content, higher resistance of UHPC to chloride penetration is obtained. Abbas, Soliman and Nehdi (2015) experimentally investigated the influence of steel fiber content on chloride penetration resistance of UHPC by RCPT. The test results show that with steel fiber content increasing from 1 to 6 vol.%, the number of charges passed decreases from the range of 60-65 Coulombs to the range of 36 to 43 Coulombs. Also, Habel et al. (2008) measured the chloride penetration resistance of UHPC with 0 vol.% and 5.5 vol.% steel fiber content by RCPT, the corresponding result is 88 Coulombs and 72 Coulombs, respectively. In addition, Ghasemzadeh Mosavinejad et al. (2020) experimentally investigated the influence of PVA fiber content on chloride penetration of UHPC by RCPT test. The test results show that with PVA fiber content increasing from 0 to 1.2 vol.%, the number of charges passed decreases from the range of 40 to 62 to the range of 29 to 51 Coulombs. More information is shown in Table 2-11. However, it is reported that chloride migration coefficient slightly increases with higher steel fiber content of UHPC. Pourjahanshahi and Madani (2021) investigated the influence of dosage of steel fibers on chloride migration coefficient. The test result shows that with increasing dosage of steel fiber from 0 to 1.5 vol.%, the migration coefficient slightly increases from 0.46×10^{-12} m^2/s (4.50×10^{-12} $ft.^2/s$) to 0.82×10^{-12} m^2/s (8.83×10^{-12} $ft.^2/s$). The author indicated the due to wall effect of steel fiber impeding precipitation of hydrate products and weaker interfacial transition zone between steel fibers than that with aggregates and cement matrix, the chloride penetration increases. Also, RCMT test results highly depends on the electric conductivity of samples. Due to conductivity of steel fiber, the chloride migration coefficient may be increased for samples with higher dosages of steel fibers. The same trends have also been observed by Song et al. (2018) that with steel fiber content increasing from 0.5 to 3.0 vol.%, chloride migration coefficient increases from 4.74 to 6.63 $\times10^{-12}$ m^2/s (5.10 to 7.14×10^{-11} $ft.^2/s$), and chloride penetration depths increases from 10.60 mm to 14.41 mm (0.42 in. to 0.57 in.).

In terms of fiber length, it is shown that with shorter fiber length, slightly higher chloride penetration resistance can be provided for UHPC. Abbas, Soliman and Nehdi (2015) experimentally investigated the influence of length of steel fiber on chloride penetration resistance of UHPC by RCPT. The test result shows that with fiber length increasing from 8 to 16 mm (0.31 to 0.62 in.), the number of charges passed slightly increases from the range of 36 - 60 Coulombs to the range of 43- 65 Coulombs.

It has been reported that with higher chloride concentration of the exposure environment, the chloride penetration resistance slightly decreases. Abbas, Soliman and Nehdi (2015) adjusted the chloride concentration of exposure solution for RCPT test from 3 wt.% to 10 wt.% chloride sodium. The test result

shows that with chloride sodium concentration increasing from 3 to 10 wt.%, the number of charges passed slightly increases from the range of 38-71 Coulombs to the range of 42-80 Coulombs. It can be explained that due to higher chloride ions in the exposure environment, more chloride ions can be migrated passing through the samples. However, due to the fine pore system of UHPC, the influence is limited.

Properly higher curing temperature also could improve the chloride penetration resistance. Graybeal (2006) experimentally investigated the curing regime of UHPC on chloride penetration resistance by RCPT test. Four different regimes were considered in this research: a) untreated group – cured in a standard laboratory environment from demolding until test; b) steam - 2 hours for increasing steam in curing environment and 2 hours for reducing steam for curing environment, leaving 44 hours of constant steaming at 90 ºC (194 ºF) with 95 % RH (as total 48 hours for steam curing regime at 95% RH); c) tempered steam - the procedure is similar to steam treatment but the only difference to steam condition is that the constant steam temperature is 60 ºC (140 ºF) (tempered stem temperature) instead of 90 ºC (194 ºF) (steam); and d) delayed steam - apply steam treatment after 15 curing days with untreated curing regime and the procedure is same to steam condition with constant steam at 90 ºC (194 ºF). The test results show that with highest curing temperature (steam and delayed steam curing regime), the lowest charges passed of 18 Coulombs is obtained compared to the 39 Coulombs for tempered curing regime and 360 Coulombs for untreated curing regime. Moreover, Ghasemzadeh Mosavinejad et al. (2020) also investigated the influence of different curing regimes on chloride penetration resistance of UHPC. Two different curing regimes were designed for samples. The first curing regime was named as standard curing as samples were immersed in 20 ℃ (68 ºF) lime water, and the second curing regime was named as hot water regime as samples were immersed in 70 ℃ (158 ºF) hot water for 72 hours, and then cured by standard curing. The test results indicate that with higher curing temperature, UHPC shows higher resistance of UHPC to chloride penetration. Compared to the results of standard curing regime (29 to 62 Coulombs), the number of charges passed for samples subjected to hot water curing regime is in the range of 30-60 Coulombs.

It has been reported that with longer curing time, the chloride penetration resistance of UHPC can be effectively improved. Graybeal (2006) experimentally investigated the influence of curing time on chloride penetration resistance of UHPC by RCPT test. The test results show that with curing time increasing from 28 days to 56 days, the number of charges passed decreases from the range of 39-360 Coulombs to the range of 26-76 Coulombs. It indicates that with longer curing time, the hydration is more complete, which leads to finer pore system and further leads to higher chloride penetration resistance of UHPC.

Riding et al. (2022) comprehensively investigated the influence of steel fiber content and curing regime on chloride migration of non-proprietary UHPC with different mixture designs for different compressive strength by a modified non-steady rapid chloride migration test. The revision was based on the standard RCMT provided by NT BUILD 492 (1999), via reducing the applied potential into 30 V and extending the testing period to solid 10 days, the influence caused by internal steel fibers with high conductivity on test results were expected to be mitigated. In this test, two different UHPC mixtures were designed: the first group of mixture with compressive strength in the range of 124~145 Mpa (18-21 ksi); the other group of UHPC with compressive strength above 145 Mpa (21 ksi). Three steel fiber contents of 0, 1.5, and 2.0 vol.% were designed for two different UHPC mixtures. Three curing regimes were designed for two different UHPC mixtures: 1) fog curing regime - specimens cured in standard moist room at 21 to 25℃ (69.8 to 77.0 ℉) with RH ≥ 95% ; 2) steam curing regime - specimens firstly partially immersed in water within a container under oven heating at 90 ℃ (194 ℉) for 2 days then placed in moist room curing for next 26 days; and 3) precast curing (simulation of realistic curing regime of precast structural members) – after four hours of curing within molds, specimens were covered by a lid (without water addition) and oven heated at 70 ℃ (158 ℉) for 22 hours with subsequently cooling in the air for 2 hours,

specimens were cured in moist room until curing age of 28 days. The test results show that the chloride migration coefficients were low for both groups of UHPC. For UHPC with compressive strength in the range of 124~145 Mpa (18-21 ksi), the chloride migration coefficient is in the range of 0.03 to 0.54 $\times 10^{-12}$ m^2/s (0.32 to 5.81 ft^2/s); and for UHPC with compressive strength above 145 Mpa (21 ksi), the chloride migration coefficient is in the range of 0.03 to 0.25 $\times 10^{-12}$ m^2/s (0.32 to 2.69 ft^2/s). It is also revealed that the UHPC with higher compressive strength tends to be with lower chloride migration coefficient. Moreover, the test results show that the steam cured specimens and precast cured specimens have lower chloride migration coefficient compared to samples cured in moist room due to accelerated hydration. In addition, after the modification of the test procedure, the influence of steel fiber on testing results are limited, which is recommended for using modified RCMT for measuring chloride migration coefficient for cementitious mixture with embedded steel fibers.

2.2.1.4.2 Chloride diffusion tests

Chlorides can diffuse into UHPC in marine environments due to the concentration gradient between the mixture and the seawater. Two major methods have been adopted to evaluate the chloride diffusion behavior of UHPC: salt ponding test and bulk diffusion test. The diffusion behavior of chloride into UHPC is separately discussed in this section.

2.2.1.4.2.1 Salt ponding test

The salt ponding test is a long-term test for measuring the penetration of chloride into concrete (Stanish, Hooton and Thomas, 2001) . It is standardized by AASHTO T 259: Standard Method of Test to Resistance of Concrete to Chloride Ion Penetration (2002) to measure the average chloride penetration of samples exposed to a chloride solution. During the test, the side surfaces of samples are sealed leaving the upper surface exposed to saltwater and bottom surface to atmosphere. The samples are ponded for at least 90 days, as shown in Figure 2-29. The average chloride content with depth can be obtained by potentiometric titration test at 1.6 to 13 mm (0.065 in. to 0.5 in.) and 13 to 25 mm (0.5 to 1 in.).

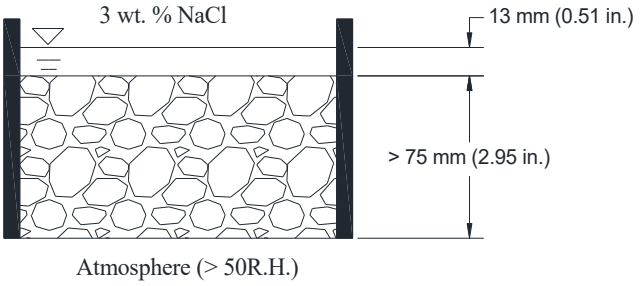

Figure 2-29 Salt ponding test scheme

Chloride ions not only diffuse into the samples, but also are transported into concrete by capillary suction in the salt ponding test. Chloride solution is absorbed into concrete because the samples are preconditioned in a dry state. Also due to the bottom drying surface, a moisture gradient can form between the specimen top and bottom, increasing the chloride penetration depth and causing an overestimation of chloride diffusion. In addition, the chloride profile obtained through this test is limited that only the average chloride content of samples can be obtained. The time for chlorides penetrating to a certain depth of samples cannot be provided by this test.

2.2.1.4.2.2 Bulk diffusion test

Bulk diffusion test is an updated test method of the salt-ponding test for measuring the chloride diffusion behavior in concrete. Variations of bulk diffusion tests are standardized by ASTM C 1556 - Standard Test Method for Determining the Apparent Chloride Diffusion Coefficient of Cementitious Mixtures by Bulk

Diffusion (2016) and NordTest NT Build 443 - Concrete, Hardened: Accelerated Chloride Penetration (1995). The test setup is shown in Figure 2-30. Specimens are pre-saturated to prevent any initial sorption of the chloride solution. The bottom surface is sealed instead of being exposed to air to prevent a moisture gradient from developing in the specimens. The chloride content is measured using at least 8 layers A chloride diffusion coefficient can be found by fitting the chloride concentration calculated using Fick's Second Law of Diffusion to the measured concrete concentration with depth, as shown in Equation 33.

$$C(x,t) = C_S - (C_S - C_i) \times erf\left(\frac{x}{\sqrt{4 \times D_a \times t}}\right) \quad \text{(Equation 33)}$$

$C(x,t)$: $C(x,t)$ chloride concentration, measured at depth of x and time t;

x: depth below the exposed surface;

t: the exposure time;

C_s: projected chloride concentration at the interface between the exposure liquid and test specimen that is determined by the regression analysis, mass %;

C_i: initial chloride concentration of the cementitious mixture prior to submersion in the exposure solution, mass %;

D_a: apparent chloride diffusion coefficient (m^2/s);

erf: the error function described in Equation 30.

$$erf(z) = 2/\sqrt{\pi} \times \int_0^z exp(-u^2)du \quad \text{(Equation 34)}$$

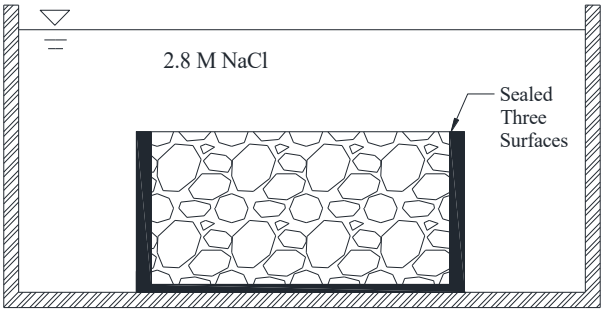

Figure 2-30 Bulk diffusion test scheme

Generally, dense microstructure, fine pore system, and low sorptivity and water permeability ensures a low value of maximum chloride content and diffusion coefficient within UHPC. In the literature, the maximum chloride content of UHPC measured at the depth in the range of 3 to 13 mm (0.11 to 0.51 in.) from ponding surface by salt ponding test is in the range of 0 – 0.055 kg/m^3 (0-0.0034 lb./ft.^{3}), that is much lower than the chloride threshold value (0.60 kg/m^3 (0.037 lb./ft.^{3})) for corrosion of steel reinforcement (Angst *et al.*, 2009; Abbas, Soliman and Nehdi, 2015). Similarly, the chloride diffusion coefficient of UHPC measured by the bulk diffusion test is in the range of 0.6×10^{-14} to 5.9×10^{-13} m^2/s (6.46×10^{-14} to 6.35×10^{-12} ft.^{2}/s), which is much lower than the chloride diffusion coefficient of normal-strength concrete usually between 0.20×10^{-12} m^2/s and 7.97×10^{-12} m^2/s (2.15×10^{-12} ft.^{2}/s to 8.58×10^{-11} ft.^{2}/s) (Shafikhani and Chidiac, 2019). Influencing factors, such as those discussed in section 2.1.1 also affect the chloride diffusion. All the experimental results are summarized in Table 2-13 and Table 2-14.

Table 2-13 Representative salt ponding test results

Reference	w/b ratio	Compressive strength (MPa – 28days)	Special Note	Exposure condition and time	Chloride content (kg/m^3) ($lb./ft.^3$)	Maximum penetration depth
Abbas, Soliman and Nehdi (2015)	0.15	151 (21.90 ksi)	0 vol.% steel fiber	10 wt.% NaCl solution for 180 days	Max. 0.055 (0.0034)	21 mm (0.83 in.)
		158 (21.92 ksi)	1 vol.% steel fiber		Max. 0.053 (0.0033)	18 mm (0.71 in.)
		166 (24.08 ksi)	3 vol.% steel fiber		Max. 0.052 (0.0032)	18 mm (0.71 in.)
		173 (25.09 ksi)	6 vol.% steel fiber		Max. 0.050 (0.00031)	18 mm (0.71 in.)
Graybeal, (2006)	-	193 (27.99 ksi)	UHPC with 2 vol.% steel fibers	Steam curing -steam at 90°C (194 °F)(95% RH) for 48 h + untreated curing	Avg. < 0.02 kg/m^3 (0.0012)	-
		126 (18.27 ksi)		Untreated curing – standard laboratory environment		
		171 (24.80 ksi)		Tempered Steam – steam at 60°C (140 °F) (95% RH) for 48 h + Untreated curing		
		171 (24.80 ksi)		Delayed Steam – untreated curing (15 days) + Steam curing (2 days) + untreated curing		

Table 2-14 Representative bulk diffusion test results

Reference	w/b ratio	Compressive strength (Mpa)	Special note	Exposure condition and time	Chloride diffusion coefficient.
El-Dieb (2009)	0.23	112 (16.24 ksi)	0.08 vol.% steel fiber	91 days	5.9×10^{-13} m^2/s (6.35×10^{-12} $ft.^2/s$)
		114 (16.53 ksi)	0.12 vol.% steel fiber		6.0×10^{-13} m^2/s (6.46×10^{-12} $ft.^2/s$)
		123 (17.84 ksi)	0.52 vol.% steel fiber		5.8×10^{-13} m^2/s (6.24×10^{-12} $ft.^2/s$)
Tanaka et al. (2010)	0.22 (w/c)	196 (28.43 ksi)	2 vol.% steel fiber	Sea for 0.5 year	1.87×10^{-14} m^2/s (2.01×10^{-13} $ft.^2/s$)
				Sea for 1.5 year	0.69×10^{-14} m^2/s (7.43×10^{-14} $ft.^2/s$)

Reference	w/b ratio	Compressive strength (Mpa)	Special note	Exposure condition and time	Chloride diffusion coefficient.
Piérard, Dooms and Cauberg (2013)	0.32 (w/c)	130-140 Mpa (18.85 – 20.31 ksi)	-	Sea for 2.5 years.	0.60×10^{-14} m^2/s (6.46×10^{-14} $ft.^2/s$)
	0.23 (w/c)	140-160 Mpa (20.31-23.21 ksi)		165 g/L salt water for 90 days	11×10^{-14} m^2/s (1.18×10^{-12} $ft.^2/s$)
	0.23 (w/c)	140-160 Mpa (20.31-23.21 ksi)			9×10^{-14} m^2/s (9.69×10^{-13} $ft.^2/s$)
Sohail et al. (2021)	0.15	161 (23.35 ksi)	No steel fiber content	3.5 wt.% saltwater for 95 days	7×10^{-14} m^2/s (7.53×10^{-13} $ft.^2/s$)
Riding et al. (2022)	0.163	124~145 (18-21 ksi)	0 vol.% steel fiber	16.5 % NaCl solution	1.42×10^{-14} m^2/s (1.53×10^{-13} $ft.^2/s$)
			1.5 vol.% steel fiber		0.28×10^{-12} m^2/s (3.01×10^{-12} $ft.^2/s$)
			2 vol.% steel fiber		0.33×10^{-12} m^2/s (3.55×10^{-12} $ft.^2/s$)
			0 vol.% steel fiber		0.19×10^{-12} m^2/s (2.05×10^{-12} $ft.^2/s$)
			1.5 vol.% steel fiber		0.21×10^{-12} m^2/s (2.26×10^{-12} $ft.^2/s$)
			2 vol.% steel fiber		0.21×10^{-12} m^2/s (2.26×10^{-12} $ft.^2/s$)
	0.156	≥145 (≥21 ksi)	0 vol.% steel fiber		0.26×10^{-12} m^2/s (2.80×10^{-12} $ft.^2/s$)
			1.5 vol.% steel fiber		0.33×10^{-12} m^2/s (3.55×10^{-12} $ft.^2/s$)
			2 vol.% steel fiber		0.15×10^{-12} m^2/s (1.61×10^{-12} $ft.^2/s$)
			0 vol.% steel fiber		0.40×10^{-12} m^2/s (4.30×10^{-12} $ft.^2/s$)
			1.5 vol.% steel fiber		0.07×10^{-12} m^2/s (0.75×10^{-12} $ft.^2/s$)
			2 vol.% steel fiber		0.04×10^{-12} m^2/s (0.43×10^{-12} $ft.^2/s$)
					0.04×10^{-12} m^2/s

Reference	w/b ratio	Compressive strength (Mpa)	Special note	Exposure condition and time	Chloride diffusion coefficient.
			0 vol.% steel fiber		$(0.43 \times 10^{-12}$ ft.^{2}/s) 0.07×10^{-12} m^2/s
			1.5 vol.% steel fiber		$(0.75 \times 10^{-12}$ ft.^{2}/s) 0.05×10^{-12} m^2/s
			2 vol.% steel fiber		$(0.54 \times 10^{-12}$ ft.^{2}/s) 0.07×10^{-12} m^2/s
			0 vol.% steel fiber		$(0.75 \times 10^{-12}$ ft.^{2}/s) 0.04×10^{-12} m^2/s
			1.5 vol.% steel fiber		$(0.43 \times 10^{-12}$ ft.^{2}/s) 0.06×10^{-12} m^2/s
			2 vol.% steel fiber		$(0.64 \times 10^{-12}$ ft.^{2}/s) 0.03×10^{-12} m^2/s
					$(0.32 \times 10^{-12}$ ft.^{2}/s)

Several researchers reported testing results on the chloride diffusion coefficient of UHPC. Piérard, Dooms and Cauberg (2013) reported that the chloride diffusion coefficients of three different mixtures of UHPC are in the range of 7 to 11 × 10^{-14} m^2/s (7.53 to 11.84 × 10^{-13} $ft.^2/s$) by bulk diffusion test. Sohail et al. (2021) experimentally investigated the UHPC without addition of steel fibers by bulk diffusion test, and the chloride diffusion coefficient is 1.42 × 10^{-14} m^2/s (1.53 × 10^{-13} $ft.^2/s$). Moreover, some scholars did not report chloride diffusion coefficient but observed the maximum chloride penetration depth for UHPC by bulk diffusion test. Dobias, Pernicova and Mandlik (2016) experimentally compared the free chloride content of UHPC and normal concrete. The test results show the maximum penetration depth of UHPC and normal-strength concrete were 5 mm (0.20 in.) and larger than 12 mm (0.47 in.), respectively, and the corresponding maximum free chloride content by the weight of binder were 1.035% and 1.901%, respectively. All these results show that the resistance of UHPC to chloride penetration is much better than normal concrete.

Steel fiber content has limited influence on maximum chloride content, maximum chloride penetration depth and chloride diffusion coefficient. Abbas, Soliman and Nehdi (2015) investigated the influence of dosage of steel fibers on chloride diffusion of UHPC by the salt ponding test. The test result is shown in Figure 2-31. With steel fiber content increasing from 0 to 6 vol.%, the maximum chloride content is in the range of 0.055 to 0.050 kg/m^3 (0.0034 to 0.0031 $lb./ft.^3$) at the depth of 3 mm (0.12 in.) from ponding surface, and maximum penetration depth is around 18 mm (0.71 in.). El-Dieb (2009) experimentally investigated the influence of steel fiber content chloride diffusion coefficient by bulk diffusion test. Test result shows that with steel fiber content increases from 0.08 to 0.52 vol.%, the chloride diffusion coefficient slightly increases from 5.8 to 5.9 × 10^{-13} m^2/s.

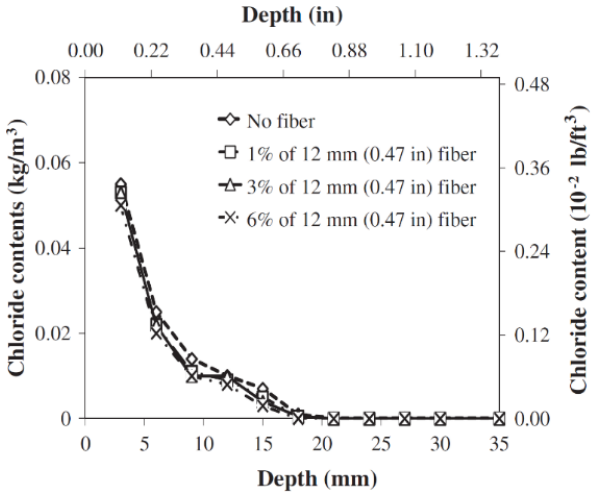

Figure 2-31 Chloride ion penetration profiles (Abbas, Soliman and Nehdi, 2015)

Past research shows that different curing regime has little effect on the chloride diffusion. Graybeal (2006) investigated the chloride diffusion behavior of UHPC under different curing regimes. The curing regime is detailed provided in section 2.2.1.4.1. The test result is shown in Figure 2-32. It can be observed for four curing regimes, the average chloride content is below 0.02 kg/m^3 (0.0012 $lb./ft.^3$). It shows that UHPC has excellent resistance to chloride diffusion under different curing regimes.

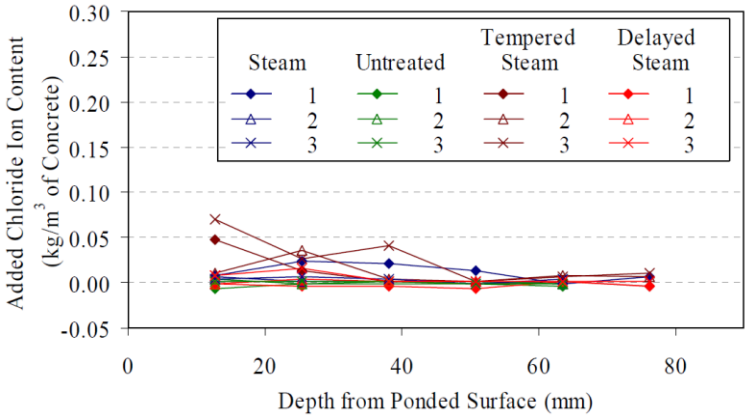

Figure 2-32 Salt ponding test results of different curing regimes (Graybeal, 2006)

It also has been reported that longer exposure period significantly reduces the chloride diffusion coefficient for UHPC. Tanaka et al. (2010) conducted a long-term bulk diffusion test to investigate the chloride penetration of UHPC. The exposure term was designed as 0.5 years, 1.5 years, and 2.5 years. The corresponding measured chloride diffusion coefficients were 1.87×10^{-14} m^2/s (2.01×10^{-13} $ft.^2/s$), 0.70×10^{-14} m^2/s (7.53×10^{-14} $ft.^2/s$), and 0.60×10^{-14} m^2/s (6.46×10^{-14} $ft.^2/s$). This is because continued hydration refines the pore system and leads to lower chloride diffusion coefficient.

Riding et al. (2022) comprehensively investigated the influence of steel fiber content and curing regime on chloride diffusion of non-proprietary UHPC with different mixture designs for different compressive strength by bulk diffusion test. In this test, two different UHPC mixtures were designed: the first group of mixture with compressive strength in the range of 124~145 Mpa (18-21 ksi); the other group of UHPC with compressive strength above 145 Mpa (21 ksi). Three steel fiber contents of 0, 1.5, and 2.0 vol.% were designed for two different UHPC mixtures. Three curing regimes were designed for two different UHPC mixtures: 1) fog curing regime - specimens cured in standard moist room at 21 to 25℃ (69.8 to 77.0 ℉) with RH ≥ 95% ; 2) steam curing regime - specimens firstly partially immersed in water within a container under oven heating at 90 ℃ (194 ℉) for 2 days then placed in moist room curing; and 3) precast curing (simulation of realistic curing regime of precast structural members) – after four hours of curing within molds, specimens were covered by a lid (without water addition) and oven heated at 70 ℃ (158 ℉) for 22 hours with subsequently cooling in the air for 2 hours, specimens were cured in moist room. All specimens were cured with 27 days of curing age and subsequently exposed to 16.5 % NaCl solution lasting for one year. The test results pointed out that with higher compressive strength, chloride diffusion coefficient of UHPC tends to be lower. For UHPC with compressive strength in the range of 124~145 Mpa (18-21 ksi), the chloride diffusion coefficient was in the range of 0.15 to 0.40×10^{-12} m^2/s (1.61 to 4.30×10^{-12} $ft.^2/s$); and for UHPC with compressive strength above 145 Mpa (21 ksi), the chloride diffusion coefficient was in the range of 0.03 to 0.07×10^{-12} m^2/s (0.32 to 0.75×10^{-12} $ft.^2/s$). In addition, test results show that the influence of steel fiber on chloride diffusion coefficient is limited, which agrees to the research of Abbas, Soliman and Nehdi (2015). Moreover, it is revealed that the curing regime has limited influence on chloride diffusion, which is agreed to the research of Graybeal (2006).

2.2.2 Corrosion of steel fibers and steel reinforcement within uncracked UHPC

Due to the low transport properties of UHPC and disconnected pore network, UHPC typically provides high corrosion protection for steel fibers and embedded steel reinforcement. In this section, the corrosion behavior of steel fiber and steel reinforcement of uncracked UHPC exposed to aggressive environments is reviewed, and the influence of corrosion degree of steel fiber on mechanical strength of UHPC is discussed. The detailed information is shown below.

2.2.2.1 Corrosion of steel fiber within uncracked UHPC

As discussed in section 2.2.1, steel fibers can provide additional tensile strength for early age UHPC to bridge microcracks and block channels for intrusion of harmful substances. Based on the concern of the potentially negative impact of mechanical strength due to corrosion of fibers, several scholars experimentally investigated the corrosion condition of steel fiber in UHPC exposed to aggressive environment by SEM and colorimetric method and the influence of corrosion of fibers on mechanical performance of UHPC by mechanical strength tests. The results showed that only the steel fibers at the exposure surface of the sample (depth < 1 mm (0.04 in.)) were corroded, and the compressive strength, splitting tensile strength, and flexural strength of UHPC increased after exposure to salt water due to the increasing bond strength between fibers and cementitious matrix.

2.2.2.1.1 Corrosion condition of steel fiber in UHPC

Only the steel fibers on the surface of samples directly exposed to chlorides corrode because of the extremely low transport properties of UHPC and disconnected pore network leading to insufficient oxygen, moisture, and chlorides for initiation and propagation of corrosion. Abbas, Soliman and Nehdi (2015) experimentally investigated the corrosion behavior of steel fibers with UHPC samples exposed to 10 wt.% NaCl solution for 180 days in a salt ponding test. The test result shows that the fibers only had corrosion up to a depth of 1 mm (0.04 in.), as shown in Figure 2-33. Pyo et al., (2019) also reported that for UHPC samples immersed in 10 wt.% NaCl solution for 365 days, corrosion was only observed using a colorimetric method for the steel fiber at a depth of less than 1 mm (0.04 in.). In addition, Pyo et al. (2017) reported that for samples with 3.0 wt.% admixed chlorides and cured in water for 100 days, there was no obvious corrosion spot for steel fiber located at the surface of samples, and only steel fibers sticking out of surfaces were corroded.

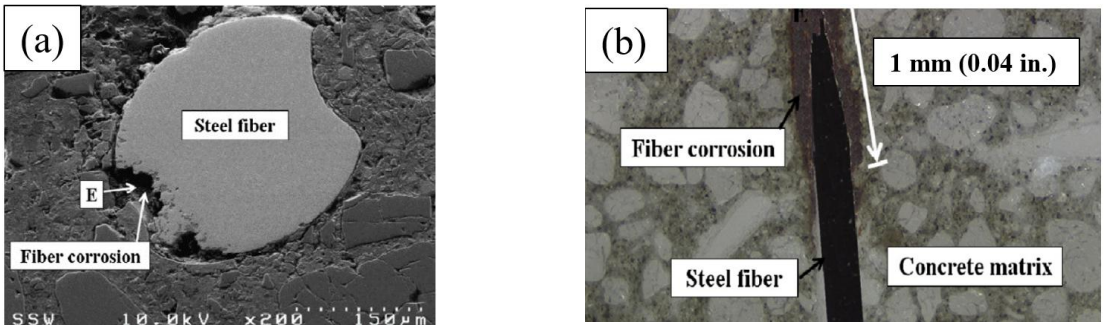

Figure 2-33 Cross section of corroded steel fiber (a) and corrosion of steel fiber (right) (Abbas, Soliman and Nehdi, 2015)

2.2.2.1.2 Influence of corroded fiber on mechanical strength of UHPC

Some studies have reported that a small amount of corrosion of steel fibers can increase the mechanical performance of UHPC, whereas high amounts of corrosion will deteriorate the mechanical strength of UHPC. Abbas, Soliman and Nehdi (2015) experimentally investigated the influence of steel fiber corrosion condition on mechanical strength by salt ponding test. With 180 days exposure to 10wt.% NaCl solution at 40 °C (104 °F) to accelerate corrosion, the compressive strength, splitting strength, and flexural strength of UHPC slightly increased to 1.09, 1.10 and 1.12 times that of the reference samples. The same trend was also observed by Pyo et al. (2019), that after UHPC samples were immersed in 10 wt.% NaCl solution for 180 days, the flexural strength is 1.31 times higher than that of samples at 28 days curing age. Pyo et al. (2019) also observed however, that samples exposed to the NaCl solution for 1 year had only 86 percent of the flexural strength of samples at 28 days curing age. A similar trend was also observed by Pyo et al. (2017) for samples with an admixed NaCl solution (0 to 3 wt.% NaCl) and water

cured for 91 days. The bending strength first increased from 23.8 to 27.3 Mpa (3.45 to 3.96 ksi) for samples mixed with an NaCl concentration increasing from 0 to 1.5 wt.%, and then decreased to 16.3 Mpa (2.36 ksi) for samples mixed with 3 wt.% NaCl solution, and Lv et al. (2021b) reported that after accelerated corrosion of steel fibers for 2 days, the tensile strength of UHPC increased from 10.75 Mpa (1.56 ksi) to 12.90 Mpa (1.87 ksi), and then decreased to 8.77 Mpa (1.27 ksi) for samples with accelerated corrosion of steel fiber for 10 days. This trend can be explained by the experiment results of Yoo, Gim and Chun (2020). Yoo, Gim and Chun (2020) reported that with a small amount of corrosion, the bond strength between the matrix and steel fiber can be strengthened because the roughness of surface of steel fiber increases and the volume of corrosion products are larger than steel, which increases the fiber pull-out force and leads to additional bond strength. Additional corrosion can decrease the fiber cross-sectional area and change the failure mode from fiber pull-out to rupture or causes a layer of weak corrosion products between the steel and concrete, which leads to decrease of pullout strength. For Yoo, Gim and Chun (2020)'s research, different corrosion degrees (estimated by weight loss ratio) of steel fibers were added into mixture. The test result shows that for corroded steel fiber, the pullout load first increased from 59.4 to 143.2 N (13.4 to 32.2 lbs.) with increasing corrosion degree from 0% to 10%, then decreased to 123.8 N (27.8 lbs.) with a corrosion degree of 15 %.

2.2.2.2 Corrosion of steel reinforcement of uncracked UHPC

In general, UHPC can provide high protection for embedded rebar against corrosion due to the low transport properties and disconnected pore system of UHPC as discussed in section 2.1. Factors such as SCM and steel fiber content that affect the transport properties of UHPC discussed in section 2.2.1 also affect the corrosion rate of steel reinforcement. In addition, the initial chloride content in the mixture also influences the maximum corrosion rate of UHPC. In general, for samples exposed to a chloride environment, the corrosion rate of reinforcement UHPC is in the range of 0.05 to 0.15 μA/cm^2 (0.32 to 0.97 μA/in.^{2}), which is much lower than that of normal reinforcement concrete in the range of 2.83 to 9.06 μA/ cm^2 (18.26 to 58.45 μA/in.^{2}) (Hornbostel, Larsen and Geiker, 2013).

Past research reported that with the addition of SCMs, corrosion current of reinforcement UHPC decreases. Ghafari et al. (2015) experimentally investigated the influence of addition of nano-silica on corrosion current of UHPC reinforcement. The w/b was 0.16, and 3 wt.% of cement was replaced by nano-silica was used for comparison. An accelerated test system connected to external power and immersed in chloride solution was used to measure the corrosion rate, as shown in Figure 2-34. After accelerating corrosion for samples with nano-silica for 8338 minutes and samples without nano-silica for 6555 minutes, the first cracks caused by rust generation were monitored respectively, and the corresponding corrosion current is 236.9 and 367.8 mA, respectively. The author stated that this trend can be regarded as higher corrosion resistance provided by UHPC with nano-silica.

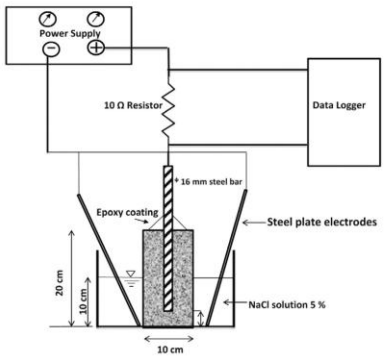

Figure 2-34 Accelerated corrosion test setup (Ghafari *et al.*, 2015a)

It has been reported that with higher steel fiber content can increase the maximum corrosion rate of UHPC. Fan et al. (2020) investigated the influence of steel fiber content on corrosion rate of reinforcement UHPC. A w/b of 0.16 was used, and 0.2 mm diameter × 13 mm length (0.008 in. diameter × 0.51 in. length) steel fibers were added into mixtures with different dosages from 0 to 3 vol.%. Specimens were cured in limewater for 28 days. Samples were immersed in 3.5 wt.% NaCl solution for 147 days, with corrosion rate results shown in Figure 2-35. As the steel fiber percentage increased from 0 to 3.0 vol.%, the maximum corrosion rate increased from 0.05 to 0.15 μA/cm^2 (0.32 to 0.97 μA/in.^{2}). The author explained that the current may pass through the steel fiber instead of being transported by ions in capillary pore system, and high conductivity of steel fiber leads to high corrosion rate. This trend was confirmed by Fan et al. (2019). In that study, samples were cured in limewater for 28 days and exposed to accelerated wetting-drying cycle of 15 days drying in the air and 15 days immersed in 3.5 wt.% chloride sodium solution after curing in limewater for 28 days. As the steel fiber amount increased from 0 to 2 vol.%, the corrosion rate increased from 0.11 to 0.15 μA/cm^2 (0.71 to 0.97 μA/in.^{2}) as shown in Figure 2-36. The reinforcing steel embedded in UHPC remained passive after 42 days of exposure in both studies (Fan et al., 2019; Fan et al., 2020), which illustrates the high corrosion protection of UHPC.

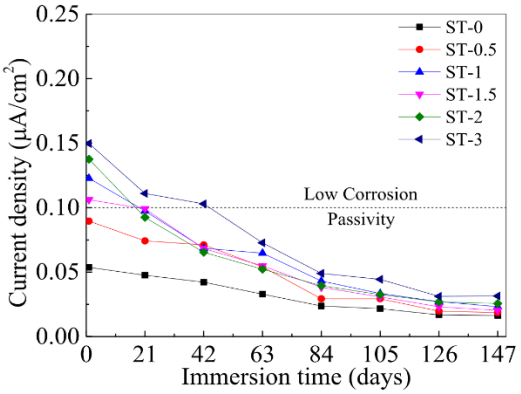

Figure 2-35 Corrosion rate of UHPC with different dosages of steel fiber (Fan *et al.*, 2020)

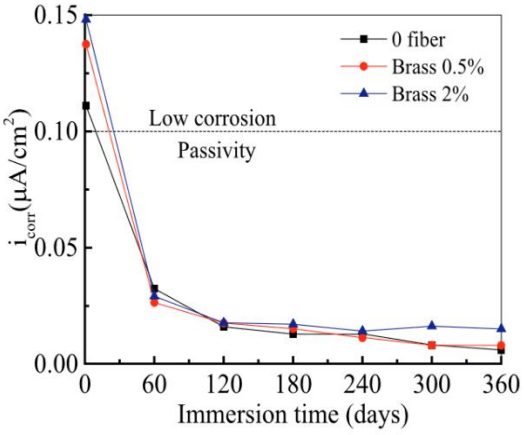

Figure 2-36 Corrosion rate of UHPC with different dosages of brass coated steel fiber (Fan *et al.*, 2019)

Past research shows that higher initial chloride content of UHPC leads to a slight increase of the corrosion rate of steel reinforcement in UHPC. Zheng et al. (2022) experimentally investigated the influence of initial chloride content in mixture on corrosion rate of UHPC. The w/b was 0.143 for all samples. Artificial sea water and DI water were used in the concrete. The samples were cured in an environmental

chamber at 22°C (72 °F) with R.H. 90% for 56 days. The total and free chloride content for sea water were 0.1957% and 0.0149% by mass of cement paste for samples mixed with cement pastes at an age of 56 days. The test results are shown in Figure 2-37. The maximum corrosion rate for samples mixed with seawater was 0.3 μA/cm^2 (1.94 μA/in.^{2}) (steel rebar active), and for samples mixed with DI water was 0.1 μA/cm^2 (0.65 μA/in.^{2}) (steel rebar passive). The corrosion rate was still low, although the corrosion of steel reinforcement was active. The author explained that most chloride ions are physically or chemically bonded with the hydration product in UHPC, which leads to lower free chloride ions in the pore system to aggravate the corrosion behavior. Also, it was observed that the corrosion rate of both samples decreased as curing time increased. The author also believed that as the curing time increased, the microstructure densified, the oxygen supply at the cathode decreased and led to a lower corrosion rate.

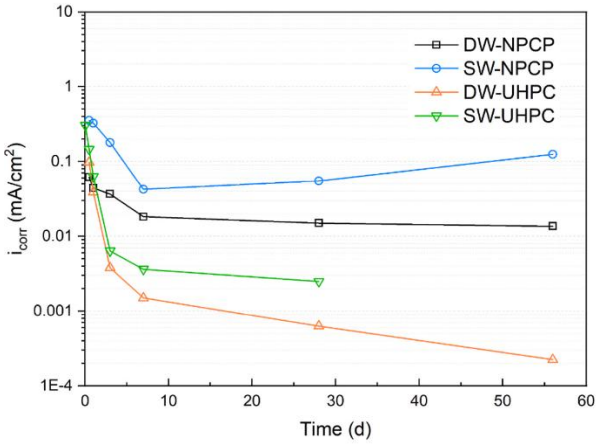

Figure 2-37 Corrosion of UHPC mixed with DI water (DI-UHPC) and seawater (SW-UHPC) (Zheng *et al.*, 2022)

2.2.3 Summary

In this section, UHPC transport properties, including porosity, sorptivity, water permeability, gas permeability, chloride penetration, and corrosion of steel fiber and steel reinforcement embedded in UHPC are reviewed. The following conclusions could be drawn:

1. UHPC has significantly lower porosity measured in the range of 2.29% to 7.52% compared to that of normal concrete in the range of 9% to 10%. The low porosity is a result of the dense micro-structure and disconnected pore systems the low w/b, addition of SCMs, and proper curing regime. Also, steel fiber can block intrusion channels for harmful substances.
2. UHPC sorptivity, water permeability, and gas permeability are all shown to be one to four orders of magnitude lower than that of normal concrete as a result of the dense microstructure and disconnected pore systems.
3. Chloride migration and diffusion properties have been investigated by various scholars using rapid chloride penetration test, rapid migration test, salt ponding test, and bulk diffusion test. Among these test methods, the rapid migration test and bulk diffusion test are considered more suitable for capturing the migration and diffusion behavior of chloride ions within concrete mixtures.
4. The chloride migration coefficient and diffusion coefficient of UHPC are one-to-two orders of magnitude lower than that of normal-strength concrete due to low porosity and disconnected pore system.

5. Steel fiber Corrosion was only reported at the very surface of samples in uncracked UHPC, and no corrosion has been reported below 1 mm (0.04 in.) from surface, which does not adversely affect the mechanical properties of UHPC.
6. The corrosion rate of steel rebar embedded in UHPC was found to be extremely low due to the low transport properties of UHPC preventing aggressive ions, water and oxygen from reaching the steel reinforcement. It has been reported that the corrosion rate of reinforcement UHPC is influenced by the SCMs content, steel fiber content, and initial chloride content within the UHPC mixture.

2.3 Influence of cracks on normal-strength concrete and UHPC

Cracks can be induced during the service life of concrete structures by different mechanisms, such as temperature- and moisture-related strains, expansive chemical reactions, and mechanical loadings (Mu, de Schutter and Ma, 2013). Transverse cracks are the most common cracks observed in structural concrete components. Transverse cracks are generated in tapered V-shape under flexure, gradually closing to the steel rebars. When cracks occur at the surface, they may act as channels for substances to penetrate the concrete rapidly, accelerating the corrosion initiation (Bertolini *et al.*, 2014). In this section, the influence of cracks on the transport properties and corrosion resistance of normal-strength concrete and UHPC are reviewed.

2.3.1 Influence of cracks on normal strength concrete

The transport properties of concrete can increase after cracking because cracks can act as channels for intrusion of gas, liquids, and ions to penetrate into the concrete. This leads to an increasing risk for corrosion of steel reinforcement. To quantify the effect of cracks on normal-strength concrete, the effect of crack width, crack depth, and crack density are reviewed at this section.

2.3.1.1 Crack types and generation methods

Generally, six methods can be adopted to generate cracks at the surface of concrete (or UHPC) samples for research purpose. According to the shape of cracks, it can be divided into two groups of methods for generating "parallel-wall" cracks or "V-shape" cracks. The following methods can be adopted to generate "parallel-wall" cracks:

1) Artificial saw-cutting method (Jin, Yan and Wang, 2010): single or multiple cracks with precise width and depth can be generated in the form of a parallel wall crack;
2) Direct tension test method (Lv *et al.*, 2021a): parallel-wall cracks can be generated by direct tension tests. By using a displacement-controlled testing system, the crack width can be controlled;
3) Brazilian splitting test method (Rocco *et al.*, 2001): by using a displacement-controlled testing system and splitting test, a single crack with desired width can be generated;
4) Expansive core method (Ismail *et al.*, 2008): almost "parallel-wall" cracks are produced with similar shape to Brazilian splitting test method using a setup involving expansive cores.

The illustrations of each method generating parallel-wall cracks are shown in Figure 2-38.

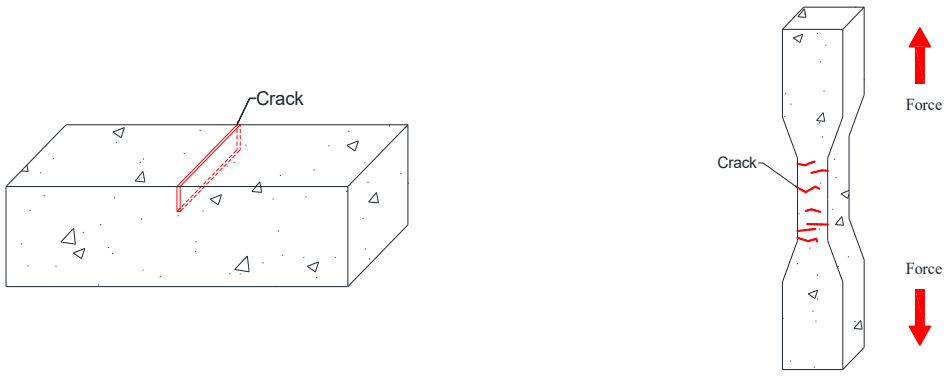

a. Artificial saw-cutting method b. direct tension test method

Figure 2-38 The illustration of methods to generate parallel-wall shape cracks

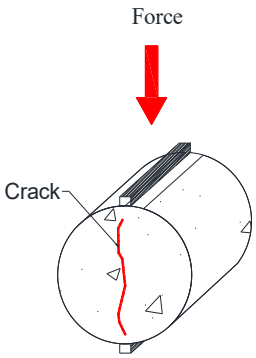

c. Brazilian splitting test method

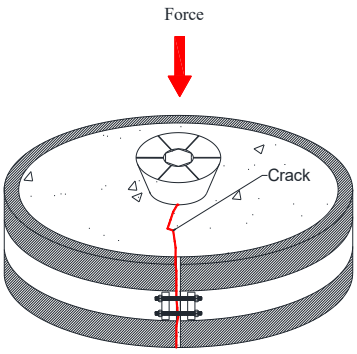

d. Expansive core method

Figure 2-38 The illustration of methods to generate parallel-wall shape cracks (continued)

"V-shape" cracks can be generated by the following methods:

1) Central-point bending or third-point bending (Gu, Ye and Sun, 2015): the most realistic V-shape cracks can be generated using displacement-controlled bending, and both single crack and multiple cracks with targeted width and depth can be generated;
2) Wedge splitting method (Löfgren, Stang and Olesen, 2007): a single crack with target crack width and depth can be generated by the wedge spliting method.

The illustration of methods to generate V-shape cracks is shown in Figure 2-39.

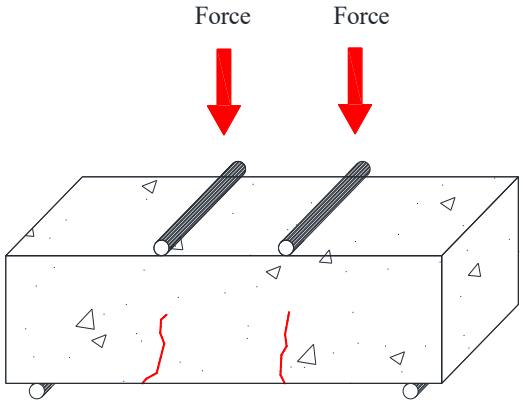

a) Four points bending test method

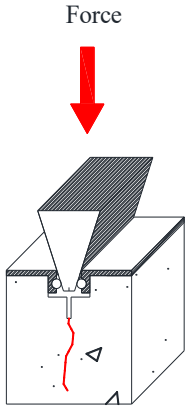

b) Wedge splitting method

Figure 2-39 The illustration of methods to generate V-shape cracks

2.3.1.2 Effect of crack width

Crack width has been considered the most critical characteristic to influence the corrosion conditions of steel reinforcement (Shaikh, 2018). Larger crack widths allow more water, oxygen, and chloride ions to penetrate the concrete, shortening the time before corrosion initiates and aggravating the propagation phase. Crack width is also the most important factor influencing the concrete self-healing ability (Gu, Ye and Sun, 2015; Shaikh, 2018). When cracks happen, the unhydrated cementitious particles contact with moisture and hydrate, filling the microcracks. Also, due to concrete carbonation, calcium carbonate ($CaCO_3$) can also be produced on the crack walls and further contribute to filling the cracks. This

phenomenon is called self-healing of cracks. Self-healing of cracks recovers some of the transport properties of cracked concrete and can reduce the risk for corrosion.

2.3.1.2.1 Effect of crack width on water permeability

Water is one of the prerequisites for corrosion of steel reinforcement. More water intrusion could aggravate the corrosion rate of steel reinforcement. Generally, as the crack width increases, the water permeability of cracked concrete increases. Also, past research reported that after the crack width exceeds a certain value (threshold value), water permeability increases more rapidly. This is because self-healing behavior can fully or partially seal the crack when crack width is below the threshold value.

Aldea, Shah and Karr (1999b) investigated the influence of crack width on water permeability of normal concrete and high-performance concrete. Single crack was generated on the samples' surface in the range of 0 to 130 μm (0 to 0.0051 in.), and 0.45 and 0.31 water-to-cement ratios were designed for normal concrete and high-performance concrete, respectively. The result of water permeability test shows that with increasing crack width, the water permeability increases for both normal concrete and high-performance concrete, as shown in Figure 2-40. For normal-strength concrete, as the crack width increased from 0 to 130 μm (0 to 0.0051 in.), the water permeability coefficient increased from the order of magnitude of 10^{-8} to 10^{-5} cm/s (3.94×10^{-9} to 10^{-6} in./s). For high-performance concrete, as the crack width increased from 0 to 110 μm (0 to 0.0043 in.), the water permeability coefficient increased from the order of magnitude of 10^{-9} to 10^{-7} cm/s (3.94×10^{-10} to 10^{-8} in./s). It can be seen that after cracking, the water permeability of normal-strength concrete and high-performance concrete increased by at least two orders of magnitude from that of uncracked samples. Also, water permeability increased more rapidly for samples with crack width above 100 μm (0.0039 in.) than of samples with crack width up to about 100 μm (0.0039 in.), as shown in Figure 2-40. The same trend was also observed by many other researchers (Gérard *et al.*, 1996; Wang *et al.*, 1997; Reinhardt and Jooss, 2003; Lepech and Li, 2005, 2009; Akhavan, Shafaatian and Rajabipour, 2012; Shin *et al.*, 2017) , and the detailed information is shown in Table 2-15.

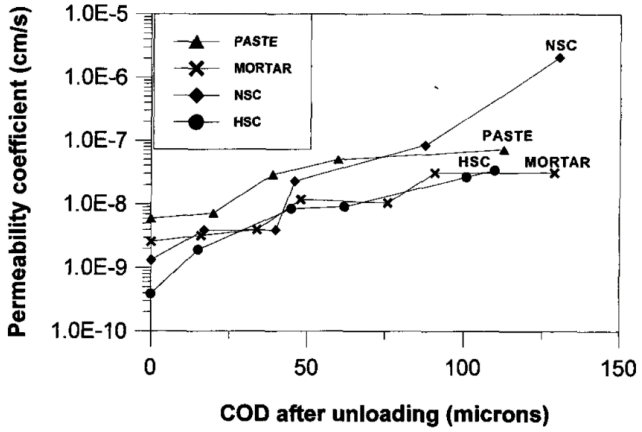

Figure 2-40 Effect of crack width on water permeability (Corina-Maria Aldea, Shah and Karr, 1999)

Table 2-15 Influence of crack width on water permeability

Reference	w/c ratio	Crack Type	Crack width	Threshold Value	Threshold Value	Result
Gérard et al. (1996)	0.54	Multiple cracks	0 to 1.0×10^{-3} (tensile strain)	1.0×10^{-3}		3.9×10^{-12} to 6.7×10^{-10} m/s

Reference	w/c ratio	Crack Type	Crack width	Threshold Value	Threshold Value	Result
		(Uniaxial tensile test)		(tensile strain)		(1.27 × 10^{-11} to 2.20 × 10^{-9} ft./s)
	0.28		0 to 1.125×10^{-3} (tensile strain)			2.9×10^{-13} to 1×10^{-8} m/s (9.51 × 10^{-13} to 3.28 × 10^{-8} ft./s)
Wang et al. (1997)	0.41	Single crack (Splitting test) Dracy law	0 to 370 µm (0 to 0.0146 in.) (Crack opening displacement)	50 µm (0.0071 in.) (COD)	200 µm	1×10^{-11} to 7.3× 10^{-5} m/s (3.28 × 10^{-11} to 2.40 × 10^{-4} ft./s)
Aldea, Shah and Karr, (1999b)	0.45	Single crack (Splitting test)	0 to 130 µm (0 to 0.0051 in.) (Crack opening displacement)	100 µm (unloading) (0.0039 in.) (COD)		1.3 ×10^{-11} to 2.1 × 10^{-8} m/s (4.3 × 10^{-11} to 6.9 × 10^{-8} ft./s)
	0.31	Dracy law	0 to 110 µm (0 to 0.0043 in.) (Crack opening displacement)	200 µm (under loading)		3.9 ×10^{-12} to 3.4 ×10^{-10} m/s (1.3× 10^{-11} to 1.1 × 10^{-9} ft./s)
Reinhardt and Jooss (2003)	0.37	Single crack (Splitting test) Poiseuille law	0 to 160 µm (0 to 0.0063 in.)	100 µm (0.0039 in.)	-	0 to the range of 4.1 ×10^{-10} - 11.6 ×10^{-10} kg/s (0 to the range of 9.04 ×10^{-10} – 25.57 ×10^{-10} lb/s)
Lepech and Li	0.25	Multiple cracks	0 to 63 µm (0 to 0.0025 in.)	52 µm	-	8.18×10^{-12} to 7.74 ×10^{-10} m/s

Reference	w/c ratio	Crack Type	Crack width	Threshold Value	Threshold Value	Result
(2005, 2009)		(Tensile strength test)				(2.68 × 10^{-11} to 2.54 × 10^{-9} ft./s)
Akhavan, Shafaatian and Rajabipour (2012)	0.35	Dracy law	0 to 500 μm (0 to 0.0197 in.)	-	240 μm	4.58×10^{-11} to 4.46×10^{-4} m/s (1.50 × 10^{-10} to 1.46 × 10^{-3} ft./s)
	0.45	Single crack (Splitting test)	0 to 92 μm (0 to 0.0036 in.)	-		5.9 ×10^{-18} to 1.7 ×10^{-10} m^2 (6.35 × 10^{-17} to 1.83 × 10^{-9} $ft.^2$)
	0.45 + 1 vol.% polypropylene fibers		0 to 190 μm (0 to 0.0075 in.)			5.9 ×10^{-18} ×2.0 ×10^{-10} m^2 (6.35 × 10^{-10} to 2.15 × 10^{-10} $ft.^2$)
Shin et al. (2017)	-	Single crack (Splitting test)	100 to 500 μm (0.0039 to 0.0197 in.)	100	270-300 μm (0.0106 to 0.0118 in.)	1.4 ×10^{-5} to the range of 1.39×10^{-3} - 1.82×10^{-3} m/s [4.59 × 10^{-5} to (4.56 × 10^{-3} – 4.59 × 10^{-3}) ft./s]
Rapoport	0.45 and steel fiber content from 0 to 0.1 vol.%	Single crack (Splitting test) Dracy law	0-300 μm (0-0.0118 in.)	100 μm (0.0039 in.)		
Akhavan	0.45	Single crack (Splitting test)	Effective crack width 0-190 μm (0-0.0075 in.)			

Reference	w/c ratio	Crack Type	Crack width	Threshold Value	Threshold Value	Result
Hubert	0.43	Poiseuille law Uniaxial tension test Poiseuille law		100 μm (0.0039 in.)		

2.3.1.2.2 Effect of crack width on gas permeability

During the propagation phase of corrosion, oxygen is consumed at the cathodic region. Thus, sufficient oxygen supply increases the risk of steel reinforcement corrosion. Past research reported that cracks highly influence the gas permeability of concrete. As the crack width increases above a threshold, the gas permeability significantly increases.

Mohammed, Otsuki and Hamada (2003) investigated the influence of a single crack on the gas permeability of normal-strength concrete with w/cm of 0.3 and 0.5, respectively. A single crack with a width of 300 μm (0.012 in.) was generated in flexure with an initial notch. The results showed that for both mixtures, the gas permeability at the cracked region was several times higher than that of the uncracked regions as shown in Figure 2-41. For example, the measured gas flow rate was about 3.5×10^{-10} mole/cm^2 second (2.26×10^{-9} mole/in^2 second) and 2.7×10^{-11} mole/cm^2 second (1.74×10^{-10} mole/in^2 second) at the cracked region for the samples with a w/cm of 0.5 and 0.3, respectively. As comparison, at the uncracked region, the gas flow rate was in the range of 1.3 to 1.7×10^{-10} mole/cm^2 second (0.84 to1.10×10^{-9} mole/in^2 second) for samples with a w/cm of 0.5 and in the range of 7.8 to 8.4×10^{-12} mole/cm^2 second (5.03 to 5.42×10^{-11} mole/in^2 second) for samples with a w/cm of 0.3. Picandet and Khelidj (2003) also investigated the influence of crack width on gas permeability of normal concrete, high-performance concrete, and fiber reinforced high-performance concrete. Single cracks with a width up to 145-253 μm (0.0057 to 0.0010 in.) were generated using a splitting test method. It can be seen from Figure 2-42 that with increasing crack width, gas permeability increases for all three mixtures. A threshold value of 15 μm (0.0006 in.) crack opening displacement was observed for normal-strength concrete, high-performance concrete, and fiber reinforced high-performance concrete, such that the gas permeability coefficient increased significantly faster after the crack width exceeded this value. For example, after a crack opening displacement larger than 100 μm (0.0039 in.), gas permeability increased more than 1 to 2 orders of magnitude for three mixtures. The same trend of influence of crack width on gas permeability was also verified by (Picandet, Khelidj and Bellegou, 2009; Mechtcherine and Lieboldt, 2011; Stehlík, Věra Heřmánková and Vítek, 2015), and the detailed information is shown in Table 2-16.

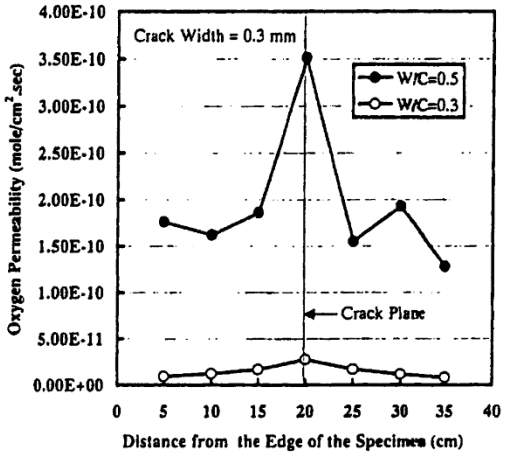

Figure 2-41 Gas (oxygen) flow rate at pre-cracked region and uncracked region of concrete in different water-to-cement ratios (Mohammed, Otsuki and Hamada, 2003)

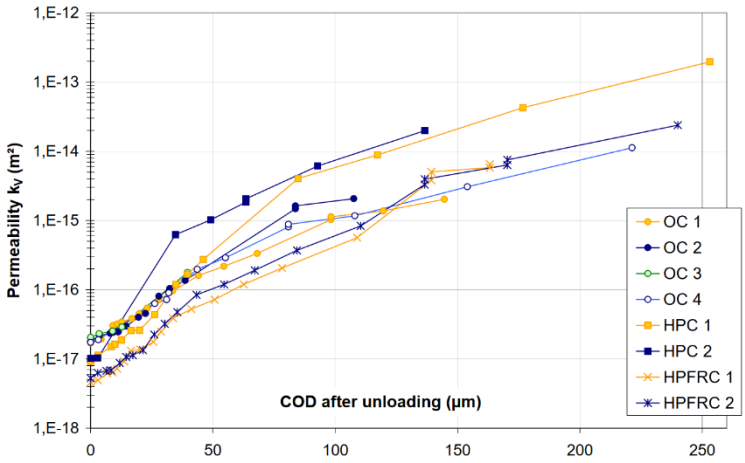

Figure 2-42 The relationship between gas permeability and crack opening displacement (Picandet and Khelidj, 2003)

Table 2-16 Influence of crack width on gas permeability

Reference	w/c ratio	Crack Type	Crack width	Threshold Value	Result
Mohammed, Otsuki and Hamada (2003)	0.5	Single crack (Bending test)	0 to 300 μm (0 to 0.0118 in.)	-	1.3 to 3.5 $\times 10^{-10}$ mole/cm^2 second (0.84 to 2.26 $\times 10^{-9}$ mole/in^2 second)
	0.3				8.7 $\times 10^{-12}$ to 2.7 $\times 10^{-11}$ mole/cm^2 second

Reference	w/c ratio	Crack Type	Crack width	Threshold Value	Result
Picandet and Khelidj (2003); Picandet, Khelidj and Bellegou (2009)	0.49	Single crack (Splitting test)	0 to 221 μm COD (0 to 0.0087 in.)	15 μm COD (0.0006 in.)	(5.61 $\times10^{-11}$ to 1.74 $\times10^{-10}$ mole/in^2 second) 1.7×10^{-17} to 1.2×10^{-14} m^2 (1.83×10^{-16} to 1.29 $\times10^{-13}$ ft.^{2})
	0.29		0 to 253 μm COD (0 to 0.0010 in.)		9.3×10^{-18} to 2.0 $\times10^{-13}$ m^2 (1.0×10^{-16} to 2.15 $\times10^{-12}$ ft.^{2})
	0.29 (1 vol.% steel fiber)		0 to 240 μm COD (0 to 0.0094 in.)		5.4×10^{-18} to 2.4×10^{-14} m^2 (5.81 $\times10^{-17}$ to 2.58 $\times10^{-13}$ ft.^{2})
Mechtcherine and Lieboldt (2011)	0.33 (w/b)	Multiple cracks (Tensile test)	0.14% to 0.45% strain level	0.2% strain level	2.5 $\times10^{-5}$ to 2.3 $\times10^{-3}$ m^3/(s m^2) (8.2 $\times10^{-5}$ to 2.58 $\times10^{-3}$ ft.^{3}/(s ft.^{2})) (Flow rate)
Stehlík, Věra Heřmánková and Vítek (2015)	0.41	Single crack (Splitting test)	30 to 100 μm (0.0012 to 0.0039 in.)	-	2.5×10^{-18} to 4.8 $\times10^{-18}$ m^2 (2.69 $\times10^{-17}$ to 5.17 $\times10^{-17}$ ft.^{2})

2.3.1.2.3 Effect of crack width on chloride penetration

In terms of chloride penetration, higher chloride penetration depth and larger chloride diffusion coefficients have been found with increasing crack width. Higher chloride penetration depth and diffusion coefficients could shorten the time to corrosion initiation. In this section, the effect of crack width on chloride penetration is reviewed.

Djerbi et al. (2008) investigated the influence of crack width on chloride diffusion coefficient of normal-strength concrete, high-performance concrete, and fiber reinforced high-performance concrete. Single cracks with a width in the range of 0 to 250 μm (0 to 0.0098 in.) were generated, and steady-state migration test was adopted to obtain the chloride diffusion coefficient. The test results showed that after cracking, the chloride diffusion coefficient of all concretes increased with crack width, as shown in Figure 2-43. For normal-strength concrete, the chloride diffusion coefficient increased from about 1.9 $\times10^{-12}$ m^2/s

(2.05×10^{-11} ft.^{2}/s) to about 6.2×10^{-12} m^2/s (6.67×10^{-11} ft.^{2}/s) with increasing crack width from 0 to 240 μm (0 to 0.0094 in.). For high-performance concrete, the chloride diffusion increased from about 0.8×10^{-12} m^2/s (8.6×10^{-12} ft.^{2}/s) to 4.8×10^{-12} m^2/s (5.17×10^{-11} ft.^{2}/s) with increasing crack width from 0 to 220 μm (0 to 0.0087 in.) For fiber reinforced high-performance concrete, the chloride diffusion coefficient increased from 0.2×10^{-12} m^2/s (2.15×10^{-12} ft.^{2}/s) to 4.4×10^{-12} m^2/s (4.74×10^{-11} ft.^{2}/s) with increasing crack width from 0 to 220 μm (0 to 0.0087 in.). Moreover, the test result of Djerbi et al. (2008)shows that for crack widths below 30 μm (0.0012 in.), almost no diffusion occurs along the crack path, whereas for crack widths between the 30 μm to 80 μm (0.0012 to 0.0031 in.), the chloride diffusion coefficient increased with increasing crack width, as shown in Figure 2-44. The self-healing behavior impeded the chloride diffusion when the crack width was small. For crack widths greater than 80 μm (0.0031 in.), the crack wall could be considered as an exposed surface, and in this case, the chloride diffusion coefficient is almost constant. More information about crack width influence can be found in Table 2-17, which extends more references based on Gu, Ye and Sun (2015).

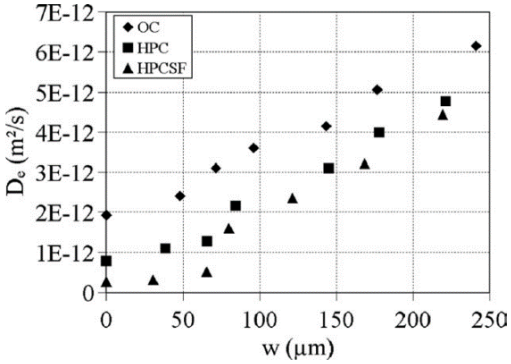

Figure 2-43 Effect of crack width on chloride diffusion coefficient (Djerbi et al., 2008)

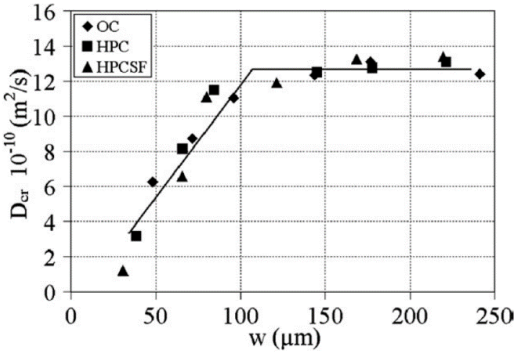

Figure 2-44 Effect of chloride coefficient through cracks on crack width (Djerbi et al., 2008)

Table 2-17 Influence of crack width on chloride transport properties of cracked concrete

Reference	No obvious influence (μm/in.)	Influence by crack width (μm/in.)	Cracks surface considered as wall (μm/in.)
Aldea, Shah and Karr (1999a)	-	-	>200 (0.0079 in.)
Ismail et al. (2008)	<60 (0.0024 in.)	60-200	>200 (0.0079 in.)

Reference	No obvious influence (μm/in.)	Influence by crack width (μm/in.)	Cracks surface considered as wall (μm/in.)
		(0.0024 – 0.0079 in.)	
Şahmaran and Yaman (2008)	<50 (0.0020 in.)	50-135 (0.0020 – 0.0053 in.)	>135 (0.0053 in.)
Djerbi et al. (2008)	< 30 (0.0011 in.)	30 – 80	>80 (0.0031 in.)
Audenaert, de Schutter and Marsavina (2009)	-	-	>100 (0.0039 in.)
Jang, Kim and Oh (2011)	<80 (0.0031 in.)	80-155 (0.0031 – 0.0061 in.)	>155 (0.0061 in.)
Park, Kwon and Jung (2012)	-	-	>200 (0.0079 in.)
Yoon and Schlangen (2014)	<40 (0.0016 in.) (long term test) < 14 (0.00055 in.) (short term test)	-	-
Wang et al. (2016)	<100 (0.0039 in.)	100-400 (0.0039 – 0.0157 in.)	>400 (0.0157 in.)
AL-Ameeri, Rafiq and Tsioulou (2021)	-	-	>150 (0.0059 in.)

In addition to increasing the diffusion coefficient, it is also reported that a wider crack width increased the maximum crack penetration depth (vertical influencing zone) and a larger horizontal influence zone (the horizontal distance from crack) of crack was observed. Audenaert, de Schutter and Marsavina (2009) investigated the influence of crack width on maximum chloride penetration depth and influencing zone of cracks by the RCMT test. A single crack with width in the range of 20 μm to 200 μm (0.00078 to 0.0079 in.) was generated by splitting test. The results show that with increasing crack width, the maximum chloride penetration depth and horizontal influencing zone increased. In terms of the maximum chloride penetration depth, as the crack width increased from 0 to 100 μm (0.0039 in.), the maximum penetration depth increased from 6.9 mm (0.27 in.) to 40.0 mm (1.57 in.), as shown in Figure 2-45. After the crack width exceeded 100 μm (0.0039 in.), the maximum penetration depth remained almost constant. The author explained that in this scenario, the after the crack width was large enough to be considered to have the same exposure to the chloride solution as the exterior surfaces, the maximum chloride penetration depth paused increasing with wider crack widths. In terms of horizontal influencing zone, as the crack width increased from 20 to 200 μm (0.00078 to 0.0079 in.), the horizontal influence zone increased from 10 mm to 30 mm (0.39 in. to 1.18 in.), as shown in Figure 2-46.

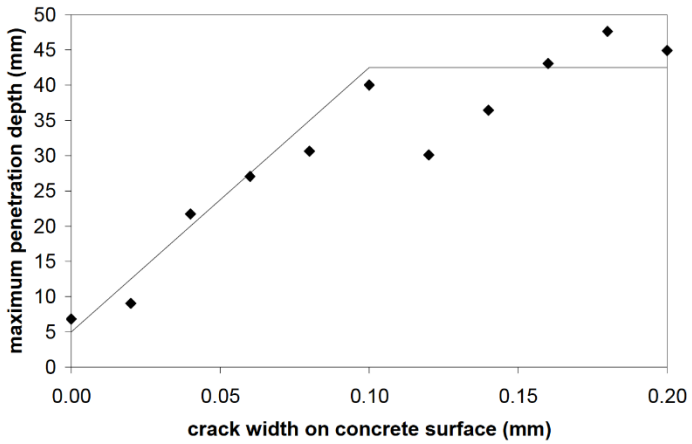

Figure 2-45 Effect of crack width on chloride penetration depth (Audenaert, de Schutter and Marsavina, 2009)

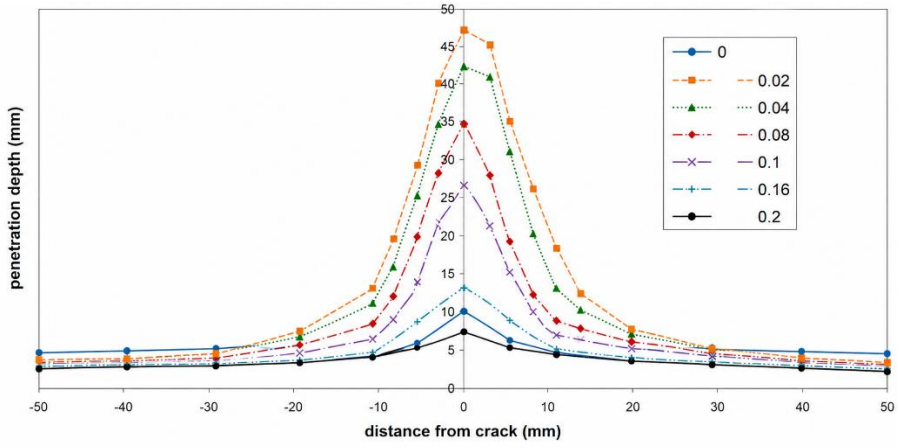

Figure 2-46 Crack influencing zone of chloride penetration (Audenaert, de Schutter and Marsavina, 2009)

2.3.1.2.4 Effect of crack width on corrosion rate of steel reinforcement

Based on the discussion of section 2.3.1.2.1 to 2.3.1.2.3, the transport properties of concrete increased with increasing crack width, the corrosion rate of steel reinforcement is also greatly influenced by crack width. Generally, the corrosion rate of steel reinforcement increases with increasing crack width of concrete. For reference, the corrosion rate for normal-strength concrete with w/cm in the range of 0.3 to 0.55 is in the range of 0 to 1.2 μA/cm^2 (0 to 7.74 0.65 μA/in.^{2}). After cracks occurred with widths between 50 μm (0.0020 in.) to 700 μm (0.028 in.), the corrosion rate increased to the range of 0.02 to 3.23 μA/cm^2 (0.13 to 20.84 0.65 μA/in.^{2}). More information is provided as follow.

Mohammed et al. (2001) experimentally investigated the influence of crack width on corrosion rate of reinforcement concrete. Beam samples were employed to generate cracks with widths between 100 μm to 700 μm (0.0039 to 0.028 in.) by flexure. After exposure to wetting-drying cycles for 13 weeks, the weight loss of steel reinforcement was measured. Test results show that as the crack width increased from 100 μm to 700 μm (0.0039 to 0.028 in.), the weight loss of steel reinforcement increased from 0.265 g to 0.3895 g (0.0093 to 0.014 oz.). The electrochemical method was employed for measuring the corrosion rate of cracked concrete with different crack widths in past studies. Otieno, Alexander and Beushausen

(2010) investigated the influence of crack width on corrosion rate represented by corrosion current density of cracked reinforcement concrete. Beam samples were artificially pre-cracked in single crack with crack width in the range of 0 to 700 μm (0 to 0.028 in.). Samples with w/cm of 0.40 and 0.55 were then subjected to wetting-drying cycles of weekly ponding by saltwater solution followed by 4 days drying in air, lasting for 31 weeks. After 31 weeks of exposure, as the crack width increased from 0 to 700 μm (0 to 0.028 in.), the corrosion current density increased from the range of 0.04 - 0.10 $\mu A/cm^2$ (0.26 - 0.65 $\mu A/in.^2$) to the range of 0.69 - 0.93 $\mu A/cm^2$ (4.45 – 6.00 $\mu A/in.^2$). The same trend was also observed by (Mohammed *et al.*, 2001; Montes, Bremner and Lister, 2004; Scott and Alexander, 2007; Lopez-Calvo *et al.*, 2018; AL-Ameeri, Rafiq and Tsioulou, 2021), with more detailed information shown in Table 2-18, which extends more review contents based on Shaikh (2018).

Table 2-18 Influence of crack width on the corrosion rate of steel reinforcement

Reference	w/c ratio	Exposure time	Uncracked	Crack width (μm/in.)											
				50 (0.0020 in.)	100 (0.0039 in.)	150 (0.0059 in.)	180 (0.0071 in.)	200 (0.0079 in.)	250 (0.0098 in.)	300 (0.0012 in.)	330 (0.0012 in.)	350 (0.014 in.)	400 (0.0016 in.)	500 (0.0020 in.)	700 (0.0028 in.)
Mohammed et al.(2001)	0.3	14 weeks	-	-	-					0.1775 g		-			-
	0.5				0.2655 g					0.3733 g					0.3896 g
	0.7				-					0.9765 g					-
Montes, Bremner and Lister (2004)	0.37	1 year	0.15 (0.97)			-				1 (6.45)		-		2 (12.09)	-
	0.45		1.2 (7.74)							1.7 (10.97)				3.3 (21.29)	
	0.37 (20 wt.% fly ash of cement)		0.45 (2.90)							1.1 (7.10)				1.6 (10.32)	
	0.45 (20 wt.% fly ash of cement)		0.75 (4.84)							1.7 (10.97)				2.9 (18.71)	
	0.37 (20 wt.% fly ash of cement)		0.15 (6.45)							0.65 (4.19)				1.0 (6.45)	
	0.45 (20 wt.% fly ash of cement)		0.25 (1.61)							1.4 (9.03)				2.4 (15.48)	
Scott and Alexander (2007)	0.58(w/b) (20 mm (0.79 in.) cover thickness)	90 weeks			-			2.65 (17.10)				-			3.23 (20.84)
	0.58(w/b)							1.20							1.48

Reference	w/c ratio	Exposure time	Uncracked	Crack width (μm/in.)											
				50 (0.0020 in.)	100 (0.0039 in.)	150 (0.0059 in.)	180 (0.0071 in.)	200 (0.0079 in.)	250 (0.0098 in.)	300 (0.012 in.)	330 (0.0012 in.)	350 (0.0014 in.)	400 (0.0016 in.)	500 (0.0020 in.)	700 (0.0028 in.)
	(40 mm (1.57 in.) cover thickness)							(7.74)							(9.55)
	0.58(w/b)– 30 wt.% fly ash (20 mm (0.79 in.) cover thickness)							0.64 (4.13)							0.71 (4.58)
	0.58(w/b)– 30 wt.% fly ash (40 mm (1.57 in.) cover thickness)							0.39 (2.52)							0.50 (3.22)
	0.58(w/b)– 50 wt.% slag (20 mm (0.79 in.) cover thickness)							0.39 (2.52)							0.51 (3.29)
	0.58(w/b)– 25 wt.% slag (40 mm (1.57 in.) cover thickness)							0.47 (3.03)							0.55 (3.55)
	0.58(w/b)– 50 wt.% slag (40 mm (1.57 in.) cover thickness)							0.35 (2.26)							0.53 (3.42)
	0.58(w/b)– 75 wt.% slag (40 mm (1.57 in.) cover thickness)							0.24 (1.55)							0.34 (2.19)
	0.58(w/b)– 7 wt.% silica fume (20 mm (0.79 in.) cover thickness)							0.67 (4.32)							1.12 (7.23)

Reference	w/c ratio	Exposure time	Uncracked	Crack width (μm/in.)											
				50 (0.0020 in.)	100 (0.0039 in.)	150 (0.0059 in.)	180 (0.0071 in.)	200 (0.0079 in.)	250 (0.0098 in.)	300 (0.012 in.)	330 (0.0012 in.)	350 (0.014 in.)	400 (0.016 in.)	500 (0.020 in.)	700 (0.028 in.)
Otieno, Alexander and Beushausen (2010)	0.58(w/b)– 7 wt.% silica fume (40 mm (1.57 in.) cover thickness)	31 weeks	-				-	0.59 (3.81)			-			-	1.03 (6.65)
	0.58(w/b)– 43 wt.% slag + 7 wt.% silica fume (40 mm (1.57 in.) cover thickness)							0.28 (1.81)							0.42 (2.71)
	0.40 (w/b)		0.04 (0.26)		0.14 (0.90)								0.36 (2.32)		0.69 (4.45)
	0.40 (w/b) (50 wt.% slag of cement)		0.04 (0.26)		0.07 (0.45)								0.26 (1.68)		0.38 (2.45)
	0.55(w/b)		0.1 (0.65)		0.31 (2.0)								0.78 (5.03)		0.93 (6.0)
	0.55 (w/b) (50 wt.% slag of cement)		0.05 (0.32)		0.07 (0.45)								0.41 (2.65)		0.55 (3.55)
Lopez-Calvo et al. (2018)	0.40 (25 mm (0.98 in.) cover thickness)	16 months	0.66 (4.26)		0.80 (5.16)	0.74 (4.7)			-		1.10 (7.10)			-	
	0.40 (45 mm (1.77 in.) cover thickness)		0.12 (0.77)	-	0.14 (0.90)	-	0.14 (0.90)	0.36 (2.32)				-			
AL-Ameeri, Rafiq and	0.4	140 days	0.05 (0.32)		0.02 (0.13)			0.1 (0.65)			0.5 (3.23)			-	
	0.5		0.01		0.88			1.45			0.79				

Reference	w/c ratio	Exposure time	Uncracked	Crack width (μm/in.)											
				50 (0.0020 in.)	100 (0.0039 in.)	150 (0.0059 in.)	180 (0.0071 in.)	200 (0.0079 in.)	250 (0.0098 in.)	300 (0.012 in.)	330 (0.0012 in.)	350 (0.0014 in.)	400 (0.0016 in.)	500 (0.0020 in.)	700 (0.0028 in.)
Tsioulou (2021)	0.6		(0.06) 1.86 (12.0)		(5.68) 1.29 (8.32)			(9.35) 1.11 (7.16)			(5.10) 1.72 (11.10)				

Note: unit “g” means weight loss.

2.3.1.3 Effect of crack depth

Crack depth is regarded as an important crack characteristic. Because cracks act as channels for chloride ingress, more chloride ions could be transported deeper into concrete structural components as the cracks become deeper. Limited research has focused on the influence of crack depth on transport properties of cracked concrete and corrosion rate of steel reinforcement. A few scholars reported that with deeper crack width, higher maximum chloride penetration depth was observed. Marsavina et al. (2009) experimentally investigated the influence of crack depth on chloride penetration of normal concrete. RCMT was employed to accelerate chloride ingress on samples made with a 0.5 w/c. An artificial crack depth in the range of 5 to 20 mm (0.20 to 0.79 in.) was generated at the surface of samples. For cracks with a width of 300 μm (0.012 in.), with crack depth increasing from 5 to 20 mm (0.20 to 0.79 in.), the maximum chloride penetration depth increased from 17.7 to 39.7 mm (0. 70 to 1.56 in.). For 200 μm (0.0079 in.) crack width, with crack depth increased from 5 to 20 mm (0.20 to 0.79 in.), the maximum chloride penetration depth increased from 15.8 to 33.4 mm (0.62 to 1.31 in.). The same trend was also observed by Audenaert, de Schutter and Marsavina (2009) and Wang et al. (2016).

2.3.1.4 Effect of crack density

Crack density has been identified as an important parameter affecting concrete durability in past research. However, there is no standard way to quantify the crack density of cracked concrete. Table 2-19 lists the various definitions scholars used to quantify the crack density. It is difficult to conduct a side-by-side comparison of experimental test results on crack density because of the different definitions used for crack density. Nevertheless, literature reported that with increasing crack density, the transport properties increase for cracked concrete.

Table 2-19 Methods to describe crack density

No.	Reference	Description
1	Litorowicz (2006); Torrijos, Giaccio and Zerbino (2010); Giaccio et al. (2015)	Total dendritic length of cracks per area
2	Jacobsen, Marchand and Boisvert (1996); Mu, de Schutter and Ma (2013)	Total number of cracks crossing the diameter divided by the diameter of samples (cylindrical sample)
3	Zhou, Li and Pang (2012; Wang et al. (2016)	The arithmetic addition of square of half of each crack length divided by the surface area
4	Li, Li and Xu (2019)	The arithmetic addition of power of half of each crack length divided by the sample volume
5	Gérard and Marchand (2000)	The mean crack spacing divided by mean crack width

2.3.1.4.1 Effect of crack density on water permeability

Past research has reported that with increasing crack density, the water permeability increases. Torrijos, Giaccio and Zerbino (2010) experimentally investigated the influence of crack density on water permeability. Cylindrical samples were prepared, and multiple cracks were generated by heat treatment. The crack density was measured by method 1 in Table 2-20, which is in the rage of 0.15 to 0.43 cm/cm^2 (0.38 to 1.09 in./in.^{2}) in this test. The result shows that with crack density increasing from 0.15 to 0.43

cm/cm^2, water permeability coefficients increased from 2.2×10^{-11} m/s to 1.2×10^{-9} m/s (7.22×10^{-11} ft/s to 13.94×10^{-9} ft/s). The same trend was verified by Litorowicz (2006) and Li, Li and Xu (2019), with detailed information shown in Table 2-20.

Table 2-20 Different methods for defining crack density of cracked concrete

Reference	Crack density measuring method	Crack density	Results
Litorowicz (2006)	Method 1	0 to 0.45 mm/mm^2 (0 to 11.43 in./in.^{2})	Maximum water penetration depth increases from 18 to 149 mm (0.71 to 5.87 in.)
Torrijos, Giaccio and Zerbino (2010)	Method 1	0.15 to 0.43 cm/cm^2 (0.38 to 1.09 in./in.^{2})	Water permeability coefficient increases from 2.2×10^{-11} m/s to 1.2×10^{-9} m/s (7.22×10^{-11} ft./s to 3.94×10^{-9} ft./s)
Li, Li and Xu (2019)	Method 4	0.2 to 0.4	Water permeability coefficient increases form the range of 2.41×10^{-9} m/s – 0.39×10^{-6} m/s to 1.04×10^{-8} m/s – 2.98×10^{-6} m/s (7.91×10^{-9} ft./s – 1.28×10^{-6} ft./s to 3.41×10^{-8} ft./s – 9.78×10^{-6} ft./s)

2.3.1.4.2 Effect of crack density on gas permeability

Studies have shown that as the crack density of normal-strength concrete increased, the gas permeability also increased. Zhou, Li and Pang (2012) experimentally investigated the influence of crack density on gas permeability of cracked concrete. Cylindrical samples were prepared, and multiple cracks were generated by compressive loading. The test results showed that with increasing crack density from 0 to 0.95, the ratio of the opposite number of the logarithm of gas permeability coefficient of cracked concrete to uncracked concrete decreased from 1 to 0.82, which indicated an increase in gas permeability. The same trend was also observed by Giaccio et al. (2015), with more details found in Table 2-21.

Table 2-21 Influence of crack density on the gas permeability of cracked concrete

Reference	Crack density measuring method	Crack density	Results
Zhou, Li and Pang (2012)	Method 3	0 to 0.95	Ratio of the opposite number of the logarithm of gas

Reference	Crack density measuring method	Crack density	Results
			permeability coefficient of cracked concrete to uncracked concrete decreases from 1 to 0.82
Giaccio et al. (2015)	Method 1	0.01 to 0.25 cm/cm^2 (0.025 to 0.635 $in./in.^2$)	Gas permeability coefficient increases from 0.09 to 2.77 × 10^{-6} m^2 (0.97 to 29.82 × 10^{-6} $ft.^2$)

2.3.1.4.3 Effect of crack density on chloride penetration

It has been reported that with increasing crack density, higher chloride transport properties were observed. Wang et al. (2016) experimentally investigated the influence of crack density on the chloride migration coefficient. Cubic samples were prepared, and multiple cracks with crack density in the range of 0 to 0.335 were generated by compressive test. The crack density was defined as method 3 in Table 2-22, and the cracked samples were subjected to the RCMT test. The test results showed that with increasing crack density from 0 to 0.335, the chloride migration coefficient increased from 1 to 2.9 times that of the uncracked samples. The same trend was also verified by Jacobsen, Marchand and Boisvert (1996), Litorowicz (2006), Mu, de Schutter and Ma (2013), and Gérard and Marchand (2000) using different tests. More information on these results can be found in Table 2-22.

Table 2-22 Influence of crack density on chloride penetration in cracked concrete

Reference	Crack density measuring method	Crack density	Results
Jacobsen, Marchand and Boisvert (1996)	Method 2	0 to 0.77 mm^{-1} (0 to 19.56 $in.^{-1}$)	Chloride migration coefficient increases from 9.70 to 76.25 × 10^{-14} m^2/s (1.04 to 8.21 × 10^{-12} $ft.^2/s$)
Gérard and Marchand (2000)	Method 5	440 to 105	Diffusion coefficient increases from 24.48 to 76.52× 10^{-13} m^2/s (2.63 to 8.24 × 10^{-11} $ft.^2/s$)
Litorowicz (2006)	Method 1	0 to the range of 0.31 to 0.38 mm/mm^2 (0 to the range of 7.87 to 9.65 $in./in.^2$)	Maximum chloride penetration depth increases from the range of 12.60-24.11 mm (0.50 – 0.95 in.) to the range of 20.71 to 54.01 mm (0.82 to 2.13 in.)

Reference	Crack density measuring method	Crack density	Results
Mu, de Schutter and Ma (2013)	Method 2	0 to 0.75 mm^{-1} (0 to 19.05 $in.^{-1}$)	Chloride diffusion coefficient increases from 2.66 to 20.82 $\times 10^{-13}$ m^2/s (2.86 to 22.41$\times 10^{-13}$ $ft.^2/s$)
Wang et al. (2016)	Method 3	0 to 0.335	Chloride migration coefficient increased from 1 to 2.9 times than that of uncracked samples

2.3.1.4.4 Effect of crack density on corrosion rate of steel reinforcement

Conflicting results on the influence of crack density on corrosion rate of reinforced concrete have been found, which was also been reported in the review of Shaikh (2018) . Arya and Ofori-Darko (1996) observed that as the crack density increased, the corrosion rate increased. During the test, the reinforced concrete beam with w/cm of 0.65 was artificially cracked for 0 to 20 transverse cracks equally distributed along the beam with the same total crack width of 2.4 mm (0.094 in.) for each case. Saltwater solution was then sprayed onto the surface of the samples for 24 months. The corrosion current density was measured by LPR. The reinforcing steel mass loss calculated from the LPR measurements is shown in Figure 2-47. As the crack number increased from 0 to 16, the corrosion rate increased from almost 0 to 358 $\mu g/cm^2$ (0 to 8.15 $\times 10^{-5}$ $oz./in.^2$) after 24 months exposure. A lower crack density (larger crack spacing) gives more electrical resistance between cracks. However, with crack number of 20, the corrosion rate decreased to 65 $\mu g/cm^2$ (1.48 $\times 10^{-5}$ $oz./in.^2$). The author suspected that for samples with 20 cracks, the corrosion rate decreased due to enhanced self-healing behavior since with increasing crack density, the crack width were smaller, giving enhanced self-healing. On the other hand, Schiessl and Raupach (1997) argued that corrosion rate would decrease with higher crack density. During their test, V-shape cracks with spacing of 10 cm to 100 cm (3.94 in. to 39.37 in.) were generated on beam samples with w/cm of 0.6. A water reservoir was later placed on top of the cracked region for periodical water ponding and saltwater ponding and corrosion current measurement for 24 weeks. The test results showed that by doubling the crack spacing from 10 cm to 20 cm (3.94 to 7.87 in.), the corrosion current almost doubled as from 27.7 μA to 50.5 μA. When the crack spacing increased to 100 cm (39.37 in), the corrosion current increased to 113 μA. The author explained that when the spacing reduced (crack density increased), the area of the cathodic region was reduced, which further restrained the corrosion rate. Ahmed and Mihashi (2010) found a similar trend during their testing of reinforced strain hardening fiber reinforced cementitious composites (SHFRCC). SHFRCC generated multiple fine cracks under loading as compared to plain concrete. The multiple cracking behavior, although leading to higher crack density however, led to a reduced corrosion current, as shown in Figure 2-48.

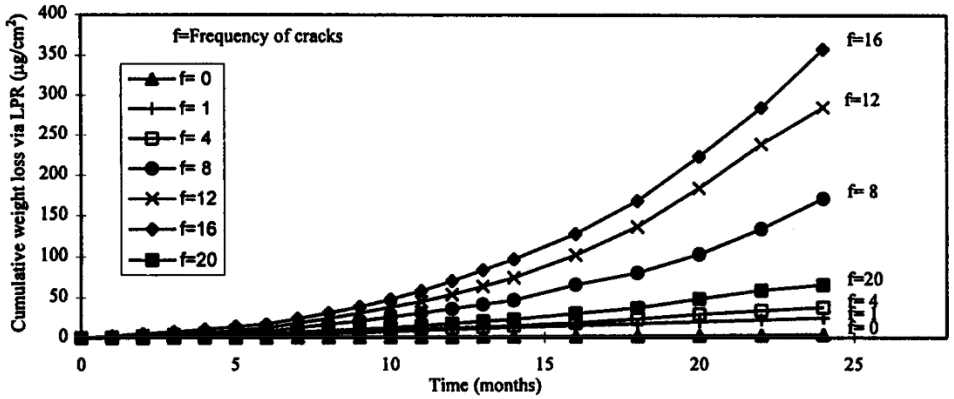

Figure 2-47 Effect of crack frequencies on corrosion rate (Arya and Ofori-Darko, 1996; Ahmed and Mihashi, 2010)

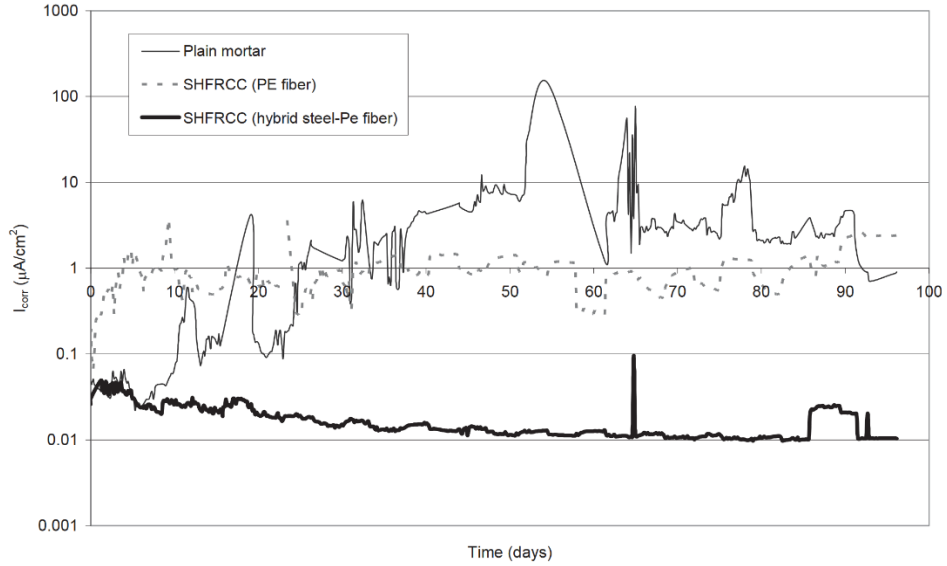

Figure 2-48 The corrosion rate for samples in multiple cracks and single crack (Ahmed and Mihashi, 2010)

In general, after cracking occurred, the penetration of water, oxygen and chloride ions significantly increased for normal-strength concrete and high-performance concrete, which further caused higher corrosion rates of reinforcement. In the literature, crack width has been reported as the most important crack characteristic affecting the corrosion condition of reinforcement concrete. Larger crack width leads to higher water permeability, gas permeability, and chloride penetration, shortening the initiation of corrosion process and accelerating the propagation of corrosion. In addition, crack depth is also related to the penetration of chloride ions. Deeper cracks led to larger maximum chloride penetration depth. Also, the influence of crack density on corrosion rate of reinforcement concrete was investigated by scholars. However, the results were mixed. On the one hand, when crack number increased, the concrete zone between cracks was smaller, which would lead to higher corrosion rate. On the other hand, when the crack density increased, the region of steel reinforcement between cracks was smaller, so that the cathodic region of steel reinforcement decreased, which tended to decrease the corrosion rate of steel reinforcement within the cracked concrete matrix. It is suspected that this phenomenon could be caused by the difference of conductivity of concrete. For concrete with higher w/c ratio, the conductivity of

concrete cover is higher, thus the resistance of concrete cover could become the control parameter for corrosion; for concrete with lower w/c ratio, the pore system would be finer, and microstructure would be denser, so the oxygen supply could become the control parameter for corrosion, which is related to the cathodic reaction in corrosion.

2.3.2 Transport properties of cracked UHPC

Similar to normal concrete, the transport properties of UHPC are also heavily influenced by cracks. Transport properties tend to increase after UHPC cracks. However, self-healing behavior of cracks also helps recover the transport properties. In this section, the influence of crack width and loading stress level on sorptivity, water permeability, gas permeability, and chloride penetration are reviewed, and the self-healing behavior of cracked UHPC is discussed. Generally, the transport properties of cracked UHPC are comparable to uncracked normal concrete, which demonstrates the high durability of UHPC even under cracked condition.

2.3.2.1 Sorptivity of cracked UHPC

Several studies have examined the influence of crack width or loading level on sorptivity of cracked UHPC. In general, with increasing crack width and/or loading stress level, the sorptivity of cracked UHPC increases. On the other hand, self-healing of cracks can fully or partially fill the cracks, which recovers some of the UHPC sorptivity properties. In general, although higher sorptivity was observed with increasing crack width, the sorptivity of cracked UHPC in the range of 0.25 to 2.519 g/m^2 s$^{0.5}$ (0.00082 to 0.0083 oz./ft^2 s$^{0.5}$) was still lower than that of uncracked normal-strength concrete [5-13 g/m^2 s$^{0.5}$ (0.016 to 0.043 oz./ft^2 s$^{0.5}$)]. Table 2-23 summarizes the findings of previous studies on cracked UHPC sorptivity.

Charron, Denarié and Brühwiler (2008) experimentally investigated the influence of crack width on sorptivity of cracked UHPC. Prismatic UHPC specimens were cracked with multiple cracks using direct tension, with the widest crack width ranging between 0 to 90 μm (0 to 0.0035 in.). The cylindrical cores were extracted from the cracked prismatic UHPC specimens for the next water absorption test. The test results showed that as the crack width increased, sorptivity of UHPC increased. The water absorption coefficient gradually increased from 0.353 g/m^2 s$^{0.5}$ to 0.656 g/m^2 s$^{0.5}$ (0.0012 to oz./ft^2 s$^{0.5}$ to 0.0022 oz./ft^2 s$^{0.5}$) with crack width increasing from 0 to 35 μm (0 to 0.0014 in.), and then increased to 2.519 g/m^2 s$^{0.5}$ (0.0083 oz./ft^2 s$^{0.5}$) for samples with 90 μm (0.0035 in.). It can be seen that for crack width lower than 35 μm (0.0014 in.), the crack had limited influence on sorptivity due to self-healing behavior which fully or partially sealed the cracks.

Ma, Zhao and Yao (2016) experimentally investigated the influence of tensile and compressive stress levels on sorptivity of cracked UHPC. Dog-bone specimens were pre-cracked for multiple cracks in direct tension at different tensile stress levels of 30% to 80% of its ultimate tensile stress level. Water ponding was applied to the cracked region to measure the sorptivity of cracked UHPC under different tensile stress levels, as shown in Figure 2-49 (a). Also, the other groups of prismatic UHPC specimens were pre-cracked in compression at different stress levels of 30% to 80% of its ultimate strength. The sample surfaces with cracks were submerged in water for measuring the sorptivity of cracked UHPC under different compressive stress levels, as shown in Figure 2-49 (b). The test results showed that with increasing stress level, the water absorption coefficient increased. As the tensile stress increased from 0% to 50%, the water absorption coefficient increased from 0.20 g/m^2 s$^{0.5}$ (0.00066 oz./ft^2 s$^{0.5}$) to 0.41 g/m^2 s$^{0.5}$ (0.0013 oz./ft^2 s$^{0.5}$), and then rapidly increased to 1.82 g/m^2 s$^{0.5}$ (0.0060 oz./ft^2 s$^{0.5}$) for samples with a stress of 80% of the strength. As the compressive stress increased from 0% to 50%, the water absorption coefficient increased from 0.83 g/m^2 s$^{0.5}$ (0.0027 oz./ft^2 s$^{0.5}$) to 1.50 g/m^2 s$^{0.5}$ (0.0049 oz./ft^2 s$^{0.5}$), and then rapidly increased to 2.07 g/m^2 s$^{0.5}$ (0.0068 oz./ft^2 s$^{0.5}$) for sample with a stress of 80% of the strength.

Thus, it can be seen that for UHPC exceeding 50% of stress level for both compressive strength and tensile strength, sorptivity increased rapidly.

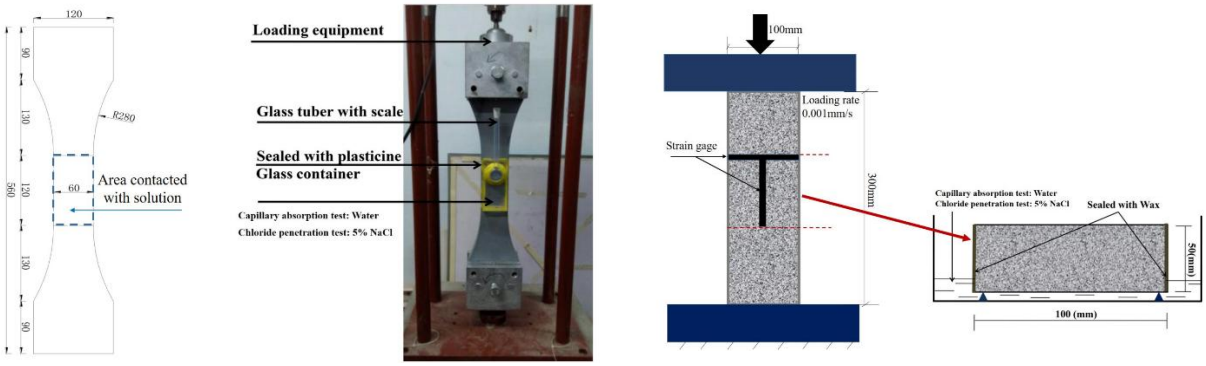

(a) Sorptivity test after tensile strength test (b) Sorptivity after compressive strength test

Figure 2-49 Sorptivity test and chloride test (Ma, Zhao and Yao, 2016)

Wang et al. (2018) experimentally investigated the influence of crack width on sorptivity of cracked UHPC. Cylindrical specimens were prepared with steel fiber dosages of 1, 2, and 3 vol.%. Single crack was generated by sample splitting at different 50 to 80% of its ultimate splitting strength. The residual crack opening distance (COD_{res}) was in the range of 15 to 43 μm (0.00059 to 0.0017 in.), 25 to 65 μm (0.00098 to 0.0026 in.), and 30 to 84 μm (0.0012 to 0.0033 in.), corresponding to the samples with steel fiber content of 1, 2, and 3 vol.%. The test results showed that for samples with three different steel fiber contents, as the crack width increased, the water absorption coefficient increased. As the sample splitting level increased from 50% to 80%, the water absorption coefficient increased from 1.83 to 3.07 g/m^2 s$^{0.5}$ (0.0060 to 0.010 oz./ft^2 s$^{0.5}$) for sample with 1 vol.% steel fiber content; the water absorption coefficient increased from 1.81 to 3.04 g/m^2 s$^{0.5}$ (0.0059 to 0.010 oz./ft^2 s$^{0.5}$) for sample with 2 vol.% steel fiber content; and the water absorption coefficient increased from 1.99 to 2.81 g/m^2 s$^{0.5}$ (0.0065 to 0.0092 oz./ft^2 s$^{0.5}$) for sample with 3 vol.% steel fiber content. Higher contents of steel fibers effectively reduced the sorptivity of UHPC with same crack width. For instance, for samples with a crack width of 40 μm (0.0016 in.), the water absorption coefficients were 2.97, 2.32 and 2.07 g/m^2 s$^{0.5}$ (0.0097, 0.0076, and 0.0068 oz./ft^2 s$^{0.5}$) for steel fiber contents of 1 vol.%, 2 vol.%, and 3 vol.%, respectively. The stitching ability of fibers shortened the cracks and diminished the area for fluid transport, which led to lower sorptivity of the cracked UHPC.

Niu and Zhang (2021) experimentally investigated the influence of crack width on sorptivity of cracked UHPC. Beam samples were prepared for single cracks generated through flexure with widths in the range of 150 to 500 μm (0.0059 in. to 0.020 in.). The pre-cracked samples were then exposed to 3.5% saltwater with 100 wetting-drying cycles of 16 hours in saltwater and 8 hours in air. The sorptivity results showed that with crack width increasing from 0 to 150 μm (0 to 0.0059 in.), the water absorption coefficient increased from 0.25 to 0.35 g/m^2 s$^{0.5}$ (0.00082 to 0.0011 oz./ft^2 s$^{0.5}$). As the crack width increased to 500 μm (0.020 in.), the corresponding water absorption coefficient increased to 0.45 g/m^2 s$^{0.5}$ (0.0015 oz./ft^2 s$^{0.5}$). The self-healing behavior of the cracked UHPC was examined under a microscope at the end of test. Cracks with a width smaller than 150 μm (0.0059 in.) were almost fully sealed, and for cracks smaller than 500 μm (0.020 in.), the cracks were partially sealed.

2.3.2.2 Permeability of cracked UHPC

Generally, the water permeability and gas permeability of cracked UHPC increases with increasing crack width, however they are still comparable to that of uncracked normal-strength concrete. Compared to the water permeability coefficient of uncracked normal concrete around 10^{-10} m/s (3.28×10^{-10} ft./s) (Bertolini *et al.*, 2014), the water permeability coefficient of cracked UHPC was in the range of 1.8×10^{-12} m/s to 2.6×10^{-9} m/s (5.9×10^{-12} ft./s to 8.5×10^{-9} ft./s). Compared to the gas permeability coefficient of uncracked normal-strength concrete in the range of 5×10^{-16} to 10^{-18} m^2 (5.38×10^{-15} to 10^{-17} $ft.^2$) (Bertolini *et al.*, 2014), the gas permeability coefficient of cracked UHPC was in the range of 2.2×10^{-14} to 9.3×10^{-18} m^2 (2.37×10^{-13} to 1.0×10^{-16} $ft.^2$). It was also reported that the self-healing behavior effectively sealed the cracks, leading to a lower water permeability coefficient.

2.3.2.2.1 Water permeability of cracked UHPC

The water permeability of cracked UHPC increases with crack width. Charron, Denarié and Brühwiler (2008) experimentally investigated the influence of crack width on cracked UHPC. Prismatic UHPC specimens were cracked by direct tension with multiple cracks with the widest crack width in the range of 0 to 520 μm (0 to 0.020 in.). The cylindrical cores were extracted from the cracked prismatic UHPC specimens for water permeability test with total testing period for 50 days. After exposure for 35 to 45 days, with increasing crack width from 15 to 90 μm (0.00059 to 0.0035 in.), the water permeability coefficient slightly increased from 1.8×10^{-12} m/s (5.9×10^{-12} ft./s) to 4.8×10^{-11} m/s (1.57×10^{-10} ft./s), and then rapidly increased to 2.6×10^{-9} m/s (8.5×10^{-9} ft./s) with a crack width of 520 μm (0.020 in.). In addition, due to self-healing behavior, the water permeability decreased with a longer exposure period to water. During the first day of testing, specimens with a crack width in the range of 0 to 520 μm (0 to 0.020 in.) had a water permeability coefficient of in the range of 8.2×10^{-11} m/s (2.69×10^{-10} ft./s) to 2.5×10^{-8} m/s (8.2×10^{-8} ft./s). After 40 to 50 days, the corresponding water permeability coefficient decreased to 1.3×10^{-12} m/s (4.27×10^{-12} ft./s) to 2.4×10^{-9} m/s (7.87×10^{-9} ft./s). More detailed information can be found in Table 3-10.

2.3.2.2.2 Gas permeability of cracked UHPC

Gas permeability increased with increasing crack width for UHPC. Wang et al. (2018) experimentally investigated the influence of crack width on gas permeability of cracked UHPC. Cylindrical specimens were prepared with dosages of steel fiber in the range of 1 to 3 vol.%. Cracks were generated by splitting at different splitting stress levels of 50 to 80% of its ultimate splitting strength. The residual crack open distances (COD_{res}) were in the range of 15 to 43 μm (0.00059 to 0.0017 in.), 25 to 65 μm (0.00098 to 0.0026 in.), and 30 to 84 μm (0.0012 to 0.0033 in.), corresponding to the samples with steel fiber contents of 1, 2, and 3 vol.%. The test results showed that for samples with three different steel fiber contents, gas permeability increased with crack width. When splitting stress level increased from 50% to 80%, the gas permeability coefficient increased from 5.0×10^{-17} to 2.2×10^{-14} m^2 (5.38×10^{-16} to 2.37×10^{-13} $ft.^2$), 2.2×10^{-17} to 9.2×10^{-16} m^2 (2.37×10^{-16} to 9.90×10^{-15} $ft.^2$), and 9.3×10^{-18} to 6.8×10^{-16} m^2 (1.00×10^{-16} to 7.32×10^{-15} $ft.^2$) for samples with steel fiber content of 1, 2, and 3 vol.%, respectively. Also, the author reported that higher contents of steel fiber effectively reduced the gas permeability of cracked UHPC. For example, for samples with crack width of 40 μm (0.0016 in.), the gas permeability coefficient decreased from about 2×10^{-14} to 3×10^{-17} m^2 (2.15×10^{-13} to 3.23×10^{-16} $ft.^2$) with increasing steel fiber content from 1 vol.% to 3 vol.%. More detailed information can be found in Table 2-23.

2.3.2.3 Chloride penetration of cracked UHPC

The influence of crack width and loading stress level on chloride penetration of cracked UHPC has been investigated in recent years. Wider and deeper regions of cracked UHPC can be penetrated by chloride

ions through wider cracks. Higher chloride content was found for cracked UHPC exposed to realistic marine environments rather than exposure in bulk diffusion test (Lv et al. 2021a). More detailed review can be found below, and the test results are summarized in Table 2-23.

Hashimoto et al. (2013) investigated the influence of crack width on chloride diffusion behavior of cracked UHPC. Beam specimens were prepared a single crack with width in the range of 0 to 1000 μm (0 to 0.039 in.) were generated at a notch in flexure. The pre-cracked samples were immersed in artificial seawater (3.4 wt.% chloride content solution) for three months. At the end of the exposure, the chloride content of the cracked cross-section of each sample were measured, with the chloride content map shown in Figure 2-50. As shown, chloride ions penetrated wider and deeper within cracked UHPC, especially for samples with crack width wider than 500 μm (0.020 in.).

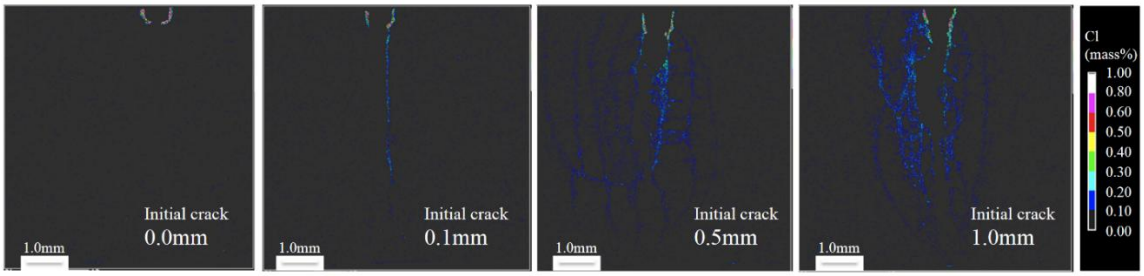

Figure 2-50 Chloride ions ingression for 3 months (Hashimoto et al., 2013)

Ma, Zhao and Yao (2016) experimentally investigated the influence of loading stress levels (tensile stress level and compressive stress level) on chloride diffusion within cracked UHPC. Dog-bone specimens were pre-cracked to generate multiple cracks by direct tension at different tensile stress levels of 30% to 80% of its ultimate tensile strength. The other groups of prismatic UHPC specimens were pre-cracked at stress levels of 30% to 80% of its ultimate compressive strength. The same setup shown in Figure 2-49 was adopted but using a 5 wt.% NaCl solution to measure the chloride diffusion behavior. Test results showed that with increasing compressive stress level and tensile stress level, the chloride diffusion coefficient of cracked UHPC increased. The chloride diffusion coefficient increased rapidly when the stress levels exceeded 50% of the strength. In terms of tensile samples, with increasing tensile stress level from 0 to 50%, the chloride diffusion coefficient gradually increased from 1.2 to 3.3 × 10^{-12} m^2/s (1.29 to 3.55 × 10^{-11} $ft.^2$/s). As the tensile stress level increased to 80%, the chloride diffusion coefficient increased to 14.4 × 10^{-12} m^2/s (1.55 × 10^{-10} $ft.^2$/s). As the compressive stress level increased from 0 to 50%, the chloride diffusion coefficient gradually increased from 1.2 to 2.4 × 10^{-12} m^2/s (1.29 to 2.58 × 10^{-11} $ft.^2$/s). As the compressive stress level further increased to 80%, the chloride diffusion coefficient increased to 3.8 × 10^{-12} m^2/s (4.09 × 10^{-11} $ft.^2$/s). The different crack patterns caused by direct tension test and compressive strength test caused different chloride diffusion behavior. The chloride diffusion coefficient of samples cracked by direct tension test was larger than that caused by compressive strength test at the same stress level.

Lv et al. (2021a) experimentally investigated the influence of crack width on chloride penetration of cracked UHPC exposed to different environments. Dog-bone UHPC specimens were prepared, and multiple cracks were generated in direct tension. The maximum crack widths of 20 μm, 25 μm, and 30 μm (0.00079 in., 0.00098 in., and 0.0012 in.) were considered in this study. Pre-cracked samples were immersed in a tidal zone of real sea with wetting-drying cycle approximate to 12 hours wetting and 12 hours drying for one year. Simultaneously, the other groups of cracked samples with the same crack widths were immersed in 4.5 mol/L saltwater tanks for one year. The total chloride content and free chloride content were measured for each sample at different depths. As the crack width increased from 20 μm to 30 μm (0.00079 in. to 0.0012 in.), the total and free chloride content both increased for cracked

samples exposed to both realistic marine environment and saltwater tank. For samples exposed to realistic marine environment, the maximum total chloride content at a depth of 4 mm (0.16 in.) increased from the range of 0.172% - 0.183% to the range of 0.238% - 0.248% by weight of cement; and the maximum free chloride content at a depth of 4 mm (0.16 in.) increased from the range of 0.145% - 0.155% to the range of 0.203% - 0.215% by weight of cement. For samples exposed to the saltwater tank, the maximum total chloride content and free chloride content at depth of 4 mm (0.16 in.) increased from 0.051% to 0.147% by weight of cement; and the maximum free chloride content at depth of 4 mm (0.16 in.) increased from 0.037 to 0.121% by weight of cement. Moreover, the results found higher total and free chloride content for samples exposed to realistic sea than that of samples exposed to saltwater tank. The author indicated that due to wetting-drying cycles, temperature variation, and variable washing with waves, chloride ingress was accelerated for samples exposed to realistic marine environments.

Table 2-23 Representative results of transport properties of pre-cracked UHPC

Reference	Measured transport properties	w/b ratio	Additional notes	Crack generation method	Crack density	Crack width	Exposure condition	Results
Charron, Denarié and Brühwiler (2008)	Sorptivity	0.14	6. vol.% steel fibers and 10 wt.% of silica fume by weight of concrete	Direct tension test	Multiple cracks	0 µm 15 µm (0.00059 in.) (widest crack width) 35 µm (0.0014 in.) (widest crack width) 90 µm (0.0035 in.) (widest crack width)	-	0.353 g/m^2 s$^{0.5}$ (0.0012 oz./ft^2 s$^{0.5}$) 0.442 g/m^2 s$^{0.5}$ (0.0014 oz./ft^2 s$^{0.5}$) 0.656 g/m^2 s$^{0.5}$ (0.0022 oz./ft^2 s$^{0.5}$) 2.519 g/m^2 s$^{0.5}$ (0.0083 oz./ft^2 s$^{0.5}$)
Ma, Zhao and Yao (2016)		0.20	6.4 wt.% steel fibers and 11.1 wt.% silica fume	Direct tension test	Multiple cracks	0% of ultimate tensile strength 30% of ultimate tensile strength 50% of ultimate tensile strength 80% of ultimate tensile strength	-	0.20 g/m^2 s$^{0.5}$ (0.00066 oz./ft^2 s$^{0.5}$) 0.21 g/m^2 s$^{0.5}$ (0.00069 oz./ft^2 s$^{0.5}$) 0.41 g/m^2 s$^{0.5}$ (0.0013 oz./ft^2 s$^{0.5}$) 1.82 g/m^2 s$^{0.5}$

Reference	Measured transport properties	w/b ratio	Additional notes		Crack generation method	Crack density	Crack width	Exposure condition	Results
Wang et al. (2018)		0.22	1 vol. % steel fibers	30 wt.% silica fume by weight of cement	Compressive test	Single crack	0% of ultimate compressive strength	-	(0.0060 oz./ft^2 s$^{0.5}$) 0.83 g/m^2 s$^{0.5}$
							30% of ultimate compressive strength		(0.0027 oz./ft^2 s$^{0.5}$) 1.30 g/m^2 s$^{0.5}$
							50% of ultimate compressive strength		(0.0043 oz./ft^2 s$^{0.5}$) 1.50 g/m^2 s$^{0.5}$
							80% of ultimate compressive strength		(0.0049 oz./ft^2 s$^{0.5}$) 2.07 g/m^2 s$^{0.5}$
					Splitting tensile test		15 to 43 µm (0.00059 to 0.0017 in.) (residual crack opening displacement)		(0.0068 oz./ft^2 s$^{0.5}$) 1.83 to 3.07 g/m^2 s$^{0.5}$ (0.0060 to 0.010 oz./ft^2 s$^{0.5}$)
			2 vol. % steel fibers				25 to 65 µm (0.00098 to 0.0026 in.) (residual crack opening displacement)		1.81 to 3.04 g/m^2 s$^{0.5}$ (0.0059 to 0.010 oz./ft^2 s$^{0.5}$)
			3 vol. %				30 to 84 µm		1.99 to 2.81 g/m^2 s$^{0.5}$

Reference	Measured transport properties	w/b ratio	Additional notes	Crack generation method	Crack density	Crack width	Exposure condition	Results
			steel fibers			(0.0012 to 0.0033 in.) (residual crack opening displacement)		(0.0065 to 0.0092 oz./ft^2 s$^{0.5}$)
Niu and Zhang (2021)		0.19	6 wt. % steel fiber and 4.2 wt.% silica fume	Bending test	Single crack	0 µm	-	0.25 g/m^3 s$^{0.5}$ (0.0082 oz./ft^2 s$^{0.5}$)
						150 µm (0.0059 in.)		0.32 g/m^3 s$^{0.5}$ (0.0010 oz./ft^2 s$^{0.5}$)
						300 µm (0.012 in.)		0.35 g/m^3 s$^{0.5}$ (0.0011 oz./ft^2 s$^{0.5}$)
						500 µm (0.020 in.)		0.45 g/m^3 s$^{0.5}$ (0.0015 oz./ft^2 s$^{0.5}$)
Charron, Denarié and Brühwiler (2008)	Water permeability	0.14	6. vol.% steel fibers and 10 wt.% of silica fume by weight of concrete	Direct tension test	Multiple cracks	0 µm	-	< 1.2 × 10^{-12} m/s (<3.93× 10^{-12} ft./s)
						15 µm (0.00059 in.)		1.8× 10^{-12} m/s (5.91× 10^{-12} ft./s)
						35 µm (0.0014 in.)		2.8× 10^{-12} m/s

Reference	Measured transport properties	w/b ratio	Additional notes	Crack generation method	Crack density	Crack width	Exposure condition	Results
								(9.19×10^{-12} ft./s)
						90 µm (0.0035 in		4.8×10^{-11} m/s (1.57×10^{-10} ft./s)
						330 µm (0.13 .)		1.0×10^{-9} m/s (3.28 ×10-9 ft./s)
						520 µm (0.020 in.)		2.6×10^{-9} m/s (8.53 ×10-9 ft./s)
Wang et al. (2018)	Gas permeability	0.22	1 vol.% steel fiber	Splitting tensile test	Single crack	15 to 43 µm (0.00059 to 0.0017 in.) (residual crack opening displacement)	-	5.0×10^{-17} to 2.2×10^{-14} m^2 (5.38×10^{-16} to 2.37×10^{-13} $ft.^2$)
			2 vol.% steel fiber			25 to 65 µm (0.00098 to 0.0026 in.) (residual crack opening displacement)		2.2×10^{-17} to 9.2×10^{-16} m^2 (2.37×10^{-16} to 9.90×10^{-15} $ft.^2$)
			3 vol.% steel fiber			30 to 84 µm (0.0012 to 0.0033 in.) (residual crack opening displacement)		9.3×10^{-18} to 6.8×10^{-16} m^2 (1.00×10^{-16} to 7.32×10^{-15} $ft.^2$)

Reference	Measured transport properties	w/b ratio	Additional notes	Crack generation method	Crack density	Crack width	Exposure condition	Results
Ma, Zhao and Yao (2016)	Chloride diffusion coefficient	0.20	6.4 wt.% steel fibers and 11.1 wt.% silica fume	Direct tension test	Multiple cracks	0% of ultimate strength	5 % saltwater for 28 days	1.2×10^{-12} m^2/s (1.29×10^{-11} $ft.^2/s$)
						30% of ultimate strength		1.4×10^{-12} m^2/s (1.51×10^{-11} $ft.^2/s$)
						50% of ultimate strength		3.3×10^{-12} m^2/s ($1.3.55 \times 10^{-11}$ $ft.^2/s$)
						80% of ultimate strength		14.4×10^{-12} m^2/s (1.55×10^{-10} $ft.^2/s$)
				Compressive test		0% of ultimate strength		1.2×10^{-12} m^2/s (1.29×10^{-11} $ft.^2/s$)
						30% of ultimate strength		1.6×10^{-12} m^2/s (1.72×10^{-11} $ft.^2/s$)
						50% of ultimate strength		2.4×10^{-12} m^2/s (2.58×10^{-11} $ft.^2/s$)
						80% of ultimate strength		3.8×10^{-12} m^2/s (4.09×10^{-11} $ft.^2/s$)

Reference	Measured transport properties	w/b ratio	Additional notes	Crack generation method	Crack density	Crack width	Exposure condition	Results
Ma, Zhao and Yao (2016)	Free chloride content (by weight of concrete mass) and penetration depth (1 to 12 mm) (0.04 in. to 0.47 in.)	0.20	6.4 wt.% steel fibers and 11.1 wt.% silica fume	Direct tension test	Multiple cracks	0% of ultimate tensile strength	5 % saltwater for 28 days	0.143 - 0.037%
						30% of ultimate tensile strength		0.165 - 0.036%
						50% of ultimate tensile strength		0.383 - 0.036%
						80% of ultimate tensile strength		0.502 - 0.037%
				Compressive test		0% of ultimate compressive strength		0.156 - 0.037%
						30% of ultimate compressive strength		0.351 - 0.041%
						50% of ultimate compressive strength		0.430 - 0.038%
						80% of ultimate compressive strength		0.466 - 0.043%
Lv et al. (2021a)	Total chloride content (by weight of concrete mass) and penetration depth (4-20mm) (0.16 in. to 0.79 in.)	0.17	2 vol.% steel fiber and 8.3 wt.% silica fume	Direct tension test	Multiple cracks	20 to 30 μm (0.00079 to 0.0012 in.)	4.5 mol/L saltwater for one year	0.051 – 0.013% to 0.147 - 0.018%
							Realistic marine environment for one year	0.183 - 0.022% to 0.248% - 0.039%
						Uncracked	4.5 mol/L saltwater for one year	0.026 – 0.015

Reference	Measured transport properties	w/b ratio	Additional notes	Crack generation method	Crack density	Crack width	Exposure condition	Results
	Free chloride content (by weight of concrete mass) and penetration depth (4-20mm) (0.16 in. to 0.79 in.)					20 to 30 µm (0.00079 to 0.0012 in.)	Realistic marine environment for one year	0.164 - 0.018%
							4.5 mol/L saltwater for one year	0.037 - 0.011% to 0.121 – 0.013%
							Realistic marine environment	0.155 - 0.013% to 0.215% - 0.029%
						Uncracked	4.5 mol/L saltwater for one year	0.015 - 0.008%
							Realistic marine environment	0.149 - 0.007%

2.3.3 Corrosion of steel fiber/ steel reinforcement of cracked UHPC

Cracks could act as flow channels in UHPC for harmful substances such as water, oxygen, and chloride ions. Thus, the steel fibers and reinforcements embedded in cracked UHPC are more likely to have higher risks of steel corrosion than in uncracked concrete. In this section, the influence of crack width on corrosion condition of steel fiber and the influence of corrosion degree of steel fiber are reviewed. The influence of UHPC crack width on steel rebar corrosion is also discussed.

2.3.3.1 Corrosion of steel fiber of cracked UHPC

The corrosion condition of steel fiber within cracked UHPC was visually and quantitatively studied by SEM imaging and electrochemical method in one study separately. Hashimoto et al. (2013) visually investigated the influence of crack width on corrosion condition of steel fiber within cracked UHPC by SEM. Beam samples were prepared with single crack widths between 0 and 1000 μm (0 to 0.039 in.) were generated in flexure with an initial artificial notch at the mid-span. The cracked surfaces of pre-cracked samples were immersed in artificial seawater (3.4 wt.% chloride content solution) for three months. At the end of exposure, the corrosion condition of steel fiber within three sections of the samples were visually measured:1) upper region, where steel fibers were located 40 to 70 mm (1.57 to 2.76 in.) above the artificial seawater; 2) lower region, where steel fibers were located 0 to 5 mm (0 to 0.20 in.) above the artificial seawater; and 3) submerged region, where steel fibers were located 0 to 5 mm (0 to 0.20 in.) below the artificial seawater. The corrosion condition of the steel fibers was visually observed in the SEM, as shown in Figure 2-51. For crack width less than 100 μm (0.0039 in.), corrosion was only found in the submerged region. For crack width larger than 500 μm (0.020 in.), corrosion was found in all three regions.

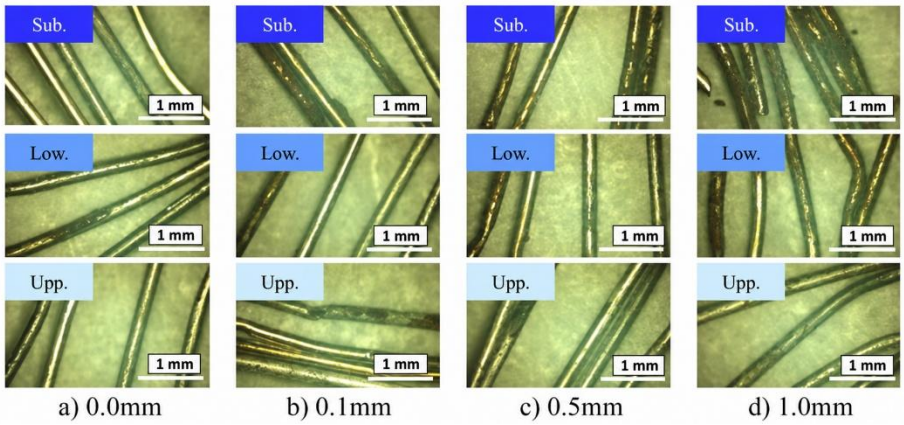

Figure 2-51 SEM results of steel fibers within three regions exposed for 3 months (Hashimoto *et al.*, 2013)

Wang et al. (2022) experimentally investigated the influence of crack width on corrosion condition of steel fibers by LPR and electrical resistivity of the cracked UHPC. The corrosion rate of the steel fiber was obtained by LPR, and because the high electrical resistivity of cracked UHPC results in a low possibility of steel fiber corrosion, electrical resistivity was also adopted as an indicator for measuring corrosion condition of steel fiber in this study. Cubic UHPC samples without steel fibers were prepared, with two steel fibers embedded at each side of an artificial single crack that were connected to a potentiostat to measure the fiber corrosion current density, as shown in Figure 2-52 (a). Simultaneously, another group of cubic UHPC samples (mixed with steel fiber of 20 wt.% by mass of cement) were prepared. Two copper meshes were embedded instead of steel fibers at each side of an artificial single crack, which were connected to a potentiostat to measure the electrical resistivity of cracked UHPC, as

shown in Figure 2-52 (b). The width of single crack was in the range of 0 to 1000 μm (0.0039 to 0.039 in.). All pre-cracked samples were subjected to wetting-drying cycles comprised of 3 days immersed in 3.5 wt.% NaCl solution and 2 days drying the air, lasting for 180 days (36 cycles). The test results showed that with increasing crack width, the steel fiber corrosion current density increased. In terms of corrosion rate of steel fiber, the corrosion current density of steel fiber in the two regions of the samples were measured: 1) upper region - the vertical distance between steel fibers to the crack was less than 15 mm (0.59 in.); and 2) lower region – the vertical distance between steel fibers to the crack was greater than 15 mm (0.59 in.). The corrosion rate of steel samples after 180 days increased from 0.78 μA/cm^2 (5.03 μA/in.^{2}) to 1.25 μA/cm^2 (8.07 μA/in.^{2}) in the upper region when the crack width increased from 0 to 1000 μm (0.0039 to 0.039 in.). The corrosion rate of steel samples increased from 0.78 μA/cm^2 (5.03 μA/in.^{2}) to 0.86 μA/cm^2(5.55 μA/in.^{2}) for fibers in the lower region as the crack width increased from 0 to 1000 μm (0.0039 to 0.039 in.). This showed that the steel fibers at a distance larger than 15 mm (0.59 in.) away from cracks are less affected by cracks compared to the steel fiber located closer to the crack. In addition, with increasing crack width, the electrical resistivity first increased and then decreased, but all cracked UHPC showed higher electrical resistivity than uncracked UHPC. The electrical resistivity increased after 180 days of exposure from 62.30 to 118.92 kΩ-m (204.40 to 390.16 kΩ-ft.) with increasing crack width from 0 to 250 μm (0 to 0.0098 in.). As the crack width increased from 250 to 1000 μm (0.0098 in. to 0.039 in.), the electrical resistivity decreased from 118.92 kΩ-m (390.16 kΩ-ft.) to 102.15 kΩ-m (335.14 kΩ-ft.). It was suspected that the rehydration of unhydrated cementitious mixture improved the UHPC micro-structure, which alleviated the corrosion of steel fibers.

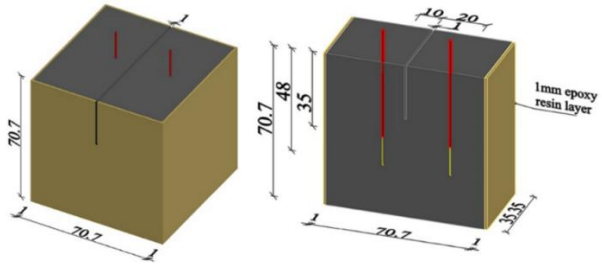

(a) Test setup for measuring corrosion rate of steel fiber embedded in cracked UHPC (without steel fiber content in mixture)

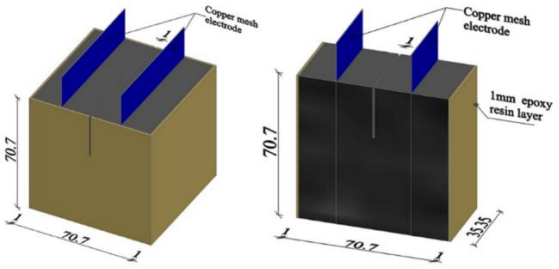

(b) Test setup for measuring electrical resistivity of UHPC (mixed with steel fiber content of 20 wt.% by mass of cement)

Figure 2-52 Corrosion of steel fiber test setup (Wang *et al.*, 2022)

The corrosion of steel fibers affects the mechanical properties of UHPC. Shin and Yoo (2020) experimentally investigated the influence of corrosion of steel fiber on tensile strength of cracked UHPC. Dog-bone samples was pre-cracked to different tensile stress levels of 45 to 60% of their ultimate tensile

strength, with corresponding average crack widths of 20.6 μm (0.00081 in.) and 26.9 μm (0.0011 in.), respectively. Pre-cracked samples were exposed to wetting-drying cycles of one week immersed in 3.5 wt.% NaCl solution followed by one week drying in the air for a total of 20 weeks. Then, the tensile strength of cracked UHPC were measured. For samples preloaded to 45% of its ultimate tensile strength, the tensile strength first increases from 14.8 MPa (2.15 ksi) to 15.5 Mpa (2.25 ksi) after exposure up to 4 weeks, then decreased to 13.1 Mpa (1.90 ksi) after exposure up to 20 weeks; and for samples preloaded to 60% of its ultimate tensile strength, the tensile strength first stayed at 14.5 Mpa (2.10 ksi) during exposure up to 4 weeks, then decreased to 13.5 Mpa (1.96 ksi) after exposure up to 20 weeks. This is because when corrosion products form on the fiber surface, it increases the surface roughness and subsequently the bond strength between steel fibers and matrix increases. However, excessive fiber corrosion leads to lower cross-sectional area of steel fibers, decreasing the tensile strength. This explanation was later verified by Yoo, Shin and Banthia (2021). During their test, the pull-out strength of corroded steel fiber with different corrosion degrees embedded in cracked UHPC was measured by single fiber pull-out test. One steel fiber was embedded in sample, and then a single crack was generated at the middle of sample with different crack width in size of 150 μm (0.0059 in.) and 500 μm (0.020 in.) by tensile stress. Then, the pre-cracked samples were immersed in 3.5 wt.% NaCl solution for 20 weeks with different corrosion degrees of steel fiber for subsequent single fiber pull-out stress measurement. The test result shows that for samples with crack widths of 150 μm (0.0059 in.), the bond strength increased from 11.5 Mpa (1.67 ksi) to 12.9 Mpa (1.87 ksi) with exposure from 4 to 20 weeks; for samples with a crack width of 500 μm (0.020 in.), the bond strength decreased from 10.9 Mpa (1.58 ksi) to 0.5 Mpa (0.07 ksi) with exposure from 4 to 20 weeks.

2.3.3.2 Corrosion of steel reinforcement of cracked UHPC

Only one related study was found in the literature on the corrosion of steel reinforcement in cracked UHPC. Fan et al. (2021) experimentally investigated the corrosion rate of steel reinforcement of cracked UHPC with different steel fiber content by salt-ponding test in wetting-drying cycles. Crack was generated by four-point bending test with primary crack width in the range of 100 μm to 400 μm (0.0039 to 0.016 in.), and steel fiber contents of 0.5 vol.% and 2.0 vol% were used for constructing the UHPC samples. Two steel rebars with diameter of 9.5 mm (0.37 in.) and 22.2 mm (22.2 in.) were placed at the top and bottom of the beams, respectively, as shown in Figure 2-53. Then, all pre-cracked samples were exposed to salt-ponding test with 3.5 wt.% NaCl solution for 174 days with monitoring of corrosion rate by LPR test and Tafel polarization test. The test results show that with increasing crack width, the corrosion rate increases, as shown in Figure 2-54. After exposure for 174 days, for samples with 0.5 vol.% steel fibers, with increasing primary crack width from 100 μm to 400 μm (0.0039 to 0.016 in.), the corrosion rate of the top rebar increased from 0.011 $\mu A/cm^2$ (0.071 $\mu A/in.^2$) to 0.076 $\mu A/cm^2$ (0.49 $\mu A/in.^2$), and the corrosion rate of bottom rebar increased from 0.0029 $\mu A/cm^2$ (0.019 $\mu A/in.^2$) to 0.0070 $\mu A/cm^2$ (0.045 $\mu A/in.^2$). Samples with 2.0 vol.% steel fibers with primary crack width increasing from 100 μm to 400 μm (0.0039 to 0.016 in.), showed that the corrosion rate of the top rebar increased from 0.0077 $\mu A/cm^2$ (0.050 $\mu A/in.^2$) to 0.034 $\mu A/cm^2$ (0.219 $\mu A/in.^2$), and the corrosion rate of the bottom rebar increased from 0.0024 $\mu A/cm^2$ to 0.0047 $\mu A/cm^2$ (0.015 $\mu A/in.^2$ to 0.030 $\mu A/in.^2$). This also indicated that with higher content of steel fiber, the maximum corrosion rate decreased. Moreover, it should be pointed out that after one month of salt-ponding exposure, all steel rebars embedded in pre-cracked UHCP samples became passive due to corrosion process suppressed by limited oxygen ingress caused by self-healing behavior.

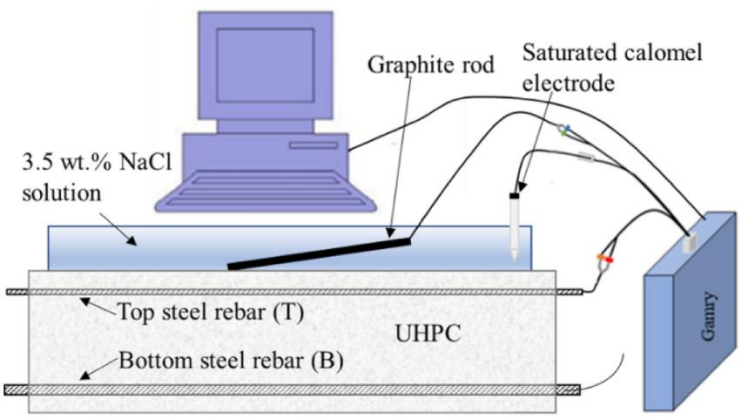

Figure 2-53 Setup for acceleration corrosion of steel rebar of cracked UHPC (Fan, Teng, Tang, Kamal H Khayat, *et al.*, 2021)

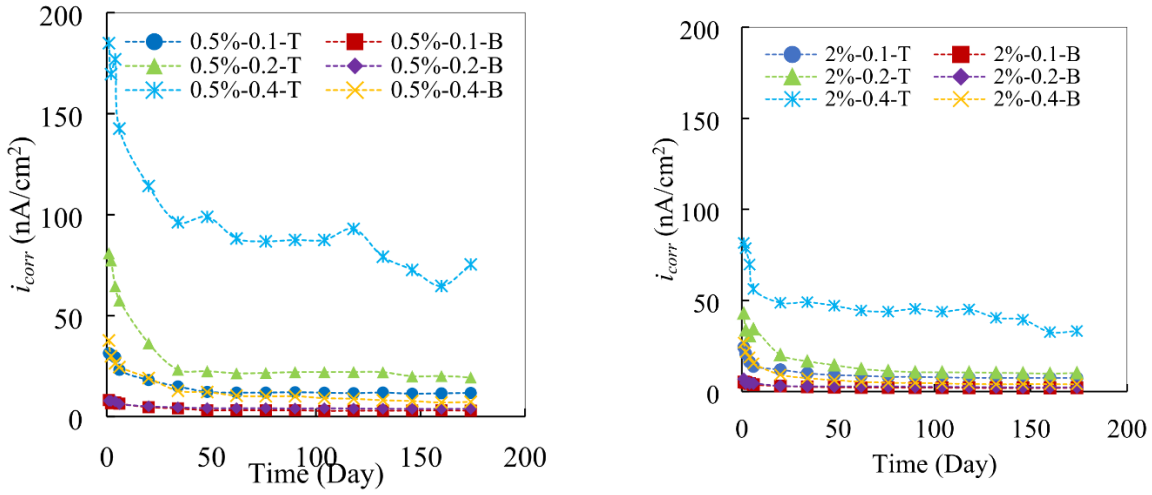

(a) (b)

Figure 2-54 Corrosion rate of steel reinforcement in cracked UHPC with fiber content of 0.5 vol.% (a) and 2.0 vol% (b) (Fan, Teng, Tang, Kamal H Khayat, *et al.*, 2021)

Based on existing research, it is also noted that the influence of V-shape crack and different crack patterns on corrosion condition of steel fiber and steel reinforcement has not been fully studied. The crack pattern and corresponding crack generation method for measuring corrosion condition of steel members of cracked UHPC is listed in Table 2-24. Only one study investigated the V-shaped bending cracks, however, in real structures, most cracking occurred in flexure and resulted in V-shape cracks. Very limited research has been done on the influence of cracks on the corrosion condition of cracked reinforced UHPC. Only one paper considered the influence of primary crack width on corrosion condition of steel rebar embedded in cracked UHPC. However, the author did not consider the influence of crack depth, density, and variability on corrosion rate of cracked reinforcement UHPC. With limited information, no direct correlation can be made between crack patterns, transport properties, and corrosion of reinforcements.

Table 2-24 Crack generation methods and corresponding measured corrosion of steel fiber/ steel reinforcement

Crack pattern	Crack generation method	Measured Items	Reference
Single crack	Artificial crack	Corrosion rate of steel fiber	Wang et al. (2022)
Multiple crack	Direct tension test	Mechanical performance of cracked UHPC with corroded steel fiber	Shin and Yoo (2020)
Single crack	Single Fiber pull-out test		Yoo, Shin and Banthia (2021)
Primary crack	Bending test	Corrosion rate of steel reinforcement	Fan et al. (2021)

2.3.4 Summary

The influence of cracks on transport properties of normal concrete and can be summarized as follows:

1. The transport properties including water permeability, gas permeability, and chloride penetration of cracked normal concrete increase two to seven orders of magnitudes as the crack width increases up to 500 μm (0.0197 in.).
2. With increasing crack width, a threshold value of crack is observed for water permeability coefficient and gas permeability coefficient. For water permeability, self-healing behavior can fully or partially fill the crack when crack width is small [below the range of 100 to 300 μm (0.0039 to 0.0118 in.)]. After crack widths exceed the threshold value, the walls of cracks behave like an outside surface exposed to environment, leading to a large increase in water permeability. For gas permeability is more sensitive to crack width than water permeability. When the crack width exceeds a threshold value of 15 μm (0.0006 in.) crack opening displacement, gas permeability increases rapidly.
3. Two threshold values were reported for crack width influencing the chloride penetration behavior of concrete. For crack widths below the lower threshold value in the range of 14 to 100 μm (0.00055 to 0.0157 in.), cracks were sealed by self-healing behavior and no obvious increase in chloride diffusion was observed. After crack width exceeded the lower threshold value, cracks were considered as flow channels for chloride ions, and the chloride diffusion coefficient increased with increasing crack width. After the crack width exceeds the upper threshold value in the range of 80 to 400 (0.0031 to 0.0157 in.), the wall of crack behaves like the outside surface exposed to chloride ions, and chloride diffusion coefficient increases rapidly.
4. Crack depth influence the chloride penetration. The maximum chloride penetration depth increased with increasing crack depth in cracked normal-strength concrete.
5. The transport properties including water permeability, gas permeability, and chloride penetration of cracked normal-strength concrete increased with increasing crack density.
6. Higher crack width leads to increasing corrosion rate of reinforcements embedded in cracked concrete. With crack width up to 700 μm (0.028 in.), corrosion rate increased more than one order of magnitude compared to uncracked normal-strength reinforcement concrete.
7. The influence of crack density on corrosion rate of reinforcements in cracked normal concrete was mixed. Since with increasing crack density, the concrete region between crack decreasing, which could lead to lower concrete resistance and higher corrosion rate, but the cathodic region of passive rebar between cracks decreases, which could suppress the circuit and lead to lower corrosion rate.\

8. Limited studies reported that cracks affect the transport properties of UHPC. As the UHPC crack width increased up to 520 μm (0.020 in.), sorptivity, water permeability, gas permeability and chloride penetration increased by one to three orders of magnitude. However, the influence of multiple crack patterns (crack density, variability of crack width), V-shaped flexural crack geometry, and crack depth have not been studied, and this represents a major knowledge gap. Nevertheless, the transport properties of cracked UHPC are reported to be better or comparable to that of uncracked normal concrete.
9. Threshold crack width values are reported for sorptivity and water permeability for cracked UHPC. For crack width below the threshold value, cracks have limited influence on sorptivity and water permeability due to self-healing behavior of cracks. For crack width above the threshold value in the range of 90 μm (0.0035 in.) to 150 μm (0.0059 in.), sorptivity and water permeability increased with wider crack width for cracked UHPC. However, the role of self-healing and the threshold crack width have not been fully studied in the literature. Currently, no paper reported the threshold crack width in UHPC for chloride penetration and corrosion condition for embedded steel.
10. Higher chloride penetration is reported for cracked UHPC samples exposed to realistic environment than samples exposed to bulk diffusion test due to wetting-drying cycles, temperature variation, and variable washing with waves.
11. Cracks could increase the risk of steel fiber corrosion. Literature reported low corrosion of steel fiber at the depth of 15 mm (0.039 in.) away from cracks with crack width up to 1000 μm (0.039 in.). However, moderate corrosion of steel fiber could increase the mechanical properties of UHPC due to higher bond strength.
12. Only one study investigated the corrosion of steel reinforcement embedded in cracked UHPC. Corrosion rate of the reinforcement was reported to increase with increasing crack width up to 400 μm (0.016 in.). However, after one month, steel reinforcement was observed to return to passive state due to self-healing behavior and short of oxygen supply. However, no direct correlation was made between the crack patterns, transport properties, and corrosion rate. There also has been no studies on the corrosion resistance of steel reinforcements in cracked UHPC under realistic marine environments. These are also major knowledge gaps.

2.4 Summary and knowledge gaps

This report provided a comprehensive review on the corrosion process of steel reinforcement in concrete, the transport properties of uncracked UHPC, the corrosion of steel fiber and steel rebar embedded in uncracked UHPC, the influence of cracks on concrete and UHPC, and the corrosion of steel fiber and steel reinforcement within cracked UHPC. The following conclusions can be drawn from the literature review:

1. The transport properties including porosity, sorptivity, water permeability, gas permeability, chloride penetration of UHPC is extremely low, about one to four orders of magnitude lower than that of normal concrete. The extremely low transport properties of UHPC are due to its dense microstructure, disconnected pore systems as a result of low water-to-binder ratio, addition of SCMs, and steel fiber. Thus, UHPC provides higher corrosion protection for embedded steel reinforcements.
2. Corrosion of steel fiber is only reported at the very surface of samples in uncracked UHPC, and no corrosion has been reported below 1 mm (0.04 in.) depth from surface, which does not adversely affect the mechanical properties of UHPC.
3. The corrosion rate of steel rebars embedded in UHPC is found to be extremely low due to the low transport properties of UHPC preventing aggressive ions, water and oxygen from reaching the steel reinforcement. It has been reported that the corrosion rate of reinforcement UHPC is influenced by the SCMs content, steel fiber content, and initial chloride content within UHPC mixture.
4. Crack width is found to be the most important crack characteristic to influence the transport properties including water permeability, gas permeability, and chloride penetration of cracked normal concrete, while crack depth and density also affect these properties. The transport properties including water permeability, gas permeability, and chloride penetration of cracked normal concrete increases by two to seven orders of magnitude with increasing crack width up to 500 μm (0.0197 in.). With increasing crack width, a threshold value of crack was observed for water permeability coefficient and gas permeability coefficient. For water permeability, self-healing behavior can fully or partially fill the crack when crack width is small, which is in the range of 100 to 300 μm (0.0039 to 0.0118 in.). After crack width exceeding a certain threshold value, the walls of cracks are considered the outside surface exposed to environment, leading to rapidly increase of water permeability. For gas permeability, it is more sensitive to crack width than water permeability. Due to lack of seal-healing behavior, when crack width exceeds a certain threshold value 15 μm (0.0006 in.), gas permeability increases rapidly. Two threshold values are reported for crack width influencing the chloride penetration behavior of concrete. For crack width below the lower threshold crack width in the range of 14 to 100 μm (0.00055 to 0.0157 in.), cracks are sealed by self-healing behavior and no obvious increase in chloride diffusion is observed. After crack width exceeding the lower threshold value, cracks are considered as flow channels for chloride ions, and chloride diffusion coefficient increases with increasing crack width. After crack width exceeds the upper threshold crack width in the range of 80 to 400 (0.0031 to 0.0157 in.), the wall of crack is considered the outside surface exposed to chloride ions, and chloride diffusion coefficient increases rapidly.
5. Crack depth and density also influence the transport properties. Literature reported that the maximum chloride penetration depth increases with increasing crack depth in cracked normal concrete. The transport properties including water permeability, gas permeability, and chloride penetration of cracked normal concrete also increases with increasing crack density.
6. Higher crack width leads to increasing corrosion rate of reinforcements embedded in cracked concrete. With crack width up to 700 μm (0.028 in.), corrosion rate increases more than order of magnitude compared to uncracked normal reinforcement concrete.

7. The influence of crack density on corrosion rate of reinforcements in cracked normal concrete is mixed. Since with increasing crack density, the concrete region between crack decreasing, which could lead to lower concrete resistance and higher corrosion rate, but the cathodic region of passive rebar between cracks decreases, which could suppress the circuit and lead to lower corrosion rate.
8. Limited studies reported that cracks also affect the transport properties of UHPC. With crack width increasing up to 520 μm (0.020 in.), sorptivity, water permeability, gas permeability and chloride penetration increases by one to three orders of magnitude for cracked UHPC. However, the influence of multiple crack patterns (crack density, variability of crack width), V-shaped flexural crack geometry, and crack depth have not been studied, and this represents a major knowledge gap. Nevertheless, the transport properties of cracked UHPC are reported to be better or comparable to that of uncracked normal concrete.
9. Threshold crack width values are also reported for sorptivity and water permeability for cracked UHPC. For crack width below the threshold value, cracks have limited influence on sorptivity and water permeability due to self-healing behavior of cracks. For crack width above the threshold value in the range of the range of 90 μm (0.0035 in.) to 150 μm (0.0059 in.), sorptivity and water permeability increase with wider crack width for cracked UHPC. However, the role of self-healing and the threshold crack width have not been fully studied in the literature. Currently, no paper reported the threshold crack width for chloride penetration and corrosion condition for embedded steel member of cracked UHPC.
10. High chloride penetration is reported for cracked UHPC samples exposed to realistic environment than samples exposed to bulk diffusion test are reported due to wetting-drying cycles, temperature variation, and variable washing with waves.
11. Cracks could also increase the risk of steel fiber corrosion. Literature reported low corrosion of steel fiber at the depth of 15 mm (0.59 in.) away from cracks with crack width up to 1000 μm (0.039 in.). However, moderate corrosion of steel fiber could increase the mechanical properties of UHPC due to higher bond strength.
12. Only one study investigated the corrosion of steel reinforcement embedded in cracked UHPC. Corrosion rate of the reinforcement was reported to increase with increasing crack width up to 400 μm (0.016 in.). However, after one month, steel reinforcement is observed to return to passive state due to self-healing behavior and short of oxygen supply. However, no direct correlation was made between the crack patterns, transport properties, and corrosion rate.

The following knowledge gaps are also identified based on the literature review.

1. Studies on transport properties, especially chloride penetration properties of cracked UHPC are still limited. Only limited studies reported the influence of crack width on the chloride diffusion properties of UHPC, however, the influence of multiple cracking patterns (crack density, variability), crack depth, and realistic V-shaped flexural crack geometry, has not been comprehensively investigated. The threshold values of crack characteristics (e.g. crack width) related to transport properties increase are not well-established.
2. There is a significant lack of research data on the corrosion of steel reinforcement within cracked UHPC. Only one study investigated the corrosion of steel reinforcement in cracked UHPC under salt-ponding test. There are no studies on corrosion of steel reinforcement in cracked UHPC under realistic marine environment exposure. Also, there is no established direct correlation between the crack characteristics, transport properties, and corrosion rates. More comprehensive studies on the influence of different crack characteristics on corrosion condition and rate of steel reinforcement are urgently needed to evaluate the durability and remaining service life of UHPC.

3. The role of self-healing on the transport properties and corrosion resistance of cracked UHPC is not well-understood. Although limited studies reported self-healing affecting the sorptivity, water permeability, chloride penetration, and corrosion of steel rebars, the self-healing was not explicitly monitored and its influence is not well documented.
4. No data has been reported on the corrosion rate of steel reinforcement in cracked UHPC exposed to the realistic marine environment, although past scholars reported more chloride ions were observed for cracked samples exposed to marine environments than laboratory salt water exposure.
5. Corrosion of fibers within cracked UHPC has been reported, however, the relationship between crack characteristics, exposure conditions, corrosion and steel fibers, and its influence on mechanical properties of cracked UHPC is not well established.
6. The influence of bridging behavior of steel fiber on chloride penetration of cracked UHPC combining self-healing behavior still needs further investigation. Due to bridging effect, steel fiber can restrict the expansion at the end of cracks, further leading to different ending area and shape of cracks, which may eventually influence of the chloride penetration of UHPC and the self-healing behavior of UHPC.

3 Mixture design and specimens preparation

3.1 Mixture selection

Four UHPC mixture designs selected in this test contain three time-tested commercial mixture (Mixture A, Mixture B, and Mixture C), and one non-proprietary mixture (Mixture D) that are backed by research and field implementations. Mixture A is the first commercial mixture, and the mixture design is shown in Table 3-1. Mixture B's mixture design is shown in Table 3-2. Mixture C's mixture design is shown in Table 3-3. The non-proprietary mixture (Mixture D) is shown in Table 3-4. All mixtures have been cast and implemented in the State of Florida.

Table 3-1 Mixture design for Mixture A

Mixture	lb./yd.^{3}	Percentage by weight	Compressive strength (Measured by 3'' X 6'' cylinder) (Characteristic strength)
Premix	3690	87.68	≥21 ksi
Premia 150	51	1.20	
Water	204	4.85	
Steel fibers (2 vol.%)	264	6.27	

Note: straight steel fiber in size of 13 mm (0.512 in.) length x 0.20 mm (0.008 in.) diameter with minimum tensile strength of 377 ksi (2600 MPa).

Table 3-2 Mixture design for Mixture B

Mixture	lb./yd.^{3}	Percentage by weight	Compressive strength (Measured by 3'' X 6'' cylinder) (Characteristic strength)
Cement	1320	29.31	≥ 25.5 ksi
Premix	1120	24.87	
Sands	1394	30.95	
Steel fibers (2 vol.%)	265	5.88	
Water	275	6.11	
Premia 150	50	1.12	
Optimum 100	50	1.12	
TC 701	24	0.53	
E5	5	0.11	

Note: straight steel fiber in size of 13 mm (0.5118 in.) length x 0.20 mm (0.008 in.) diameter with minimum tensile strength of 295 ksi (2034 MPa).

Table 3-3 Mixture design for Mixture C

Mixture	lb./yd.^{3}	Percentage by weight	Compressive strength (Measured by 3'' X 6'' cylinder) (average strength)
Premix	3869	86.5	
Steel fibers	271	6.1	
Carbon nano fibers (CNF) paste	22	0.5	22.3 ksi
Accelerator	20	0.4	
Water	292	6.5	

Note: straight steel fiber in size of 13 mm (0.512 in.) length x 0.20 mm (0.008 in.) diameter

Table 3-4 Mixture design for Mixture D

Mixture	Product	lb./yd.^{3}	Kg/m^3	Percentage by weight	Compressive strength (Measured by 3'' X 6'' cylinder) (average strength)
Cement	Type IL Cement (Titan, Patras Greece)	1573	933	37.8	
Silica Fume	BASF MasterLife SF 100	393	233	9.4	
Sand	Mason Sand (ER Jahna, Independent North Mine)	1526	905	36.7	18-21 ksi
High-range Water Reducer	BASF MasterGlenium 7920	59	35	1.4	
Rheology Modifying Admixture	GCP V-MAR F100	8	5	0.2	
Steel fiber	Steel Fiber	263	156	6.3 (2.0 vol.%)	
Water	-	338	201	8.1	

Note: straight steel fiber – in size of 13 mm (0.5118 in.) length x 0.20 mm (0.008 in.) diameter with minimum tensile strength of 290 ksi (2000 Mpa).

3.2 Raw mixture characterization

The cementitious mixtures (cement and silica fume) and aggregates for the acquired non-proprietary UHPC mixture is characterized (Mixture D). Specifically, X-ray diffraction, X-ray fluorescence, laser particle size diffraction, and gas pycnometry were performed to characterize the chemical composition, specific density, and particle size of the cementitious mixtures of the non-proprietary UHPC mixture. The specific gravity, absorption capacity, and gradation of the fine aggregates of the non-proprietary UHPC was also tested. All testing procedures and results are documented in this report.

The manufacturer information of the fine aggregate and the cementitious mixtures is provided below:

1) Mason sands (#product number 1008) produced in FDOT mine #11-490 was provided by Jahna;
2) Type IL portland-limestone cement was provided by Titan Florida; and
3) MasterLife SF 100 silica fume was provided by Master Builders Solutions.

3.2.1 Gas pycnometry

The helium pycnometry setup as specified in ASTM C604-18 Standard Test Method for True Specific Gravity of Refractory Mixtures by Gas-Comparison Pycnometer (ASTM Committee C08, 2018) was used to compute the densities of cement and silica fume. Five runs were performed and averaged, as shown in Table 3-5.

Table 3-5 Density of cementitious mixture

Mixture	Density (g/cm^3)	Density (oz./in.^{3})
Cement	3.1550	1.8237
Silica Fume	2.3254	1.3442

3.2.2 Laser particle size distribution

Laser particle size diffraction was performed according to ASTM E3340-22 Standard Guide for Development of Laser Diffraction Particle Size Analysis Methods for Powder Mixtures (ASTM Committee E29, 2022) on cement and silica fume specimens in isopropanol alcohol as the carrier fluid. Figure 3-1 presents the cumulative particle size distribution for the cement and silica fume. The mean size obtained for the cement was 13.9 µm (0.00055 in.). An ultrasonic wand was used to reduce silica fume agglomeration between its fine particles. However, agglomeration was still seen, resulting in a mean size of 20.1 µm (0.00079 in.) which is higher than the expected silica fume particle size. Results of the cumulative volume percentages for each mixture are presented in Table 3-6.

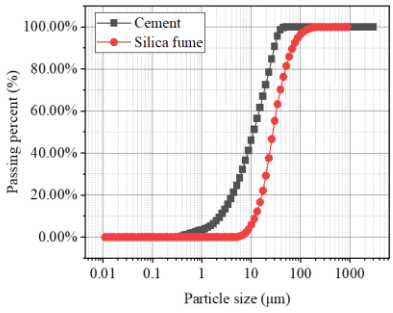

Figure 3-1 Cementitious mixture particle size distribution as measured by laser diffraction

Table 3-6 Cumulative volume percentages of cementitious mixtures obtained by laser diffraction

Mixture	D10 (μm)	D10 (in.)	D50 (μm)	D50 (in.)	D90 (μm)	D90 (in.)
Cement	2.39358	9.4235×10^{-5}	11.19891	4.4090×10^{-4}	29.43871	1.1590×10^{-3}
Silica Fume	6.04914	2.3816×10^{-4}	16.37176	4.4456×10^{-4}	37.38224	1.4717×10^{-3}

3.2.3 X-ray fluorescence

The mixture oxide composition for cementitious mixtures was determined using x-ray fluorescence spectroscopy (XRF) on fused glass beads after performing loss on ignition (LOI) for each mixture. The results are tabulated in Table 3-7.

Table 3-7 XRF results for oxide chemical composition of cementitious mixtures in percentage by weight

Parameter	Cement	Silica Fume
SiO_2	20.82	96.89
TiO_2	0.50	0.01
Al_2O_3	4.41	0.29
Fe_2O_3	3.45	1.03
MnO	0.00	0.082
MgO	0.92	0.59
CaO	66.35	0.80
Na_2O	0.07	0.12
K_2O	0.32	0.69
P_2O_5	0.12	0.08
SO_3	2.56	0.24
LOI	4.41	3.08

3.2.4 X-ray diffraction

X-ray diffraction (XRD) was conducted for determining the crystalline composition in the cement used in the non-proprietary UHPC mixture as per ASTM C1365-18 Standard Test Method for Determination of the Proportion of Phases in Portland Cement and Portland-Cement Clinker Using X-Ray Powder Diffraction Analysis (ASTM Committee C01, 2018). A voltage of 45mV and a current of 40 mA were applied. A step size of 0.008° and a time interval of 20 seconds per step were used over a scan range (2θ) of 5° to 70°. A 20% corundum internal standard was intermixed with the specimen before scanning. The data obtained from XRD was refined by Rietveld refinement using the Profex software. The cement composition results are presented in Table 3-8.

Table 3-8 Non-proprietary mixture cement crystalline composition

Analyte	Type IL Cement
Alite	52.57
Belite	10.57
Aluminate	5.03

Analyte	Type IL Cement
Ferrite	10.3
Gypsum	2.39
Calcite	12.72
Portlandite	1.43
Quartz	3.76
Bassanite	1.25

3.2.5 Specific gravity and absorption of fine aggregates

Specific gravity and absorption of fine aggregates were examined according to ASTM C128-22 Standard Test Method for Relative Density (Specific Gravity) and Absorption of Fine Aggregate (ASTM Committee 09, 2022). The test results are shown in Table 3-9.

Table 3-9 Specific gravity and absorption rate of fine aggregates for non-proprietary mixtures

Item	Description	Result
OD (oven-dry)	Relative density (specific gravity)	2.64
SSD (saturated-surface-dry)	Relative density (specific gravity)	2.64
Apparent Relative Density	Apparent Relative Density (specific gravity)	2.66
Absorption	%	0.32

3.2.6 Sieve analysis and particle size distribution of fine aggregates

Sieve analysis was conducted for fine aggregates of non-proprietary UHPC mixtures according to ASTM C136-19 Standard Test Method for Sieve Analysis of Fine and Coarse Aggregate (ASTM Committee 09, 2019). The calculated passing percentage of the fine aggregates is shown in Table 3-10, and the fineness modulus (FM) is measured to be 1.30. Also, the particle size distribution is shown in Figure 3-2.

Table 3-10 Passing percent of fine aggregates of non-proprietary mixture measured by sieve analysis

	Sieve	Passing percent (%)
Procedure	#4 (4.75 mm/ 0.19 in.)	100.00
	#8 (2.36 mm/ 0.093in.)	100.00
	#16 (1.18 mm/ 0.046 in.)	99.22
	#30 (0.6 mm/ 0.024in.)	94.00
	#50 (0.3 mm/ 0.012 in.)	71.10
	#100 (0.15 mm/ 0.0059 in.)	5.26
	#200 (75 μm/ 0.0030 in.)	0.07
	Pan	0.00
FM	1.30	

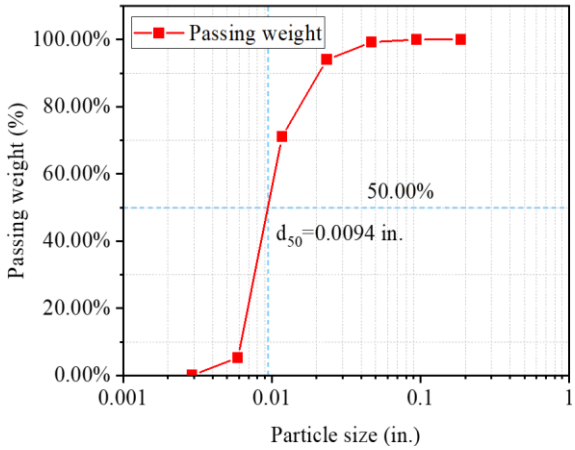

Figure 3-2 Particle size distribution of fine aggregate of non-proprietary mixture measured by sieve analysis

3.3 Mixing procedure for UHPC mixtures

The mixing procedures for the four UHPC mixtures were developed based on the mixture characteristics and admixture requirements of each mixture. For Mixture A, the dry-premix was first added to the mixer and dry mixed for 2 min to improve the uniformity of the powder components. Water and admixtures were then added, and the mixture was mixed for 8 min until a well-fluidized consistency was achieved. Steel fibers were gradually introduced into the fresh mixture to avoid fiber clumping, followed by an additional 5 min of mixing until the fibers were uniformly distributed. The static flow was then measured after 2 min of flow, with a target range of 216 to 222 mm (8.5 to 8.75 in.). After the target flowability was confirmed, the fresh UHPC was discharged and cast into the prepared specimens.

For Mixture B, the dry components were added sequentially into the mixer, including sand, dry-premix, and cement. Water was then added, followed by the four different chemical admixtures. After all liquid components and admixtures were introduced, the mixture was mixed for 6 min to allow the dry Mixtures to become fully wetted and to develop adequate workability. Steel fibers were then slowly added to the mixture, and mixing continued for an additional 10 min to ensure homogeneous fiber dispersion. The flowability of the fresh UHPC was evaluated after 2 min of flow, with an acceptable flow range of approximately 152 to 229 mm (6 to 9 in.). Once the required flowability and fiber distribution were achieved, the mixture was discharged and used for specimen casting.

For Mixture C, all liquid components were first combined to prepare the CNF suspension, including water, NiCal, and paste. The liquid suspension was mixed briefly before being added to the UHPC dry-premix. The dry-premix was placed into the mixer while the mixer was operating, and the CNF suspension was then gradually added at maximum mixing speed to promote uniform dispersion. The mixing time was recorded from the beginning of suspension addition. After 5 min of mixing, steel fibers were slowly introduced into the mixture. Mixing was continued for approximately 1 to 2 min after fiber addition, or until the total mixing time reached at least 10 min, whichever was longer. The flowability of the fresh UHPC was then tested, and the mixture was discharged for casting after the required consistency was obtained.

For Mixture D, sand and silica fume were first added to the mixer and dry mixed for 1 min. Approximately 30% of the batch water and 30% of the Glenium 7920 high-range water reducer were then added, followed by 1 min of mixing. Cement was subsequently introduced and mixed for another 1 min. The remaining water and V-MAR F100 rheology-modifying admixture were then added and mixed for 1 min. The remaining Glenium 7920 was added afterward, and mixing continued until the mixture turned

which refers to the transition from a dry or powdery consistency to a wet and flowable consistency. The mixture was then mixed for an additional 2 min to eliminate dry agglomerates. Grout flow was measured using a grout flow cone, with a target flow range of 229 to 279 mm (9 to 11 in.). If the flow was within the target range, steel fibers were added and mixed for 1 min. The fresh UHPC was then discharged, followed by additional flow testing and sample collection as needed.

4 Mechanical properties for UHPC mixtures

The testing matrix for measuring mechanical properties of four different UHPC mixtures is shown in Table 4-1.

Table 4-1 Testing matrix for mechanical property measurements

Mixture	Mechanical properties	Fiber orientation	No. of specimens
Mixture A	Compressive strength	-	6
	Tensile strength	-	3
	Flexural strength	Parallel distribution	3
		Random distribution	3
Mixture B	Compressive strength	-	6
	Tensile strength	-	3
	Flexural strength	Parallel distribution	3
		Random distribution	3
Mixture C	Compressive strength	-	6
	Tensile strength	-	3
	Flexural strength	Parallel distribution	3
		Random distribution	3
Mixture D	Compressive strength	-	6
	Tensile strength	-	3
	Flexural strength	Parallel distribution	3
		Random distribution	3

4.1 Compressive strength

The specimen preparation of compressive strength test was conducted according to ASTM C 39 Standard Test Method for Compressive Strength of Cylindrical Concrete Specimens (2021). Six 3 in. diameter × 6 in. height cylindrical specimens were cast for each mixture design, as shown in Figure 4-1, and compressive strength of each mixture was tested at 28 days of curing age (curing in air). Before the test, the loading surface and bearing surface of cylindrical specimens was polished. Forney machine was used to test the compressive strength of three mixtures, the loading rate is 1.0 ± 0.05 MPa/s [145 ± 7 psi/s] according to ASTM C 1856 Standard Practice for Fabricating and Testing Specimens of Ultra-High Performance Concrete (2017). The average compressive strength of three specimens was regarded as the compressive strength of the tested mixture.

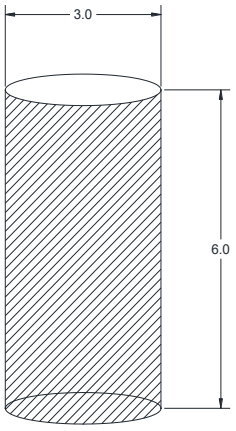

Figure 4-1 Specimen for compressive strength test (in.)

The compressive strength after 28 days curing for all four UHPC mixtures is shown in Table 4-2. All mixtures reached the minimum compressive strength of 18 ksi

Table 4-2 Compressive strength

Mixture	Compressive strength (ksi.)
Mixture A	24.152 ± 1.178
Mixture B	20.952 ± 0.370
Mixture C	21.441 ± 0.666
Mixture D	18.918 ± 0.588

4.2 Tensile strength

Tensile response of three mixtures was measured according to AASHTO T 397 Standard Method of Test for Uniaxial Tensile Response of Ultra-High Performance Concrete(AASHTO T397, 2022) , the test setup is shown in Figure 4-2 (a). Three prismatic specimens in size of 2 in. × 2 in. × 17 in. was cast for each mixture design, as shown in Figure 4-2 (b), and stress-strain curve with tensile strength of each mixture was tested at 28 days of curing age (cured in air). Before the test, the side surface of specimens was polished and bonded with aluminate plate with one taper end by epoxy. A clamping force was applied at the aluminate plates located at the side surfaces of the top and bottom regions of prismatic specimens. Then, the test setup is connected to MTS for tension with a loading rate of 0.00254 mm/s (0.0001 in./s). The average tensile strength of three specimens was regarded as the tensile strength of the tested mixture.

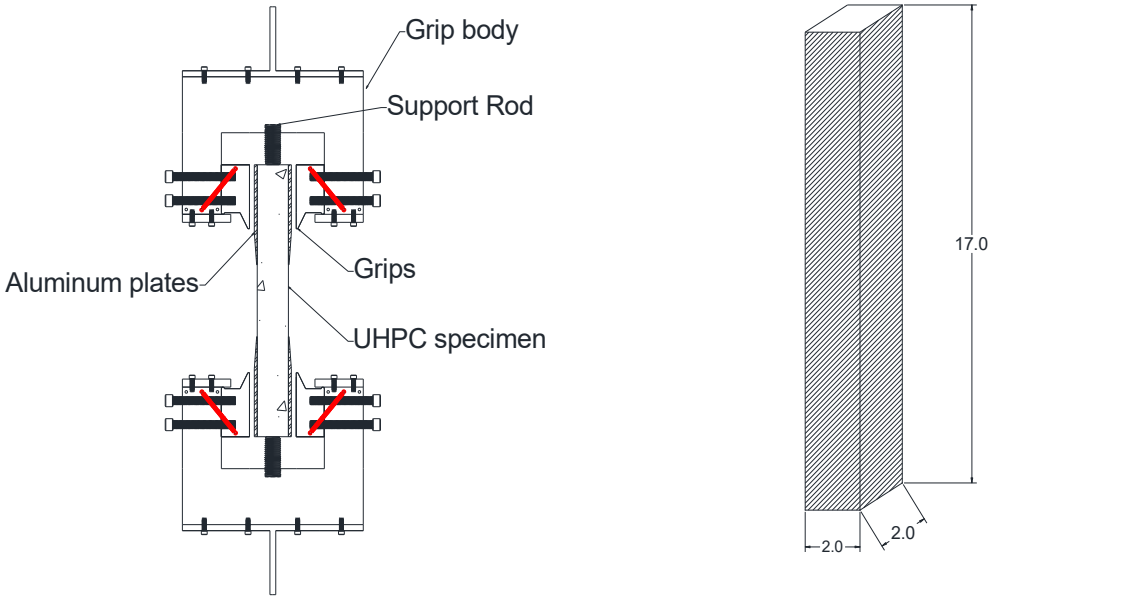

(a) Direct tension test setup (b) Specimen for tensile strength test

Figure 4-2 Tensile strength test setup (in.)

The peak tensile strength is shown in Table 4-3. Mixture A exhibits the highest compressive strength, and mixture C shows the highest tensile strength. However, Mixture D shows the highest ductility.

Table 4-3 Peak tensile strength

Mixture	Tensile strength (psi.)
Mixture A	1404.73 ± 186.39
Mixture B	1,201.27 ± 13.22
Mixture C	1490.73 ±90.30
Mixture D	1120.41 ± 80.51

The strain-stress curve for four UHPC mixtures is shown in Figure 4-3.

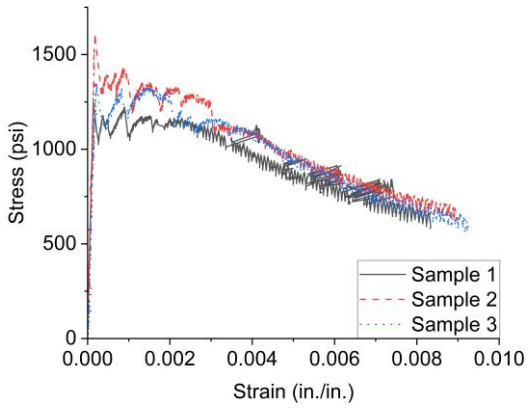

(a) Mixture A

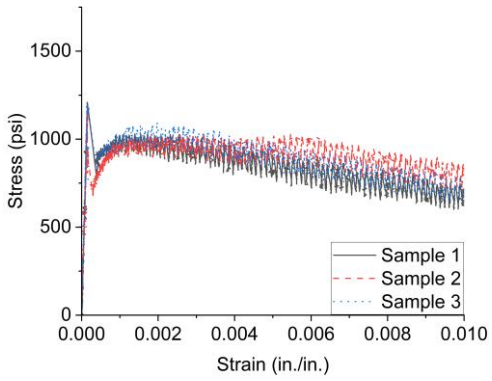

(b) Mixture B

Figure 4-3 Strain-stress curve for UHPC mixture under tension

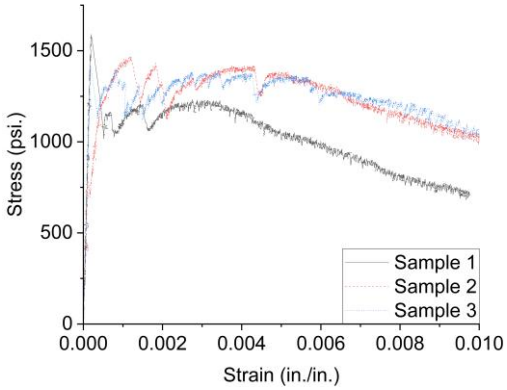

(c) Mixture C

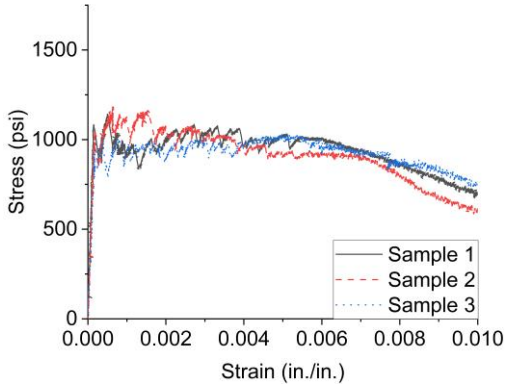

(d) Mixture D

Figure 4-3 Strain-stress curve for UHPC mixture under tension (continued)

4.3 Flexural strength

Flexural strength test of UHPC in three mixture designs were tested according to ASTM C1609 Standard Test Method for Flexural Performance of Fiber-Reinforced Concrete (Using Beam with Third-Point Loading) (2012). The test was conducted at the curing age of 28 days (cured in air) of each UHPC mixture. Six prismatic specimens as a batch in size of 6 in. × 6 in. × 21 in. was cast for each mixture design, as shown in Figure 4-4 (b). For each mixture, two casting methods were adopted to generate different distributions of steel fibers: parallel distribution and random distribution (Wille and Parra-

Montesinos,2012; Nguyen, Nguyen and Pansuk, 2017; Teng, Meng and Khayat, 2020), as shown in Figure 4-5. The load-deflection behavior of the specimens was measured by third point bending test, as shown in Figure 4-4 (a). and the average flexural strength was also be determined. Six specimens by two different casting methods were cast for each UHPC mixture.

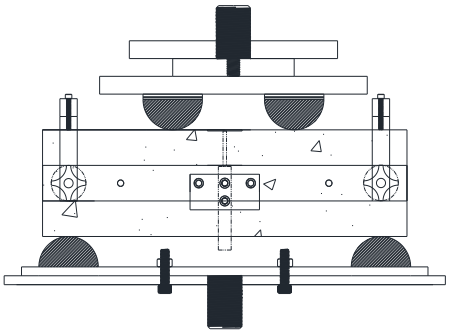

(a) Bending test setup

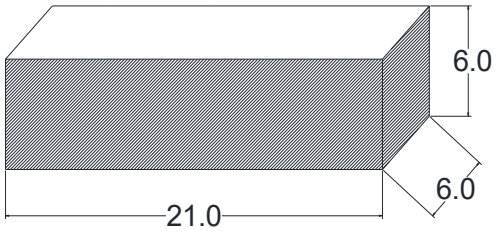

(b) Specimen size for bending test

Figure 4-4 Specimen for flexural strength test (in.)

(a) Casting at end for parallel distribution of steel fiber

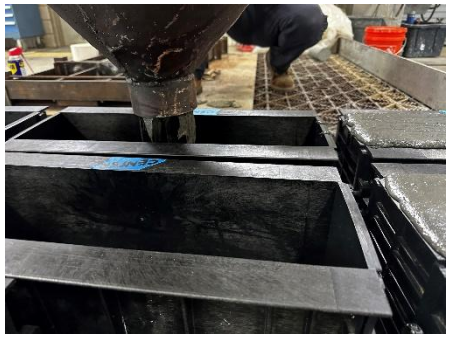

(b) Casting at center for random distribution of steel fiber

Figure 4-5 Different casting methods for various fiber orientation

Figure 4-6 shows the flexural strength–net deflection curves. Mixture A exhibited the highest flexural strength, while Mixture D demonstrated the greatest ductility, showing a trend similar to that observed for tensile strength. In addition, for all four UHPC mixtures, the specimens cast at the ends of the molds showed higher flexural strength and ductility. These results indicate that different casting methods can produce different crack patterns under similar stress conditions.

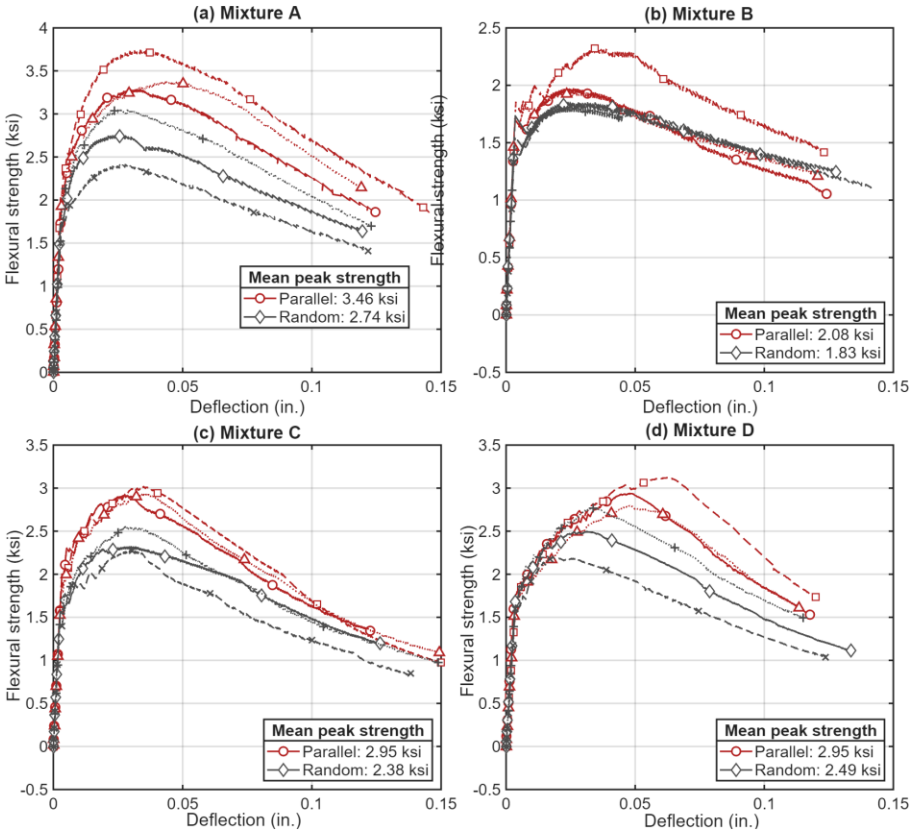

Figure 4-6 Strength-deflection curve for UHPC mixtures

5 Chloride penetration in cracked UHPC

To assess the durability of cracked UHPC, electrochemical migration was used to accelerate the chloride ingress in specimens. Cracked UHPC specimens were extracted from cracked UHPC beams. 6×6×21 in. beams were first cracked by means of a four-point bending test following ASTM C1609 (ASTM C1609, 2012) to generate multiple cracks, as shown in Figure 5-1 (a) and (c). Loading was performed at two displacement levels: displacement level 1 at 50% and displacement level 2 at 80% of the displacement at peak load achieved during the flexural strength testing, as shown in Figure 5-2. Four in. diameter (150 mm) x six in. (150mm) long cylindrical cores were extracted from each beam.

(a) Multiple cracks generation (b) Multiple cracks generation

Figure 5-1 Illustration of crack generation by bending test

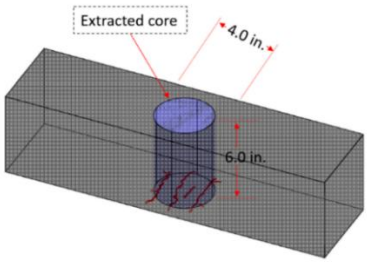

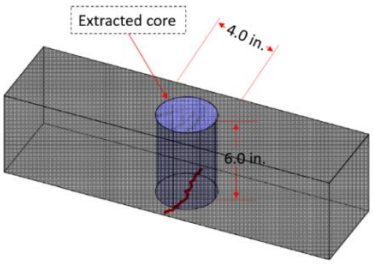

(c) Cored cylinders with multiple cracks (d) Cored cylinders with single crack

Figure 5-1 Illustration of crack generation by bending test (continued)

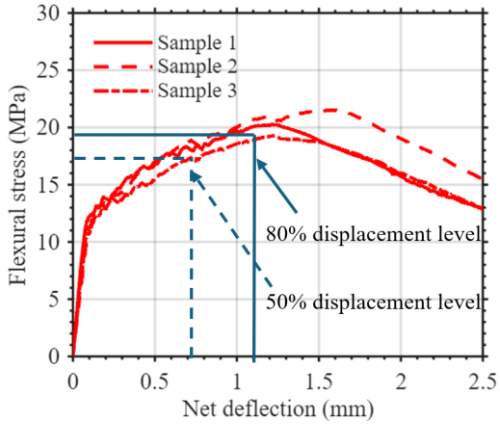

Figure 5-2 Example of force-displacement curve

5.1 Rapid chloride migration test

All samples were vacuum saturated by placing the samples under vacuum for 3 hours under a pressure of 1–5 kPa. A saturated calcium hydroxide solution was then introduced to the tank, with the vacuum pump running, until all samples were fully immersed in the solution. The vacuum was then maintained for an additional hour and subsequently released. Samples were kept in the solution for 18 ± 2 hours. Once vacuum saturation was completed, samples were removed from the saturation tank, rinsed with deionized (DI) water, and prepared for electrochemical chloride migration testing. The catholyte reservoir was filled with 12 liters of a 10% NaCl solution. The samples were then fitted in the 12-inch rubber sleeves and clamped from the top and bottom to ensure no leakage occurred. The sleeves were filled with a 0.3M NaOH solution. The sleeves were then placed on the plastic stand in the catholyte (NaCl solution) on top of a steel plate acting as the cathode. A steel disc, acting as the anode, was immersed in the anolyte (NaOH solution). The cathode was then connected to the negative terminal of the DC power supply and the anode was connected to the positive one. The power supply was turned on, and the current and temperatures of the catholyte and anolyte were recorded at the beginning and the end of the test. The voltage of the power supply was adjusted as needed to maintain 30V for the duration of all tests in this report. Figure 5-3 shows the schematic diagram of the testing setup.

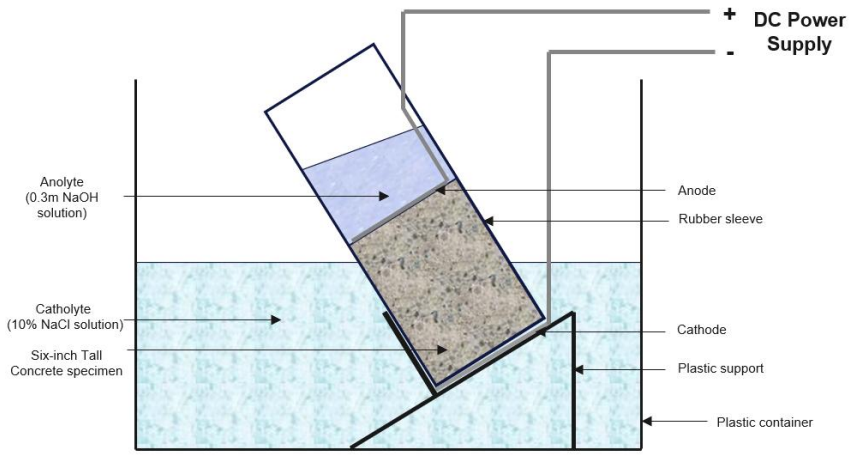

Figure 5-3 Schematic diagram of electrochemical chloride migration testing setup

5.1.1 Specimens preparation

Samples were labeled with the first letter representing the crack pattern (M for multiple and S for single), the second letter representing the fiber distribution (P for parallel and R for random), the third letter representing the mixture, the first number representing the displacement level, and the second number after the hyphen representing the sample number. For example, MPA1-1 would represent a multiple cracking pattern, parallel fiber orientation, from Mixture A, cracked under displacement level 1, with a sample number of 1. For each healing age and from each fiber distribution, one sample was cracked at each displacement level. All samples used for electrochemical migration testing were coated with a layer of epoxy on the sides before testing to prevent leakage from side cracks.

5.1.1.1 Specimen with multi-cracked pattern

Four curing durations were considered for each mixture with multiple cracks: 0, 1, 7, and 28 days to study the effect of self-healing with time on the durability of cracked UHPC. Samples were then prepared to measure chloride ingress using an electric migration test, following a modified version of NT Build 492 (NT BUILD 492 - NORDTEST, 1999). Samples to be tested at day 0, without any further curing after cracking, were prepared for testing, while the remaining samples with healing ages of 1, 7, and 28 days were put in the fog room on day 0 and cured following ASTM C192 (ASTM C192, 2014). Cracks in all samples were documented before any curing and after removal from the fog room, prior to testing, to monitor the change in cracks and their self-healing over time. Samples with a 6-inch (150mm) height were considered for testing instead of 2-inch (50mm) height to avoid leakage between solutions through cracks that were shown to extend up to 5 inches (125mm) deep. Additionally, to contain the larger concrete samples considered for the test, 12-inch (300mm) sleeves were used instead of the 6-inch (150mm) sleeves recommended by the testing standard.

Once the test duration was over, samples were removed from the rubber sleeves and cut in half using a dry-cutting saw. A wet-cutting saw was not used to prevent water from washing out the chlorides, which would have affected the test results. Grit and dust were removed from the surface with compressed air. The freshly cut surface was then sprayed with 0.1M silver nitrate solution for colorimetric analysis. Once the contrast was clear enough, images were taken of each sample with a ruler at the bottom of the image for scaling purposes. It was observed that chloride penetration was influenced by the crack depth, regardless of its width. Thus, penetration depth was not a suitable parameter for assessing the extent of chloride ingress in samples, and penetration area was considered instead. The images were then loaded into ImageJ, scaled, and the penetration area was measured.

5.1.1.2 Specimen with single-cracked pattern

A single cracking pattern was used to eliminate the effect of adjacent cracks, which cannot indicate the influence of crack width on chloride ingress. Since UHPC is known for its ductile behavior, generating single cracks in UHPC was challenging with a 2% fiber content by volume, due to the ductility induced by this fiber addition. Therefore, the fiber percentage was adjusted after several trials for each mixture to obtain samples with single cracks using a three-point bending test, as shown in Figure 5-1 (b) and (d). Four crack widths were targeted: 0.00197 in. (50 μm), 0.00394 in. (100 μm), 0.00787 in. (200 μm), and 0.01181 in. (300 μm). Triplicates of each crack width were tested after 0, 28, and 91 days of curing after cracking to assess the influence of self-healing. Cracks were monitored before any further curing, at day 0, and immediately after removal from the fog room on the day of testing.

A modified electrochemical chloride migration test was run for samples following the previously adopted modified version of NT Build 492 (NT BUILD 492 - NORDTEST, 1999) test method. Six-inch (150mm) samples were considered for testing instead of two-inch ones, as the depth of the cracks in the samples reached up to 5 in. (125mm). Additionally, the testing duration was fixed at 24 hours, regardless of the current measurement at the beginning of the test. Once the testing duration was over, the samples were dry-cut and sprayed with a 0.1M silver nitrate solution for colorimetric analysis. Images of the cut and sprayed surface were taken, and the penetration area was measured in ImageJ software. Further analysis was performed on each image by cropping the cracked area and converting it to a grayscale image, as presented in Figure 5-4. Based on the grayscale value that separated the crack from the uncracked matrix, the width of the penetration was measured along the depth, and the variation of the width of penetration as a function of depth was plotted to comprehend the influence of self-healing on the width of penetration. An example of the image analysis process is depicted in Figure 5-4 for sample RSA100-day0.

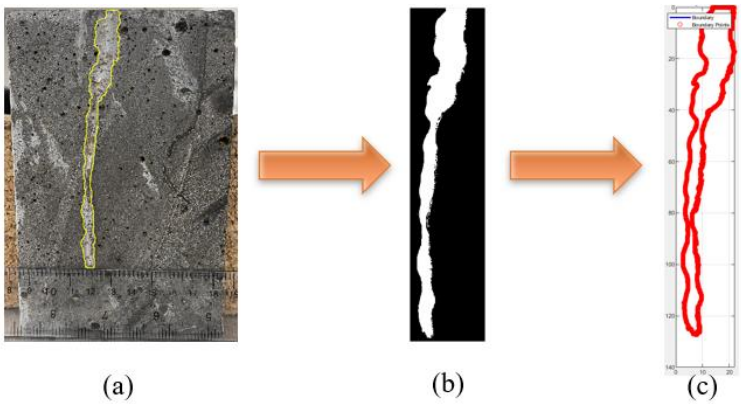

Figure 5-4 (a) cut and sprayed surface with chloride penetration area marked in ImageJ, (b) grayscale image of marked penetration area, (c) width and depth of marked penetration area calculated in MATLAB

5.1.2 Testing results

5.1.2.1 Electrochemical migration testing for samples with multiple cracks

5.1.2.1.1 Results of Mixture A

Self-healing monitoring results showed that cracks in the range of 0.0079 in. (20 μm) showed surface healing after 24 hours of curing, cracks in the range of 0.00197 in. (50 μm)seemed to be healed on the surface after 7 days of curing, and cracks in the range of 0.00394 in. (100 μm) seemed to be healed on the

surface after 28 days of curing. An example of the images presenting a comparison of the cracks at day 0 and after curing is illustrated in Figure 5-5.

An example of a scaled and marked sample for chloride penetration is presented in Figure 5-6. The list of samples to be tested, with their corresponding curing periods, number of cracks, maximum crack width, and chloride penetration area, is tabulated in Table 5-1. Crack widths were measured along the line in the center of the sample, where the samples were cut after the test was completed. The chloride penetration area for each sample, along with the maximum crack width, is illustrated in Figure 5-7.

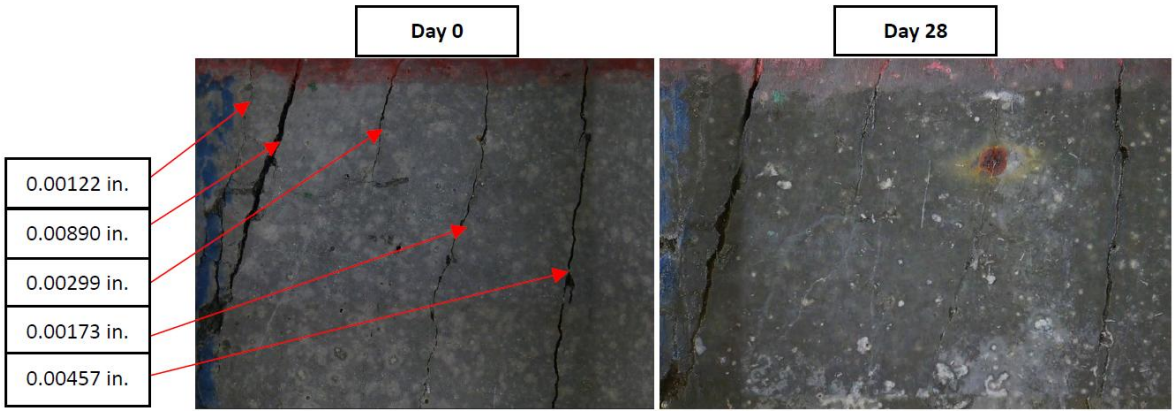

Figure 5-5 Cracks before and after being cured for 28 days of sample MPA1-4

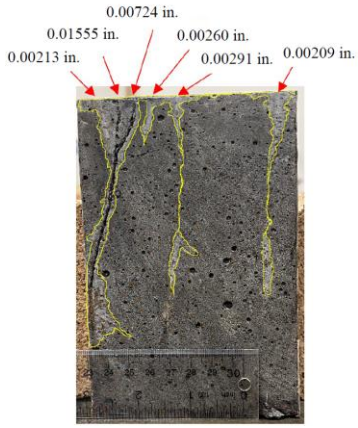

Figure 5-6 Cut and sprayed sample MPA2-4 with yellow marked area being the chloride penetration area after scaling in ImageJ

Table 5-1 Chloride penetration areas for samples of Mixture A with different crack widths at different healing ages

Sample	Curing Period (days)	Number of Cracks	Max Crack Width in. (μm)	Penetration Area in^2 (mm^2)
MPA1-1	0	4	0.00571 (145)	4.893 (3157)
MPA2-1	0	3	0.01839 (467)	2.825 (1823)
MRA1-1	0	5	0.01055 (268)	1.541 (994)

Sample	Curing Period (days)	Number of Cracks	Max Crack Width in. (μm)	Penetration Area in^2 (mm^2)
MRA2-1	0	3	0.00594 (151)	1.772 (1143)
MPA1-2	1	2	0.01866 (474)	3.013 (1944)
MPA2-2	1	1	0.06417 (1630)	2.872 (1853)
MRA1-2	1	1	0.02520 (640)	1.666 (1075)
MRA2-2	1	2	0.02591 (658)	3.215 (2074)
MPA1-3	7	3	0.00882 (224)	1.431 (923)
MPA2-3	7	1	0.04449 (1130)	1.742 (1124)
MRA1-3	7	3	0.01646 (418)	1.505 (971)
MRA2-3	7	1	0.06665 (1693)	2.171 (1401)
MPA1-4	28	7	0.00898 (228)	1.761 (1136)
MPA2-4	28	6	0.01555 (395)	2.891 (1865)
MRA1-4	28	2	0.01969 (500)	1.291 (833)
MRA2-4	28	3	0.01039 (264)	0.474 (306)

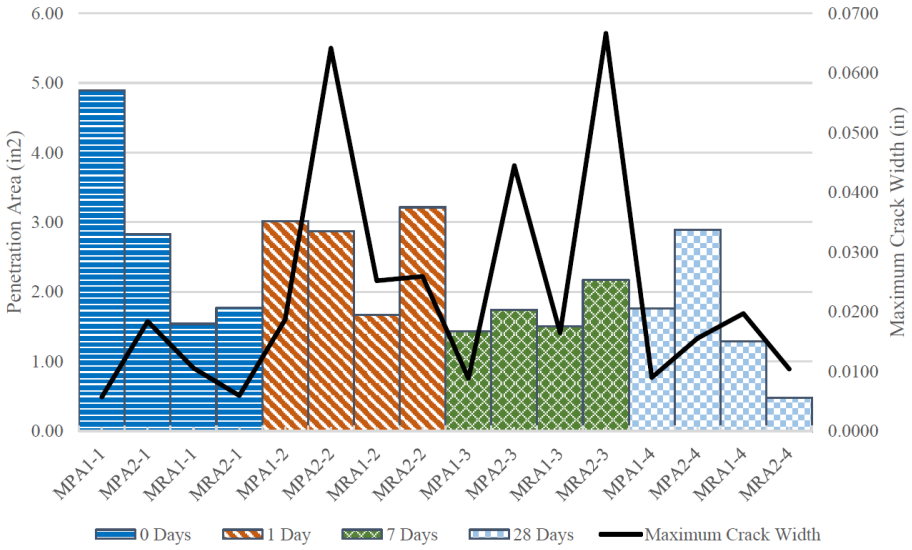

Figure 5-7 Chart showing the penetration area as a function of the curing age and the maximum crack width of Mixture A

The obtained results show that samples with the same maximum crack width exhibit wide variability in penetration areas, with no correlation between the two parameters or a discernible trend observed. This indicates that the crack width does not represent a sole indication of the extent of chloride penetration. Several additional factors, including crack width, length, tortuosity, and the distance between adjacent cracks, influence chloride penetration in UHPC. Additionally, cracks that appeared to be healed on the surface still let chlorides in. This can be justified by the low permeability of the substances filling the

cracks compared to that of the uncracked UHPC matrix, in addition to the extended test duration of 10 days, which is intense.

5.1.2.1.2 Results of Mixture B

The same testing procedure followed for Mixtures A was applied to Mixture B, except that the voltage was only applied to the specimens for 24 hours instead of 10 days. Cracks were monitored before and after curing. Minimal self-healing occurred in this mixture because of the limited presence of smaller crack widths that could heal within the specified curing durations. The same procedure was followed after the test was terminated for cutting, spraying, and analyzing the chloride penetration area. The list of samples to be tested, with their corresponding curing periods, number of cracks, maximum crack width, and chloride penetration area, are tabulated in Table 5-2. Crack widths were measured along the central line of the sample. chloride penetration area for each sample, along with the maximum crack width, is shown in Figure 5-8.

Table 5-2 Chloride penetration areas for samples of Mixture B with different crack widths at different healing ages

Sample	Curing Period (days)	Number of Cracks	Max. Crack Width in. (μm)	Penetration Area in^2 (mm^2)
MPB1-1	0	2	0.00717 (182)	2.579 (1664)
MPB2-1	0	2	0.02012 (511)	5.575 (3597)
MRB1-1	0	2	0.01398 (355)	4.256 (2746)
MRB2-1	0	1	0.01685 (428)	3.971 (2562)
MPB1-2	1	3	0.00799 (203)	3.447 (2224)
MPB2-2	1	1	0.03571 (907)	2.829 (1825)
MRB1-2	1	1	0.01236 (314)	3.974 (2564)
MRB2-2	1	1	0.02819 (716)	1.958 (1263)
MPB1-3	7	1	0.00843 (214)	1.586 (1023)
MPB2-3	7	7	0.00244 (62)	2.072 (1337)
MRB1-3	7	1	0.01382 (351)	2.024 (1306)
MRB2-3	7	1	0.01783 (453)	2.078 (1341)
MPB1-4	28	2	0.00799 (203)	2.272 (1466)
MPB2-4	28	1	0.01835 (466)	2.353 (1518)
MRB1-4	28	1	0.01138 (289)	1.048 (676)
MRB2-4	28	2	0.01260 (320)	0.769 (496)

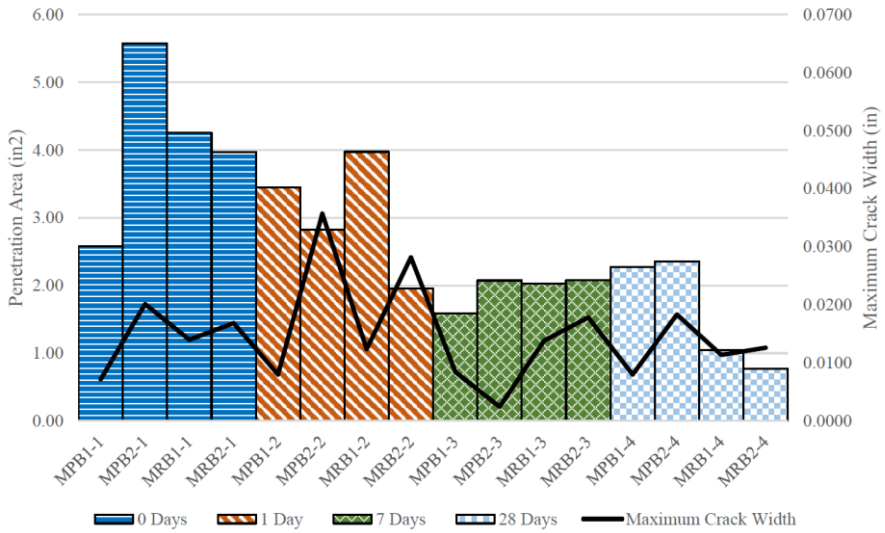

Figure 5-8 Chart showing the penetration area as a function of the curing age and the maximum crack width of Mixture B

To better understand the results, the cracks were divided into width ranges from 0 – 0.00197 in. (0 – 50 μm), 0.00394 – 0.00787 in. (100 – 200 μm), 0.00787 – 0.01181 in. (200 – 300 μm), 0.001181 – 0.01575 in. (300 – 400 μm), and larger than 0.01575 in. (400 μm). Only one crack fell within the 0.00197 – 0.00394 in. (50 – 100 μm) range, so it was not considered as it did not serve the purpose of comparison. The normalized penetration area was considered for comparison, which was calculated as the ratio of the penetration area to the penetration depth. The charts of normalized penetration area versus the crack width are represented in Figure 5-9 through Figure 5-13.

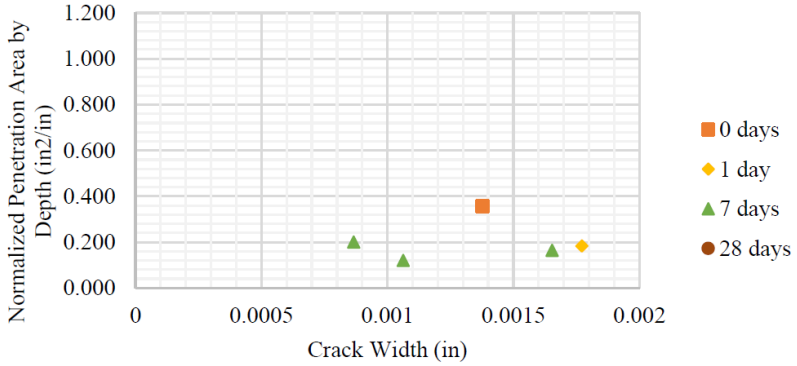

Figure 5-9 Penetration area normalized by penetration depth as a function of crack width for crack widths between 0 and 0.00197 in. (0 and 50μm)

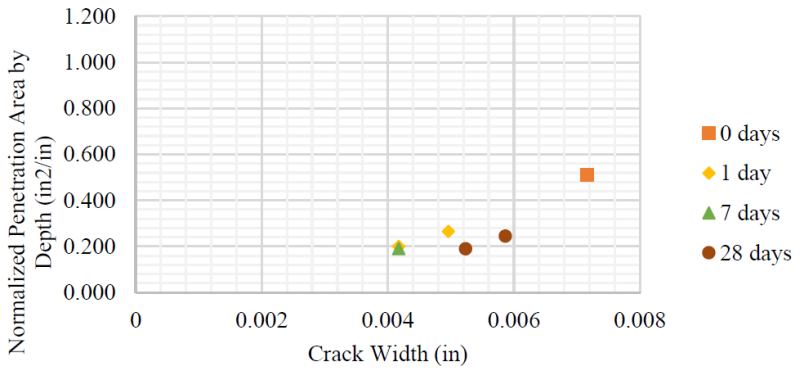

Figure 5-10 Penetration area normalized by penetration depth as a function of crack width for crack widths between 0.00394 and 0.00787 in. (100 and 200µm)

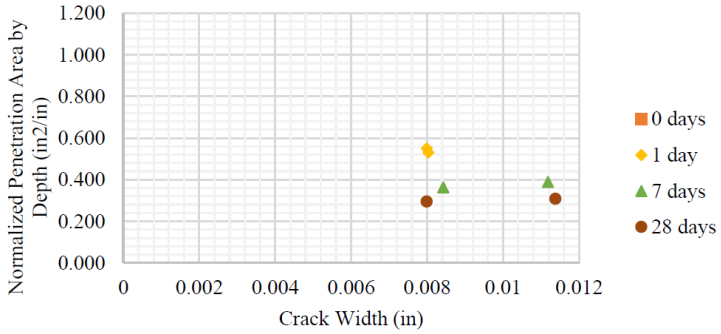

Figure 5-11 Penetration area normalized by penetration depth as a function of crack width for crack widths between 0.00787 and 0.01181 in. (200 and 300µm)

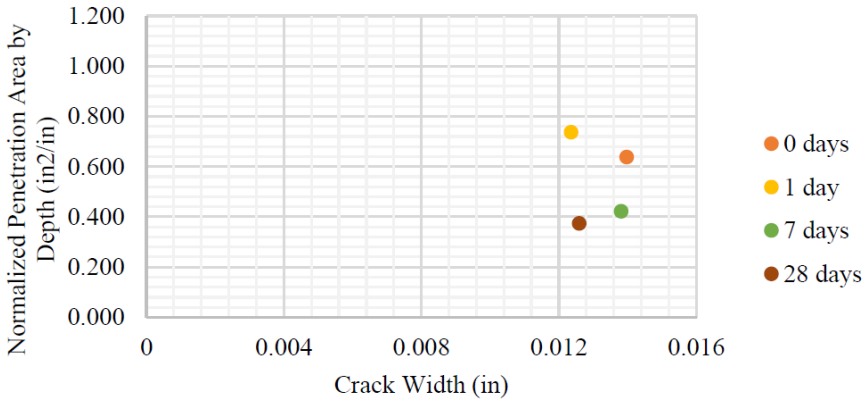

Figure 5-12 Penetration area normalized by penetration depth as a function of crack width for crack widths between 0.001181 and 0.01575 in. (300 and 400µm)

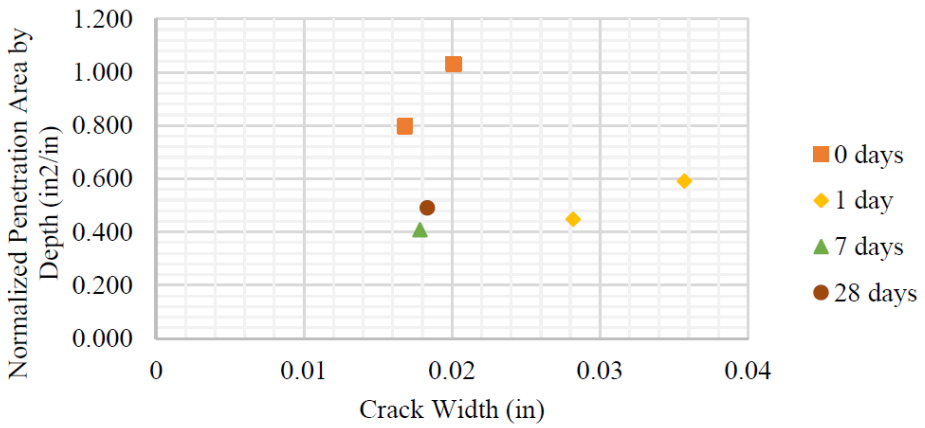

Figure 5-13 Penetration area normalized by penetration depth as a function of crack width for crack widths greater than 0.01575 in. (400µm)

The following results showed that for smaller cracks, with crack widths less than 0.00394 in. (100 µm), increased curing durations reduced the normalized penetration area with depth due to self-healing. Also, the penetration area was smaller for smaller crack widths falling in the same cack width range. The effect of self-healing on larger cracks was not obvious, as these cracks did not exhibit surface healing within the adopted curing durations and required a significantly longer time for healing.

5.1.2.1.3 Results of Mixture C

The same procedure previously adopted for all Mixtures was considered for Mixture C. The testing duration was 24 hours. Self-healing observations were similar to those of Mixtures A. The list of samples to be tested, with their corresponding curing periods, number of cracks, maximum crack width, and chloride penetration area, are tabulated in Table 5-3. Crack widths were measured along the central line of the sample, at which the sample was cut after the voltage was removed. The chloride penetration area for each sample, along with the maximum crack width, is illustrated in Figure 5-14.

Table 5-3 Chloride penetration areas of Mixture C with different crack widths at different healing ages

Sample	Curing Period (days)	Number of Cracks	Max Crack Width in. (µm)	Penetration Area in^2 (mm^2)
MPC1-1	0	2	0.00504 (128)	1.641 (1059)
MPC2-1	0	5	0.00319 (81)	2.379 (1535)
MRC1-1	0	2	0.00303 (77)	1.100 (710)
MRC2-1	0	1	0.01417 (360)	4.667 (3011)
MPC1-2	1	2	0.01000 (254)	1.922 (1240)
MPC2-2	1	2	0.00992 (252)	4.073 (2628)
MRC1-2	1	3	0.00579 (147)	2.567 (1656)
MRC2-2	1	5	0.00362 (92)	2.040 (1316)
MPC1-3	7	3	0.00150 (38)	1.020 (658)
MPC2-3	7	6	0.00587 (149)	1.252 (808)

Sample	Curing Period (days)	Number of Cracks	Max Crack Width in. (μm)	Penetration Area in^2 (mm^2)
MRC1-3	7	2	0.00571 (145)	1.231 (794)
MRC2-3	7	4	0.00610 (155)	2.219 (1432)
MPC1-4	28	2	0.00079 (20)	0.369 (238)
MPC2-4	28	3	0.00709 (180)	3.493 (2254)
MRC1-4	28	1	0.00894 (227)	2.728 (1760)
MRC2-4	28	9	0.00150 (38)	1.711 (1104)

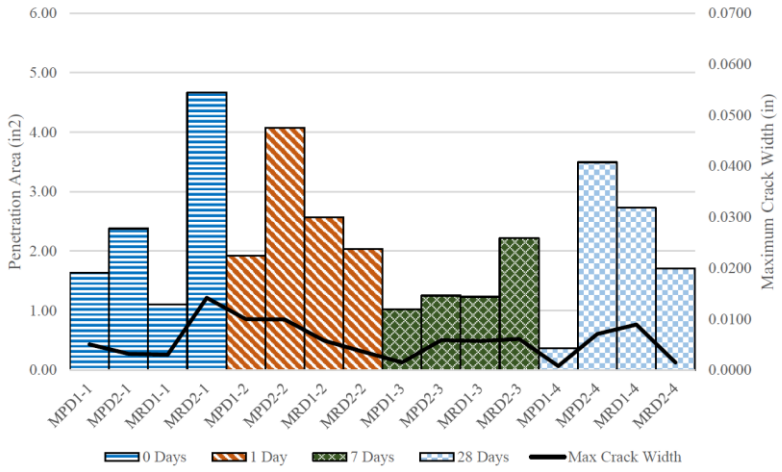

Figure 5-14 Chart showing the penetration area as a function of the curing age and the maximum crack width of Mixture C

Crack widths alone also did not correlate well with the area of penetration. Also, samples with cracks that appeared to be healed on the surface presented chloride penetration, but with a narrower width. To better represent this trend, samples with 1 to 2 cracks in the same penetration area were considered and divided into four groups: 0 to 0.00197 in. (0 to 50 μm), 0.00197 to 0.00394 in. (50 to 100 μm), 0.00394 to 0.00787 in. (100 to 200 μm), and greater than 000787 in. (400 μm). The penetration area of each group was normalized by the penetration depth. The curves are represented in Figure 5-15 through Figure 5-18.

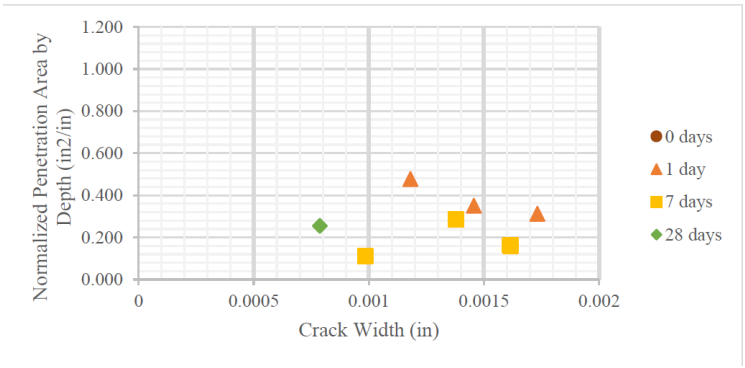

Figure 5-15 Penetration area normalized by penetration depth as a function of crack width for crack widths between 0 and 0.00197 in. (0 and 50μm)

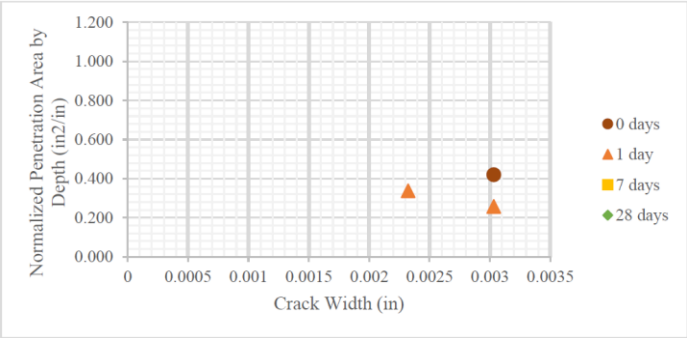

Figure 5-16 Penetration area normalized by penetration depth as a function of crack width for crack widths between 0.00197 in. and 0.00384 in. (50 and 100µm)

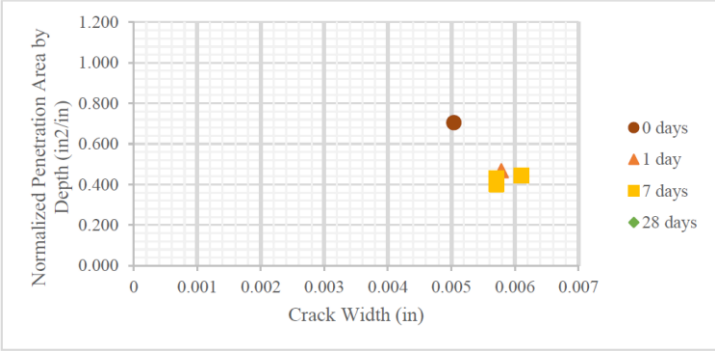

Figure 5-17 Penetration area normalized by penetration depth as a function of crack width for crack widths between 0.00384 and 0.00787 in. (100 and 200 µm)

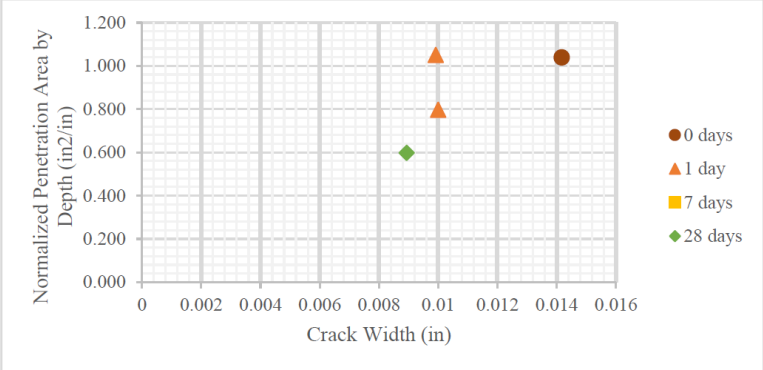

Figure 5-18 Penetration area normalized by penetration depth as a function of crack width for crack widths greater than 0.00787 in. (200 µm)

Mixture C also showed that the penetration depth was controlled by the crack depth, which was not related to the crack width. The penetration area normalized by the penetration depth was reduced due to self-healing, which had a more pronounced effect on smaller cracks. Self-healing, in this case, reduced chloride penetration but did not prevent it, as the products accumulated in the cracks due to healing are not as impermeable as the uncracked UHPC matrix.

5.1.2.1.4 Results of Mixture D

The same testing procedure was followed for samples from Mixture D, with a 10-day testing duration and a 30V voltage from a DC power supply. Once the test duration was over, samples were also dry-cut and sprayed with 0.1M silver nitrate solution. Images of the cut and sprayed samples were taken and uploaded into Image J for scaling and measuring the chloride penetration area. Self-healing observations were similar to those of Mixture A. The list of samples to be tested, with their corresponding curing periods, number of cracks, maximum crack width, and chloride penetration area, is tabulated in Table 5-4. Crack widths were measured in the same way as Mixture A. The chloride penetration area for each sample, along with the maximum crack width, is shown in Figure 5-19.

Table 5-4 Chloride penetration areas for samples of Mixture D with different crack widths at different healing ages

Sample	Curing Period (days)	Number of Cracks	Max Crack Width in. (μm)	Penetration Area in^2 (mm^2)
MPD1-1	0	9	0.00736 (187)	3.241 (2091)
MPD2-1	0	10	0.00350 (89)	4.272 (2756)
MRD1-1	0	4	0.00374 (95)	1.917 (1237)
MRD2-1	0	3	0.01366 (347)	2.681 (1730)
MPD1-2	1	8	0.00673 (171)	2.720 (1755)
MPD2-2	1	13	0.00382 (97)	3.594 (2319)
MRD1-2	1	2	0.00472 (120)	1.457 (940)
MRD2-2	1	3	0.00413 (105)	2.418 (1560)
MPD1-3	7	12	0.00409 (104)	2.846 (1836)
MPD2-3	7	12	0.00256 (65)	4.740 (3058)
MRD1-3	7	3	0.00610 (155)	2.481 (1601)
MRD2-3	7	4	0.00531 (135)	4.484 (2893)
MPD1-4	28	9	0.00264 (67)	2.545 (1642)
MPD2-4	28	12	0.03287 (835)	4.265 (2752)
MRD1-4	28	8	0.01339 (340)	2.734 (1764)
MRD2-4	28	3	0.02075 (527)	2.202 (1421)

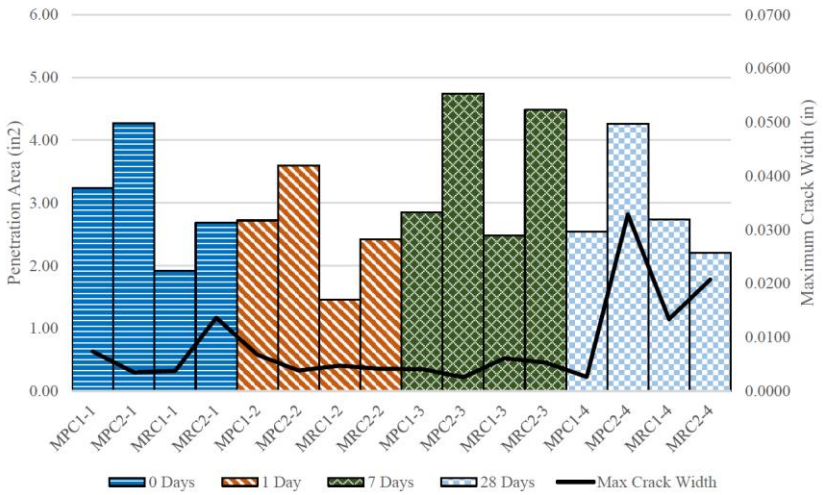

Figure 5-19 Chart showing the penetration area as a function of the curing age and the maximum crack width of Mixture D

The results of Mixture D also did not present a clear correlation or trend between the penetration area and the maximum crack width. As concluded for Mixture A, several other factors also influenced the extent of chloride penetration, including the number and length of cracks, as well as the distance between adjacent cracks. Additionally, cracks that exhibited surface healing still allowed chloride penetration. This may be a result of the increased permeability that the Mixtures filling the cracks possess compared to the uncracked UHPC matrix. Additionally, it may be due to the intense duration of testing, which is 10 days. For the remaining Mixtures, the testing duration was reduced.

5.1.2.2 Electrochemical chloride migration testing for samples with single cracks

5.1.2.2.1 Results of Mixture A

Samples with crack widths of 0.00197 in. (50 μm) showed visual complete surface healing after 91 days of curing, while those with larger cracks presented partial self-healing, with the efficiency decreasing with increasing crack widths. After the test was over, samples tested after 0 and 91 days of curing after being cracked were cut right after the voltage was stopped, while those tested after 28 days of curing were cut after 24 hours of the test's end date. For those samples, the white discoloration marking the presence of chlorides on the sample was lower, and the contrast was lower compared to those cut right away. This may be explained by the chloride-binding phenomenon, which allows free chlorides to bind to tricalcium aluminate in the matrix to form Friedel's salt. The absence of free chlorides to react with silver nitrate can result in a lower amount of silver chloride formed on the surface, which is responsible for the white discoloration marking the presence of chlorides. The chloride penetration area for each sample is presented in Table 5-5.

Table 5-5 Chloride penetration area for samples with single cracks from Mixture A with different crack widths at different curing ages

Crack Width in. (μm)	Curing Period (days)	Penetration Area in^2 (mm^2)
0.00197 (50)	0	0.367 (237)
0.00394 (100)	0	1.226 (791)
0.00787 (200)	0	1.333 (860)

Crack Width in. (µm)	Curing Period (days)	Penetration Area in^2 (mm^2)
0.01181 (300)	0	1.522 (982)
0.00197 (50)	28	0.232 (150)
0.00394 (100)	28	0.626 (404)
0.00787 (200)	28	1.026 (662)
0.01181 (300)	28	0.879 (567)
0.00197 (50)	91	0.527 (340)
0.00394 (100)	91	0.931 (601)
0.00787 (200)	91	1.751 (1130)
0.01181 (300)	91	1.832 (1182)

To better understand the influence of self-healing on the penetration area properties, the width versus depth at different curing ages was plotted for each crack width. The curves are represented in Figure 5-20 through Figure 5-23.

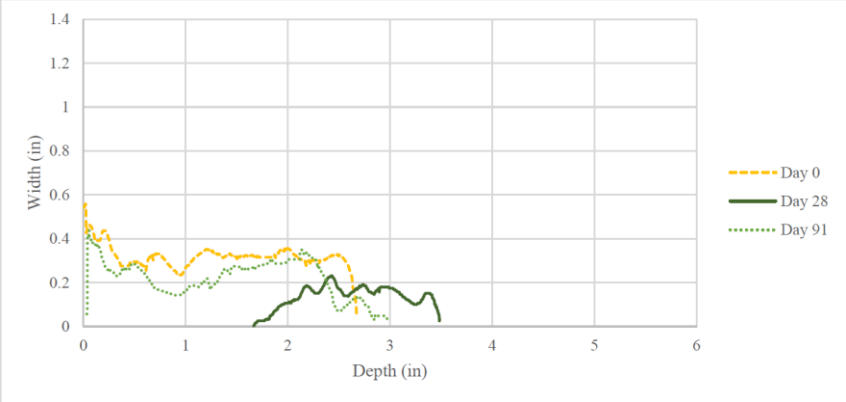

Figure 5-20 Width of chloride penetration as a function of its depth for Mixture A with a crack width of 0.00197 in. (50µm) at different healing ages

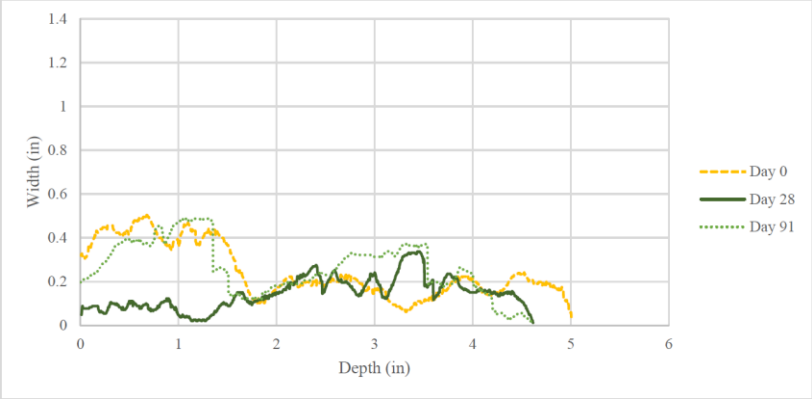

Figure 5-21 Width of chloride penetration as a function of its depth for Mixture A with a crack width of 0.00384 in. (100µm) at different healing ages

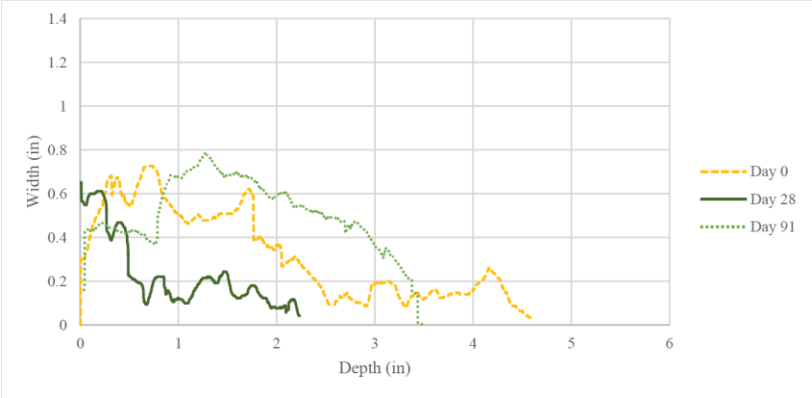

Figure 5-22 Width of chloride penetration as a function of its depth for Mixture A with a crack width of 0.00787 in. (200 µm) at different healing ages

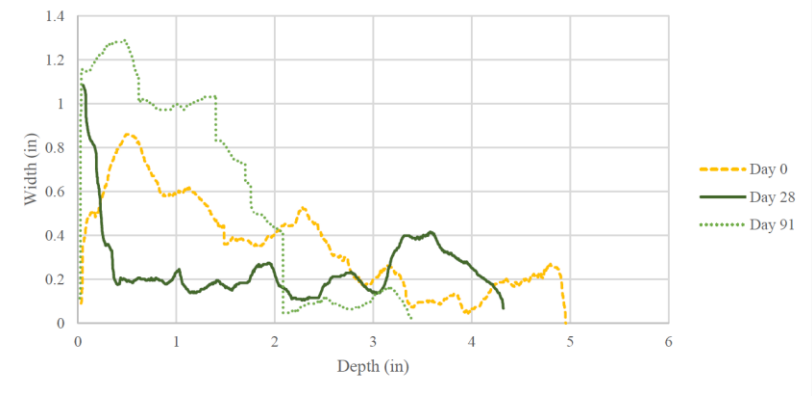

Figure 5-23 Width of chloride penetration as a function of its depth for Mixture A with a crack width of 0.01181 in. (300µm) at different healing ages

The results at 28 days of curing were not considered in the analysis due to the loss of contrast in the samples caused by the delayed cutting and potential chloride binding.

By analyzing the relationship between the width and depth of penetration, it was observed that the penetration width decreased as the depth increased in most samples, which varied in crack width and had

been cured for different durations. Increased crack widths resulted in a larger penetration width at the cracks, which is attributed to crack webbing caused by the higher damage levels required to achieve these larger widths. For the 0.00197 in. (50 μm) crack width, the penetration width at 91 days of curing was lower than at 0 days, with the reduction becoming more pronounced along the depth, likely due to the self-healing of the crack during curing. Exposure to moisture facilitated crack healing over time, thereby limiting chloride penetration across the crack. This comparison was more challenging for larger cracks, as they require a relatively longer curing period to achieve significant healing. Additionally, this may be related to the lower fiber content present in those samples. Due to the decreased ductility, cracks might be wider at greater depths, making it more difficult for healing products to fill them.

5.1.2.2.2 Results of Mixture D

Samples tested at day 0 did not present any discoloration after being cut and sprayed with the silver nitrate solution at the end of the test. A power outage may have occurred during testing, causing this issue. For this reason, samples from day 0 were excluded from further analysis, and only the results from day 28 and day 91 were analyzed and compared. Self-healing observations were similar to those of Mixture A, even at 28 days of curing. Samples with crack widths of 0.00197 in. (50 μm) presented complete surface healing after 28 and 91 days of curing. Samples tested after 28 and 91 days of curing, after being cracked, were cut immediately after the test was completed. Table 5-6 represents the penetration area for each crack width at the two considered healing ages.

Table 5-6 Chloride penetration area for samples with single cracks from Mixture D with different crack widths at different curing ages

Crack Width in. (μm)	Curing Period (days)	Penetration Area in^2 (mm^2)
0.00197 (50)	28	0.296 (191)
0.00394 (100)	28	1.203 (776)
0.00787 (200)	28	2.249 (1451)
0.01181 (300)	28	2.091 (1349)
0.00197 (50)	91	0.609 (393)
0.00394 (100)	91	1.586 (1023)
0.00787 (200)	91	1.634 (1054)
0.00181 (300)	91	2.576 (1662)

To better understand the influence of self-healing on the penetration area properties, the width versus depth at different curing ages was plotted for each crack width. The curves are represented in Figure 5-24 through Figure 5-27.

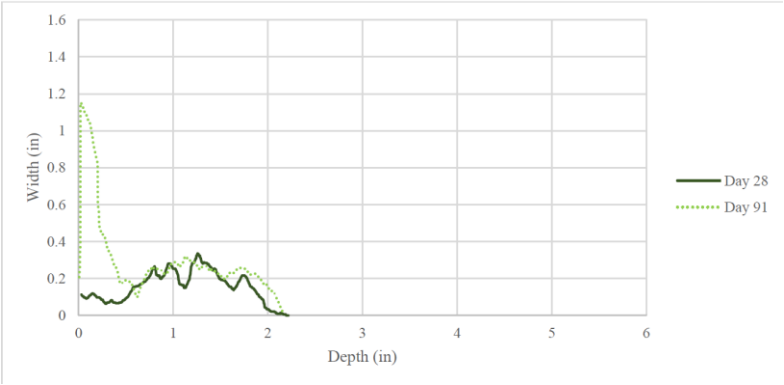

Figure 5-24 Width of chloride penetration as a function of its depth for Mixture D with a crack width of 0.00197 in. (50 μm) at different healing ages

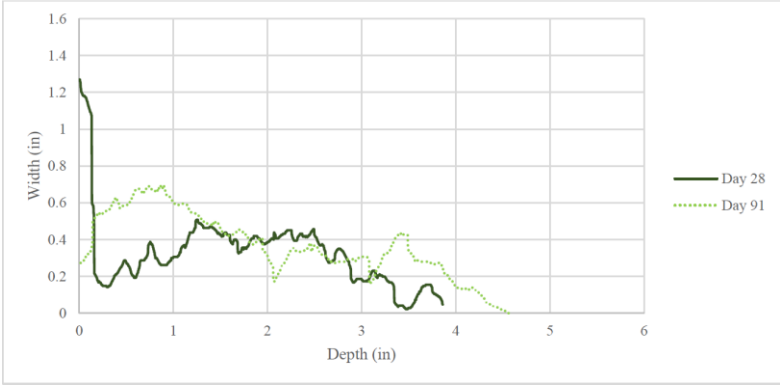

Figure 5-25 Width of chloride penetration as a function of its depth for Mixture D with a crack width of 0.00384 in. (100 μm) at different healing ages

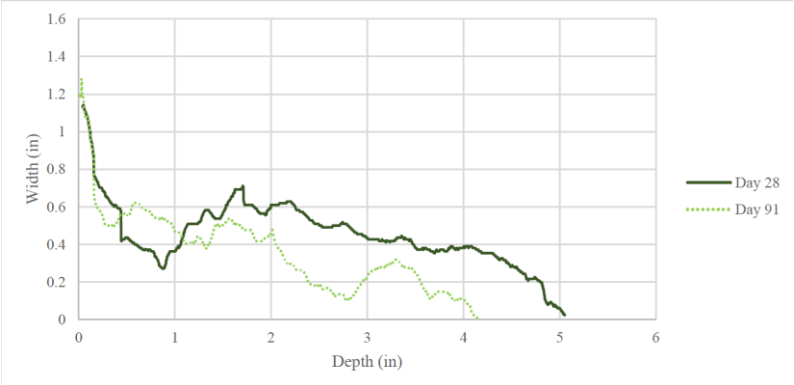

Figure 5-26 Width of chloride penetration as a function of its depth for Mixture D with a crack width of 0.00787 in. (200 μm) at different healing ages

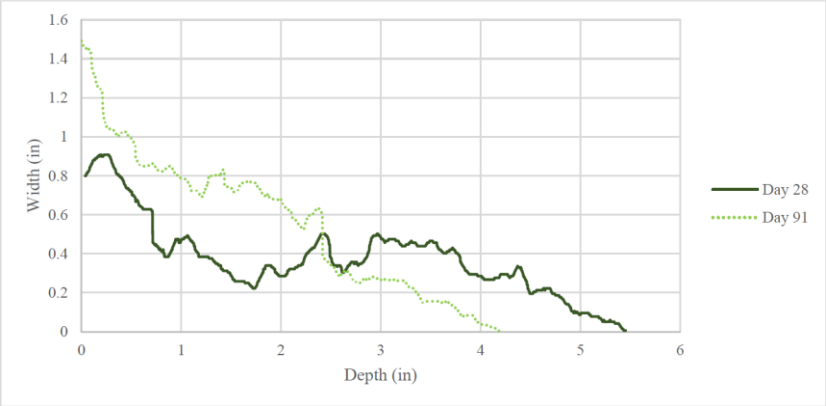

Figure 5-27 Width of chloride penetration as a function of its depth for Mixture D with a crack width of 0.01181 in. (300 μm) at different healing ages

Upon analyzing the results obtained for Mixture D with single cracks, the penetration area for both curing ages generally increased with increasing crack widths, regardless of the curing duration. Longer curing durations did not result in a significantly lower penetration area; even for small cracks, the penetration widths were similar for both 28 and 91 days of curing.

5.1.3 Summary

Based on the results of the electric chloride migration testing performed on samples with single and multiple cracks, the following conclusions can be drawn:

1. Chloride penetration is affected by the geometric properties of the crack, not just the crack width.
2. Penetration was restricted to the cracked region and not observed in the uncracked matrix.
3. Samples with multiple cracks exhibited increased chloride penetration, with closely spaced cracks resulting in overlapping penetration zones that expanded the affected area.
4. Surface-healed cracks reduced chloride ingress but did not prevent it. This is likely due to the nature of the products filling the cracks, which is not as impermeable as the uncracked UHPC matrix.
5. The decreased fiber content in samples with single cracks may be the reason for the reduced self-healing efficiency.
6. For samples with single cracks, larger cracks resulted in wider penetration widths, which may be attributed to crack webbing.

5.2 Bulk diffusion test

The chloride content of cracked UHPC, including Mixture A, Mixture B, Mixture C, and a non-proprietary Mixture D, was evaluated using a titration test after around 1 year of exposure to a 16.5 wt.% sodium chloride solution. After crack generation, 4 × 6 in. (102 × 152 mm) cylindrical specimens with a multiple-cracked pattern were cored from regions exhibiting the greatest number of cracks, while 4 × 6 in. (102 × 152 mm) cylindrical specimens with a single-cracked pattern were cored from regions with the longest surface crack length.

5.2.1 Specimens' preparation

The crack generation process is similar to the process illustrated in section 5.1.1. Mixture A and Mixture D were used for single-crack generation, and the multi-cracked pattern was generated for four different UHPC mixtures.

Samples were labeled with the first letter representing the bulk diffusion test (B for bulk diffusion test), the second letter representing the crack pattern (M for multiple and S for single), the third letter representing the mixture, the first number representing the displacement level for multi-cracked specimen and group number for single-cracked specimens. For example, BSA1 would represent a single-cracked Mixture A specimens with crack width in group 1 exposed to bulk diffusion test; and BMB1 would represent a multi-cracked Mixture B specimens cracked by displacement level 1 exposed to bulk diffusion test. The crack profiles for cracked UHPC are summarized in Table 5.7 and Table 5.8 for single-cracked and multiple-cracked specimens, respectively. Also, uncracked specimens were extracted from uncracked regions of the cracked UHPC beams.

Table 5-7 Crack profile for specimen with single crack pattern

Mixture	Crack width (μm/ in.)			
Mixture A	63/ 0.00248	102/ 0.00402	198/ 0.00780	414/ 0.01630
Mixture D	137/ 0.00539	240/ 0.00945	399/ 0.01571	87/ 0.03425

Table 5-8 Crack profile for specimen with multi-crack pattern

Mixture	# of specimen	Primary crack width (μm/in.)	# of cracks	Average crack width (μm/in.)
Mixture A	BMA1	72 (0.00283 in.)	14	20.9 (0.00082 in.)
	BMA2	233 (0.00917 in.)	16	36.2 (0.00143 in.)
Mixture B	BMB1	83 (0.00327 in.)	4	37.04 (0.00146 in.)
	BMB2	480 (0.01890 in.)	3	284.4 (0.01120 in.)
Mixture C	BMC1	72 (0.00283 in.)	3	57 (0.00224 in.)
	BMC2	402 (0.01583 in.)	4	151 (0.00594 in.)
Mixture D	BMD1	46 (0.00181 in.)	9	28.9 (0.00114 in.)
	BMD2	210 (0.00827 in.)	26	40.3 (0.00159 in.)

After core extraction, all surfaces of both cracked and uncracked specimens, except the side surface, were coated with epoxy (Sikadur 32). The specimens were then immersed in a fully saturated calcium hydroxide water bath at 73 ± 4 °F (23 ± 2 °C) for 48 hours and subsequently exposed to a saltwater tank containing a 16.5 wt.% sodium chloride solution at SMO, as shown in Figure 5-28. The chloride concentration in the exposure solution was monitored twice per week.

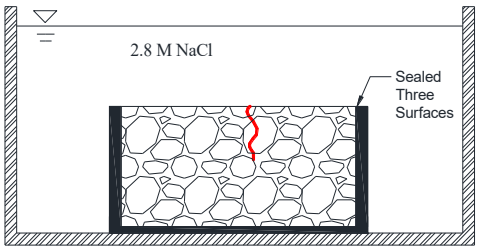

(a) Bulk diffusion test scheme

(b) Saltwater tank

Figure 5-28 Bulk diffusion test

In addition, a digital microscope was used to take pictures at the cracking surface for single-crack specimens after exposure of 0, 1, 3, 10, 28, 56, 90, 181, 282, 370 days of exposure to monitor the closing of cracks due to self-healing effect. The crack mouth closure rate (%) was measured at approximate quarter point along the crack, as shown in Equation 35.

$$Crack\ mouth\ closure\ rate = \frac{Crack\ width_{before\ exposure} - Crack\ width_{after\ exposure}}{Crack\ width_{before\ exposure}} \quad \text{(Equation 35)}$$

After exposure, the cracked specimens were removed from the saltwater tank. The exposure duration was 372 days for the multiple-cracked specimens from Mixtures A, B, and D, 450 days for the multiple-cracked specimens from Mixture C, and 370 days for the uncracked and single-cracked specimens. All specimens were stored in watertight resealable polyethylene bags for 3 to 4 hours during the trip from SMO to FSU. After arriving at FSU, all specimens were stored in a freezer maintained at 5 ± 9 °F (−15 ± 5 °C) until the time of grinding according to ASTM C1556-16 (ASTM Committee C09, 2016).

On the testing day, the specimens were first brought to room temperature by placing them under ambient conditions for at least 8 hours. The surfaces of the cracked specimens were cleaned several times using lint-free dry tissue, whereas deionized (DI) water was sprayed on the uncracked specimens and the surfaces were wiped repeatedly to ensure cleanliness. To eliminate possible contamination from the exposure solution, the top 1 mm (0.03937 in.) surface layer was ground off from all specimens. Each specimen was then sectioned at one-third of its diameter.

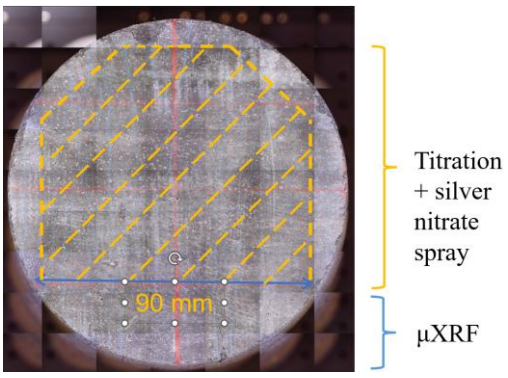

(a) Top surface for specimen with multi-cracks pattern

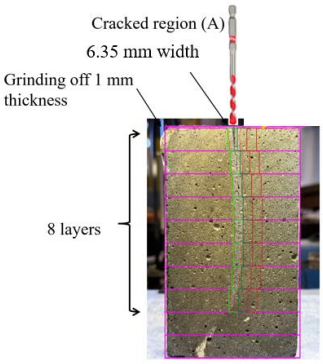

(b) Elevation for specimen with single crack pattern

Figure 5-29 Chloride concentration measurement

For specimens with multiple cracks, the samples were dry cut at the location of the blue line in Figure 5-29 (a). The smaller section was used for micro-XRF analysis. The exposed cut cross-section of the larger portion was sprayed with a 0.1 N silver nitrate solution to visualize the chloride penetration region. After this observation, approximately 1 mm (0.03937 in.) of the sprayed surface layer was ground off to eliminate any potential influence from the silver nitrate. The specimens were then trimmed along the orange-marked area to minimize chloride ingress from the side surface using dry cutting. Subsequently, 5 mm (0.19685 in.)-thick slices were sequentially ground to obtain Powdered specimens for chloride titration analysis.

For specimens with single-crack pattern, micro-XRF characterization was not conducted. Instead, the exposed cross-section surface of the smaller section was sprayed with a 0.1 N silver nitrate solution. Instead of profile grinding approach, powders were collected using a 6.35 mm (0.25000 in.)-diameter drill at the crack region for a total of 8 layers with a layer depth of 15 mm (0.59055 in.), as shown in Figure 5-29 (b). After drilling each layer, the exposed surface was dry cut to observe the crack path before proceeding to the next layer.

For uncracked specimens, powder was collected from ten successive 1 mm (0.03937 in.)-thick layers across the entire shaded orange region illustrated in Figure 5-29 (a) using a profile grinding approach.

Each powdered specimen weighing 4.0000 ± 0.0005 g (0.14110 ± 0.00002 oz.) was analyzed to determine the acid-soluble chloride content following the Florida Department of Transportation (FDOT) test FM 5-516 (FDOT State Mixture Office, 2018).

5.2.2 Testing results

5.2.2.1 Chloride diffusion in uncracked and single-cracked specimens

Chloride diffusion behavior in UHPC specimens with a single-cracked pattern was evaluated to examine the influence of crack width on chloride ingress under long-term bulk exposure. Compared with uncracked specimens, single-cracked specimens exhibited localized chloride transport dominated by crack-controlled pathways, while the surrounding UHPC matrix maintained strong resistance to diffusion. Chloride penetration was assessed using self-healing monitoring, colorimetric observation, and quantitative titration testing.

5.2.2.1.1 Self-healing monitoring

The crack mouth closure rate for single-cracked samples is shown in Figure 5-30 for both mixture A and D, respectively. As the results indicate, with increasing crack width, the crack mouth closure rate decreased. It was observed that cracks with widths smaller than approximately 400 μm (0.01575 in.) could be fully sealed. For cracks narrower than 400 μm (0.01575 in.), most specimens achieved complete sealing after 56 days of exposure, with the majority of crack closure occurring within the first 28 days. In contrast, cracks with widths greater than 400 μm (0.01575 in.) exhibited only partial sealing. For specimens with crack widths exceeding this threshold, most self-healing occurred within the first 56 days of exposure, after which further closure was limited.

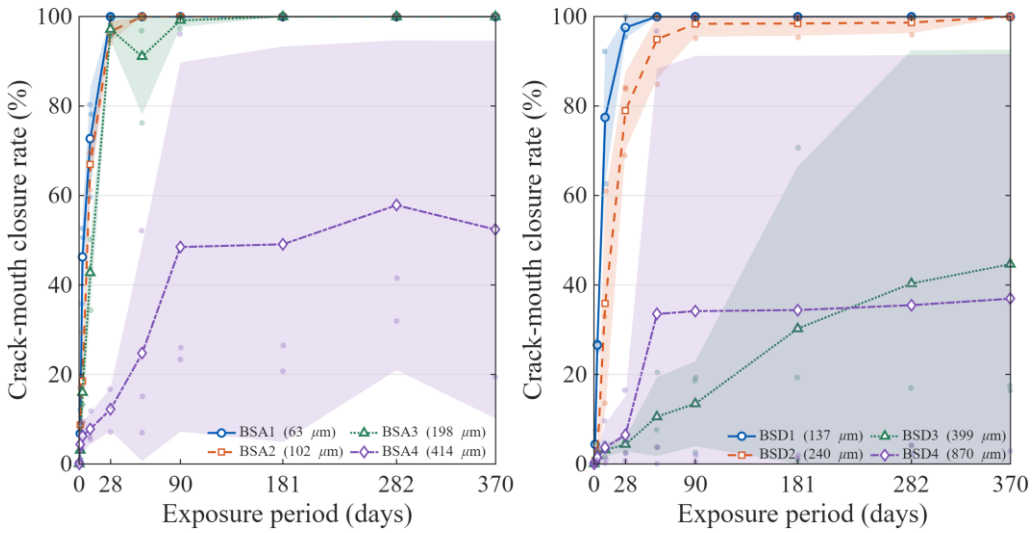

(a)Mixture A (b)Mixture D

Figure 5-30 Self-healing monitoring for single-cracked specimen

5.2.2.1.2 Colorimetric method

Figure 5-31 shows the chloride penetration in single-cracked samples observed using the colorimetric method. From this observation, chloride ingress primarily occurred through the cracked regions of the specimens, while the uncracked areas exhibited diffusion behavior comparable to that of uncracked UHPC, as shown in Figure 5-31. The maximum chloride penetration depth in the uncracked regions was determined by averaging measurements taken at ten equally spaced points across the cutting edge. For the uncracked reference specimens, the maximum chloride penetration depths were 3.55 mm (0.13976 in.) for mixture A and 2.54 mm (0.10000 in.) for Mixture D. In the cracked specimens, the corresponding values at uncracked regions were 3.31 ± 1.17 mm (0.13031 ± 0.04606 in.) for mixture A and 2.09 ± 0.05 mm (0.08228 ± 0.00197 in.) for Mixture D. These results indicate that chloride ions predominantly penetrated along the cracks, while the surrounding uncracked matrix maintained similar resistance to chloride ingress as the uncracked control specimens.

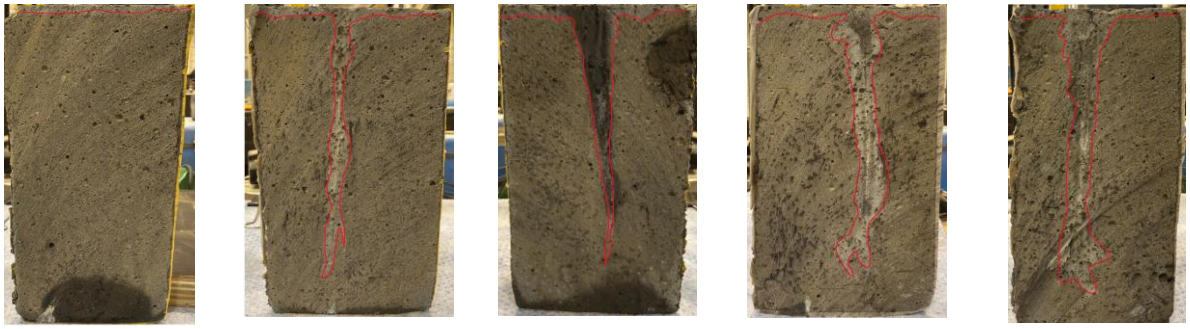

BPA-uncrack BSA1-63 μm (0.00248 in.) BSA2-102 μm (0.00402 in.) BSA3-198 μm (0.00780 in.) BSA4-414 μm (0.01630 in.)

Figure 5-31 0.1 N silver nitrate spray at the cross section

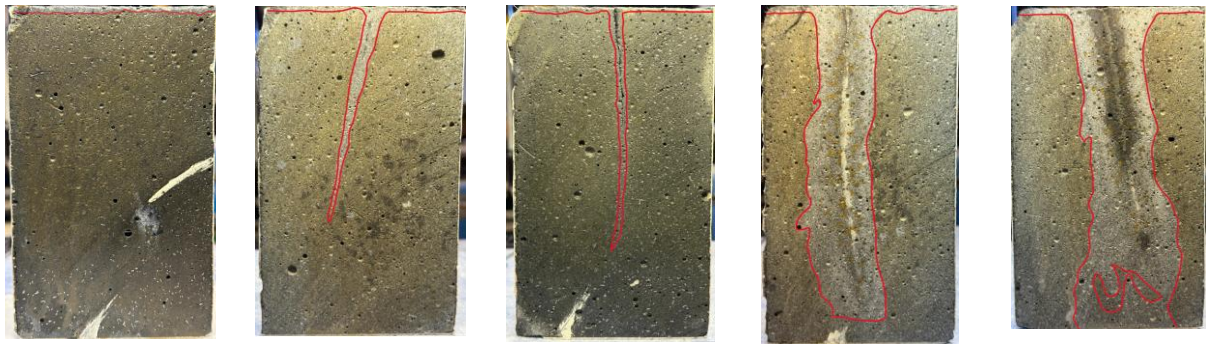

BPD-uncrack | BSD1-137 μm (0.00539 in.) | BSD2-240 μm (0.00945 in.) | BSD3-399 μm (0.01571 in.) | BSD4-870 μm (0.03425 in.)

Figure 5-31 0.1 N silver nitrate spray at the cross section (continued)

In addition, it was observed that once the crack width exceeded a certain range, the increase in chloride penetration area began to slow down. For Mixture A, this transition occurred at a crack width greater than approximately 198 μm (0.00780 in.)**,** while for Mixture D, a similar trend was observed beyond approximately 399 μm (0.01571 in.)**.** Beyond these crack widths, further increases in crack width resulted in only a gradual expansion of the chloride penetration area. These values may represent an upper threshold crack width for chloride penetration in cracked UHPC, beyond which crack-controlled transport no longer increases proportionally with surface crack opening.

The difference in the observed threshold crack widths between the two mixtures is likely related to differences in steel fiber dosage and crack morphology. Mixture A contained a higher steel fiber content of 1.25 vol.%**,** which promoted stronger crack bridging and confinement effects compared to 0.75 vol.% steel fiber content for Mixture D. As surface crack width increased, fiber bridging limited crack opening along the depth and reduced crack continuity, thereby restraining further expansion of chloride penetration. In contrast, Mixture D, with a lower fiber dosage, exhibited wider and more continuous cracks, resulting in a higher threshold crack width before the slowing of chloride penetration became evident.

5.2.2.1.3 Titration test

The measured chloride contents for both uncracked and cracked specimens are plotted in Figure 5-32. For uncracked specimens, the data represent the average chloride concentration measured at each successive grinding layer from the exposed surface. For single-cracked specimens, the reported values correspond to the chloride concentration measured within the cracked region at each layer, representing the localized chloride ingress along the crack path.

The apparent chloride diffusion coefficient was obtained from the titration data in accordance with ASTM C1556-16 (ASTM Committee C09, 2016). The measured chloride concentration profiles were fitted to the analytical solution of Fick's second law for one-dimensional diffusion, with the apparent diffusion coefficient and surface chloride concentration treated as fitting parameters. The fitting was performed using a nonlinear regression approach following the procedure specified in ASTM C1556-16 (ASTM Committee C09, 2016). The quality of the fitting was evaluated using the coefficient of determination (R^2), which represents the degree of agreement between the measured chloride concentrations and the fitted diffusion curve. An R^2 value closer to 1.0 indicates a better fit and greater confidence in the calculated apparent diffusion coefficient.

For uncracked specimens, the apparent chloride diffusion coefficient of mixture A was approximately 61.18% of that of Mixture D; however, both values remained extremely low and consistent with those reported in previous studies on uncracked UHPC, as shown in Table 5-9.

Table 5-9 Chloride diffusion coefficients for uncracked and cracked specimens

Mixture A			Mixture D		
Crack condition	m^2/s ($ft.^2/s$)	R^2	Crack condition	m^2/s	R^2
Uncrack	4.289e-14 (4.616e-13)	0.998	Uncrack	7.010e-14 (7.544e-13)	0.952
63 μm (0.00248 in.)	3.665e-11 (3.946e-10)	0.960	137 μm (0.00539 in.)	4.014e-11 (4.322e-10)	0.948
102 μm (0.00402 in.)	5.100e-11 (5.489e-10)	0.966	240 μm (0.00945 in.)	9.256e-11 (9.960e-10)	0.921
198 μm (0.00780 in.)	5.362e-11 (5.773e-10)	0.961	399 μm (0.01571 in.)	1.045e-10 (1.125e-09)	0.708
414 μm (0.01630 in.)	6.555e-11 (7.056e-10)	0.732	870 μm (0.03425 in.)	1.000e-10 (1.076e-09)	0.911

For single-cracked specimens, the chloride concentration measured within the cracked region at the surface zone (shallower than 10 mm [0.39370 in.]) was more than 20 times higher than that measured in uncracked specimens, as shown in Figure 5-32. It should be noted that the powders for cracked specimens were collected only from the cracked region; therefore, the results should be interpreted as the chloride transport behavior along the crack rather than a direct comparison with the bulk uncracked matrix.

Consistent with the measured concentration profiles, the apparent diffusion coefficient within the cracked region increased by approximately three orders of magnitude as the crack width increased from the uncracked condition to about 63 μm (0.00248 in.), as shown in Figure 5-33. As the crack width further increased from approximately 63 μm (0.00248 in.) to 400 μm (0.01575 in.), the apparent diffusion coefficient increased from 3.665×10^{-11} m^2/s (5.68×10^{-8} in^2/s) to 1.045×10^{-10} m^2/s (1.62×10^{-7} in^2/s). The results indicate a substantially higher chloride transport rate along the cracked region compared with the uncracked matrix. Differences in the apparent diffusion coefficients at similar crack widths are likely associated with variations in steel fiber content between mixtures. Higher fiber contents tend to reduce the effective crack width along the depth through fiber-bridging and confinement effects, which may limit chloride penetration.

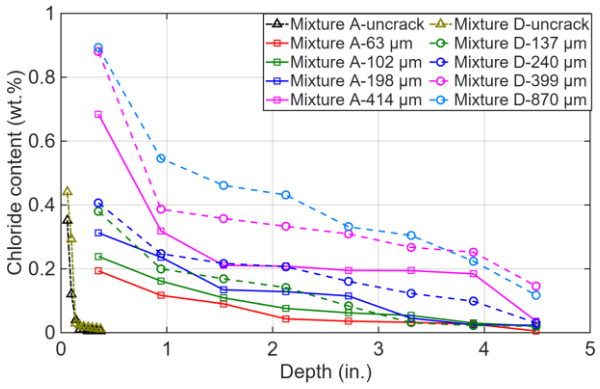

Figure 5-32 Chloride concentration for specimen with single crack pattern

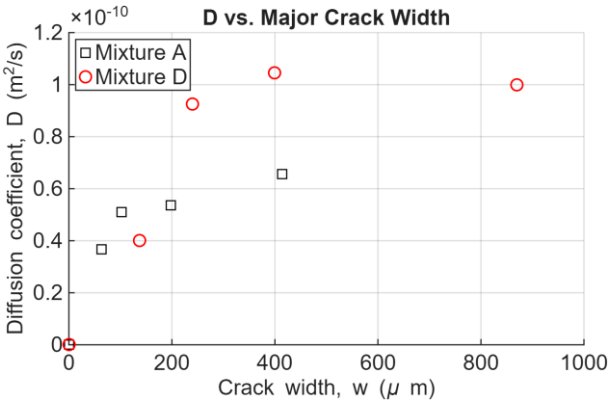

Figure 5-33 Chloride diffusion coefficient vs. crack width

The R^2 values in Table 5-9 represent the goodness-of-fit of the one-dimensional Fickian diffusion model to the measured chloride concentration profiles. For most crack widths, satisfactory agreement is observed, indicating that the apparent diffusion coefficient provides a reasonable effective representation of transport behavior. However, a noticeable reduction in R^2 is observed for specimens with crack widths around 400 μm (0.0157 in.) [414 μm (0.0163 in.) in Mixture A and 399 μm in Mixture D].

This reduction in R^2 likely reflects a transition in the governing transport mechanism at intermediate crack widths. At relatively small crack widths, chloride ingress is partially moderated by crack self-healing and limited crack permeability, resulting in a concentration profile that more closely resembles diffusive transport. At very large crack widths, transport may become predominantly crack-controlled and more uniformly governed by rapid penetration along the crack path. However, at intermediate crack widths near 400 μm, the interaction between crack-assisted transport and bulk matrix diffusion may produce a more heterogeneous and non-uniform chloride distribution. The coexistence of crack-dominated transport near the surface and matrix-controlled diffusion at greater depths can lead to deviations from the idealized homogeneous one-dimensional Fickian assumption, thereby reducing the R^2 of the fitted profile.

In addition, crack geometry at these widths may involve partial self-healing, localized tortuosity, or irregular crack opening along depth, further contributing to non-uniform transport behavior. Therefore, the lower R^2 values at approximately 400 μm (0.0157 in.) should be interpreted as evidence of complex coupled transport mechanisms rather than as experimental inconsistency.

5.2.2.2 Chloride diffusion in multiple-cracked specimens

Chloride diffusion behavior in UHPC specimens with multiple-cracked patterns was evaluated to examine the combined influence of primary crack width, crack number, and crack interaction on chloride ingress. Compared with single-cracked specimens, multiple-cracked specimens exhibited more complex chloride transport behavior due to the presence of several closely spaced cracks and potential overlap of crack-influenced regions. Chloride penetration was assessed using colorimetric observation, μXRF analysis, and quantitative titration testing.

5.2.2.2.1 Colorimetric method and μXRF testing results

Chloride penetration in multiple-cracked UHPC specimens was evaluated using the colorimetric method by spraying 0.1 N silver nitrate solution on freshly exposed cross sections, as shown in Figure 5-34. The results showed that chloride ingress occurred primarily along cracked regions, with penetration fronts aligned with individual cracks, indicating that cracks served as the dominant transport pathways. In specimens with closely spaced cracks, overlapping penetration zones were observed, demonstrating interaction among adjacent crack-controlled transport pathways and resulting in a more spatially distributed penetration pattern than that observed in single-cracked specimens. Chloride penetration was not confined to the primary crack locations but extended into regions influenced by neighboring cracks, producing a broader affected zone.

(a)BPA

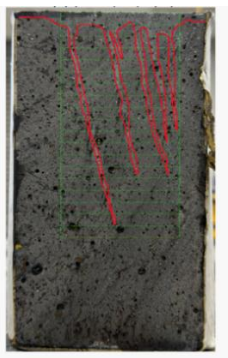

(b)BMA1

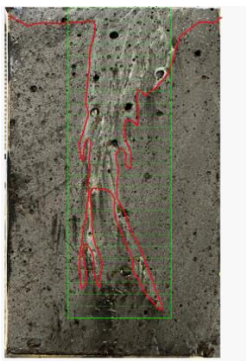

(c)BMA2

(d) BPB

(e) BMB1

(f) BMB2

(g)BPC

(h) BMC1

(i) BMC2

Figure 5-34 0.1 N silver nitrate spray results for cracked and uncracked specimens

(j)BPD (k)BMD1 (l)BMD2

Figure 5-34 0.1 N silver nitrate spray results for cracked and uncracked specimens (continued)

For the uncracked specimens, the maximum chloride penetration depths were very similar among the four UHPC mixtures. The measured maximum penetration depths from the exposure surface were 3.31 ± 1.17 mm (0.130 ± 0.046 in.), 1.45 ± 0.16 mm (0.057 ± 0.006 in.), 2.36 ± 0.15 mm (0.093 ± 0.006 in.), and 2.09 ± 0.05 mm (0.082 ± 0.002 in.) for Mixtures A, B, C, and D, respectively.

Moreover, Figure 5-34 shows that chloride ions primarily penetrated through the cracked regions. This observation further confirms that chloride ingress in cracked UHPC is governed mainly by crack-controlled transport rather than uniform diffusion through the intact matrix. The red-outlined chloride penetration regions were concentrated along visible crack paths and extended downward from the exposed surface, indicating that cracks served as preferential pathways for chloride movement. For specimens with relatively small primary crack widths, such as BMB1 and BMC1, with primary crack widths of 83 μm (0.0033 in.) and 72 μm (0.0028 in.), respectively, the chloride penetration zones remained narrow and were mostly confined to discrete vertical pathways. Although these specimens contained multiple cracks, four cracks in BMB1 and three cracks in BMC1, the limited penetration area indicates that small cracks restricted both downward ingress and lateral spreading.

μXRF analysis confirmed these observations by identifying elevated chloride concentrations not only along major cracks but also in regions with relatively small surface crack widths and in areas between adjacent cracks, as shown in Figure 5-35. This behavior indicates that chloride transport was influenced by crack geometry and crack connectivity rather than by surface crack width alone. Variability in crack morphology further introduced uncertainty in the relationship between surface crack width and chloride penetration depth, as the deepest chloride penetration was not always associated with the largest surface crack at the cutting location. This discrepancy is attributed to nonuniform crack opening with depth, crack branching, and internal crack continuity that are not fully captured by surface measurements, indicating that internal crack morphology plays a critical role in governing chloride penetration in multiple-cracked UHPC specimens.

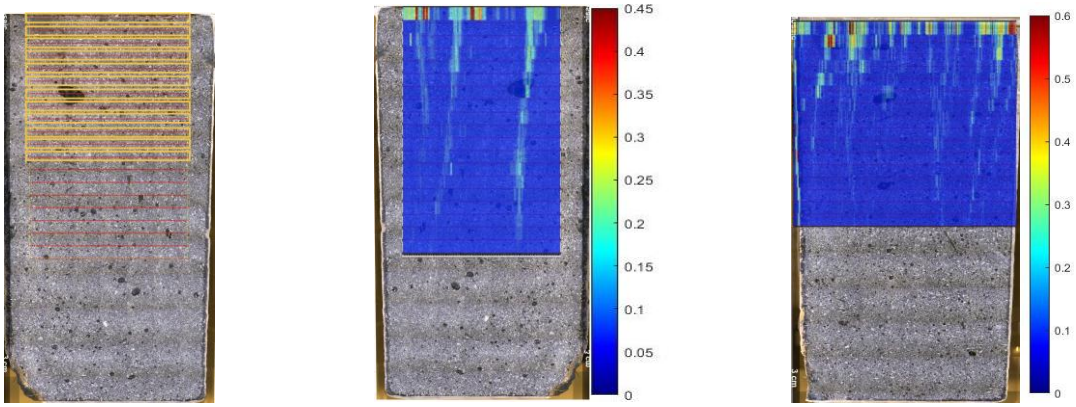

(a)μXRF scanning scheme (b)μXRF for BMD1 (c)μXRF for BMD2

Figure 5-35 0.1 N silver nitrate spray for cracked and uncracked specimen

In contrast, specimens with larger primary crack widths, including BMB2 and BMC2, exhibited more extensive chloride penetration. The primary crack widths of BMB2 and BMC2 were 480 μm and 402 μm, respectively, and both specimens showed wider and more continuous penetration zones, with apparent lateral spreading from the main crack paths into the adjacent matrix. This suggests that increasing primary crack width not only promotes chloride transport along the crack depth direction but also enhances lateral penetration into the surrounding UHPC. As shown in Figure 5-36(a), the chloride penetration area exhibited a positive relationship with primary crack width across Mixtures A to D. These results indicate that the extent of chloride penetration in cracked UHPC is controlled by the presence of cracks and the severity of cracking, with the primary crack width serving as a key parameter governing chloride ingress. An increasing trend between chloride penetration area and average crack width is also observed, as shown in Figure 5-36(b). However, this trend should be interpreted with caution because average crack width and primary crack width are not independent. Therefore, the observed correlation with average crack width does not necessarily indicate an independent effect of average crack width. Instead, it may partly reflect the influence of the primary crack width, while also suggesting that the overall crack pattern could contribute to chloride ingress. However, when the chloride penetration area is correlated only with the number of cracks, the relationship is relatively weak, as shown in Figure 5-36(c).

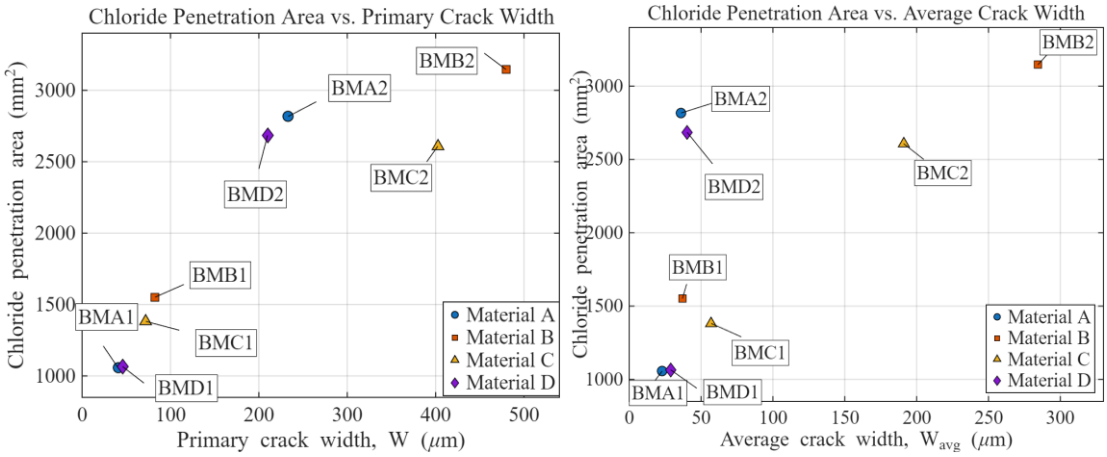

(a) Cl penetration area vs. primary crack width (b) Cl penetration vs. average crack width

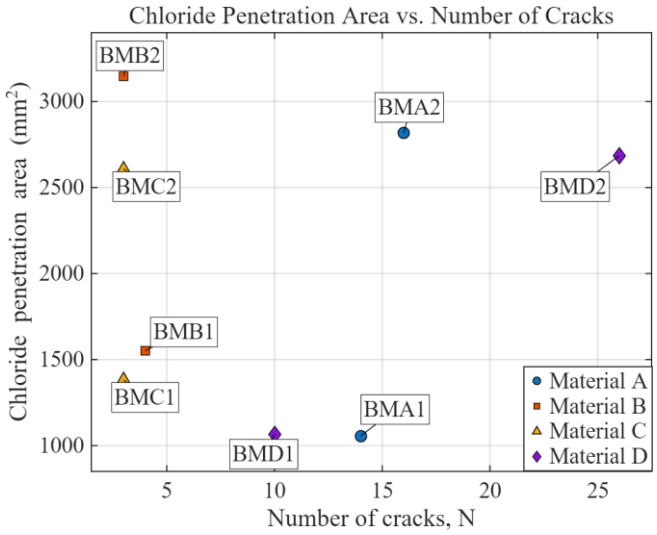

(C) Cl penetration vs. number of cracks

Figure 5-36 Chloride penetration area to crack patterns

5.2.2.2.2 Titration test

The acid-soluble chloride concentration profiles for all four mixtures were determined in accordance with FM 5-516 (FDOT State Mixture Office, 2018) and are shown in Figure 5-37. For the uncracked specimens and the multi-cracked specimens with primary crack widths below 100 μm (0.0039 in.), Mixtures B and C showed chloride concentration profiles comparable to those of Mixtures A and D. This result indicates that chloride ingress remained limited when the primary cracks were relatively small, leading to similar chloride profiles among the four UHPC mixtures.

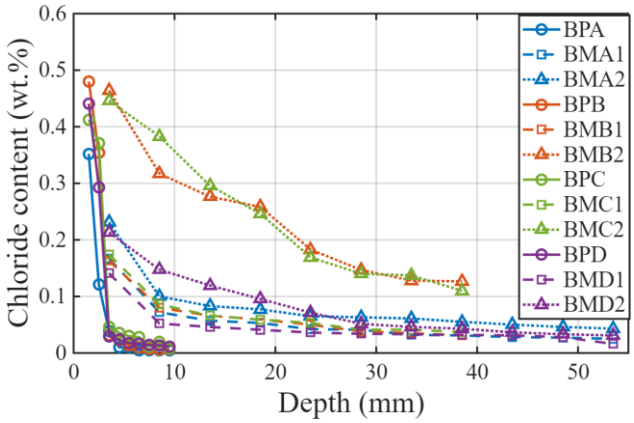

Figure 5-37 Chloride concentration vs. depth

As shown in Figure 5-37, the chloride concentration increased at each depth as the primary crack width increased up to 480 μm (0.0189 in.). At depths greater than 38.5 mm (1.52 in.), specimens with primary crack widths of approximately 200 μm (0.0079 in.) had chloride concentrations similar to those of specimens with primary crack widths of approximately 100 μm (0.0039 in.). In contrast, specimens with primary crack widths of approximately 440 μm (0.0173 in.) exhibited significantly higher chloride concentrations than specimens with primary crack widths of approximately 200 μm (0.0079 in.), even at depths up to 38.5 mm (1.52 in.). It is suspected that number of cracks, crack depth and tortuosity of crack system could also impact on the chloride penetration.

The apparent chloride diffusion coefficient was calculated from the chloride concentration–depth profile by fitting the measured chloride contents to the Fick's second-law solution, consistent with ASTM C1556-25 for bulk diffusion testing of cementitious mixtures. For each specimen with multi-cracked patterns, the regression was performed using the top eight profile-ground layers below the surface, while the top 1 mm layer was excluded from the fit to minimize surface-layer effects. For uncracked specimens, the top 10 profile-ground layers below the surface was used to run regression model to calculate the apparent chloride diffusion coefficient excluding the top 1 mm (0.039 in.) layer.

The apparent chloride diffusion coefficients for UHPC specimens with multi-cracked patterns are summarized in Table 5-10. The uncracked specimens of both mixtures exhibited apparent chloride diffusion coefficients on the order of 10^{-14} m²/s (10^{-13} ft²/s) (1.08×10^{-13} ft²/s). After cracking, the apparent chloride diffusion coefficient increased from approximately 10^{-14} m²/s (10^{-13} ft²/s) (1.08×10^{-13} ft²/s) to 10^{-12} m²/s (1.08×10^{-11} ft²/s), as shown in Table 5-10. With increasing crack width, the apparent chloride diffusion coefficients of the multi-cracked specimens did not increase rapidly. Instead, they remained within the range of approximately 10^{-12} to 10^{-11} m²/s (1.08×10^{-11} to 1.08×10^{-10} ft²/s), even as the primary crack width increased up to 480 μm (0.0189 in.).

The apparent chloride diffusion coefficient increased with increasing primary crack width, as shown in Figure 5-38 (a). A more rapid increase was observed when the primary crack width exceeded approximately 400 μm (0.0157 in.), possibly suggesting that this crack width may represent a upper threshold crack width for chloride diffusion in UHPC with multi-cracked patterns. Previous studies have reported a similar phenomenon for normal-strength concrete, high-strength concrete, and steel fiber-reinforced high-strength concrete, although the reported a upper threshold crack width was approximately 80 μm (0.0031 in.) (Assia Djerbi *et al.*, 2008). The apparent chloride diffusion coefficient is also positively correlated with the average crack width, as shown in Figure 5-38 (b). In contrast, the correlation between the apparent chloride diffusion coefficient and the number of cracks is relatively weak, as shown in Figure 5-38 (c). The relationship between crack pattern to chloride penetration area is

similar to the trend between crack patterns to apparent chloride diffusion coefficient. Figure 5-39 draws the correlation between chloride penetration area to apparent chloride diffusion coefficient. It shows a clear positive relationship between chloride penetration areas to apparent chloride diffusion coefficient.

Table 5-10 Chloride diffusion coefficients for multiple-cracked specimens

	BMA1 – 72 μm (0.00283 in.)		BMA2 – 233 μm (0.00917 in.)		BMB1 – 83 μm (0.00327 in.)		BMB2 – 480 μm (0.01890 in.)	
	m^2/s (ft^2/s)	R^2	m^2/s (ft^2/s)	R^2	m^2/s (ft^2/s)	R^2	m^2/s (ft^2/s)	R^2
D_{appr}	7.217e-12 (7.767e-11 ft^2/s)	0.7379	1.042e-11 (1.122e-10 ft^2/s)	0.6549	8.633e-12 (9.291e-11 ft^2/s)	0.8049	1.392e-11 (1.498e-10 ft^2/s)	0.9219
	BMC1- 72 μm (0.00283 in.)		BMC2- 402 μm (0.01583 in.)		BMD1 – 46 μm (0.00181 in.)		BMD2 – 210 μm (0.00827 in.)	
	m^2/s (ft^2/s)	R^2	m^2/s (ft^2/s)	R^2	m^2/s (ft^2/s)	R^2	m^2/s (ft^2/s)	R^2
	7.216e-12 (7.766e-11 ft^2/s)	0.9774	1.003e-11 (1.080e-10 ft^2/s)	0.9774	8.348e-12 (8.986e-11 ft^2/s)	0.6137	9.457e-12 (1.018e-10 ft^2/s)	0.9604

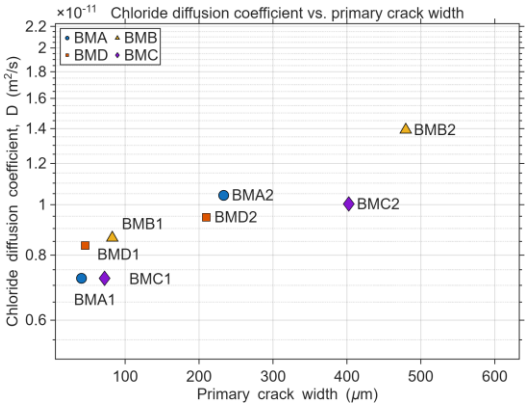

(a) D_{appr} vs. primary crack width

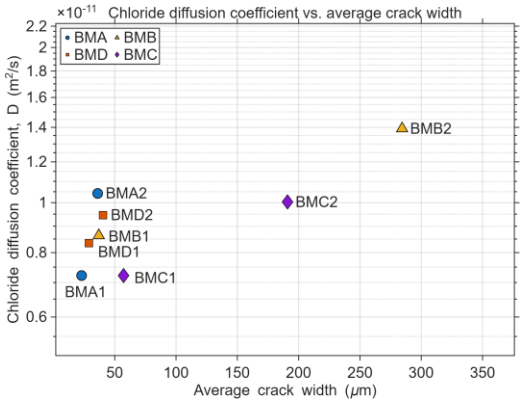

(b) D_{appr} vs. average crack width

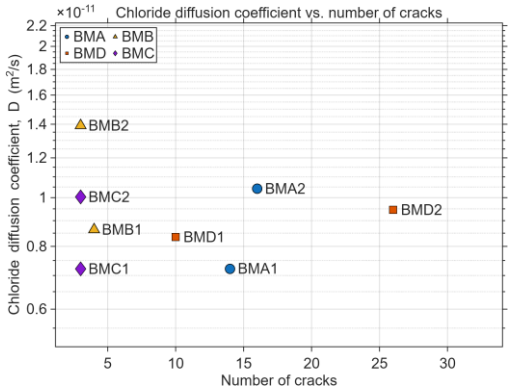

(c) D_{appr} vs. number of cracks

Figure 5-38 The apparent chloride diffusion coefficient vs. crack pattern

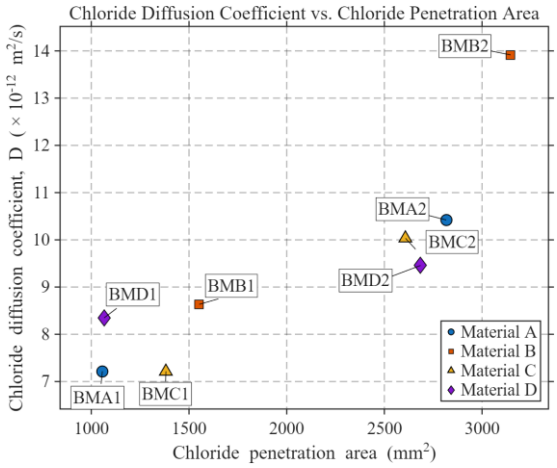

Figure 5-39 The relationship between apparent chloride diffusion coefficient to chloride penetration area

5.2.3 Summary

This study investigated chloride transport behavior in UHPC under uncracked, single-cracked, and multi-cracked conditions following long-term bulk exposure to a 16.5 wt.% sodium chloride solution. Chloride ingress was quantified using colorimetric analysis verified by μXRF and acid-soluble chloride titration, and apparent diffusion coefficients were determined to characterize transport behavior.

1. For uncracked UHPC, chloride penetration remained extremely limited, and apparent diffusion coefficients were on the order of 10^{-14} m²/s (10^{-13} ft²/s), confirming the high intrinsic resistance of the dense matrix.
2. For single-cracked specimens, chloride transport was primarily governed by crack-assisted pathways. The apparent diffusion coefficient in the crack region increased by approximately two to three orders of magnitude compared with the uncracked condition, reaching the order of 10^{-12}–10^{-11} m²/s. The diffusion coefficient generally increased with crack width within the investigated range, while narrower cracks exhibited more pronounced self-healing behavior over time.
3. For multi-cracked specimens, chloride transport was governed by the combined effects of crack width, crack number, and crack interaction. Apparent chloride diffusion coefficients increased by approximately two to three orders of magnitude relative to intact UHPC. However, the relationship between diffusion coefficient and primary crack width was not strictly monotonic, indicating that crack multiplicity and spatial distribution significantly influence chloride ingress.

Overall, the results demonstrate that chloride transport in cracked UHPC is controlled by crack geometry and crack network characteristics. While single cracks primarily act as localized transport pathways, multiple cracks introduce interacting and overlapping penetration zones that significantly modify overall transport behavior.

6 Corrosion of steel rebar in cracked UHPC

This chapter evaluates the corrosion behavior of steel rebar embedded in UHPC of Mixture A, Mixture B, and Mixture D under wetting–drying exposure conditions. Reinforced UHPC prism specimens were prepared with controlled crack widths ranging from approximately 30 to 800 μm (0.0012 to 0.0315 in.) and cover thicknesses of 12.7 and 25.4 mm (0.5 and 1.0 in.). Reinforced UHPC prismatic specimens were exposed to 3.5 wt.% NaCl under partial immersion wetting–drying cycles for a total duration of 98~448 days. During exposure, corrosion potential and corrosion current density were periodically measured using electrochemical methods, including open circuit potential (OCP) or half-cell potential, linear polarization resistance (LPR), and Tafel extrapolation. Crack mouth closure was also monitored using a digital microscope during the air-drying phase. The objective of this task is to quantify corrosion activity and assess the influence of crack width and mixture type on the corrosion performance of steel reinforcement in UHPC.

In addition, another set of UHPC beams fabricated by Mixture A, Mixture B, Mixture C, and Mixture D were exposed to Seahorse Key Island for realistic marine exposure lasting for 270 days. During exposure, the corrosion potential and corrosion current density was tested by half-cell potential and linear polarization resistance test after exposure of 28, 180, and 270 days. Meanwhile, the crack mouth closure rate was also documented by a portable microscope. The testing results of corrosion of steel rebar embedded in cracked UHPC exposed to realistic marine environment was compared to that of cracked UHPC exposed to laboratory wetting-drying cycles exposure.

6.1 Laboratory wetting-dry cycles exposure

6.1.1 Specimens preparation

Reinforced UHPC specimens were prepared to evaluate the corrosion behavior of steel reinforcement embedded in UHPC mixtures A, B, and D under chloride exposure. Mixtures A and B were evaluated using controlled chloride wetting–drying cycles in the earlier testing program, while Mixture D was prepared using a similar reinforced prism configuration with additional specimen variations.

For Mixtures A and B, a total of twelve reinforced UHPC prism specimens were cast. The specimens had dimensions of 152.4 mm × 152.4 mm × 533.4 mm (6 in. × 6 in. × 21 in.). Six specimens were prepared for each mixture. For each mixture, three specimens were cast with a thick steel cover of 12.7 mm (0.5 in.), and three specimens were cast with a cover thickness of 25.4 mm (1.0 in.). At each cover thickness, two specimens were cracked, and one specimen was kept uncracked as a reference specimen.

Each specimen contained one No. 4 black steel reinforcing bar with a diameter of 12.7 mm (0.5 in.) and a length of 457.2 mm (18 in.). The rebar was embedded longitudinally along the centerline of the specimen and served as the working electrode during electrochemical testing. Before casting, the steel rebars were mechanically polished using abrasive papers with grit sizes ranging from 80 to 1500 to remove rust and mill scale. Bars were then degreased with acetone and dried.

To reduce the likelihood of corrosion initiation at the exposed bar ends, 316L stainless-steel threaded rods were connected to both ends of each carbon-steel rebar using 316L stainless-steel couplers. The threaded rods had dimensions of 12.7 mm × 95.25 mm (0.5 in. × 3.75 in.) and 12.7 mm × 38.1 mm (0.5 in. × 1.5 in.). The stainless-steel couplers had a length of 19.05 mm (0.75 in.). In addition, a 316L stainless-steel rod with dimensions of 12.7 mm × 609.6 mm (0.5 in. × 24 in.) was embedded in the compression zone of the specimens with 25.4 mm (1.0 in.) cover, as shown in Figure 6-1. This rod was intended to serve as a backup counter electrode for electrochemical testing; however, it was not used in the present study.

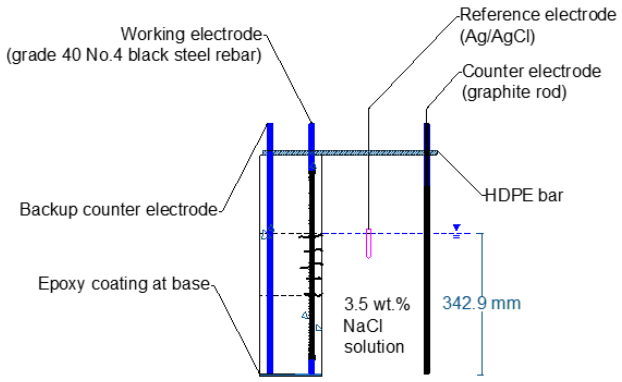

Figure 6-1 Testing scheme for Mixture A and B specimen with wetting-drying cycles

After casting, all specimens were demolded after 48 hours and cured in a standard moisture room for 26 days. Following curing, the selected cracked specimens were loaded using a third-point bending configuration at a displacement rate of 0.5 mm/min (0.02 in./min) to generate controlled flexural cracks. The target primary crack widths were approximately 300 μm (0.0118 in.) and 550 μm (0.0217 in.) for Mixture A, and 800 μm (0.0315 in.) and 1400 μm (0.0551 in.) for Mixture B. Crack widths were measured using a digital microscope. The representative primary crack width was determined at the location closest to the embedded steel rebar along a continuous crack path. The uncracked specimens were used as control specimens for comparison. The crack characteristic for Mixture A and Mixture B is shown in Table 6-1.

Table 6-1 Crack characteristics of reinforced UHPC specimens

Mixture	Target primary crack width (μm/ in.)	Cover thickness (mm/ in.)	Primary crack width at central line (μm/ in.)
Mixture A	300/ 0.0118	12.7/ 0.5	312/ 0.0123
		25.4/ 1.0	284/ 0.0112
	550/ 0.0217	12.7/ 0.5	522/ 0.0206
		25.4/ 1.0	595/ 0.0234
Mixture B	800/ 0.0315	12.7/ 0.5	779/ 0.0307
		25.4/ 1.0	776/ 0.0306
	1400/ 0.0551	12.7/ 0.5	1374/ 0.0514
		25.4/ 1.0	1466/ 0.0577
Mixture C	0	12.7/ 0.5	-
		25.4/ 1.0	-
	30/ 0.0012	12.7/ 0.5	26/ 0.0010
		12.7/ 0.5*	23*/ 0.0009*
		25.4/ 1.0	27/ 0.0011
	80/ 0.0031	12.7/ 0.5	75/ 0.0030
		25.4/ 1.0	79/ 0.0031

Mixture	Target primary crack width (μm/ in.)	Cover thickness (mm/ in.)	Primary crack width at central line (μm/ in.)
	100/ 0.0039	12.7/ 0.5	98/ 0.0039
		25.4/ 1.0	103/ 0.0041
	200/ 0.0079	12.7/ 0.5	221/ 0.0087
		25.4/ 1.0	230/ 0.0091
	400/ 0.0157	12.7/ 0.5	394/ 0.0155
		12.7/ 0.5*	435*/ 0.0171
		25.4/ 1.0	418/ 0.0165
	600/ 0.0236	12.7/ 0.5	672/ 0.0265
		25.4/ 1.0	614/ 0.0242
	800/ 0.0315	12.7/ 0.5	838/ 0.0330
		25.4/ 1.0	777/ 0.0306

Note:* represent the specimen without epoxy coating at the connection between stainless-steel to steel rebar.

For Mixture D, reinforced UHPC specimens were prepared to evaluate the corrosion behavior of embedded steel reinforcement in cracked UHPC subjected to controlled chloride wetting–drying cycles. The same general prism geometry was used. No. 4 Grade 60 black steel reinforcing bars, with a nominal diameter of 12.7 mm (0.5 in.) and a length of 457.2 mm (18 in.), were embedded longitudinally along the central axis of each UHPC prism. These bars served as the working electrodes during electrochemical monitoring, as shown in Figure 6-2.

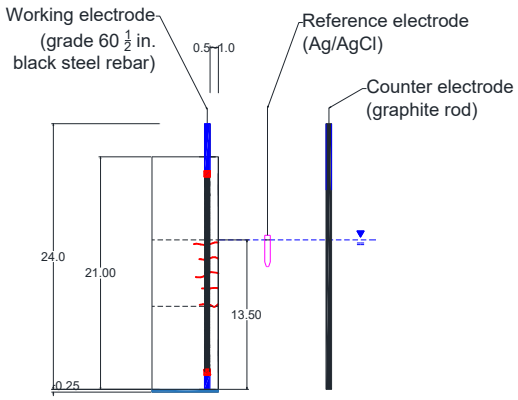

Figure 6-2 Testing scheme for Mixture D specimen with wetting-drying cycles

Before casting, the Mixture D reinforcing bars were mechanically polished using abrasive papers with grit sizes ranging from 80 to 1500 to remove rust and mill scale. The rebars were then degreased with acetone and dried. To minimize corrosion initiation at the exposed bar ends, 316L stainless-steel threaded rods with dimensions of 12.7 mm × 95.25 mm (0.5 in. × 3.75 in.) and 12.7 mm × 38.1 mm (0.5 in. × 1.5 in.) were connected to both ends of each carbon-steel reinforcing bar using 316L stainless-steel couplers with a length of 19.05 mm (0.75 in.).

A total of 16 reinforced UHPC prism specimens were prepared for the Mixture D controlled chloride wetting–drying exposure program. The specimens had dimensions of 152.4 mm × 152.4 mm × 533.4 mm (6 in. × 6 in. × 21 in.). Two reinforcement cover thicknesses were used: 12.7 mm (0.5 in.) and 25.4 mm (1.0 in.). For each cover thickness, one uncracked specimen was prepared as a reference specimen.

The structural epoxy was also applied at the connection between the carbon-steel reinforcing bar and the stainless-steel connector to reduce the possibility of galvanic corrosion at the junction for 14 specimens of Mixture D. Two companion cracked specimens with a cover depth of 12.7 mm (0.5 in.) were prepared without epoxy coating at the connection between the carbon-steel bar and the stainless-steel rod, following the same coating scheme used for the Mixture A and Mixture B specimens. These specimens were included to evaluate the possible influence of galvanic corrosion. After curing and crack generation, the exposed bottom surfaces of all cracked UHPC specimens were sealed with structural epoxy, Sikadur 31, to prevent fluid ingress through the steel–UHPC interface and to maintain controlled exposure conditions.

Mixture D specimens with a target crack width of approximately 30 μm (0.0012 in.) were cracked using third-point bending at a displacement rate of 0.20 mm/min (0.0079 in./min) over a span length of 457.2 mm (18.0 in.). For specimens with target crack widths greater than 30 μm (0.0012 in.), the beams were first loaded under third-point bending at the same displacement rate until the applied load reached approximately 200 kN (45.0 kips). Center-point bending was then used at a displacement rate of 0.20 mm/min (0.0079 in./min) to further open the primary crack until the target crack width was approximately achieved.

For Mixture D, crack widths were measured at the location of the embedded reinforcement, corresponding to the centerline of the beam. Five measurements were taken for each primary crack, and the average value was reported as the representative crack width. The crack characteristics of the Mixture D specimens are summarized in Table 6-1.

6.1.2 Exposure environment and testing method

After crack generation and crack-width documentation, the reinforced UHPC specimens fabricated with Mixture A and Mixture B were subjected to chloride wetting–drying cycles using a 3.5 ± 0.1 wt.% sodium chloride (NaCl) solution to simulate marine exposure conditions, as shown in Figure 6-3. The exposure program consisted of three stages with different wetting–drying cycle durations. From Day 0 to Day 112, each cycle consisted of 7 days of partial immersion followed by 7 days of air drying. From Day 112 to Day 168, the cycle duration was temporarily extended to 28 days of partial immersion followed by 28 days of air drying. This change was introduced because, after 112 days of exposure, the corrosion current density continued to decrease over time and stabilized within the low-corrosion or near-passive range. The extended cycle duration was used to evaluate whether prolonged saturation and enhanced oxygen replenishment during drying would influence the governing corrosion kinetics. From Day 168 to Day 448, the exposure program returned to 7 days of partial immersion followed by 7 days of air drying. The total exposure duration for Mixture A and Mixture B specimens was 448 days.

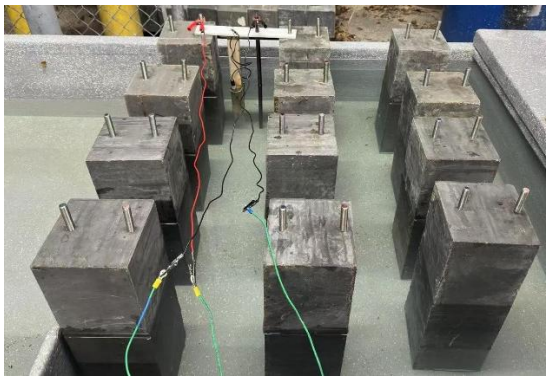

Figure 6-3 Exposure of reinforced UHPC in wetting cycles

After crack generation and crack-width documentation, all reinforced Mixture D UHPC specimens were also subjected to chloride wetting–drying cycles using a 3.5 ± 0.1 wt.% NaCl solution to simulate marine exposure conditions under laboratory conditions. Each wetting–drying cycle consisted of 7 days of partial immersion in a saltwater tank followed by 7 days of air drying. The total exposure duration was 98 days, corresponding to seven complete wetting–drying cycles. The chloride concentration of the solution was measured twice per week to ensure consistency throughout the exposure period.

The self-healing behavior of Mixture A and Mixture B specimens was evaluated by monitoring crack-mouth closure during the air-drying phase using a digital microscope. Images of the crack region along the centerline of each specimen were captured periodically, and crack widths were measured at multiple locations near the embedded steel reinforcement. The crack-mouth closure rate was calculated as the relative reduction in crack width compared with the initial crack width before exposure. Self-healing behavior was evaluated after 7, 21, 35, 63, 105, 175, 273, and 441 days of exposure by monitoring the crack-mouth closure rate.

Corrosion monitoring of the embedded steel reinforcement was conducted periodically using electrochemical testing with a Gamry Reference 1010E potentiostat. The testing scheme for Mixture A and Mixture B specimens is shown in Figure 6-1, and the corresponding testing scheme for Mixture D specimens is shown in Figure 6-2. For all specimens, the corrosion potential was monitored using open-circuit potential (OCP) measurements in a two-electrode configuration. The embedded carbon-steel reinforcing bar served as the working electrode, and an external Ag/AgCl saturated KCl electrode served as the reference electrode.

The corrosion current density was determined using linear polarization resistance (LPR) and Tafel polarization tests in a three-electrode configuration. In this configuration, the embedded carbon-steel reinforcing bar was used as the working electrode, the Ag/AgCl saturated KCl electrode was used as the reference electrode, and a graphite rod was used as the counter electrode. The graphite rod was positioned parallel to the working electrode along the cracked surface to promote uniform current distribution during testing.

The LPR test was conducted by scanning the potential within ±15 mV of the corrosion potential at a scan rate of 0.167 mV/s to determine the polarization resistance. The Tafel polarization test was conducted by scanning the potential within ±75 mV of the corrosion potential at a scan rate of 0.1 mV/s to obtain the anodic and cathodic Tafel slopes. The corrosion current density was then calculated using the Stern–Geary relationship based on the measured polarization resistance and Tafel coefficients, as shown in Equation 36 to 38. All electrochemical measurements were performed periodically throughout the exposure period to evaluate corrosion initiation and progression in cracked and uncracked UHPC specimens.

$$R_p = \frac{\Delta E}{\Delta I} \quad \text{(Equation 36)}$$

R_p: Polarization resistance (kΩ);
ΔE: Increment of voltage near corrosion potential (mV);
ΔI: Increment of current near corrosion potential (μA).

$$i_{corr} = \frac{B}{AR_p} \quad \text{(Equation 37)}$$

i_{corr}: corrosion current density (μA/cm^2);
B: Stern-Geary coefficient (mV);
A: Exposure area of working electrode (cm^2).

$$B = \frac{\beta_a \times \beta_c}{2.3(\beta_a + \beta_c)} \quad \text{(Equation 38)}$$

β_a: Tafel coefficient at anodic polarization (mV/decade);
β_c: Tafel coefficient at cathodic polarization (mv/decade).

6.1.3 Testing results

6.1.3.1 Self-healing behavior

The crack mouth closure rate was monitored throughout the 448-day exposure to evaluate the long-term self-healing performance of cracked UHPC specimens. Representative cracks with different initial crack widths were selected for Mixture A and Mixture B, and the closure rates over time are shown in Figure 6-4 and Figure 6-5, respectively.

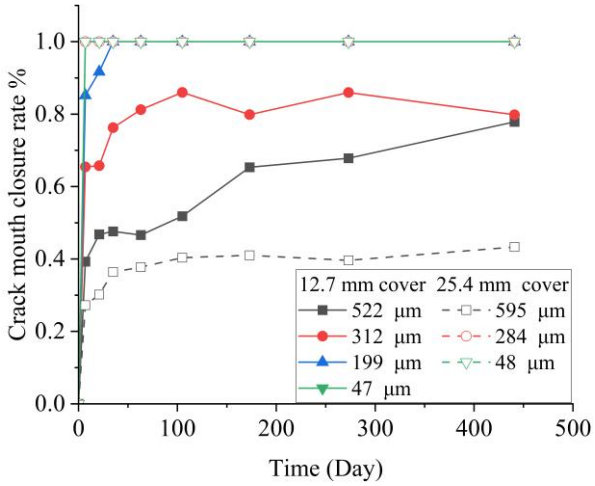

Figure 6-4 Self-healing behavior of Mixture A

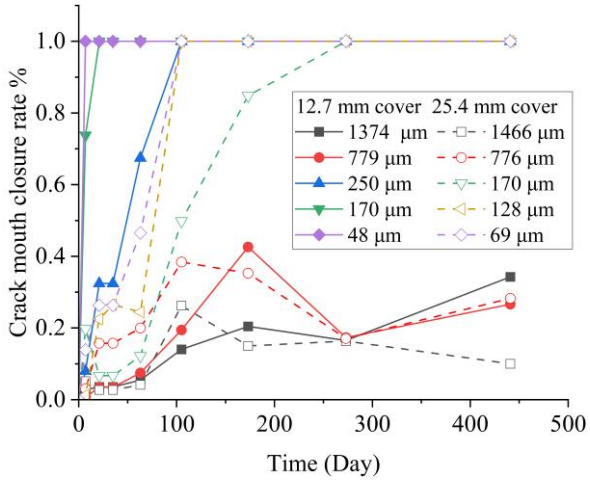

Figure 6-5 Self-healing behavior of Mixture B

For Mixture A, the crack mouth closure rate generally decreased with increasing crack width, as shown in Figure 6-4 Very tight cracks less than approximately 50 μm (0.002 in.) were fully sealed within the first 7 days of exposure and remained fully closed throughout the entire exposure period. Cracks with widths up to approximately 200 μm (0.008 in.) were also fully sealed within 35 days and maintained complete closure through 448 days. Cracks around 300 μm (0.012 in.) exhibited substantial but incomplete closure, reaching approximately 80.0–100% closure depending on cover thickness, with most closure occurring within the first 98 days and only minor additional closure afterward. Wider cracks in the range of 522–

595 μm (0.021–0.023 in.) showed limited healing, reaching approximately 43.3–77.9% closure by 448 days. For these larger cracks, gradual closure continued beyond the initial exposure period, indicating ongoing but slow self-healing over long-term exposure.

Mixture B exhibited a similar overall trend but with greater variability and generally lower healing efficiency for wider cracks, as shown in Figure 6-5. Tight cracks less than approximately 130 μm (0.005 in.) were fully sealed within 105 days and remained sealed throughout the remainder of the exposure. Cracks in the range of 170–250 μm (0.007–0.010 in.) showed significant healing and eventually reached complete closure after exposure of 63-173 days, although the healing process required a longer duration compared to Mixture A. In contrast, wider cracks around 780 μm (0.031 in.) and 1400 μm (0.055 in.) exhibited limited healing, reaching approximately 26.6-28.3% and 10–34.3% closure, respectively, by the end of the 448-day exposure. Most healing for Mixture B occurred within the first 105 days, with only gradual additional closure observed afterward.

For cracks larger than approximately 780 μm (0.031 in.), the crack mouth closure rate exhibited noticeable fluctuations during long-term exposure, as shown in Figure 6-5. Unlike tight cracks that showed stable and progressive closure, wider cracks demonstrated periods of apparent closure followed by partial reopening. This behavior is likely due to the nature of the healing products formed within large cracks. In wide cracks, a significant portion of the observed crack closure was caused by loosely bonded white precipitates originating from sedimentation and precipitation of minerals present in the exposure solution, rather than dense and well-integrated healing products formed from continued cement hydration or carbonation. These sediment-derived deposits may temporarily fill the crack mouth during immersion but can be partially removed, redistributed, or detached during drying cycles, resulting in fluctuating closure measurements. As a result, the apparent closure in wide cracks does not necessarily indicate permanent crack sealing, and these cracks remain more vulnerable to chloride ingress and corrosion propagation compared to narrower cracks that exhibit stable and durable self-healing.

Overall, the results demonstrate that crack width strongly influences self-healing performance in UHPC. Tight cracks less than approximately 200 μm (0.008 in.) showed complete closure and stable healing throughout the entire exposure period. Moderate cracks exhibited partial healing with gradual improvement over time, while wide cracks greater than approximately 500 μm (0.020 in.) showed limited closure even after long-term exposure. Additionally, Mixture A generally exhibited faster and more effective healing compared to Mixture B, likely due to differences in mixture composition and crack characteristics. These results indicate that UHPC possesses strong autogenous self-healing capacity, particularly for tight cracks, which may help maintain durability and delay corrosion initiation during long-term chloride exposure.

6.1.3.2 Corrosion potential

Corrosion potential, also referred to as open-circuit potential (OCP), was used to assess the thermodynamic tendency for corrosion initiation in the embedded steel reinforcement. In this study, corrosion potential was measured using an Ag/AgCl reference electrode and interpreted according to ASTM C876-22(ASTM C 876, 2022). It should be noted that corrosion potential does not directly represent the corrosion rate. The measured potential may be influenced by oxygen availability, moisture condition, chloride concentration, and concrete resistivity, particularly in dense cementitious mixtures such as UHPC.

Figure 6-6 shows the measured corrosion potential of the Mixture A and Mixture B specimens during the 448-day chloride wetting–drying exposure.

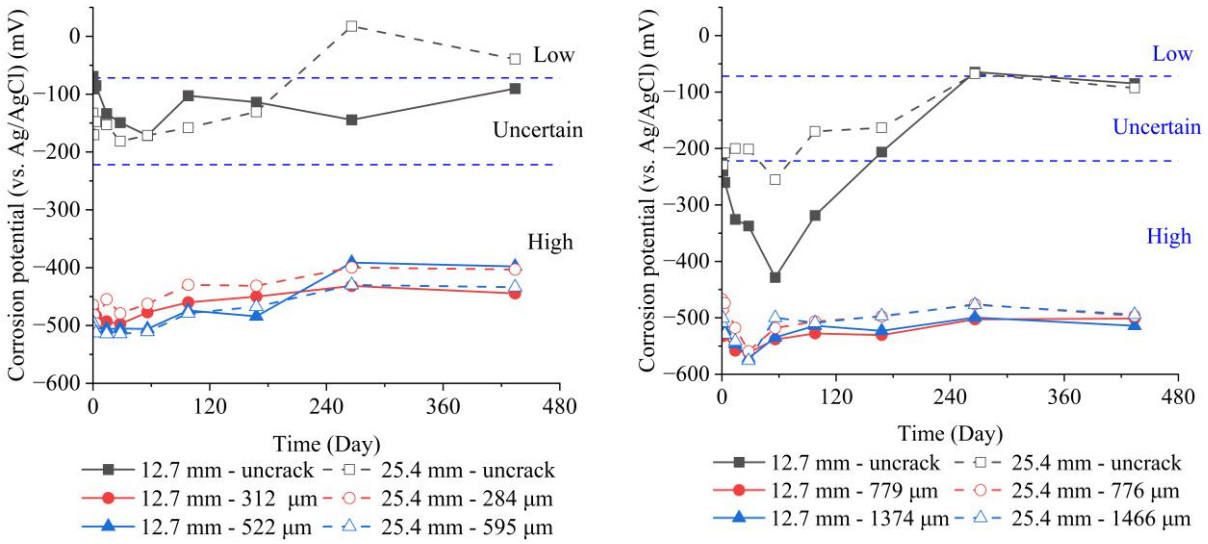

(a) Mixture A (b) Mixture B

Figure 6-6 Measured corrosion potential over time: (a) Mixture A and (b) Mixture B

The corrosion potential, E_{corr}, of the Mixture D specimens is shown in Figure 6-7. Figure 6-7(a) and 6-7(b) present the results for specimens with cover thicknesses of 12.7 mm (0.5 in.) and 25.4 mm (1.0 in.), respectively. The corrosion-risk classifications shown in the Figure 6-7are based on ASTM C876-22.

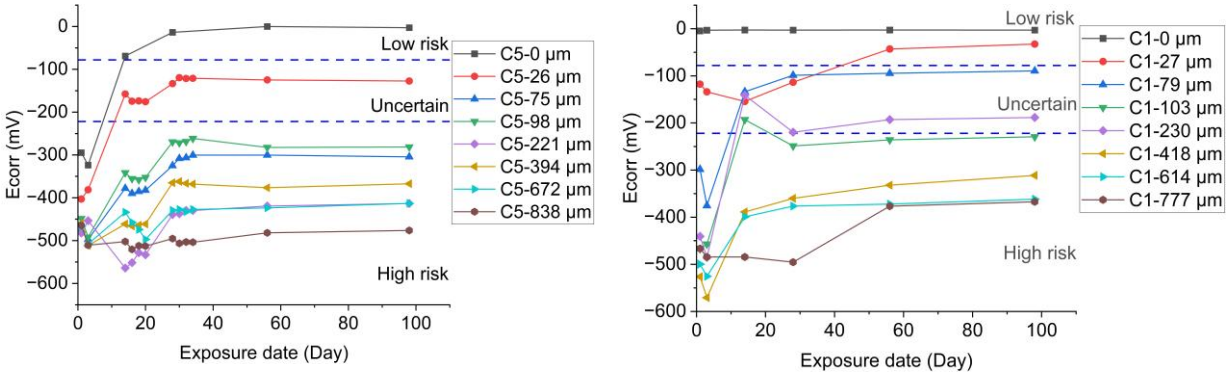

(a) E_{corr} for Mixture D with 12.7 mm (0.5 in.) cover

(b) E_{corr} for Mixture D with 25.4 mm (1.0 in.) cover

Figure 6-7 E_{corr} for Mixture D over time

For the uncracked specimens, both Mixture A and Mixture B generally remained within the low or uncertain corrosion-risk ranges throughout the exposure period. The corrosion potential gradually shifted in the positive, or more noble, direction after approximately 98 days of exposure. For example, the uncracked Mixture A specimen with a cover thickness of 25.4 mm (1.0 in.) increased from approximately −181 mV at Day 28 to approximately +17 mV on Day 266. This trend indicates stable passive conditions and effective protection provided by the dense UHPC matrix. Similar behavior was observed for the uncracked Mixture B specimens, confirming that uncracked UHPC provided strong resistance to chloride-induced corrosion during long-term exposure.

For the uncracked Mixture D specimen with a cover thickness of 12.7 mm (0.5 in.), E_{corr} shifted rapidly in the positive direction after approximately 14 days of exposure and eventually reached the low-corrosion-risk region. A similar positive shift was observed for Mixtures A and B; however, the change occurred more gradually in those specimens. In contrast, the uncracked Mixture D specimen with a cover thickness of 25.4 mm (1.0 in.) maintained an E_{corr}value close to 0 mV throughout the monitoring period. This result indicates that the embedded reinforcing steel was not measurably affected by the chloride-rich environment during the exposure period.

In contrast, the cracked specimens for Mixture A and Mixture B initially exhibited much more negative corrosion potentials, typically ranging from approximately −450 mV to −520 mV after exposure began. These values indicate a higher probability of localized depassivation at crack locations due to preferential chloride ingress through the cracks. However, the corrosion potentials of the cracked specimens also gradually shifted in the positive direction after approximately 98 days and remained relatively stable through 448 days. For example, the Mixture A specimen with a crack width of 522 μm (0.0206 in.) and a cover thickness of 12.7 mm (0.5 in.) improved from approximately −506 mV at Day 56 to approximately −391 mV at Day 266. Similar recovery trends were observed for Mixture B, although the corrosion potentials generally remained more negative because of the larger crack widths.

The gradual positive shift in corrosion potential of Mixture A and Mixture B suggests stabilization of the electrochemical condition at the steel surface during wetting–drying exposure. This behavior may be associated with self-healing and precipitation of healing products within cracks, which can reduce the transport of chloride ions and oxygen to the steel surface. In general, wider cracks resulted in more negative corrosion potentials, while thicker concrete cover provided slightly more positive values because of the longer transport path and greater protection around the embedded reinforcement.

For the cracked Mixture D specimens, E_{corr} also generally shifted toward more positive values with increasing exposure time, suggesting a gradual reduction in corrosion susceptibility or partial recovery of surface passivation during wetting–drying exposure. However, the final corrosion-risk classification depended strongly on both crack width and cover thickness. For specimens with a cover thickness of 12.7 mm (0.5 in.), only the uncracked specimen reached the low-risk region, whereas the cracked specimens remained within either the uncertain-risk or high-risk regions. For specimens with a cover thickness of 25.4 mm (1.0 in.), the uncracked specimen remained in the low-risk region, and the specimen with a crack width of 27 μm (0.0011 in.) also shifted into the low-risk region. Specimens with larger crack widths generally showed more negative E_{corr} values, indicating a higher probability of corrosion activity according to ASTM C876-22.

Figure 6-8 presents the relationship between E_{corr} and crack width for Mixtures A, B, and D. E_{corr} tended to shift to the negative direction as crack width increased. This trend indicates that wider cracks provide more direct pathways for chloride, moisture, and oxygen transport to the embedded steel reinforcement, thereby increasing the likelihood of corrosion initiation. Although some scatter was observed among the different mixtures, the results consistently show that crack width is a critical parameter governing the corrosion risk of reinforced UHPC exposed to chloride environments.

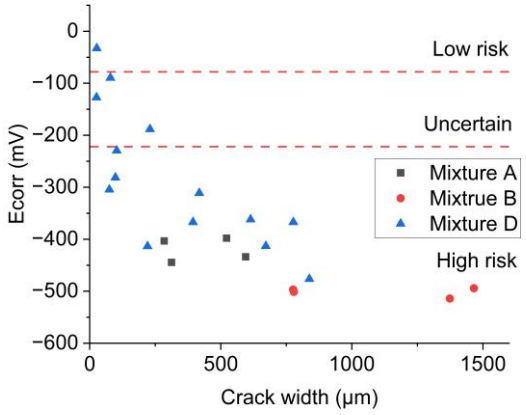

Figure 6-8 Relationship between E_{corr} and crack width for cracked reinforced UHPC specimens

The corrosion-potential results indicate that uncracked UHPC specimens maintained stable passive conditions during chloride wetting–drying exposure. Cracked specimens showed initial depassivation because cracks provided direct pathways for chloride ingress to the embedded reinforcement. However, the subsequent positive shift in corrosion potential suggests that electrochemical conditions at the steel surface gradually stabilized with time. The results also show that crack width and cover thickness are important factors controlling corrosion risk: larger cracks increased the probability of corrosion activity, while greater cover thickness improved protection of the embedded steel reinforcement.

6.1.3.3 Corrosion current density

Figure 6-9 compares the corrosion current density obtained from the linear polarization resistance (LPR) test using Tafel coefficients derived from Tafel extrapolation with the corrosion current density measured directly from the Tafel extrapolation method. Overall, good agreement was observed between the two methods, with only minor deviations. Similar discrepancies have been reported in previous studies and are attributed to differences in fitting range, signal sensitivity, and assumptions associated with each method (Ghafari *et al.*, 2015b; Fan, Teng, Tang, Kamal H. Khayat, *et al.*, 2021). In this study, corrosion current density obtained from the LPR test was used for subsequent analysis, as LPR is widely recognized as a reliable and commonly used method for monitoring corrosion activity in reinforced concrete systems. In addition, LPR is particularly suitable for UHPC due to its low corrosion rates and dense microstructure, which allow accurate and stable measurement of small corrosion current densities over long-term exposure without significantly disturbing the electrochemical condition at the steel surface.

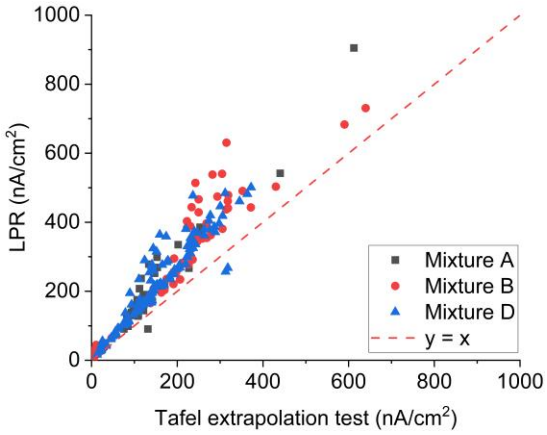

Figure 6-9 i_{corr} measured by LPR vs. Tafel polarization test

According to the Durar Network Specification (Durar, 1998), corrosion current density can be classified into different corrosion levels. Passive conditions correspond to corrosion current density less than 0.10 μA/cm² (0.645 μA/in.²), low corrosion corresponds to values between 0.10 and 0.50 μA/cm² (0.645 and 3.226 μA/in.²), high corrosion corresponds to values between 0.50 and 1.0 μA/cm² (3.226 and 6.452 μA/in.²), and very high corrosion corresponds to values greater than 1.0 μA/cm² (6.452 μA/in.²). These classifications provide a useful framework for evaluating corrosion severity and interpreting corrosion behavior during long-term exposure.

As shown in Figure 6-10, the steel rebar remained in stable passive condition for both uncracked Mixture A and Mixture B throughout the entire 434-day exposure period. The corrosion current density of uncracked Mixture A ranged from 10.1 to 33.4 nA/cm² (0.0065 to 0.0215 μA/in.²) for specimens with 12.7 mm (0.5 in.) cover thickness and from 6.4 to 33.4 nA/cm² (0.0041 to 0.0215 μA/in.²) for specimens with 25.4 mm (1.0 in.) cover thickness. Similarly, uncracked Mixture B exhibited corrosion current densities ranging from 6.6 to 44.5 nA/cm² (0.0043 to 0.0287 μA/in.²) and from 6.6 to 64.5 nA/cm² (0.0043 to 0.0416 μA/in.²) for cover thicknesses of 12.7 mm (0.5 in.) and 25.4 mm (1.0 in.), respectively. In all cases, corrosion current densities remained well below 100 nA/cm² (0.0645 μA/in.²), confirming that the steel rebar remained in a passive condition throughout the exposure period. These results indicate that UHPC provides excellent corrosion protection under uncracked conditions even after long-term chloride exposure.

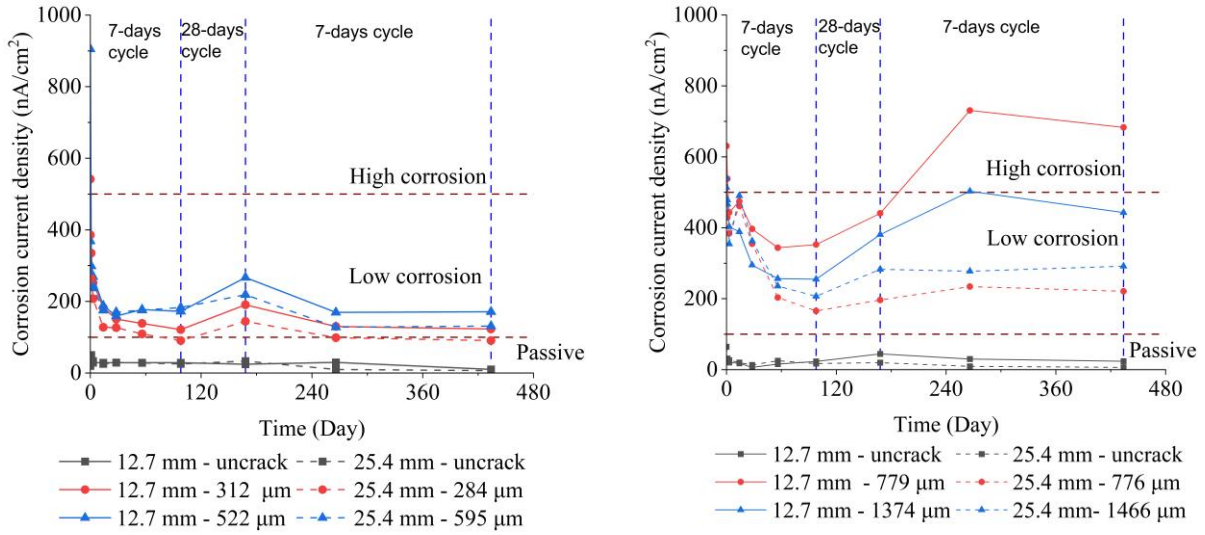

(a) Mixture A (a) Mixture B

Figure 6-10 Corrosion current density (i_{corr}) over exposure period

In addition, for the uncracked specimens of Mixture D, i_{corr} remained within the passive range for both cover thicknesses throughout the exposure period. The corrosion current density, i_{corr}, of Mixture D specimens with cover thicknesses of 12.7 mm (0.5 in.) and 25.4 mm (1.0 in.) is shown in Figure 6-11(a) and 6-11(b), respectively. For the cracked specimens, i_{corr} generally decreased with exposure time after initial fluctuations, indicating a gradual reduction in corrosion activity. This decrease was more pronounced for specimens with the larger cover thickness.

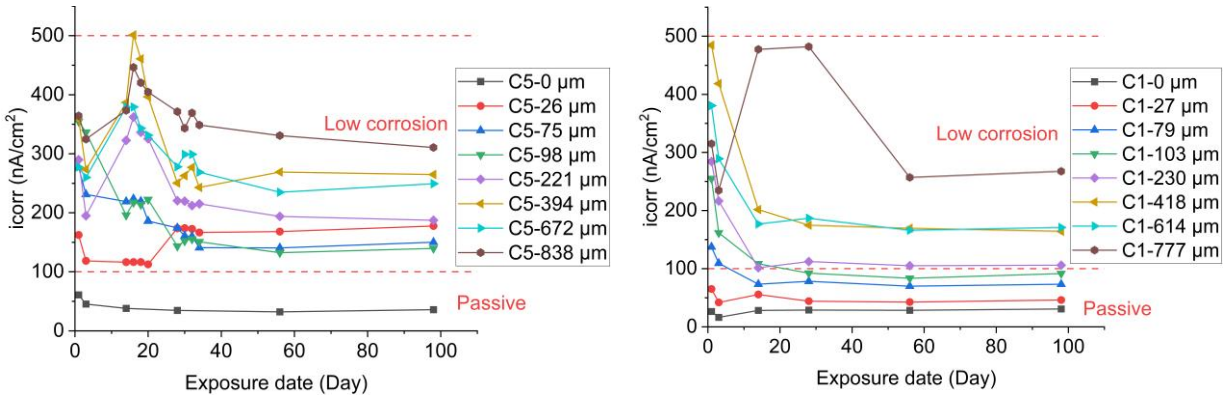

(a) i_{corr} for Mixture D with 12.7 mm (0.5 in.) cover

(b) i_{corr} for Mixture D with 25.4 mm (1.0 in.) cover

Figure 6-11 Corrosion current density (i_{corr}) of embedded reinforcing steel in Mixture D specimens during chloride wetting–drying exposure

In contrast, cracked specimens exhibited significantly higher corrosion current densities, particularly during the initial exposure stage. For Mixture A, initial corrosion current density ranged from 368.5 to 905.2 nA/cm² (0.238 to 0.584 µA/in.²) at Day 0, indicating active corrosion immediately after chloride exposure. However, corrosion current density decreased rapidly within the first 28 days, reaching values between 126.6 and 170.0 nA/cm² (0.082 to 0.110 µA/in.²) for specimens with 25.4 mm (1.0 in.) cover thickness and between 150.7 and 159.3 nA/cm² (0.097 to 0.103 µA/in.²) for specimens with 12.7 mm (0.5 in.) cover thickness. During long-term exposure, corrosion current density remained relatively stable or showed gradual reduction. At Day 266, corrosion current density ranged from 98.8 to 128.1 nA/cm² (0.064 to 0.083 µA/in.²) for specimens with 25.4 mm (1.0 in.) cover thickness, and from 130.2 to 169.5 nA/cm² (0.084 to 0.109 µA/in.²) for specimens with 12.7 mm (0.5 in.) cover thickness. By Day 434, corrosion current density further decreased to 90.8 to 131.1 nA/cm² (0.059 to 0.085 µA/in.²) and 123.0 to 171.0 nA/cm² (0.079 to 0.110 µA/in.²) for specimens with 25.4 mm (1.0 in.) and 12.7 mm (0.5 in.) cover thickness, respectively. These results indicate that corrosion activity decreased and stabilized over long-term exposure.

Mixture B exhibited similar initial trends but showed greater fluctuations due to larger crack widths. Initial corrosion current density ranged from 437.2 to 630.7 nA/cm² (0.282 to 0.407 µA/in.²) at Day 0. After 98 days, corrosion current density decreased to 165.6 to 352.6 nA/cm² (0.107 to 0.227 µA/in.²). However, during extended exposure, some specimens showed temporary increases. For example, the specimen with 12.7 mm (0.5 in.) cover thickness exhibited an increase from 352.6 nA/cm² (0.227 µA/in.²) at Day 98 to 730.9 nA/cm² (0.472 µA/in.²) at Day 266, followed by a decrease to 683.2 nA/cm² (0.441 µA/in.²) at Day 434. Specimens with 25.4 mm (1.0 in.) cover thickness showed more stable behavior, with corrosion current density ranging from 165.6 to 291.7 nA/cm² (0.107 to 0.188 µA/in.²) after 98 days.

The reduction in corrosion current density over time could be attributed to continued hydration and autogenous self-healing of cracks, which reduced transport of chloride, oxygen, and moisture to the steel surface. The oxygen is insufficient to sustain corrosion propagation. Continued hydration and precipitation of healing products refined the microstructure and increased electrical resistivity, limiting electrochemical reactions at the steel surface. However, specimens with larger crack widths exhibited fluctuating corrosion current densities due to incomplete and unstable crack sealing and oxygen supply.

Furthermore, the cracked specimens of Mixture D could be divided into three groups based on crack width after 98 days of 7-day wetting–drying cycles. For specimens with a 25.4 mm (1.0 in.) cover, cracks

smaller than approximately 200 μm (0.0079 in.) returned to the passive range after 56 days of exposure. Specimens with crack widths of approximately 400–700 μm (0.0157–0.0276 in.) had final i_{corr}values of about 164–171 nA/cm², while the specimen with a crack width larger than 800 μm (0.0315 in.) showed an i_{corr}greater than 267 nA/cm². For specimens with a 12.7 mm (0.5 in.) cover, the corresponding i_{corr}values were higher. Specimens with cracks up to approximately 200 μm (0.0079 in.) had final i_{corr}values of about 139–187 nA/cm², specimens with crack widths of approximately 400–700 μm (0.0157–0.0276 in.) had values of about 249–264 nA/cm², and the specimen with a crack width larger than 800 μm (0.0315 in.) had an i_{corr}greater than 310 nA/cm².

In addition, Figure 6-12 shows the relationship between i_{corr} and crack width for cracked UHPC specimens made with Mixtures A, B, and D after 98 days of wetting–drying exposure. In general, i_{corr} increased with increasing crack width, indicating that wider cracks promoted greater chloride and moisture access to embedded steel reinforcements. The results also show that cover thickness affected the corrosion response: for similar crack-width ranges, specimens with a 25.4 mm (1.0 in.) cover generally exhibited lower corrosion current densities than those with a 12.7 mm (0.5 in.) cover. These results confirm that both crack width and cover thickness are important parameters governing corrosion risk in reinforced UHPC exposed to chloride wetting–drying conditions.

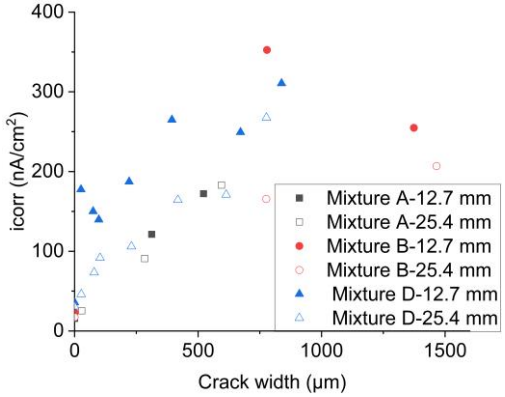

Figure 6-12 Relationship between i_{corr} and crack width for cracked reinforced UHPC specimen

6.1.3.4 Correlation between corrosion potential and current density

Figure 6-13 compares corrosion potential and corrosion current density and shows that the potential-based risk categories do not consistently correspond to the measured corrosion current density. Although ASTM criteria (ASTM G109, 2021; ASTM C 876, 2022; ASTM G01 Committee, 2024) provide a convenient framework for assessing corrosion risk based on corrosion potential, several specimens classified as high risk based on corrosion potential exhibited low corrosion current densities. This discrepancy indicates that corrosion potential alone may not accurately represent corrosion activity in cracked UHPC.

These results suggest that existing corrosion potential criteria developed for conventional concrete may not be directly applicable to UHPC due to its dense microstructure, high electrical resistivity, and self-healing capability. Therefore, corrosion potential should be interpreted together with corrosion current density for more reliable assessment of corrosion behavior in UHPC. Furthermore, there is a need to develop new corrosion assessment specifications and predictive models specifically for UHPC to improve the accuracy of corrosion evaluation and enable more reliable service life prediction of UHPC structures.

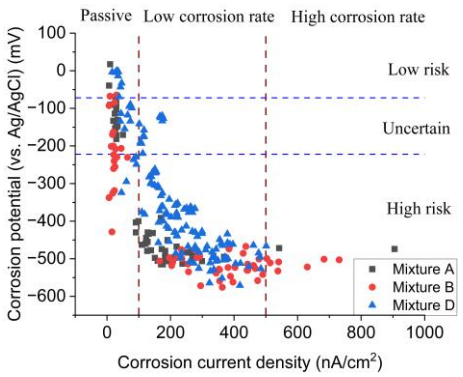

Figure 6-13 Corrosion potential versus corrosion current density

6.1.3.5 Galvanic corrosion within cracked UHPC

To evaluate the possible influence of galvanic corrosion at the stainless-steel–carbon-steel connection, two companion specimens with a cover thickness of 12.7 mm (0.5 in.) were prepared without epoxy coating at the connection joint. These specimens were included because the stainless-steel–carbon-steel connections in Mixtures A and B were not epoxy-coated; therefore, it was necessary to determine whether the absence of epoxy coating at the dissimilar-metal connection could influence the measured electrochemical response or introduce galvanic corrosion effects. The results are shown in Figure 6-14. In the specimen designation, "C" indicates that the stainless-steel–carbon-steel connection was coated with epoxy, whereas "R" indicates that the connection was not coated. The number "5" denotes a cover thickness of 12.7 mm (0.5 in.), and the final number represents the measured primary crack width in micrometers.

As shown in Figure 6-14 (a), the specimens without epoxy coating, R5-23 μm and R5-435 μm, generally exhibited slightly more positive E_{corr}values than the corresponding coated specimens, C5-26 μm and C5-394 μm. However, Figure 6-14 (b) shows that the uncoated specimens did not exhibit higher i_{corr}values. Instead, their i_{corr}values were comparable to or lower than those of the coated specimens with similar crack widths. Therefore, no evidence of accelerated galvanic corrosion was observed at the uncoated stainless-steel–carbon-steel connection under the test conditions.

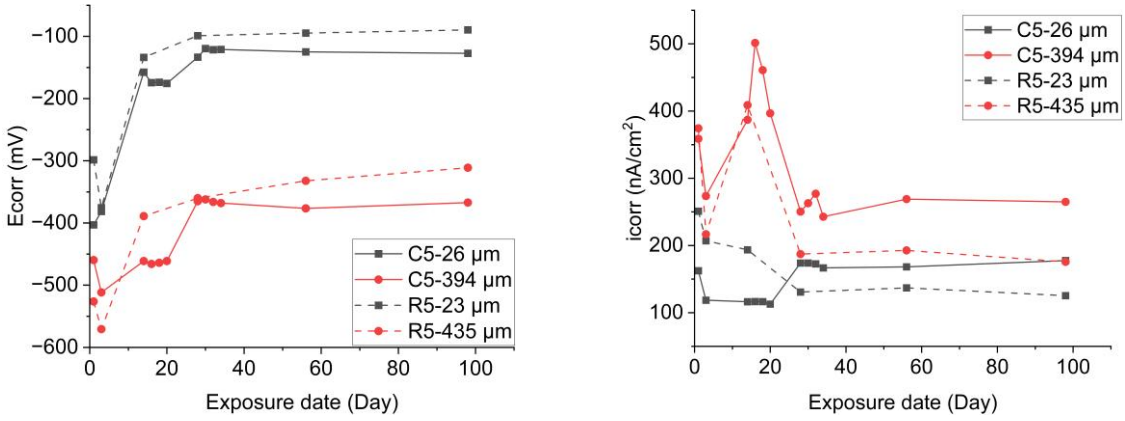

(a) E_{corr} (b) i_{corr}

Figure 6-14 Corrosion for specimens without epoxy coating at stainless steel – steel rebar connection

The slightly more positive E_{corr}values measured for the uncoated specimens may be attributed to a mixed-potential effect caused by electrical coupling between the stainless steel and the carbon-steel

reinforcement. Because stainless steel typically has a more noble corrosion potential than carbon steel, the measured potential may shift in the positive direction and slightly underestimate the corrosion condition of the carbon-steel reinforcement. Therefore, although galvanic corrosion was not evident in this study, epoxy coating at the stainless steel/carbon steel connection is still recommended to minimize mixed-potential effects and improve the reliability of electrochemical measurements.

6.1.4 Summary

The following conclusions can be drawn from the laboratory chloride wetting–drying exposure tests on reinforced UHPC specimens. Mixtures A and B were exposed to 3.5 wt.% NaCl wetting–drying cycles for up to 448 days, while Mixture D was exposed to the same chloride solution for 98 days. Although the exposure durations and specimen configurations were different, the results showed consistent trends in the corrosion behavior of steel reinforcement embedded in cracked and uncracked UHPC.

1. Uncracked UHPC provided strong corrosion protection under chloride exposure. For Mixtures A and B, the corrosion current densities of uncracked specimens remained within the passive range throughout the 448-day exposure period, ranging from 6.4 to 64.5 nA/cm² (0.041 to 0.416 μA/in.²). Corrosion potentials also generally remained within the low or uncertain corrosion-risk ranges. Similar behavior was observed for the uncracked Mixture D specimens during the 98-day exposure period. These results indicate that dense UHPC can effectively protect embedded steel reinforcement under chloride wetting–drying exposure, even with a cover thickness as low as 12.7 mm (0.5 in.) when no cracking is present.
2. Cracking increased corrosion activity at the beginning of exposure, but corrosion activity generally decreased with time. Cracked specimens initially exhibited more negative corrosion potentials and higher corrosion current densities than uncracked specimens. For Mixtures A and B, corrosion current density reached values as high as 905.2 nA/cm² (5.84 μA/in.²) immediately after chloride exposure, indicating active corrosion at crack locations. However, the corrosion current density decreased rapidly during the early exposure period and then stabilized at lower levels. A similar trend was observed for most cracked Mixture D specimens, where corrosion activity decreased during the 98-day wetting–drying exposure. These results suggest that corrosion initiation can occur at cracks, but corrosion propagation in UHPC may remain limited over time.
3. Crack width was the primary factor controlling corrosion performance. The results from both exposure programs showed that corrosion activity increased with increasing crack width. For Mixtures A and B, specimens with crack widths of approximately 284 to 312 μm (0.011 to 0.012 in.) generally maintained low corrosion levels after long-term exposure, whereas specimens with crack widths greater than approximately 776 μm (0.031 in.) exhibited higher corrosion current densities. For Mixture D, specimens with smaller cracks and 25.4 mm (1.0 in.) cover showed lower corrosion activity, while specimens with larger cracks remained more susceptible to corrosion.
4. Cover thickness improved corrosion resistance, but its effect was secondary to crack width. Increasing the reinforcement cover thickness from 12.7 mm (0.5 in.) to 25.4 mm (1.0 in.) generally reduced corrosion activity, particularly in cracked specimens. The larger cover thickness increased the transport path for chloride ions and moisture and reduced electrolyte access to the steel surface. However, the effect of cover thickness was less dominant than the effect of crack width. A specimen with a smaller crack and thinner cover may therefore show lower corrosion activity than a specimen with a wider crack and thicker cover.
5. Corrosion potential should not be used alone to evaluate corrosion activity in UHPC. Several cracked UHPC specimens were classified as having high corrosion risk based on corrosion potential, but their measured corrosion current densities remained low. This discrepancy is likely caused by the dense microstructure, high electrical resistivity, limited oxygen transport, and self-

healing capacity of UHPC. Therefore, corrosion potential is useful for identifying possible corrosion risk, but it should be interpreted together with corrosion current density, crack condition, and cover thickness.

6. Autogenous self-healing contributed to the reduction in corrosion activity. The decrease in corrosion current density and the positive shift in corrosion potential over time are likely associated with autogenous self-healing and precipitation of healing products inside cracks. These processes reduce the transport of chloride ions, oxygen, and moisture to the steel surface. Tight cracks smaller than approximately 200 μm (0.0079 in.) were more likely to seal effectively and return to passive or low-corrosion conditions. Wider cracks showed only partial healing, but even partial crack closure helped reduce corrosion activity during continued exposure.
7. No clear evidence of accelerated galvanic corrosion was observed in the Mixture D specimens. The Mixture D test program included companion specimens without epoxy coating at the carbon-steel/stainless-steel connection to evaluate the possible influence of galvanic corrosion. Within the 98-day exposure period, no clear evidence of accelerated galvanic corrosion was observed. However, epoxy coating at the connection is still recommended to reduce uncertainty and improve the reliability of electrochemical measurements.
8. Existing corrosion assessment criteria developed for conventional concrete may not be directly applicable to UHPC. The results showed that UHPC specimens can exhibit corrosion potentials associated with high corrosion risk while maintaining low corrosion current density. This behavior differs from typical reinforced conventional concrete and reflects the unique transport properties, high electrical resistivity, and self-healing capacity of UHPC. Therefore, corrosion assessment criteria and service-life prediction models specifically developed for UHPC are needed.

Overall, the laboratory wetting–drying exposure programs confirm that UHPC provides strong resistance to corrosion propagation under chloride exposure. Uncracked UHPC maintained passive steel conditions, while cracked UHPC showed initial corrosion activity followed by gradual stabilization. Crack width was the primary factor controlling corrosion performance, cover thickness provided additional protection, and self-healing helped reduce long-term corrosion activity.

6.2 Tidal zone marine exposure

6.2.1 Sample preparation

The second batch of reinforced UHPC specimens was prepared for field exposure in the tidal zone at Seahorse Key Island. This batch consisted of four prismatic reinforced UHPC specimens fabricated using Mixtures A, B, C, and D. Each specimen had dimensions of 203.2 mm × 203.2 mm × 914.4 mm (8 in. × 8 in. × 36 in.), as illustrated in Figure 6-15.

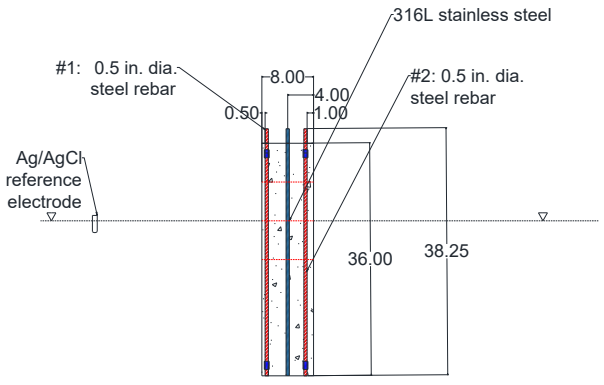

Figure 6-15 Testing scheme of cracked UHPC column at Seahorse Key Island

Each specimen contained two embedded No. 4 Grade 60 black steel reinforcing bars, with one bar positioned near each side surface of the UHPC prism. The carbon-steel reinforcing bars had a diameter of 12.7 mm (0.5 in.) and a length of 838.2 mm (33 in.). 316L stainless-steel threaded rods with dimensions of 12.7 mm × 95.25 mm (0.5 in. × 3.75 in.) and 12.7 mm × 38.1 mm (0.5 in. × 1.5 in.) were connected to the ends of the carbon-steel bars using 316L stainless-steel couplers with a length of 19.05 mm (0.75 in.). The embedded carbon-steel reinforcing bars served as working electrodes during corrosion monitoring.

The reinforcement cover thicknesses were 12.7 mm (0.5 in.) on one side and 25.4 mm (1.0 in.) on the opposite side. The side with the 12.7 mm (0.5 in.) cover was selected as the cracking side. In addition, a stainless-steel bar with a diameter of 12.7 mm (0.5 in.) and a length of 971.6 mm (38.25 in.) was embedded at the center of each UHPC specimen and served as the counter electrode during electrochemical measurements.

The embedded carbon-steel reinforcing bars were prepared using the same surface preparation procedure described for the laboratory wetting–drying specimens. The bottom surface of each UHPC specimen was also sealed with Sikadur 31 epoxy to prevent chloride ingress along the steel–UHPC interface.

After curing under ambient laboratory conditions for 30 to 60 days, the specimens were cracked using third-point bending. A span length of 838.2 mm (33 in.) and a displacement rate of 0.20 mm/min (0.0079 in./min) were used. The target crack width was defined as the primary crack width corresponding to 80% of the peak displacement during flexural loading. Because of the large self-weight of the specimens, crack widths could only be estimated from measurements taken on the two side surfaces perpendicular to the cracking surface during the tests. Therefore, deviations between the target crack width and the residual primary crack width were unavoidable during crack generation. The crack characteristics of the UHPC specimens exposed at Seahorse Key Island are summarized in Table 6-2.

Table 6-2 Crack characteristics of UHPC specimens exposed at Seahorse Key Island

Mixture	Target crack width (μm/ in.)	Residual primary crack width (μm/ in.)
Mixture A	422/ 0.0166	447
Mixture B	1411/ 0.0555	603
Mixture C	287/ 0.0113	309
Mixture D	467/ 0.0184	771

6.2.2 Exposure environment

For the field exposure at Seahorse Key Island, all four reinforced UHPC specimens were placed in the tidal zone on the lee side of the island, as shown in Figure 6-16 (a). The exposure site is characterized by semi-diurnal tidal behavior, resulting in repeated wetting and drying approximately every 12.4 h. Based on the tidal conditions, the specimens were estimated to experience approximately 4 to 8 h of seawater wetting followed by approximately 4 to 8 h of atmospheric drying during each tidal cycle. The annual air temperature at the site typically ranges from approximately 5 to 32 °C (41 to 90 °F), while summer temperatures commonly exceed 30 °C (86 °F). The presence of oyster beds and marine biological growth on and near the specimens, as shown in Figure 6-16(b), further indicates sustained saline tidal-water conditions and continuous marine chloride exposure. In addition, a very thin biofilm layer was observed on the cracked surfaces, as shown in Figure 6-16 (c), which interfered with crack-mouth closure monitoring and reduced the reliability of crack-closure rate measurements.

(a) Tide zone

(b) Oyster growth on specimens after 6 months of exposure

(c) Biofilm on cracked surface.

Figure 6-16 Exposure site and marine exposure conditions at Seahorse Key Island

6.2.3 Testing results

6.2.3.1 Self-healing behavior

The self-healing performance of the field-exposed UHPC specimens was evaluated using the crack mouth closure rate, as shown in Figure 6-17. After 270 days of marine exposure, the specimen with a primary crack width of 309 μm (0.0122 in.) exhibited complete crack-mouth closure. In contrast, specimens with larger primary crack widths of 447–771 μm (0.0176–0.0304 in.) showed only partial sealing. The crack mouth closure rate decreased as the primary crack width increased, from 100% for the fully sealed 309 μm (0.0122 in.) crack to 50% and 32% for cracks with widths of 447 μm and 771 μm (0.0176 and 0.0304 in.), respectively. This result indicates that the self-healing capacity of UHPC under marine exposure was strongly affected by the initial primary crack width, with narrower cracks showing a greater likelihood of complete closure. After approximately 180 days of exposure, sediment and biofilm accumulation on the cracked surfaces made crack tracing difficult; therefore, only the primary crack that could be consistently identified was used for self-healing evaluation.

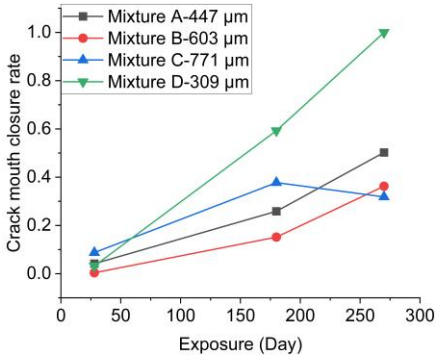

Figure 6-17 Self-healing indicator of cracked UHPC specimens exposed to the marine environment at Seahorse Key Island

6.2.3.2 Corrosion potential and corrosion current density

After 270 days of exposure, the corrosion potential, E_{corr}, of the cracked specimens indicated a high corrosion risk, as shown in Figure 6-18(a). Following cracking, E_{corr} shifted significantly in the negative direction, decreasing from an initial range of −67.3 to 186.4 mV to approximately −326.9 to −532.2 mV. As the crack width increased, E_{corr} generally became more negative, changing from −410.4 to −480.7 mV after 270 days of exposure. However, some fluctuation was observed for the specimen with a crack width of approximately 771 μm (0.0304 in.).

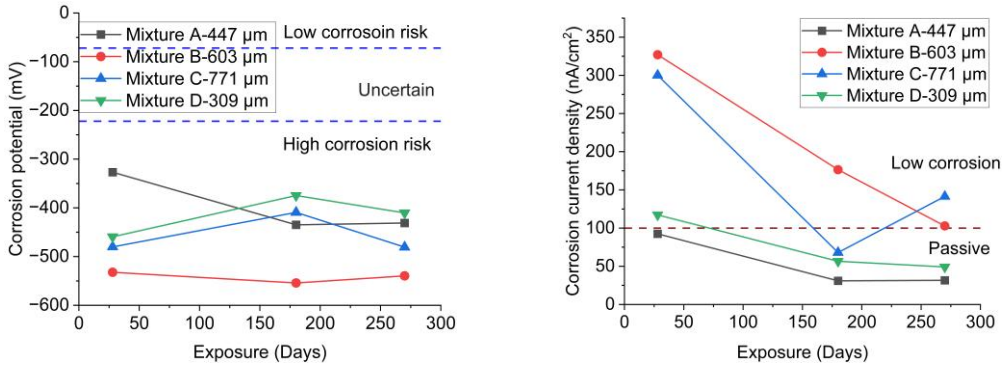

(a) E_{corr} (b) i_{corr}

Figure 6-18 Corrosion for specimens exposed to Seahorse Key Island

6.2.3.3 Correlation between corrosion current density to primary crack width

During exposure, the corrosion current density, i_{corr}, of specimens with crack widths below approximately 603 μm (0.0237 in.) gradually decreased from an initial range of 92.5–327.0 nA/cm² (596.8–2109.7 nA/in.²) to 31.6–141.5 nA/cm² (203.9–912.9 nA/in.²), as shown in Figure 6-18 (b), indicating a transition toward a passive condition. In contrast, the specimen with a larger crack width of approximately 771 μm (0.0304 in.) showed fluctuations in i_{corr} during exposure. After 270 days, i_{corr} increased from 31.64 to 141.5 nA/cm² (204.1 to 912.9 nA/in.²) as the crack width increased from 309 to 771 μm (0.0122 to 0.0304 in.), suggesting that wider cracks promoted higher corrosion activity.

Overall, the cracked specimens subjected to indoor wetting–drying cycles exhibited higher measured i_{corr}values than those exposed to a realistic marine environment, as shown in Figure 6-19, possibly due to the more aggressive or concentrated exposure conditions used in the laboratory cycles.

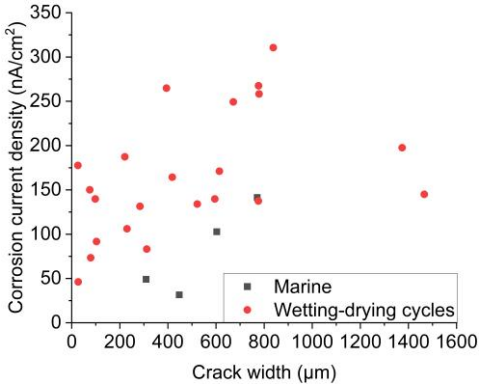

Figure 6-19 i_{corr} for specimens exposed to indoor wetting-drying cycles and realistic marine environment

6.2.4 Summary

The realistic marine exposure results at Seahorse Key Island showed that cracked UHPC also performed well under tidal chloride exposure for 270 days. Crack self-healing was observed in all monitored specimens, with the specimen having an initial crack width of approximately 309 μm (0.0122 in.) achieving complete crack-mouth closure. Specimens with larger cracks, ranging from approximately 447 to 771 μm (0.0176 to 0.0304 in.), showed partial closure, indicating that the self-healing capacity decreased as initial crack width increased. Although corrosion potential measurements indicated a high probability of corrosion after cracking, the measured corrosion current densities remained low or

decreased during exposure for specimens with crack widths below approximately 603 μm. After 270 days, corrosion current density increased with crack width, confirming that wider cracks allowed greater chloride and moisture access to the embedded reinforcement. Compared with the indoor wetting–drying exposure, the marine-exposed specimens generally exhibited lower corrosion current densities, suggesting that the laboratory wetting–drying cycles created a more aggressive exposure condition.

7 Conclusion and recommendations

7.1 Conclusion

This project evaluated chloride transport, crack self-healing, and corrosion performance of reinforced UHPC under uncracked, single-cracked, and multi-cracked conditions. The investigation included electric chloride migration testing, long-term bulk chloride exposure using 16.5 wt.% NaCl solution, controlled laboratory wetting–drying exposure using 3.5 wt.% NaCl solution, and realistic marine tidal exposure at Seahorse Key Island. The following project-level conclusions can be drawn from the combined results.

1. Uncracked UHPC provided excellent resistance to chloride ingress and reinforcement corrosion. The uncracked UHPC matrix showed very limited chloride penetration under both accelerated migration and bulk chloride exposure conditions. Apparent chloride diffusion coefficients for uncracked UHPC were on the order of 10^{-14} m²/s (10^{-13} ft²/s), confirming the very low permeability of the dense UHPC matrix. In the reinforced corrosion specimens, uncracked UHPC maintained passive corrosion conditions during chloride wetting–drying exposure. For Mixtures A and B, corrosion current densities of uncracked specimens remained within the passive range throughout the 448-day exposure period, ranging from 6.4 to 64.5 nA/cm² (0.041 to 0.416 μA/in.²). Similar passive behavior was observed for uncracked Mixture D specimens during the 98-day exposure period. These results indicate that intact UHPC provides strong protection for embedded steel reinforcement, even with cover thicknesses as low as 12.7 mm (0.5 in.) under the exposure conditions investigated.
2. Cracking changed the dominant chloride transport mechanism from matrix-controlled diffusion to crack-assisted ingress. The results showed that chloride penetration in cracked UHPC was concentrated near cracks, while the surrounding uncracked matrix remained highly resistant to chloride ingress. In single-cracked specimens, cracks acted as preferential transport pathways and increased the apparent chloride diffusion coefficient in the cracked region by approximately two to three orders of magnitude compared with uncracked UHPC, reaching values on the order of 10^{-12} to 10^{-11} m²/s. Therefore, once cracking occurred, chloride transport was no longer controlled only by the intrinsic permeability of the UHPC matrix, but also by the properties of the crack.
3. Autogenous self-healing reduced chloride ingress and corrosion activity, but it did not fully restore the cracked region to the same resistance as the uncracked matrix. Self-healing was observed in both laboratory and field exposure conditions. Narrow cracks showed greater healing efficiency, while wider cracks generally showed only partial closure. In the field-exposed specimens at Seahorse Key Island, the specimen with an initial crack width of approximately 309 μm (0.0122 in.) achieved complete crack-mouth closure, while specimens with larger cracks, ranging from approximately 447 to 771 μm (0.0176 to 0.0304 in.), showed partial closure. The chloride transport results also showed that surface-healed cracks reduced chloride ingress but did not completely prevent it, suggesting that the healing products were less impermeable than the original UHPC matrix. Overall, self-healing improved durability performance, but its effectiveness depended strongly on crack width, crack configuration, and mixture characteristics such as fiber distribution.
4. Cracking increased the probability of corrosion initiation, but UHPC limited long-term corrosion propagation in many cracked specimens. Cracked reinforced UHPC specimens initially exhibited more negative corrosion potentials and higher corrosion current densities than uncracked specimens, indicating localized depassivation at crack locations. For Mixtures A and B, corrosion current density reached values as high as 905.2 nA/cm² (5.84 μA/in.²) shortly after chloride exposure. However, corrosion current density generally decreased rapidly during the early exposure period and then stabilized at lower levels during continued wetting–drying exposure. Similar behavior was observed for most cracked Mixture D specimens during the 98-day exposure period. These results indicate that cracking can initiate corrosion activity, but the dense

UHPC matrix, limited transport capacity, and self-healing response can reduce corrosion propagation over time.

5. Crack width was the primary factor controlling corrosion performance. The combined laboratory and field results showed that corrosion activity increased with increasing crack width. For Mixtures A and B, specimens with crack widths of approximately 284 to 312 μm (0.011 to 0.012 in.) generally maintained low corrosion levels after long-term exposure, while specimens with crack widths greater than approximately 776 μm (0.031 in.) showed higher corrosion current densities. In the Seahorse Key Island exposure, corrosion current density after 270 days also increased with crack width.
6. Reinforcement cover thickness improved corrosion resistance, but its effect was secondary to crack characteristics. Increasing the cover thickness from 12.7 mm (0.5 in.) to 25.4 mm (1.0 in.) generally reduced corrosion activity, particularly in cracked specimens. The larger cover thickness increased the transport path for chloride ions and moisture and reduced direct electrolyte access to the steel surface. However, the results showed that crack width had a stronger influence than cover thickness. A specimen with a smaller crack and thinner cover could perform better than a specimen with a wider or more connected crack and thicker cover. Therefore, crack control is more critical than cover thickness alone for improving the corrosion performance of reinforced UHPC.
7. The controlled laboratory wetting–drying exposure provided a conservative, chloride-rich exposure condition compared with the field tidal exposure. The Seahorse Key Island field exposure results showed that cracked UHPC performed well under realistic marine tidal conditions during the 270-day exposure period. Although corrosion potential measurements indicated a high probability of corrosion after cracking, measured corrosion current densities remained low or decreased during exposure for specimens with crack widths below approximately 603 μm (0.0237 in.). Field-exposed specimens generally exhibited lower corrosion current densities than specimens subjected to the indoor wetting–drying exposure. These results suggest that the controlled laboratory wetting–drying cycles created a more aggressive exposure condition than the natural tidal environment used in this project.
8. Corrosion potential alone may not be sufficient to evaluate corrosion activity in UHPC. Several cracked UHPC specimens were classified as having a high probability of corrosion based on corrosion potential, while their measured corrosion current densities remained low. This discrepancy is likely related to the dense microstructure, high electrical resistivity, restricted oxygen transport, and self-healing capacity of UHPC. Therefore, corrosion potential should be used as an indicator of possible corrosion risk, but it should not be used alone to evaluate corrosion activity in UHPC. A more reliable assessment should combine corrosion potential, corrosion current density, crack characteristics, cover thickness, chloride transport behavior, and exposure condition.
9. No clear evidence of accelerated galvanic corrosion was observed at the carbon-steel/stainless-steel connection in Mixture D specimens. The Mixture D test program included companion specimens without epoxy coating at the carbon-steel/stainless-steel connection to evaluate the possible influence of galvanic corrosion. Within the 98-day laboratory exposure period, no clear evidence of accelerated galvanic corrosion was observed. However, applying epoxy coating at the connection remains recommended because it reduces uncertainty, limits unintended corrosion at the connection region, and improves the reliability of electrochemical measurements.
10. Existing chloride transport and corrosion assessment criteria developed for conventional concrete may not be directly applicable to UHPC. The results showed that UHPC behaves differently from conventional concrete because of its dense matrix, low chloride diffusivity, high electrical resistivity, and self-healing capability. In particular, cracked UHPC can show corrosion potentials associated with high corrosion risk while maintaining low corrosion current density. Similarly, chloride ingress in cracked UHPC is controlled not only by crack width but also by crack

geometry, crack interaction, and healing behavior. Therefore, durability assessment methods and service-life prediction models for UHPC should explicitly account for crack characteristics, self-healing, cover thickness, and exposure condition instead of directly applying criteria developed for conventional reinforced concrete.

Overall, this project confirms that UHPC provides strong resistance to chloride ingress and reinforcement corrosion, especially when the matrix remains uncracked or when cracks are narrow enough to promote effective self-healing. Cracks provide preferential pathways for chloride transport and can initiate localized corrosion, but corrosion propagation is often limited by the dense UHPC matrix and healing of the crack region. Crack width, crack connectivity, and crack network geometry are the most important factors controlling long-term durability, while cover thickness provides additional protection. These findings support the use of UHPC in chloride-rich environments, provided that crack development is controlled and UHPC-specific durability assessment methods are used.

7.2 Recommendation

For UHPC under direct chloride exposure, the recommended action levels for UHPC specimens with cover greater than 25.4 mm (1.0 in.) are shown in Table 7-1. For uncracked UHPC specimens, the corrosion resistance provided by 12.7 mm (0.5 in.) UHPC cover was similar to that provided by 25.4 mm (1.0 in.) cover. However, after cracking, the 25.4 mm (1.0 in.) cover showed much better corrosion resistance than the 12.7 mm (0.5 in.) cover.

Based on these results, a nominal cover of at least 25.4 mm (1.0 in.) is recommended for UHPC members with black steel reinforcement under direct chloride exposure, in order to ensure adequate performance after cracking. Where additional conservatism is desired, the values recommended in the French AFGC guide specification, *Ultra-High Performance Fibre-Reinforced Concrete — Interim Recommendations* (in French: *Bétons Fibrés à Ultra-hautes Performances — Recommandations provisoires*) (AFGC/SETRA Working Group, 2002; Islam, Zhang and Jin, 2022), 32 mm (1.25 in.) to 38 mm (1.5 in.), may also be adopted. These recommendations recognize the low chloride transport of UHPC and the strong influence of crack characteristics on durability. They are not service-life-based design provisions, however, because this project directly evaluated only 12.7 mm (0.5 in.) and 25.4 mm (1.0 in.) cover thicknesses. Additional long-term field testing and UHPC-specific service-life modeling are needed before these values can be adopted as prescriptive code requirements.

Before cracking, UHPC exhibited very limited chloride penetration and no active corrosion of the embedded steel reinforcement. The apparent chloride diffusion coefficient of uncracked UHPC was approximately 10^{-14} m²/s (10^{-13} ft.²/s), and the maximum chloride penetration depth measured using 0.1 N silver nitrate spray was only about 1 to 4 mm (0.04 to 0.16 in.). In addition, the corrosion current density, i_{corr}, of all embedded steel rebars remained within the passive range throughout the exposure period.

After cracking, the durability response can be classified into four crack width ranges: <0.20 mm (<0.008 in.); 0.20 to 0.40 mm (0.008 to 0.016 in.); 0.40 to 0.80 mm (0.016 to 0.031 in.); and >0.80 mm (>0.031 in.).

For cracks narrower than 0.20 mm (0.008 in.), chloride penetration was generally limited to the local region surrounding the crack, and the embedded steel reinforcement in UHPC remained close to a passive corrosion condition. When the primary crack width exceeded approximately 0.20 mm (0.008 in.), chloride transport became more pronounced. As shown in section 5.2, the chloride penetration area increased by more than 1.86 times when the primary crack width increased from approximately 80 μm to 200 μm (0.080 to 0.200 mm; 0.0031 to 0.0079 in.). A similar trend was observed in section 6.1, where the corrosion current density of UHPC specimens with 25.4 mm (1.0 in.) cover increased from 73 to 106 nA/cm² as the crack width increased from 79 μm to 230 μm (0.079 to 0.230 mm; 0.0031 to 0.0091 in.)

after 98 days of chloride wetting–drying exposure. This value still corresponds to an almost passive corrosion condition. However, for specimens with only 12.7 mm (0.5 in.) cover, the corrosion current density was already approximately 150 nA/cm² at a crack width of about 80 μm (0.080 mm; 0.0031 in.). Therefore, within this crack-width range, a 25.4 mm (1.0 in.) UHPC cover provided extremely high corrosion resistance.

The second crack-width range is 200 to 400 μm (0.008 to 0.016 in.) for UHPC. Within this range, the apparent chloride diffusion coefficient increased slightly with increasing crack width, and the corrosion current density also increased as the cracks became wider. Section 5.2 indicates that a transition point occurred at approximately 400 μm (0.40 mm; 0.016 in.), which may be considered a possible upper threshold crack width for durability evaluation. Within this range, chloride transport through cracks became more pronounced. The apparent chloride diffusion coefficient increased from approximately 5.3 to 9.3×10^{-11} m²/s to approximately 6.5 to 10.5×10^{-11} m²/s. Meanwhile, as shown in Section 6.1, the corrosion current density increased from 106 to 164 nA/cm² for UHPC with 25.4 mm (1.0 in.) cover and from 198 to 265 nA/cm² for UHPC with 12.7 mm (0.5 in.) cover. Section 6.1 also showed a similar trend when the crack width increased from approximately 300 to 550 μm (0.012 to 0.022 in.). Therefore, for conservative durability classification, cracks within this range should be treated as a transition zone in which both chloride diffusion and corrosion current density increase gradually with increasing crack width.

The third crack-width range is 400 to 800 μm (0.016 to 0.031 in.) for UHPC. In this range, chloride penetration became more severe, with deeper and wider penetration regions observed around the crack. Section 5.2 shows that when the crack width exceeded approximately 400 μm (0.016 in.), chloride could penetrate not only along the crack depth but also laterally into the surrounding UHPC matrix. Therefore, although the apparent chloride diffusion coefficient through the crack did not increase markedly with increasing crack width in this range, the overall chloride concentration increased rapidly because chloride transport expanded significantly in the horizontal direction. Under this condition, the crack wall can be regarded as an additional exposure surface. The corrosion current density also increased substantially as the crack width increased from approximately 400 μm to 800 μm (0.016 to 0.031 in.). Specifically, i_{corr} increased from 164 to 267 nA/cm² for UHPC with 25.4 mm (1.0 in.) cover and from 264 to 310 nA/cm² for UHPC with 12.7 mm (0.5 in.) cover. These results indicate that cracks wider than approximately 400 μm (0.40 mm; 0.016 in.) can substantially increase chloride accumulation and corrosion activity, even if the crack path diffusion coefficient does not increase proportionally with crack width.

The fourth crack width range is greater than 800 μm (>0.80 mm; >0.031 in.). Under this condition, chloride ions can penetrate into UHPC more efficiently because the crack network becomes more open and connected. The increased connectivity of pores along the crack surface and the reduced tortuosity of the transport path provide a more direct route for chloride ingress. As a result, further increases in crack width may not significantly change the transport properties of UHPC, because chloride penetration is already governed by the open crack pathway rather than by the dense UHPC matrix. Although the increase in corrosion current density may become less rapid with further crack widening, the corrosion activity is expected to remain relatively stable at a high level. This is because the supply of chloride ions, oxygen, and water is sufficient to sustain corrosion propagation once the crack width exceeds approximately 800 μm (0.031 in.). However, even in this severe crack width range, a 25.4 mm (1.0 in.) cover still effectively reduced the corrosion current density compared with a 12.7 mm (0.5 in.) cover. The reduction was approximately 67.8% for cracks around 800 μm (0.031 in.) and approximately 32.6% for cracks around 1400 μm (0.055 in.).

Table 7-1 Recommended crack-width action levels for UHPC with cover thicknesses greater than 1.0 in

Category	Crack-width	Recommended action
Preferred design target / routine field acceptance range	<0.20 mm (<0.0079 in.)	Use as the preferred design target and routine inspection acceptance range. Document representative and maximum crack widths, crack length, spacing or crack density, location relative to reinforcement, and crack pattern. Photograph or map the cracks. No repair is required based on crack width alone when the crack system is stable, non-leaking, not through depth, and not known to form a continuous path to reinforcement.
Exposure-sensitive monitoring preventive sealing range	0.20 to 0.40 mm (0.0079 to 0.0157 in.)	Map and photograph the crack pattern. Verify whether the cracks are stable, isolated or distributed, fiber-bridged, non-leaking, and not through depth. Review exposure severity, cover thickness, reinforcement type, crack orientation, crack depth or connectivity, and access for future inspection. Consider surface sealing in severe exposure zones, inaccessible locations, or areas where cracks are likely to remain wet.
Durability engineering review presumptive treatment range	0.40 to 0.80 mm (0.0157 to 0.0315 in.)	Do not treat this range as routine acceptable cracking. Require prompt engineering review. Seal or repair the cracks unless a project-specific durability assessment justifies continued service. Evaluate crack depth, crack connectivity, cover thickness, reinforcement type, exposure severity, chloride profile where applicable, corrosion potential and corrosion current density where applicable, and whether crack closure or self-healing is stable.
Immediate repair and durability / structural review range	>0.80 mm (>0.0315 in.)	Require immediate engineering review and repair. Require structural review when the crack is active, through-depth, leaking, associated with rust staining, delamination, spalling, impact damage, exposed reinforcement, abnormal deflection, or rapid crack growth. Consider corrosion testing and follow-up inspection after repair.

References

AASHTO (2010) *AASHTO LRFD bridge design specifications.* American Association of State Highway and Transportation Officials.

AASHTO T 259 (2002) *AASHTO T 259: Standard Method of Test to Resistance of Concrete to Chloride Ion Penetration*.

AASHTO T 260 (1997) *AASHTO T 260: Sampling and Testing for Chloride Ion in Concrete and Concrete Raw Materials*.

AASHTO T358 (2021) *Standard Method of Test for Surface Resistivity Indication of Concrete's Ability to Resist Chloride Ion Penetration*. Available at: www.salmanco.comwww.salmanco.com.

AASHTO T397 (2022) *Standard Method of Test for Uniaxial Tensile Response of Ultra-High Performance Concrete*. DC: Washington.

Abbas, S., Soliman, A.M. and Nehdi, M.L. (2015) 'Exploring mechanical and durability properties of ultra-high performance concrete incorporating various steel fiber lengths and dosages', *Construction and Building Materials*, 75, pp. 429–441. Available at: https://doi.org/10.1016/j.conbuildmat.2014.11.017.

ACI Committee 318 (2019) *318-19 Building Code Requirements for Structural Concrete and Commentary*, *318-19 Building Code Requirements for Structural Concrete and Commentary*. American Concrete Institute. Available at: https://doi.org/10.14359/51716937.

ACI Committee 522 (2010) *Report on pervious concrete*. American Concrete Institute.

AFGC/SETRA Working Group (2002) *Ultra High Performance Fibre-Reinforced Concretes-Interim Recommendations*. Paris. Available at: https://api.semanticscholar.org/CorpusID:139414306.

AFPC-AFREM (1997) *AFPC-AFREM: Durabilite´des be´tons, me´thodes recommande´espour la mesure des grandeurs associe´es a`la durabilite´, Modeope´ratoire recommande´, essai de carbonatation acce´le´re´,mesure del'e´paisseurde be´ton carbonate´, (Durability of Concretes: Recommended methods for measuring the quantities associated with durability)*. Paris.

Ahmad, S. (2003) 'Reinforcement corrosion in concrete structures, its monitoring and service life prediction—a review', *Cement and Concrete Composites*, 25(4–5), pp. 459–471. Available at: https://doi.org/10.1016/S0958-9465(02)00086-0.

Ahmed, S.F.U. and Mihashi, H. (2010) 'Corrosion durability of strain hardening fibre-reinforced cementitious composites', *Australian Journal of Civil Engineering*, 8(1), pp. 13–26. Available at: https://doi.org/10.1080/14488353.2010.11463959.

Aïtcin, P.-C. (2016) 'Accelerators', *Science and Technology of Concrete Admixtures*. Elsevier, pp. 405–413. Available at: https://linkinghub.elsevier.com/retrieve/pii/B9780081006931000199.

Akhavan, A., Shafaatian, S.-M.-H. and Rajabipour, F. (2012) 'Quantifying the effects of crack width, tortuosity, and roughness on water permeability of cracked mortars', *Cement and Concrete Research*, 42(2), pp. 313–320. Available at: https://doi.org/10.1016/j.cemconres.2011.10.002.

AL-Ameeri, A.S., Rafiq, M.I. and Tsioulou, O. (2021) 'Combined impact of carbonation and crack width on the Chloride Penetration and Corrosion Resistance of Concrete Structures', *Cement and Concrete Composites*, 115, p. 103819. Available at: https://doi.org/10.1016/j.cemconcomp.2020.103819.

Aldea, Corina-Maria, Shah, S.P. and Karr, A. (1999) 'Effect of Cracking on Water and Chloride Permeability of Concrete', *Journal of Materials in Civil Engineering*, 11(3), pp. 181–187. Available at:

https://doi.org/10.1061/(ASCE)0899-1561(1999)11:3(181).

Aldea, C -M., Shah, S.P. and Karr, A. (1999) 'Permeability of cracked concrete', *Materials and Structures*, 32(5), pp. 370–376. Available at: https://doi.org/10.1007/BF02479629.

Alharbi, Y.R. *et al.* (2021) 'Effect of using available metakaoline and nano materials on the behavior of reactive powder concrete', *Construction and Building Materials*, 269, p. 121344. Available at: https://doi.org/10.1016/j.conbuildmat.2020.121344.

Andrade, C. *et al.* (1992) 'The effect of macrocells between active and passive areas of steel reinforcements', *Corrosion Science*, 33(2), pp. 237–249. Available at: https://doi.org/10.1016/0010-938X(92)90148-V.

Angst, U. *et al.* (2009) 'Critical chloride content in reinforced concrete — A review', *Cement and Concrete Research*, 39(12), pp. 1122–1138. Available at: https://doi.org/10.1016/j.cemconres.2009.08.006.

Ann, K.Y. and Song, H.-W. (2007) 'Chloride threshold level for corrosion of steel in concrete', *Corrosion Science*, 49(11), pp. 4113–4133. Available at: https://doi.org/10.1016/j.corsci.2007.05.007.

Arya, C. and Ofori-Darko, F.K. (1996) 'Influence of crack frequency on reinforcement corrosion in concrete', *Cement and Concrete Research*, 26(3), pp. 345–353. Available at: https://doi.org/10.1016/S0008-8846(96)85022-8.

Asmatulu, R. and Khan, W.S. (2019) 'Characterization of electrospun nanofibers', *Synthesis and Applications of Electrospun Nanofibers*. Elsevier, pp. 257–281. Available at: https://linkinghub.elsevier.com/retrieve/pii/B9780128139141000134.

ASTM C 39 (2021) *Standard Test Method for Compressive Strength of Cylindrical Concrete Specimens*. West Conshohocken. Available at: https://doi.org/10.1520/C0039_C0039M-21.

ASTM C 642 (2021) *ASTM C 642 : Standard Test Method for Density, Absorption, and Voids in Hardened Concrete*. West Conshohocken.

ASTM C 876 (2022) *ASTM C 876: Standard Test Method for Corrosion Potentials of Uncoated Reinforcing Steel in Concrete*. Available at: https://doi.org/10.1520/C0876-15.

ASTM C 1202 (2022) *ASTM C 1202: Standard Test Method for Electrical Indication of Concrete's Ability to Resist Chloride Ion Penetration*. West Conshohocken. Available at: https://doi.org/10.1520/C1202-22E01.

ASTM C 1218 (2020) *ASTM C 1218: Standard Test Method for Water-Soluble Chloride in Mortar and Concrete*. West Conshohocken. Available at: https://doi.org/10.1520/C1218_C1218M-20.

ASTM C 1585 (2020) *ASTM C 1585: Standard Test Method for Measurement of Rate of Absorption of Water by Hydraulic Cement Concretes*. West Conshohocken.

ASTM C 1609 (2012) *Standard Test Method for Flexural Performance of Fiber-Reinforced Concrete (Using Beam With Third-Point Loading)*. West Conshohocken. Available at: https://doi.org/10.1520/C1609_C1609M-12.

ASTM C 1856 (2017) *Standard Practice for Fabricating and Testing Specimens of Ultra-High Performance Concrete*. West Conshohocken. Available at: https://doi.org/10.1520/C1856_C1856M-17.

ASTM C192 (2014) 'Practice for Making and Curing Concrete Test Specimens in the Laboratory', p. 8. Available at: https://doi.org/10.1520/C0192_C0192M-14.

ASTM C1609 (2012) ‘Test Method for Flexural Performance of Fiber-Reinforced Concrete (Using Beam With Third-Point Loading)’, pp. 1–9. Available at: https://doi.org/10.1520/C1609_C1609M-12.

ASTM Committee 09 (2019) *ASTM C136/136M-19 Standard Test Method for Sieve Analysis of Fine and Coarse Aggregates*. West Conshohocken. Available at: https://doi.org/10.1520/C0136_C0136M-19.

ASTM Committee 09 (2022) *ASTM C128-22 Standard Test Method for Relative Density (Specific Gravity) and Absorption of Fine Aggregate*. West Conshohocken. Available at: https://doi.org/10.1520/C0128-22.

ASTM Committee C01 (2018) *ASTM C1365-18 Standard Test Method for Determination of the Proportion of Phases in Portland Cement and Portland-Cement Clinker Using X-Ray Powder Diffraction Analysis*. West Conshohocken. Available at: https://doi.org/10.1520/C1365-18.

ASTM Committee C08 (2018) *ASTM C604-18 Standard Test Method for True Specific Gravity of Refractory Materials by Gas-Comparison Pycnometer*. West Conshohocken,. Available at: https://doi.org/10.1520/C0604-18.

ASTM Committee C09 (2016) *ASTM C1556-16: Standard Test Method for Determining the Apparent Chloride Diffusion Coefficient of Cementitious Mixtures by Bulk Diffusion*. West Conshohocken. Available at: https://doi.org/10.1520/C1556-11AR16.

ASTM Committee E29 (2022) *ASTM E3340-22 Standard Guide for Development of Laser Diffraction Particle Size Analysis Methods for Powder Materials*. West Conshohocken. Available at: https://doi.org/10.1520/E3340-22.

ASTM D 4404 (2018) *ASTM D 4404: Standard Test Method for Determination of Pore Volume and Distribution of Soil and Rock by Mercury Intrusion Porosimetry*. West Conshohocken.

ASTM D5084 (2016) *ASTM D5084: Standard Test Methods for Measurement of Hydraulic Conductivity of Saturated Porous Materials Using a Flexible Wall Permeameter*. West Conshohocken. Available at: https://doi.org/10.1520/D5084-16A.

ASTM G01 Committee (2024) *ASTM G3: Standard Practice for Conventions Applicable to Electrochemical Measurements in Corrosion Testing*. Available at: https://doi.org/10.1520/G0003-14R19.

ASTM G59 (2020) *ASTM G 59:Standard Test Method for Conducting Potentiodynamic Polarization Resistance Measurements*. West Conshohocken. Available at: https://doi.org/10.1520/G0059-97R20.

ASTM G109 (2021) *ASTM G 109 Determining Effects of Chemical Admixtures on Corrosion of Embedded Steel Reinforcement in Concrete Exposed to Chloride Environments*. West Conshohocken.

Audenaert, K., de Schutter, G. and Marsavina, L. (2009) ‘Influence of cracks and crack width on penetration depth of chlorides in concrete’, *European Journal of Environmental and Civil Engineering*, 13(5), pp. 561–572. Available at: https://doi.org/10.1080/19648189.2009.9693134.

Azarsa, P. and Gupta, R. (2017) ‘Electrical Resistivity of Concrete for Durability Evaluation: A Review’, *Advances in Materials Science and Engineering*. Hindawi Limited. Available at: https://doi.org/10.1155/2017/8453095.

Banaś, J. *et al.* (2007) ‘Effect of CO2 and H2S on the composition and stability of passive film on iron alloys in geothermal water’, *Electrochimica Acta*, 52(18), pp. 5704–5714. Available at: https://doi.org/10.1016/j.electacta.2007.01.086.

Bao, J. and Wang, L. (2017) ‘Effect of Short-Term Sustained Uniaxial Loadings on Water Absorption of

Concrete', *Journal of Materials in Civil Engineering*, 29(3), p. 04016234. Available at: https://doi.org/10.1061/(ASCE)MT.1943-5533.0001746.

Berrocal, C.G., Lundgren, K. and Löfgren, I. (2016) 'Corrosion of Steel Bars Embedded in Fibre Reinforced Concrete Under Chloride Attack: State-of-the-Art', *Cement and Concrete Research*, 80, pp. 69–85.

Bertolini, L. *et al.* (2014) *Corrosion of Steel in Concrete: Prevention, Diagnosis, Repair*. 2nd ed. John Wiley & Sons,.

Brown, M.C., Thelemann, A. and Sletten, J. (2020) *BRIDGE DECK CHLORIDE TESTING PROTOCOLS: Study of US-40 Bridges over the Provo River*. Utah Department of Transportation.

Bu, Y., Spragg, R. and Weiss, W.J. (2014) 'Comparison of the Pore Volume in Concrete as Determined Using ASTM C642 and Vacuum Saturation', *Advances in Civil Engineering Materials*, 3(1), p. 20130090. Available at: https://doi.org/10.1520/ACEM20130090.

Charron, J.-P., Denarié, E. and Brühwiler, E. (2008) 'Transport properties of water and glycol in an ultra high performance fiber reinforced concrete (UHPFRC) under high tensile deformation', *Cement and Concrete Research*, 38(5), pp. 689–698. Available at: https://doi.org/10.1016/j.cemconres.2007.12.006.

Chaudhry, R.H. (2018) *Determination of Air Voids, Capillary, and Gel Porosity in Hardened Concrete using Mass-Based Saturation Techniques*. Available at: https://tspace.library.utoronto.ca/handle/1807/82872.

Chen, G. *et al.* (2012) *Concrete surface with nano-particle additives for improved wearing resistance to increasing truck traffic (Report #MATC-MST: 441)*.

Chen, Y. *et al.* (2018) 'Evaluation and optimization of Ultra-High Performance Concrete (UHPC) subjected to harsh ocean environment: Towards an application of Layered Double Hydroxides (LDHs)', *Construction and Building Materials*, 177, pp. 51–62. Available at: https://doi.org/10.1016/j.conbuildmat.2018.03.210.

Covino, J., Bernard, S. and Stephen, D.C. (2012) *ASM Handbook: Corrosion: fundamentals, testing, and protection*.

Daniyal, M. and Akhtar, S. (2020) 'Corrosion assessment and control techniques for reinforced concrete structures: a review', *Journal of Building Pathology and Rehabilitation*, 5(1). Available at: https://doi.org/10.1007/s41024-019-0067-3.

DIN 1048 (1978) *DIN 1048 Test Methods of Concrete Impermeability to water: Part 2*.

Djerbi, A *et al.* (2008) 'Influence of traversing crack on chloride diffusion into concrete', *Cement and Concrete Research*, 38(6), pp. 877–883. Available at: https://doi.org/10.1016/j.cemconres.2007.10.007.

Djerbi, Assia *et al.* (2008) 'Influence of traversing crack on chloride diffusion into concrete', *Cement and Concrete Research*, 38(6), pp. 877–883. Available at: https://doi.org/10.1016/j.cemconres.2007.10.007ï.

Dobias, D., Pernicova, R. and Mandlik, T. (2016) 'Water Transport Properties and Depth of Chloride Penetration in Ultra High Performance Concrete', *Key Engineering Materials*, 711, pp. 137–142. Available at: https://doi.org/10.4028/www.scientific.net/KEM.711.137.

Durar, R. (1998) 'Manual de inspección, evaluación y diagnóstico de corrosión en estructuras de hormigón armado', *CYTED, Programa Iberoamericano de Ciencia y Tecnología para el Desarrollo, Subprograma XV Corrosión/Impacto Ambiental sobre Materiales (Maracaibo, Venezuela: CYTED, 1997)*

[Preprint].

El-Dieb, A.S. (2009) ‘Mechanical, durability and microstructural characteristics of ultra-high-strength self-compacting concrete incorporating steel fibers’, *Materials & Design*, 30(10), pp. 4286–4292. Available at: https://doi.org/10.1016/j.matdes.2009.04.024.

EN 12390 (2019) *EN 12390: Testing Hardened Concrete Depth of Penetration of Water under Pressure*.

Fan, L. *et al.* (2019) ‘Effect of steel fibers with galvanized coatings on corrosion of steel bars embedded in UHPC’, *Composites Part B: Engineering*, 177, p. 107445. Available at: https://doi.org/10.1016/j.compositesb.2019.107445.

Fan, L. *et al.* (2020) ‘Effects of lightweight sand and steel fiber contents on the corrosion performance of steel rebar embedded in UHPC’, *Construction and Building Materials*, 238, p. 117709. Available at: https://doi.org/10.1016/j.conbuildmat.2019.117709.

Fan, L., Teng, L., Tang, F., Khayat, Kamal H, *et al.* (2021) ‘Corrosion of steel rebar embedded in UHPC beams with cracked matrix’, *Construction and Building Materials*, 313, p. 125589. Available at: https://doi.org/10.1016/j.conbuildmat.2021.125589.

Fan, L., Teng, L., Tang, F., Khayat, Kamal H., *et al.* (2021) ‘Corrosion of steel rebar embedded in UHPC beams with cracked matrix’, *Construction and Building Materials*, 313. Available at: https://doi.org/10.1016/j.conbuildmat.2021.125589.

FDOT (2004) *Florida Method of Test For Concrete Resistivity as an Electrical Indicator of its Permeability (FM 5-578)*. Florida.

FDOT (2022) *FDOT Specification Section 346 -Portland Cement Concrete*.

FDOT FM(5-565) (2015) *Florida Method of Test for MEASUREMENT OF WATER PERMEABILITY OF COMPACTED ASPHALT PAVING MIXTURES Designation: FM 5-565*.

FDOT State Material Office (2018) *Florida Method of Test For Determining Low-Levels of Chloride in Concrete and Raw Materials Designation: FM 5-516*. Gainesville.

FHWA (2022) *Ultra-High Performance Concrete Bridges in the United States*, *FHWA*.

François, R., Laurens, S. and Deby, F. (2018) ‘Steel Corrosion in Reinforced Concrete’, *Corrosion and its Consequences for Reinforced Concrete Structures*. Elsevier, pp. 1–41. Available at: https://linkinghub.elsevier.com/retrieve/pii/B9781785482342500019.

Gao, P. *et al.* (2015) ‘Multi-scale simulation of capillary pores and gel pores in Portland cement paste’, p. 14.

Geng, J. *et al.* (2016) ‘Effect of carbonation on release of bound chlorides in chloride-contaminated concrete’, *Magazine of Concrete Research*, 68(7), pp. 353–363. Available at: https://doi.org/10.1680/jmacr.15.00234.

Gérard, B. *et al.* (1996) ‘Cracking and permeability of concrete under tension’, *Materials and Structures*, 29(3), pp. 141–151. Available at: https://doi.org/10.1007/BF02486159.

Gérard, B. and Marchand, J. (2000) *Influence of cracking on the diffusion properties of cement-based materials Part I: Influence of continuous cracks on the steady-state regime*, *Cement and Concrete Research*.

Ghafari, E. *et al.* (2014) ‘The effect of nanosilica addition on flowability, strength and transport properties

of ultra high performance concrete', *Materials & Design*, 59, pp. 1–9. Available at: https://doi.org/10.1016/j.matdes.2014.02.051.

Ghafari, E. *et al.* (2015a) 'Influence of nano-silica addition on durability of UHPC', *Construction and Building Materials*, 94, pp. 181–188. Available at: https://doi.org/10.1016/j.conbuildmat.2015.07.009.

Ghafari, E. *et al.* (2015b) 'Influence of nano-silica addition on durability of UHPC', *Construction and Building Materials*, 94, pp. 181–188. Available at: https://doi.org/10.1016/j.conbuildmat.2015.07.009.

Ghasemzadeh Mosavinejad, S.H. *et al.* (2020) 'Electrical and microstructural analysis of UHPC containing short PVA fibers', *Construction and Building Materials*, 235, p. 117448. Available at: https://doi.org/10.1016/j.conbuildmat.2019.117448.

Giaccio, G. *et al.* (2015) 'Contribution of fiber reinforcement in concrete affected by alkali-silica reaction', *Cement and Concrete Research*, 67, pp. 310–317. Available at: https://doi.org/10.1016/j.cemconres.2014.10.016.

Glass, G.K. (2003) 'Reinforcement corrosion', *Advanced Concrete Technology*. Elsevier, pp. 1–27. Available at: https://linkinghub.elsevier.com/retrieve/pii/B9780750656863502561.

Goyal, A. *et al.* (2018) 'A Review of Corrosion and Protection of Steel in Concrete', *Arabian Journal for Science and Engineering*, 43(10), pp. 5035–5055. Available at: https://doi.org/10.1007/s13369-018-3303-2.

Graybeal, B.A. (2006) *Material Property Characterization of Ultra-High Performance Concrete*. Federal Highway Administration.

Gu, C. ping, Ye, G. and Sun, W. (2015) 'A review of the chloride transport properties of cracked concrete: experiments and simulations', *Journal of Zhejiang University: Science A*. Zhejiang University, pp. 81–92. Available at: https://doi.org/10.1631/jzus.A1400247.

GWT (2002) *GWT(German Water permeation Test) 4000*.

Habel, K. *et al.* (2008) 'Ultra-high performance fibre reinforced concrete mix design in central Canada', *Canadian Journal of Civil Engineering*, 35(2), pp. 217–224. Available at: https://doi.org/10.1139/L07-114.

Hansson, C.M., Poursaee, A. and Laurent, A. (2006) 'Macrocell and microcell corrosion of steel in ordinary Portland cement and high performance concretes', *Cement and Concrete Research*, 36(11), pp. 2098–2102. Available at: https://doi.org/10.1016/j.cemconres.2006.07.005.

Hashimoto, K. *et al.* (2013) 'TENSION-SOFTENING BEHAVIOR AND CHLORIDE ION DIFFUSIVITY OF CRACKED ULTRA HIGH STRENGTH FIBER REINFORCED CONCRETE', *Reinforced Concrete*, p. 8.

Hornbostel, K., Larsen, C.K. and Geiker, M.R. (2013) 'Relationship between concrete resistivity and corrosion rate – A literature review', *Cement and Concrete Composites*, 39, pp. 60–72. Available at: https://doi.org/10.1016/j.cemconcomp.2013.03.019.

Hossain, S. *et al.* (2022) 'Properties and Behavior of Soil - Online Lab Manual', p. 125.

Islam, M.M., Zhang, Q. and Jin, Q. (2022) 'A review of existing codes and standards on design factors for UHPC placement and fiber orientation', *Construction and Building Materials*, 345, p. 128308. Available at: https://doi.org/10.1016/J.CONBUILDMAT.2022.128308.

Ismail, M. *et al.* (2008) 'Effect of crack opening on the local diffusion of chloride in cracked mortar

samples', *Cement and Concrete Research*, 38(8–9), pp. 1106–1111. Available at: https://doi.org/10.1016/j.cemconres.2008.03.009.

Jacobsen', S., Marchand', J. and Boisvert', L. (1996) *EFFECT OF CRACKING AND HEALING ON CHLORIDE TRANSPORT IN OPC CONCRETE*, *Cement and Concrete Research*.

Jang, S.Y., Kim, B.S. and Oh, B.H. (2011) 'Effect of crack width on chloride diffusion coefficients of concrete by steady-state migration tests', *Cement and Concrete Research*, 41(1), pp. 9–19. Available at: https://doi.org/10.1016/j.cemconres.2010.08.018.

Jenkins, A. (2015) *Surface resistivity as an alternative for rapid chloride permeability test of hardened concrete (Tech. Rep. FHWA-KS-14-15)*. Topeka.

Jin, W.L., Yan, Y.D. and Wang, H.L. (2010) 'Chloride diffusion in the cracked concrete', p. 7.

Karim, R., Najimi, M. and Shafei, B. (2019) 'Assessment of transport properties, volume stability, and frost resistance of non-proprietary ultra-high performance concrete', *Construction and Building Materials*, 227, p. 117031. Available at: https://doi.org/10.1016/j.conbuildmat.2019.117031.

Kollek, J.J. (1989) 'The determination of the permeability of concrete to oxygen by the Cembureau method—a recommendation', *Materials and Structures*, 22(3), pp. 225–230. Available at: https://doi.org/10.1007/BF02472192.

Kumaran, M.K. (1999) 'Moisture Diffusivity of Building Materials from Water Absorption Measurements', *Journal of Thermal Envelope and Building Science*, 22(4), pp. 349–355. Available at: https://doi.org/10.1177/109719639902200409.

de la Cruz, J.C., Colorado, D. and del Campo, J.M. (2015) 'Comparative study on porosity and permeability of conventional concrete and concrete with variable proportions of natural zeolite additions', *Revista de la construcción*, 14(3), pp. 72–78. Available at: https://doi.org/10.4067/S0718-915X2015000300009.

Leemann, A. *et al.* (2006) 'Influence of compaction on the interfacial transition zone and the permeability of concrete', *Cement and Concrete Research*, 36(8), pp. 1425–1433. Available at: https://doi.org/10.1016/j.cemconres.2006.02.010.

Leemann, A., Loser, R. and Münch, B. (2010) 'Influence of cement type on ITZ porosity and chloride resistance of self-compacting concrete', *Cement and Concrete Composites*, 32(2), pp. 116–120. Available at: https://doi.org/10.1016/j.cemconcomp.2009.11.007.

Lepech, M. and Li, V.C. (2005) 'WATER PERMEABILITY OF CRACKED CEMENTITIOUS COMPOSITES', p. 6.

Lepech, M.D. and Li, V.C. (2009) 'Water permeability of engineered cementitious composites', *Cement and Concrete Composites*, 31(10), pp. 744–753. Available at: https://doi.org/10.1016/j.cemconcomp.2009.07.002.

Li, X., Li, D. and Xu, Y. (2019) 'Modeling the effects of microcracks on water permeability of concrete using 3D discrete crack network', *Composite Structures*, 210, pp. 262–273. Available at: https://doi.org/10.1016/j.compstruct.2018.11.034.

Litorowicz, A. (2006) 'Identification and quantification of cracks in concrete by optical fluorescent microscopy', *Cement and Concrete Research*, 36(8), pp. 1508–1515. Available at: https://doi.org/10.1016/j.cemconres.2006.05.011.

Liu, R. *et al.* (2019) 'Improving the microstructure of ITZ and reducing the permeability of concrete with various water/cement ratios using nano-silica', *Journal of Materials Science*, 54(1), pp. 444–456. Available at: https://doi.org/10.1007/s10853-018-2872-5.

Löfgren, I., Stang, H. and Olesen, J.F. (2007) 'The WST method, a fracture mechanics test method for FRC', *Materials and Structures*, 41(1), pp. 197–211. Available at: https://doi.org/10.1617/s11527-007-9231-3.

Lopez-Calvo, H.Z. *et al.* (2018) 'Influence of crack width, cover depth and concrete quality on corrosion of steel in HPC containing corrosion inhibiting admixtures and fly ash', *Cement and Concrete Composites*, 88, pp. 200–210. Available at: https://doi.org/10.1016/j.cemconcomp.2018.01.016.

Lv, L.-S. *et al.* (2021a) 'Chloride ion transport properties in microcracked ultra-high performance concrete in the marine environment', *Construction and Building Materials*, 291, p. 123310. Available at: https://doi.org/10.1016/j.conbuildmat.2021.123310.

Lv, L.-S. *et al.* (2021b) 'Influence of steel fiber corrosion on tensile properties and cracking mechanism of ultra-high performance concrete in an electrochemical corrosion environment', *Construction and Building Materials*, 278, p. 122338. Available at: https://doi.org/10.1016/j.conbuildmat.2021.122338.

Ma, Z., Zhao, T. and Yao, X. (2016) 'Influence of Applied Loads on the Permeability Behavior of Ultra High Performance Concrete with Steel Fibers', *Journal of Advanced Concrete Technology*, 14(12), pp. 770–781. Available at: https://doi.org/10.3151/jact.14.770.

Marsavina, L. *et al.* (2009) 'Experimental and numerical determination of the chloride penetration in cracked concrete', *Construction and Building Materials*, 23(1), pp. 264–274. Available at: https://doi.org/10.1016/j.conbuildmat.2007.12.015.

Mather, B. and Ozyildirim, C. (2002) *SP-1(02): Concrete Primer*.

Mechtcherine, V. and Lieboldt, M. (2011) 'Permeation of water and gases through cracked textile reinforced concrete', *Cement and Concrete Composites*, 33(7), pp. 725–734. Available at: https://doi.org/10.1016/j.cemconcomp.2011.04.001.

Mohammed, T.U. *et al.* (2001) 'Effect of Crack Width and Bar Types on Corrosionof Steel in Concrete', *Journal of Materials in Civil Engineering*, 13(3), pp. 194–201. Available at: https://doi.org/10.1061/(ASCE)0899-1561(2001)13:3(194).

Mohammed, T.U., Otsuki, N. and Hamada, H. (2003) 'Corrosion of Steel Bars in Cracked Concrete under Marine Environment', *Journal of Materials in Civil Engineering*, 15(5), pp. 460–469. Available at: https://doi.org/10.1061/(ASCE)0899-1561(2003)15:5(460).

Montes, P., Bremner, T.W. and Lister, D.H. (2004) 'Influence of calcium nitrite inhibitor and crack width on corrosion of steel in high performance concrete subjected to a simulated marine environment', *Cement and Concrete Composites*, 26(3), pp. 243–253. Available at: https://doi.org/10.1016/S0958-9465(03)00043-X.

Mu, S., de Schutter, G. and Ma, B. (2013) 'Non-steady state chloride diffusion in concrete with different crack densities', *Materials and Structures*, 46(1–2), pp. 123–133. Available at: https://doi.org/10.1617/s11527-012-9888-0.

Neville, A. (1995) 'Chloride attack of reinforced concrete: an overview', *Materials and Structures*, 28, pp. 63–70.

Nguyen, T.N., Nguyen, T.T. and Pansuk, W. (2017) 'Experimental study of the punching shear behavior

of high performance steel fiber reinforced concrete slabs considering casting directions', *Engineering Structures*, 131, pp. 564–573. Available at: https://doi.org/10.1016/j.engstruct.2016.10.031.

Niu, L. and Zhang, S. (2021) 'Performance of Cracked Ultra-High-Performance Fiber-Reinforced Concrete Exposed to Dry-Wet Cycles of Chlorides', *Advances in Materials Science and Engineering*. Edited by L. Evangelista, 2021, pp. 1–11. Available at: https://doi.org/10.1155/2021/4625972.

NT BUILD 208 (1996) *NT BUILD 208 CONCRETE, HARDENED: CHLORIDE CONTENT BY VOLHARD TITRATION*. ESPOO.

NT Build 443 (1995) *NT Build 443: CONCRETE, HARDENED: ACCELERATED CHLORIDE PENETRATION*. ESPOO. Available at: www.nordtest.org.

NT BUILD 492 (1999) *NT Build 492: Concrete, Mortar and Cement-based Repair Materials: Chloride Migration Coefficient from Non-steady-state Migration Experiments*. ESPOO.

NT BUILD 492 - NORDTEST (1999) *Concrete, mortar and cement-based repair materials: Chloride migration coefficient from non-steady-state migration experiments*.

Otieno, M.B., Alexander, M.G. and Beushausen, H.-D. (2010) 'Corrosion in cracked and uncracked concrete – influence of crack width, concrete quality and crack reopening', *Magazine of Concrete Research*, 62(6), pp. 393–404. Available at: https://doi.org/10.1680/macr.2010.62.6.393.

Parangusan, H., Bhadra, J. and Al-Thani, N. (2021) 'A review of passivity breakdown on metal surfaces: influence of chloride- and sulfide-ion concentrations, temperature, and pH', *Emergent Materials*, 4(5), pp. 1187–1203. Available at: https://doi.org/10.1007/s42247-021-00194-6.

Park, S.-S., Kwon, S.-J. and Jung, S.H. (2012) 'Analysis technique for chloride penetration in cracked concrete using equivalent diffusion and permeation', *Construction and Building Materials*, 29, pp. 183–192. Available at: https://doi.org/10.1016/j.conbuildmat.2011.09.019.

Peng, Y.Z., Chen, K. and Hu, S.G. (2011) 'Durability and Microstructure of Ultra-High Performance Concrete Having High Volume of Steel Slag Powder and Ultra-Fine Fly Ash', *Advanced Materials Research*, 255–260, pp. 452–456. Available at: https://doi.org/10.4028/www.scientific.net/AMR.255-260.452.

Pia, G., Casnedi, L. and Sanna, U. (2016) 'Pore size distribution influence on suction properties of calcareous stones in cultural heritage: Experimental data and model predictions', *Advances in Materials Science and Engineering*, 2016, pp. 1–10. Available at: https://doi.org/10.1155/2016/7853156.

Picandet, V. and Khelidj, A. (2003) 'Gas and water permeability of cracked concrete', p. 11.

Picandet, V., Khelidj, A. and Bellegou, H. (2009) 'Crack effects on gas and water permeability of concretes', *Cement and Concrete Research*, 39(6), pp. 537–547. Available at: https://doi.org/10.1016/j.cemconres.2009.03.009.

Piérard, J., Dooms, B. and Cauberg, N. (2013) 'DURABILITY EVALUATION OF DIFFERENT TYPES OF UHPC', *Reinforced Concrete*, p. 10.

Polder, R.B. (2001) 'Test methods for on site measurement of resistivity of concrete ҭ a RILEM TC-154 technical recommendation', p. 7.

Popov, B.N. (2015) *Corrosion Engineering: Principles and Solved Problems*. Oxford: Elservier.

Pourjahanshahi, A. and Madani, H. (2021) 'Chloride diffusivity and mechanical performance of UHPC

with hybrid fibers under heat treatment regime', *Materials Today Communications*, 26, p. 102146. Available at: https://doi.org/10.1016/j.mtcomm.2021.102146.

Pyo, S. *et al.* (2017) 'Effect of chloride content on mechanical properties of ultra high performance concrete', *Cement and Concrete Composites*, 84, pp. 175–187. Available at: https://doi.org/10.1016/j.cemconcomp.2017.09.006.

Pyo, S. *et al.* (2019) 'Chloride-induced corrosion of steel fiber near the surface of ultra-high performance concrete and its effect on flexural behavior with various thickness', *Construction and Building Materials*, 224, pp. 206–213. Available at: https://doi.org/10.1016/j.conbuildmat.2019.07.063.

Qian, R. *et al.* (2020) 'Investigation on parameters optimization for gas permeability testing of concrete: Inlet-gas pressure and confining pressure', *Construction and Building Materials*, 250. Available at: https://doi.org/10.1016/j.conbuildmat.2020.118901.

Reinhardt, H.-W. and Jooss, M. (2003) 'Permeability and self-healing of cracked concrete as a function of temperature and crack width', *Cement and Concrete Research*, 33(7), pp. 981–985. Available at: https://doi.org/10.1016/S0008-8846(02)01099-2.

Riding, K. *et al.* (2022) *Ultra-High-Performance Concrete (UHPC) Use in Florida Structural Applications (BDV31 977-105)*. Tallahassee.

RILEM TC 116-PCD (1999) *RILEM TC 116-PCD: Permeability of Concrete as a Criterion of its Durability*.

Rocco, C. *et al.* (2001) 'Review of the splitting-test standards from a fracture mechanics point of view', *Cement and Concrete Research*, 31(1), pp. 73–82. Available at: https://doi.org/10.1016/S0008-8846(00)00425-7.

Rodrigues, R. *et al.* (2021) 'Reinforced concrete structures: A review of corrosion mechanisms and advances in electrical methods for corrosion monitoring', *Construction and Building Materials*, 269, p. 121240. Available at: https://doi.org/10.1016/j.conbuildmat.2020.121240.

Rupnow, T. and Icenogle, P. (2012) *Evaluation of surface resistivity measurements as an alternative to the rapid chloride permeability test for quality assurance and acceptance (Tech. Rep. 2290)*. Baton Rouge.

Şahmaran, M. and Yaman, İ.Ö. (2008) 'Influence of transverse crack width on reinforcement corrosion initiation and propagation in mortar beams', *Canadian Journal of Civil Engineering*, 35(3), pp. 236–245. Available at: https://doi.org/10.1139/L07-117.

San Nicolas, R.V.R., Walkley, B. and van Deventer, J.S.J. (2017) 'Fly ash-based geopolymer chemistry and behavior', *Coal Combustion Products (CCP's)*. Elsevier, pp. 185–214. Available at: https://linkinghub.elsevier.com/retrieve/pii/B9780081009451000071.

Sandoval, G.F.B. *et al.* (2017) 'Comparison between the falling head and the constant head permeability tests to assess the permeability coefficient of sustainable Pervious Concretes', *Case Studies in Construction Materials*, 7, pp. 317–328. Available at: https://doi.org/10.1016/j.cscm.2017.09.001.

Schiessl, P. and Raupach, M. (1997) 'Laboratory Studies and Calculations on the Influence of Crack Width on Chloride-Induced Corrosion of Steel in Concrete', *ACI Materials Journal*, 94(1). Available at: https://doi.org/10.14359/285.

Scott, A. and Alexander, M.G. (2007) 'The influence of binder type, cracking and cover on corrosion rates of steel in chloride-contaminated concrete', *Magazine of Concrete Research*, 59(7), pp. 495–505.

Available at: https://doi.org/10.1680/macr.2007.59.7.495.

Scrivener, K.L. and Gartner, E.M. (1987) 'Microstructural Gradients in Cement Paste Around Aggregate Particles', *MRS Proceedings*, 114, p. 77. Available at: https://doi.org/10.1557/PROC-114-77.

Shafikhani, M. and Chidiac, S.E. (2019) 'Quantification of concrete chloride diffusion coefficient – A critical review', *Cement and Concrete Composites*, 99, pp. 225–250. Available at: https://doi.org/10.1016/j.cemconcomp.2019.03.011.

Shaikh, F.U.A. (2018) 'Effect of Cracking on Corrosion of Steel in Concrete', *International Journal of Concrete Structures and Materials*, 12(1), p. 3. Available at: https://doi.org/10.1186/s40069-018-0234-y.

Shanmugasundaram, A. and Jayakumar, K. (2022) 'Effect of curing regimes on microstructural and strength characteristics of UHPC with ultra-fine fly ash and ultra-fine slag as a replacement for silica fume', *Arabian Journal of Geosciences*, 15(4), p. 345. Available at: https://doi.org/10.1007/s12517-022-09617-y.

Shin, K.J. *et al.* (2017) 'Parameters influencing water permeability coefficient of cracked concrete specimens', *Construction and Building Materials*, 151, pp. 907–915. Available at: https://doi.org/10.1016/j.conbuildmat.2017.06.093.

Shin, W. and Yoo, D.-Y. (2020) 'Influence of steel fibers corroded through multiple microcracks on the tensile behavior of ultra-high-performance concrete', *Construction and Building Materials*, 259, p. 120428. Available at: https://doi.org/10.1016/j.conbuildmat.2020.120428.

Sohail, M.G. *et al.* (2021) 'Durability characteristics of high and ultra-high performance concretes', *Journal of Building Engineering*, 33, p. 101669. Available at: https://doi.org/10.1016/j.jobe.2020.101669.

Song, H.-W. and Saraswathy, V. (2007) 'Corrosion Monitoring of Reinforced Concrete Structures - A Review', *Int. J. Electrochem. Sci.*, 2, p. 29.

Song, Q. *et al.* (2018) 'Steel fibre content and interconnection induced electrochemical corrosion of Ultra-High Performance Fibre Reinforced Concrete (UHPFRC)', *Cement and Concrete Composites*, 94, pp. 191–200. Available at: https://doi.org/10.1016/j.cemconcomp.2018.09.010.

Song, Q. *et al.* (2019) 'Physical and chemical coupling effect of metakaolin induced chloride trapping capacity variation for Ultra High Performance Fibre Reinforced Concrete (UHPFRC)', *Construction and Building Materials*, 223, pp. 765–774. Available at: https://doi.org/10.1016/j.conbuildmat.2019.07.047.

Stanish, K.D., Hooton, R.D. and Thomas, M.D.A. (2001) *Testing the Chloride Penetration Resistance of Concrete: A Literature Review*. Toronto: University of Civil Engineering.

Stehlík, M., Věra Heřmánková, V.H. and Vítek, L. (2015) 'OPENING OF MICROCRACKS AND AIR PERMEABILITY IN CONCRETE', *Journal of Civil Engineering and Management*, 21(2), pp. 177–184. Available at: https://doi.org/10.3846/13923730.2013.802721.

Tafraoui, A., Escadeillas, G. and Vidal, T. (2016) 'Durability of the Ultra High Performances Concrete containing metakaolin', *Construction and Building Materials*, 112, pp. 980–987. Available at: https://doi.org/10.1016/j.conbuildmat.2016.02.169.

Tai, Y.-S. *et al.* (2020) 'Parameters Influencing Fluidity of UHPC and Their Effect on Mechanical and Durability Properties', *Journal of Materials in Civil Engineering*, 32(10), p. 04020298. Available at: https://doi.org/10.1061/(ASCE)MT.1943-5533.0003392.

Tam, C.M., Tam, V.W.Y. and Ng, K.M. (2012) 'Assessing drying shrinkage and water permeability of

reactive powder concrete produced in Hong Kong', *Construction and Building Materials*, 26(1), pp. 79–89. Available at: https://doi.org/10.1016/j.conbuildmat.2011.05.006.

Tam, W. (2005) *Recycled aggregate from concrete waste for higher grades of concrete construction*.

Tanaka, Y. *et al.* (2010) 'Durability performance of UFC sakata-mira footbridge under sea environment', p. 7.

Teng, L., Meng, W. and Khayat, K.H. (2020) 'Rheology control of ultra-high-performance concrete made with different fiber contents', *Cement and Concrete Research*, 138. Available at: https://doi.org/10.1016/j.cemconres.2020.106222.

Torrent, R.J. (1992) 'A two-chamber vacuum cell for measuring the coefficient of permeability to air of the concrete cover on site', *Materials and Structures*, 25, pp. 358–365.

Torrijos, M.C., Giaccio, G. and Zerbino, R. (2010) 'Internal cracking and transport properties in damaged concretes', *Materials and Structures/Materiaux et Constructions*, 43(SUPPL. 1), pp. 109–121. Available at: https://doi.org/10.1617/s11527-010-9602-z.

Wang, H.-L. *et al.* (2016) 'Characteristics of concrete cracks and their influence on chloride penetration', *Construction and Building Materials*, 107, pp. 216–225. Available at: https://doi.org/10.1016/j.conbuildmat.2016.01.002.

Wang, J. *et al.* (2020) 'Effect of nano-silica on chemical and volume shrinkage of cement-based composites', *Construction and Building Materials*, 247, p. 118529. Available at: https://doi.org/10.1016/j.conbuildmat.2020.118529.

Wang, K. *et al.* (1997) 'Permeability study of cracked concrete', *Cement and Concrete Research*, 27(3), pp. 381–393. Available at: https://doi.org/10.1016/S0008-8846(97)00031-8.

Wang, R. *et al.* (2018) 'Influence of splitting load on transport properties of ultra-high performance concrete', *Construction and Building Materials*, 171, pp. 708–718. Available at: https://doi.org/10.1016/j.conbuildmat.2018.03.174.

Wang, S. *et al.* (2022) 'Direct characterization of steel fibre corrosion in pre-cracked ultra-high performance concrete (UHPC) with different crack widths', *Construction and Building Materials*, 315, p. 125769. Available at: https://doi.org/10.1016/j.conbuildmat.2021.125769.

Wang, W. *et al.* (2014) 'Durability of an Ultra High Performance Fiber Reinforced Concrete (UHPFRC) under progressive aging', *Cement and Concrete Research*, 55, pp. 1–13. Available at: https://doi.org/10.1016/j.cemconres.2013.09.008.

Wille, K. and Parra-Montesinos, G.J. (2012) 'Effect of Beam Size, Casting Method, and Support Conditions on Flexural Behavior of Ultra-High-Performance Fiber-Reinforced Concrete', *ACI Material Journal*, 109(3), pp. 379–388.

Xue, J. *et al.* (2020) 'Review of ultra-high performance concrete and its application in bridge engineering', *Construction and Building Materials*, 260, p. 119844. Available at: https://doi.org/10.1016/j.conbuildmat.2020.119844.

Yang, Z., Weiss, W.J. and Olek, J. (2006) 'Water Transport in Concrete Damaged by Tensile Loading and Freeze–Thaw Cycling', *Journal of Materials in Civil Engineering*, 18(3), pp. 424–434. Available at: https://doi.org/10.1061/(ASCE)0899-1561(2006)18:3(424).

Yazıcı, H. (2007) 'The effect of curing conditions on compressive strength of ultra high strength concrete

with high volume mineral admixtures', *Building and Environment*, 42(5), pp. 2083–2089. Available at: https://doi.org/10.1016/j.buildenv.2006.03.013.

Ye, H. *et al.* (2017) 'An Experimental Study on Relationship among Water Sorptivity, Pore Characteristics, and Salt Concentration in Concrete', *Periodica Polytechnica Civil Engineering* [Preprint]. Available at: https://doi.org/10.3311/PPci.9621.

Yoo, D.-Y., Gim, J.Y. and Chun, B. (2020) 'Effects of rust layer and corrosion degree on the pullout behavior of steel fibers from ultra-high-performance concrete', *Journal of Materials Research and Technology*, 9(3), pp. 3632–3648. Available at: https://doi.org/10.1016/j.jmrt.2020.01.101.

Yoo, D.-Y., Shin, W. and Banthia, N. (2021) 'Corrosion of partially and fully debonded steel fibers from ultra-high-performance concrete and its influence on pullout resistance', *Cement and Concrete Composites*, 124, p. 104269. Available at: https://doi.org/10.1016/j.cemconcomp.2021.104269.

Yoon, I.-S. and Schlangen, E. (2014) 'Experimental examination on chloride penetration through micro-crack in concrete', *KSCE Journal of Civil Engineering*, 18(1), pp. 188–198. Available at: https://doi.org/10.1007/s12205-014-0196-9.

Zhang, P. *et al.* (2019) 'Durability of Steel Fiber-Reinforced Concrete Containing SiO2 Nano-Particles', *Materials*, 12(13), p. 2184. Available at: https://doi.org/10.3390/ma12132184.

Zhang, Y. *et al.* (2020) 'Comparative laboratory measurement of pervious concrete permeability using constant-head and falling-head permeameter methods', *Construction and Building Materials*, 263, p. 120614. Available at: https://doi.org/10.1016/j.conbuildmat.2020.120614.

Zheng, H. *et al.* (2022) 'Corrosion behavior of carbon steel in chloride-contaminated ultra-high-performance cement pastes', *Cement and Concrete Composites*, 128, p. 104443. Available at: https://doi.org/10.1016/j.cemconcomp.2022.104443.

Zhou, C., Li, K. and Pang, X. (2012) 'Geometry of crack network and its impact on transport properties of concrete', *Cement and Concrete Research*, 42(9), pp. 1261–1272. Available at: https://doi.org/10.1016/j.cemconres.2012.05.017.